REPORT DOCUMENTATION PAGE

AFOSR-TR-97

0514

1. AGENCY USE ONLY (Leave blank)	2. REPORT DATE	3. REPORT TYPE AND DATES COVERED
	19 August 1997	Technical 1 June 1996 - 31 May 1997

4. TITLE AND SUBTITLE
(U) ARO and AFOSR Contractors Meeting in Chemical Propulsion

5. FUNDING NUMBERS
PE - 61102A
61102F

6. AUTHOR(S)
David M. Mann and Julian M. Tishkoff

7. PERFORMING ORGANIZATION NAME(S) AND ADDRESS(ES)
Air Force Office of Scientific Research
Bolling AFB DC 20332-8050

Army Research Office
Research Triangle Park NC 27709-2211

NA

8. PERFORMING ORGANIZATION REPORT NUMBER

9. SPONSORING/MONITORING AGENCY NAME(S) AND ADDRESS(ES)
Same as 7

10. SPONSORING/MONITORING AGENCY REPORT NUMBER

11. SUPPLEMENTARY NOTES

12a. DISTRIBUTION/AVAILABILITY STATEMENT
Approved for public release; distribution is unlimited

12b. DISTRIBUTION CODE

13. ABSTRACT *(Maximum 200 words)*

Abstracts are given for research in chemical propulsion supported by the Air Force Office of Scientific Research and the Army Research Office.

14. SUBJECT TERMS	15. NUMBER OF PAGES
Flames, Propulsion, Gas Turbines, Diesel Engines, Scramjets, Ram Accelerators, Soot, Sprays, Turbulence, Siagnostics	196
	16. PRICE CODE

17. SECURITY CLASSIFICATION OF REPORT	18. SECURITY CLASSIFICATION OF THIS PAGE	19. SECURITY CLASSIFICATION OF ABSTRACT	20. LIMITATION OF ABSTRACT
Unclassified	Unclassified	Unclassified	UL

Ohio Aerospace Institute
June 17–19, 1997

ARO/AFOSR Contractors Meeting in Chemical Propulsion

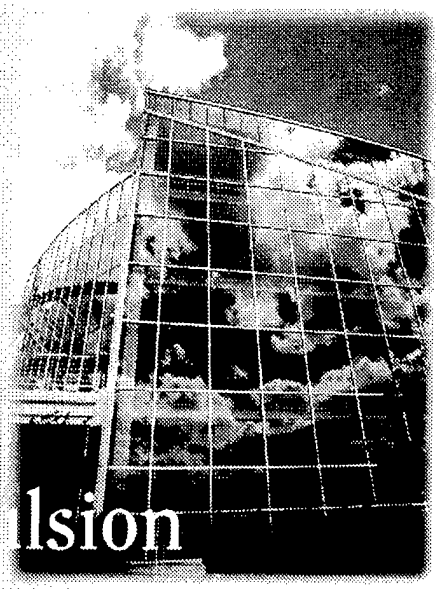

NASA Lewis Research Center
ADVANCED SUBSONIC COMBUSTION RIG

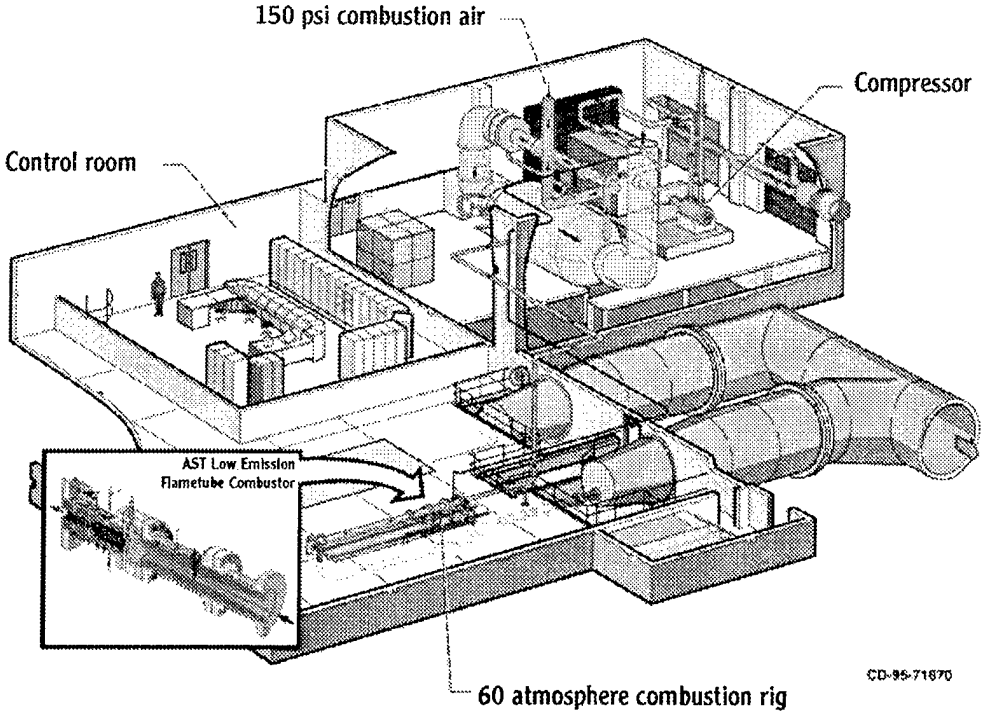

ARO/AFOSR CONTRACTORS MEETING

IN

CHEMICAL PROPULSION

Ohio Aerospace Institute
(adjacent to the NASA Lewis Research Center)
Cleveland OH
June 17-19, 1997

TUESDAY, 17 JUNE

12:45 - 1:30	Registration
1:30 - 1:45	Army Research Office Overview David Mann
1:45 - 2:00	Air Force Office of Scientific Research Overview Julian Tishkoff
2:00 - 2:30	Promoting University - Industry - Government Collaboration Michael Salkind, Ohio Aerospace Institute
2:30 - 3:00	BREAK

TOPIC: Ram Acclerators

Session Chairman: Dr. William Anderson, US Army Research Laboratory

3:00 - 3:30	Investigation of Gasdynamic Phenomena in the Ram Accelerator Adam P. Bruckner, University of Washington
3:30 - 4:00	Shock Tube Studies of Ram Accelerator Phenomena Ronald K. Hanson, Stanford University
4:00 - 4:30	Ignition Delay Times and Structure of Detonation Waves in $CH_4/O_2/N_2$ and $H_2/O_2/N_2$ Kal Seshradi, University of California, San Diego
4:45 - 5:45	Tour of Selected NASA Experimental Combustion Facilities
6:00 - 7:30	DINNER at OAI

7:30 - 10:00 WORKSHOP - Conducting Research at Government Laboratories

Panel Representatives
Air Force Wright Laboratory
NASA Lewis Research Center
NASA Langley Research Center
Sandia Laboratory, Combustion Research Facility

WEDNESDAY, 18 JUNE

7:45 - 8:15 Continental Breakfast

8:15 - 8:30 Announcements

Topic: Diesel Engines

Session Chairman: Dr. Ernest Schwarz, US Army Tank-Automotive Command

8:30 - 9:00 Analysis of Advanced Direct-Injection Diesel Engine Development Strategies
K. T. Rhee, Rutgers University

9:00 - 9:30 Visualization High Power-Density Diesel Engine Combustion
Ming-Chia Lai, Wayne State University

9:30 - 10:00 Large Eddy Simulation of Diesel Combustion Chambers
Ismail Celik, West Virginia University

10:00 - 10:30 BREAK

10:30 - 11:00 A University Research Initiative Program for Advanced Diesel Engine Research
David E. Foster, University of Wisconsin

11:00 - 11:30 Research Instrumentation and Collaborative Research in Diesel Engine Combustion
David E. Klett, North Carolina Agricultural and Technical State University

11:30 - 12:00 Engineering Model Development for Diesel Performance and Emissions
A. M. Mellor, Vanderbilt University

12:00 - 1:15 LUNCH

TOPIC: Combustion Physics and Chemistry

Session Chairman: Andrew DePristo, Department of Energy

1:15 - 1:45	High pressure Preignition Chemistry of Hydrocarbons and Hydrocarbon Mixtures Nicholas Cernansky, Drexel University
1:45 - 2:15	Ignition in Convective-Diffusive Systems C. K. Law, Princeton University
2:15 - 2:45	Studies on High-Pressure and Unsteady Flame Phenomena C. K. Law, Princeton University
2:45 - 3:15	BREAK
3:15 - 3:45	Flamelet Surface Density and Burning Rate Integral In Premixed Combustion Frederick C. Gouldin, Cornell University
3:45 - 4:15	Turbulence-Chemistry Models for Highly Turbulent Flames Sanjay Correa, General Electric Corporate Research and Development
4:15 - 4:45	Two- and Three-Dimensional Measurements in Flames Marshall B. Long, Yale University
5:00 - 5:15	BUSINESS SESSION - Contractors in Dr. Mann's Program Only
5:15 - 5:45	BUSINESS SESSION - Contractors in Dr. Tishkoff's Program Only
6:00 - 9:00	DINNER at NASA Lewis Picnic Grounds

THURSDAY, 19 JUNE

7:45 - 8:15	Continental Breakfast
8:15 - 8:30	Announcements

TOPIC: Turbulent Combustion

Session Chairman: Gabriel Roy, Office of Naval Research

8:30 - 9:00	Modeling Mixing and Reaction in Turbulent Combustion Stephen B. Pope, Cornell University

9:00 - 9:30	Evaluation of Closure Models for Turbulent Diffusion Flames George Kosaly and James J. Riley, University of Washington
9:30 - 10:00	Combustion Research W. M. Roquemore, Wright Laboratory
10:00 - 10:30	BREAK

Topic: Interdisciplinary Nonmetallic Materials-Combustion Research

10:30 - 11:30	Alexander Pechenik, Air Force Office of Scientific Research
11:30 - 12:30	LUNCH

Topic: Supersonic Combustion

Session Chairman: J. P. Drummond, NASA Langley Research Center

12:30 - 1:15	Chemical Reactions in Turbulent Mixing Flows Paul E. Dimotakis and Anthony Leonard, California Institute of Technology
1:15 - 1:45	Compressible Turbulent Reactive Flows Forman A. Williams, Paul A. Libby, and Satanu Sarkar, University of California, San Diego
1:45 - 2:15	Mechanisms and Control of Unsteady Flow in Scramjet Combustors Frank E. Marble and Edward E. Zukoski, California Institute of Technology
2:15 - 2:45	BREAK
2:45 - 3:15	High Resolution Measurements of Supersonic Mixing and Combustion in Coflowing Turbulent Jets Werner J. A. Dahm and James F. Driscoll, University of Michigan
3:15 - 3:45	Ramjet Research Abdollah S. Nejad, Wright Laboratory
3:45	ADJOURN

TABLE OF CONTENTS

INVESTIGATION OF REACTIVE GASDYNAMIC PHENOMENA IN THE RAM ACCELERATOR

ARO Grant No. DAAL03-92-G-0100

Adam P. Bruckner

Aerospace and Energetics Research Program
University of Washington
Seattle, WA 98195-2250

SUMMARY/OVERVIEW:

Experimental investigations have been performed to improve the understanding of the gasdynamics of the starting process of the ram accelerator and to optimize the thrust performance of the thermally choked propulsive mode. Aspects of the starting process that have been investigated include the effects of Mach number, propellant chemistry, obturator geometry and mass, launch tube residual pressure, launch tube venting, and projectile throat area variations. An operational envelope has been developed which places the possible start outcomes relative to one another in a parameter space based on entrance Mach number and propellant composition. Experiments have also been performed with a reduced mass projectile in various combustible mixtures, wherein Mach number and heat release of combustion were varied to obtain very high accelerations. Sustained accelerations of nearly 40,000 g over a single 2-m-long stage and 35,000 g in two and three stage configurations were observed.

TECHNICAL DISCUSSION:

The ram accelerator is a hypervelocity launcher in which a subcaliber projectile, similar in shape to the centerbody of a ramjet, travels supersonically through a tube filled with premixed gaseous fuel and oxidizer. A conventional powder gun or gas gun initially boosts the projectile to supersonic entrance velocity. One goal of the investigations has been to improve the understanding of transition from the conventional gun to the ram accelerator; this is referred to as the "starting process". Developing a robust starting process is key to the utilization of the ram accelerator in a variety of applications of interest to the Armed Forces. Four possible outcomes of a start attempt have been identified. A successful start is achieved when supersonic flow is maintained throughout the diffuser, and the shock system is stabilized on the projectile body through propellant energy release. A sonic diffuser unstart is caused by conditions upstream of the throat resulting in subsonic flow in the diffuser. A wave fall-off occurs when insufficient energy is released from the propellant to keep the shock system on the projectile body. A wave unstart is caused by conditions downstream of the throat resulting in disgorgement of the shock system on the body into the diffuser. Projectile start attempt experiments were used to explore the limits to successful starting, study the association of detonations with the wave unstart process, improve understanding of the flowfield in the launch tube and ram accelerator tube in the vicinity of the entrance diaphragm, and investigate the effects of Mach number, propellant chemistry, obturator geometry and mass, and projectile throat area variations on the starting process. The lack of a sufficient number of detailed parametric experiments precludes the presentation of quantitative starting envelopes at this time, but a qualitative envelope has been developed which places the possible start outcomes relative to one another in a parameter space based on entrance Mach number and propellant composition (Fig. 1). Increased propellant energy release (Q) is conducive to a wave unstart, while decreased Q eventually leads to a wave fall-off. Wave unstarts were found to occur at Mach numbers above and below successful

starting conditions, and wave fall-offs were limited to Mach numbers below conditions which resulted in a successful start or wave unstart. Detonations were often observed in conjunction with wave unstarts, and for relatively high Q and Mach number these occurred immediately after the projectile entered the ram accelerator.

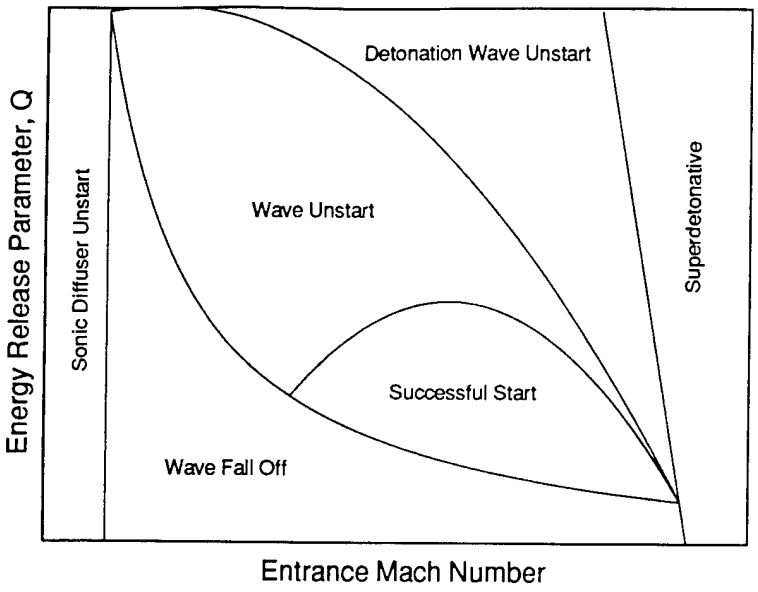

Fig. 1 Generalized ram accelerator starting envelope.

Conditions in the launch tube of the conventional gun also influence the starting dynamics. Normal operation of the ram accelerator involves the use of a perforated vent tube to relieve the launch tube gases into an evacuated dump tank before the projectile enters the ram accelerator tube. The need for a large dump tank and the equipment to evacuate it makes this venting process impractical for many applications. Experiments were performed to determine the feasibility of operating with a ventless launch tube and at elevated launch tube pressure levels, i.e., above a few torr. The starting process was successful in ventless configuration for propellant fill pressures of 30 atm and above, but failed repeatedly at 25 atm. These results are encouraging because most applications of the ram accelerator involve fill pressures greater than 30 atm. The start failures at 25 atm were a result of a large transient pressure buildup in front of the obturator. This pressure rise was caused by repeated reflections of the obturator-generated shock wave between the moving projectile/obturator and the entrance diaphragm. It appears that the start failures were caused by the diaphragm bursting prematurely due to high launch tube gas compression levels in the ventless configuration. Experiments were also performed in vented configuration with the residual launch tube air pressure varied from 1 to 4 psi, with the ram accelerator tube containing propellant at 50 atm. For launch tube pressures greater than 3 psi, start failure was determined to be a result of relatively high levels of launch tube gas compression that led to premature diaphragm rupture. Thickening the entrance diaphragm is expected to permit starts at higher launch tube pressures; the desired goal is to achieve successful starts at atmospheric pressure.

Methods of optimizing thrust performance and obtaining higher velocities in the thermally choked ram accelerator have also been investigated. By demonstrating the potential of the ram accelerator to accelerate projectiles to speeds on the order of 3 km/s in relatively short tubes, the technology will become suitable to a wide variety of defense applications, as well as research into hypersonic propulsion cycles, aeroballistic ranges and hypervelocity impact. The approach

taken was to first develop a projectile design which achieved sustained ram acceleration through the thermally choked regime with a low mass, allowing very high acceleration levels. Increasing the nose angle and reducing the body length allowed a reduction in mass from 75 gm to 50 gm for a projectile manufactured from aluminum alloy. According to quasi-one-dimensional theory, the thrust of a thermally choked ram accelerator is dependent on the freestream Mach number of the projectile relative to the propellant mixture *(M)* and the mixture's heat release *(Q)** as shown in Fig. 2. Experiments were performed to find a mixture which could successfully initiate ram accelerator operation at a relatively low entrance Mach number (M_{in}) and high Q. As seen in Fig. 2, as the projectile accelerates past about Mach 3, the thrust begins to fall off rapidly. This is the motivation for staging, a common practice in ram accelerators, wherein the projectile transitions into a mixture with a higher sound speed, thus lowering M. The stage length is limited to the length of the individual tubes of the ram accelerator, which is 2 m for the University of Washington facility.

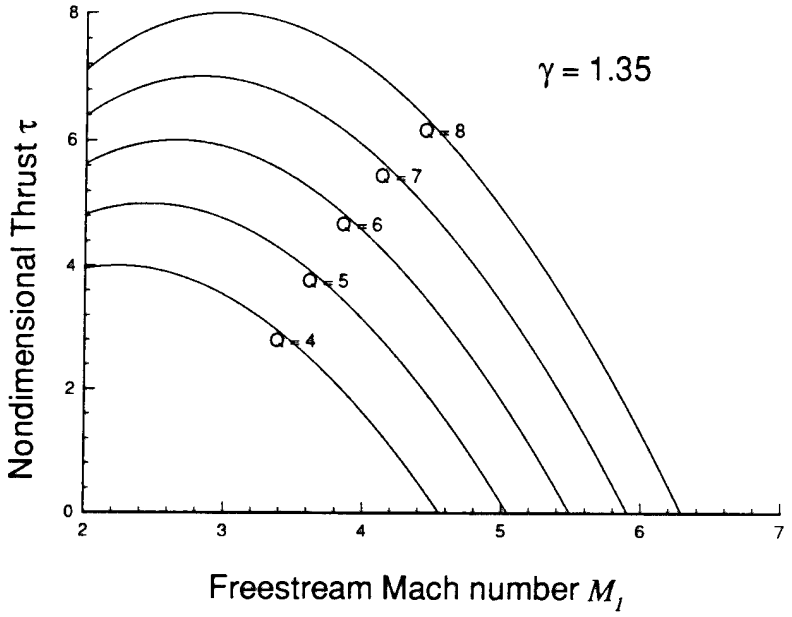

Fig. 2 Variation of thrust with free stream Mach number at various values of Q.

The experiments were performed to find the lowest value of M_{in} and highest value of Q that would support thermally choked ram acceleration in a 2 m stage. These two parameters are highly coupled; therefore, to better understand their relationship and to guide the experiments, a "mixture map" was created which shows how M_{in} and Q vary with mixture composition. Figure 3 shows such a map for a methane-oxygen-helium propellant mixture at 50 atm fill pressure and 1800 m/sec projectile entrance velocity. Methane content is plotted along the X-axis, helium content along the Y-axis, and the oxidizer content is set at $2O_2$. Q is computed using a chemical equilibrium code; lines of constant Q, or "iso-Q lines" are plotted as shown in Fig. 3. If the entrance velocity to the mixture is known, then M_{in} can be plotted as a function of composition; in Fig. 3, lines of constant M_{in} are plotted. Using thermally choked theory, a model of the performance of the ram accelerator was developed which, knowing the propellant mixture composition, allows the average acceleration of a projectile of given mass over a given stage length to be predicted. The acceleration levels then vary as a function of mixture composition, and are plotted on the mixture map as well.

---

* Q is the non-dimensional heat release: $Q = \Delta q / C_p T$, where Δq is the heat of combustion, and C_p and T are the specific heat at constant pressure and the temperature, respectively, of the undisturbed gas mixture.

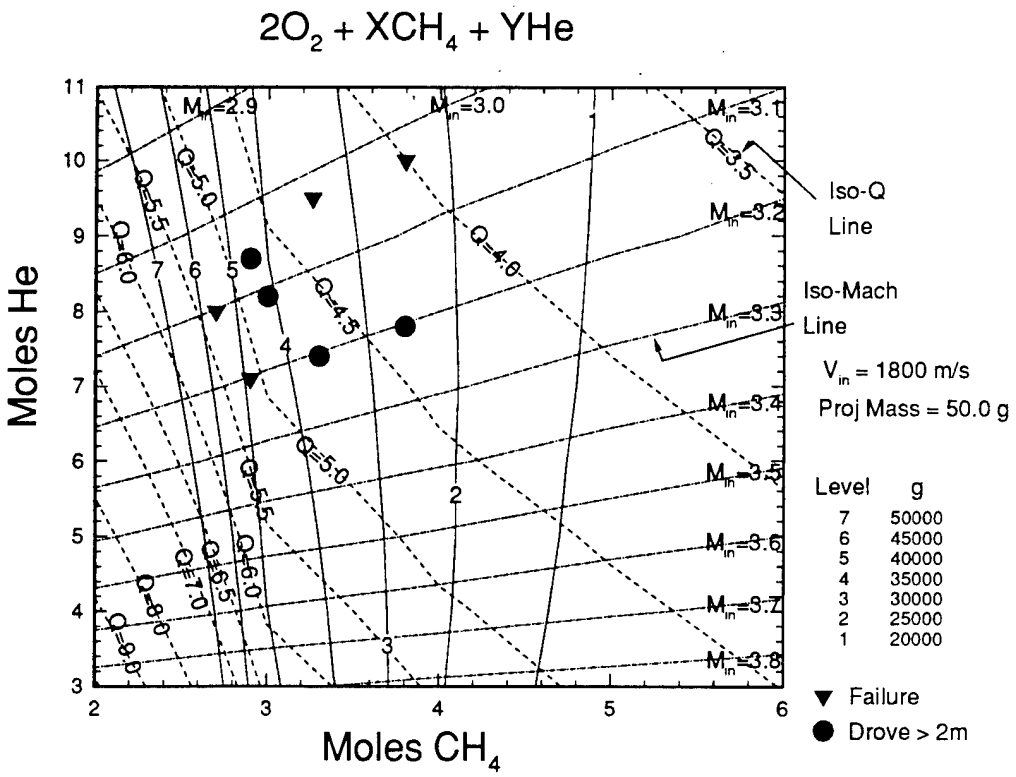

Fig. 3 Helium-methane mixture map for 1800 m/sec entrance velocity.

Using a mixture map such as that of Fig. 3 the influence on acceleration of small changes in chemistry and Mach number can be deduced. Prior experiments have shown that it is impossible to operate above some level of Q or to enter below some value of M_{in}, and that those levels are highly dependent on the propellant constituents. In the experiments, a value of M_{in} was chosen and experiments were performed moving to left on the iso-M_{in} line to higher values of Q until the projectile failed to accelerate through the stage. A mixture with a slightly lower value of M_{in} was then chosen, and experiments were performed using the highest value of Q that was shown to work for the first value of M_{in}. Q was again varied to see if any higher accelerations could be obtained. In this way, propellant mixtures which provided high accelerations in a 2-m stage length were identified within a small number of experiments. Figure 3 shows the progression of experiments which produced a nearly 40,000 g result, accelerating from 1800 m/s to 2190 m/s in 2 m. The propellant mixtures for three stages were developed in this manner, culminating in the demonstration of sustained accelerations of 35,000 g over all three stages.

SHOCK TUBE STUDIES OF RAM ACCELERATOR PHENOMENA

ARO DAAH04-94-G-0032

Principal Investigator: Ronald K. Hanson

High Temperature Gasdynamics Laboratory
Department of Mechanical Engineering
Stanford University, Stanford, CA

SUMMARY/OVERVIEW

This research is aimed at developing an improved understanding of hypersonic exothermic flows through the application of modern experimental methods and finite-rate-chemistry flowfield modeling. Thus far, the emphasis has been on providing fundamental data, of flowfield structure and combustion ignition times, which are relevant to the ongoing development of the ram accelerator concept. These data are critically needed to improve the accuracy of computational modeling of ram accelerator flows.

TECHNICAL DISCUSSION

Primary activities are highlighted below. Related publications are cited at the end.

Imaging and Modeling Study of Hypersonic Exothermic Flows

The imaging experiments are performed in a dedicated expansion tube facility at Stanford University. An expansion tube is a type of impulse wind tunnel which can simulate the high-velocity, exothermic gas flow conditions of a ram accelerator. A small model, chosen to simulate relevant aspects of ram accelerator flows, is held fixed at the exit of the tube, and the gas is discharged around it at supersonic velocity. This approach allows for the application of PLIF and Schlieren imaging to obtain detailed information about the flow physics and chemistry around the model. Pressure transducers are also embedded inside the model to measure the time history of the pressure on the body. The expansion tube approach has the critical advantage of accelerating premixed reactive gases to high velocity without subjecting them to the high stagnation temperatures and pressures of a reflected-type shock tunnel.

The expansion tube facility has been successfully used to accelerate hydrogen-, methane- and ethylene-based fuels to velocities ranging from 1700-2200 m/s (Mach 4-7). A significant accomplishment in the last year was the development of a simultaneous OH PLIF and Schlieren imaging technique to investigate the flowfields around specific models. This is the first time these complementary techniques have been applied simultaneously, and enables detailed study of both gasdynamic effects and reaction fronts. The simultaneous technique has recently been applied to study hypersonic reactive flows around hemispherically-blunted cylinders. Both steady and unsteady flows have been observed; overlaid OH PLIF and Schlieren images of the latter

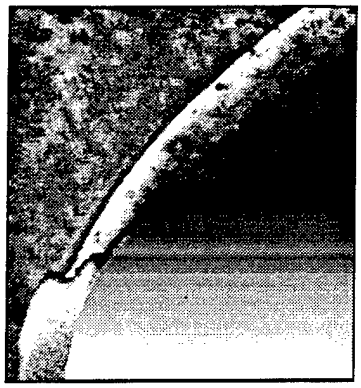

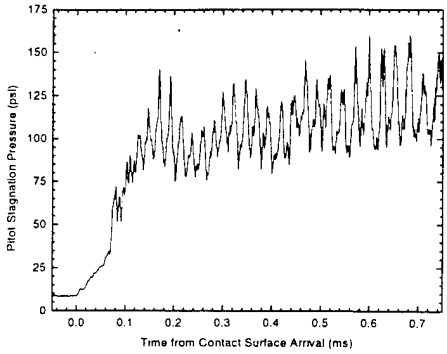

(a) (b)

Figure 1: (a) Simultaneous PLIF and Schlieren image of $C_2H_4 + 3O_2 + 6N_2$ at T_∞ = 280 K, P_∞ = 0.23 atm, V_∞ = 1730 m/s (M_∞ = 5.1) over a 1-inch-diameter hemispherically blunted cylinder. $V_\infty = 0.9V_{CJ}$. (b) Measured pitot stagnation pressure history. Oscillation frequency = 43 kHz.

case, obtained at a subdetonative ($V_\infty < V_{CJ}$) flow velocity, are shown in Figure 1a. Both flame front and pressure oscillations (Fig. 1b) have been observed in the stagnation region of the body. Current modeling work is aimed at correlating the strength and frequency of the oscillations with the body diameter and curvature, and mixture ignition and heat release properties.

Simultaneous OH PLIF and Schlieren imaging has also been applied to study oblique detonation wave formation in 2-D wedge flows. As shown in Figure 2a, if the ignition time behind an attached oblique shock is relatively short, the resulting deflagration waves behind the shock can strengthen it sufficiently to form a pressure-coupled oblique detonation wave. Experimental work thus far has primarily employed a 40° (half-angle) wedge body, while varying the gas mixture composition and pressure to alter the proximity and extent of the transition region (Fig. 2b). Current analysis is focused on studying the transition and resultant detonation wave angle through shock-polar methods and finite-rate kinetic modeling.

Additional experiments are studying confined flows between wedges and a wall. This work will investigate ignition through shock-reflection and viscous flow phenomena, issues which are critically important in actual ram accelerator flows. Work is in progress to compare the experimental results with Stanford and ARL CFD codes.

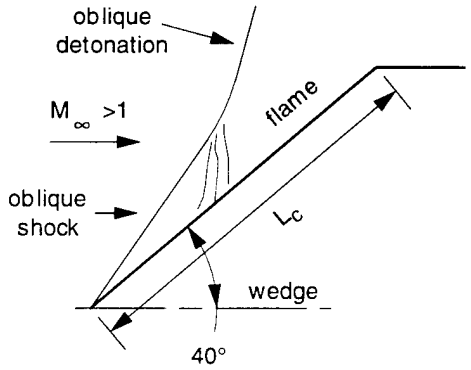

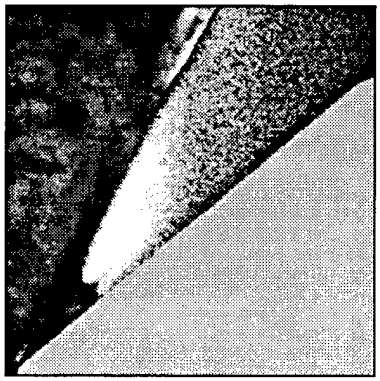

(a) (b)

Figure 2: (a) Schematic of transition from shock-induced combustion to oblique detonation on a wedge. (b) Simultaneous PLIF and Schlieren image of $2H_2 + O_2 + 17N_2$ at T_∞ = 290 K, P_∞ = 0.18 atm, V_∞ = 2130 m/s (M_∞ = 5.8) over a 40° half-angle wedge; $V_\infty = 1.6V_{CJ}$, L_c = 20 mm.

High-Pressure Ignition Kinetics

In a parallel effort, conducted in a high-pressure shock tube, kinetics measurements are performed in support of the ARL ram accelerator effort at Aberdeen. This helium-driven, double-diaphragm shock tube can access pressures as high as 800 atm behind the reflected shock wave, where optical diagnostic techniques are used to measure combustion species of interest. In particular, ignition delay time measurements have been performed for mixtures of direct interest to ARL. Prior to these measurements, no data existed at conditions representative of the ram accelerator (i.e., pre-ignition pressures greater than 50 atm, temperatures less than 1400 K, and fuel-rich CH_4 mixtures with less than 70% diluent gas). Ignition chemistry is important in the design of the ram accelerator to prevent premature combustion near the projectile forebody, and ignition delay time measurements provide the necessary data to extend detailed kinetics models into the appropriate operating region of interest. Such data are of fundamental concern not only to the ram accelerator, but to the general development of finite-rate-chemistry models for detonation and ballistics studies as well.

Major accomplishments in the kinetics program have been both experimental and analytical in nature. For example, ignition delay times for a number of methane-based mixtures of importance to the ARL ram accelerator program were measured; the combination of test conditions (up to 260 atm) and mixtures has provided a range of empirical correlations that completely characterize the expected range of ARL methane-based ram accelerator mixtures. To improve agreement between detailed kinetics models and the experimental data, a state-of-the-art, 175-reaction methane mechanism was improved by adding reactions and species of importance at the higher-pressure, lower-temperature, fuel-rich conditions where ram accelerator ignition may occur. Figure 3 shows a comparison between the shock tube ignition data and the kinetics model. Good agreement is obtained between the updated model and the experimental data, particularly at lower temperatures and higher pressures, where the original mechanism does a poor job of predicting ignition delay time.

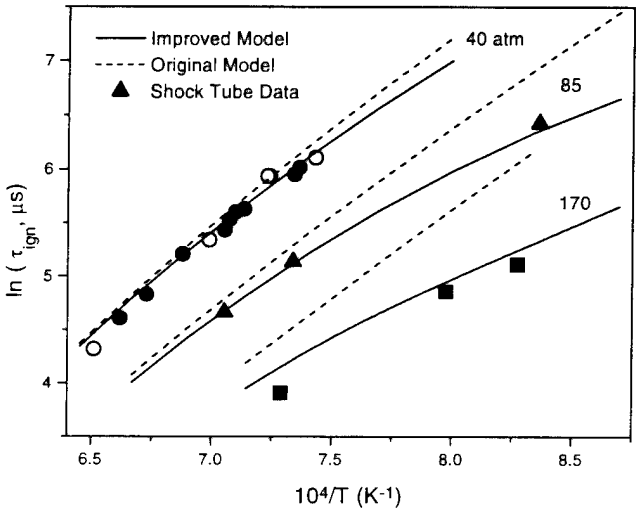

Figure 3: Comparison between Stanford ignition time data and both the improved and original kinetics models for the standard ARL mixture $3CH_4 + 2O_2 + 10N_2$.

Additional work will seek to improve understanding of the chemistry at conditions representative of forebody ignition. Further shock tube experiments will address optimum ram accelerator mixtures and lesser known rate coefficients.

PUBLICATIONS/PRESENTATIONS

M. R. Kamel, C. I. Morris, and R. K. Hanson, "PLIF Imaging of Hypersonic Reactive Flow Around Blunt Bodies," *Twenty-Sixth Symposium (Int.) on Combustion*, The Combustion Institute, Pittsburgh, 1996, pp. 2909-2915.

C. I. Morris, M. R. Kamel, and R. K. Hanson, "Investigation of Ram-Accelerator Projectile Flow Fields in an Expansion Tube," 1996 JANNAF Combustion Subcommittee Meeting, Vol. I, 1997, pp. 383-393.

M. R. Kamel, C. I. Morris, and R. K. Hanson, "Simultaneous PLIF and Schlieren Imaging of Hypersonic Reactive Flows Around Blunted Cylinders," paper AIAA-97-0913 at AIAA 35th Aerospace Sciences Meeting, Reno, Jan. 6-9, 1997.

E. L. Petersen, D. F. Davidson, and R. K. Hanson, "Ignition Delay Times of Ram Accelerator Mixtures," Paper AIAA 96-2681, 32nd Joint Prop. Conf., Lake Buena Vista, FL, July 1996; submitted to *J. Propulsion and Power.*

E. L. Petersen, D. F. Davidson, and R. K. Hanson, "Ram Accelerator Mixture Chemistry: Kinetics Modeling and Ignition Measurements," 1996 JANNAF Combustion Subcommittee Meeting, Vol. I, 1997, pp. 395-407.

E. L. Petersen, D. F. Davidson and R. K. Hanson, "Kinetics Modeling of Shock-Induced Ignition in Low-Dilution CH_4/O_2 Mixtures at High Pressures and Intermediate Temperatures," Paper 97S-066, 1997 Spring Meeting, Western States Section of the Combustion Institute, Livermore, CA, April 14-15, 1997; submitted to *Combustion and Flame.*

IGNITION DELAY TIMES AND STRUCTURE OF DETONATION WAVES IN $CH_4/O_2/N_2$ AND $H_2/O_2/N_2$ MIXTURES
(ARO Grant/Contract No: DAAH-95-1-0108)

Principal Investigator: Dr. K. Seshadri

Center for Energy and Combustion Research
Department of Applied Mechanics and Engineering Sciences
University of California at San Diego
La Jolla, California 92093-0411

SUMMARY/OVERVIEW

The specific aims of this research are to develop reduced chemical-kinetic mechanisms for describing ignition delay times in the dark zone formed over the burning surface of solid propellants and ignition delay times in combustible mixtures used in the Ram Accelerator. Attention was focussed on the former. The research was performed in collaboration with scientists at the U.S. Army Research Laboratory at Aberdeen Proving Grounds, Maryland. Skeletal chemical-kinetic mechanisms comprising few elementary reactions and reduced chemical-kinetic mechanisms were deduced from a detailed chemical-kinetic mechanism. The ignition delay times and structures of the dark zones calculated using the reduced mechanisms were compared with those calculated using the detailed mechanism. The reduced chemical-kinetic mechanisms are expected to be useful in interior ballistics calculations.

TECHNICAL DISCUSSION

Many double base and nitramine propellants exhibit a two-stage flame zone during combustion. In this two stage combustion process, a nonluminous region separates the primary reaction zone, near the surface of the propellant, from the luminous secondary flame zone. The nonluminous region is commonly referred to as the dark zone. In the primary reaction zone the decomposition of the solid propellant takes place and moderately reactive intermediate species are formed. These intermediate species are convected away from the surface and they ignite after a short delay. Recent experiments show that chemical effects caused by the use of propellants of differing chemical composition can lead to major differences in ignition delay times during typical large calibre gun ballistic cycles [1–4] (note that the ignition delay times in guns are not the same as the dark zone chemical delays). For some propellants, these delays are undesirably long. It is believed that the range of ignition delay times for various propellants arise from differences in the chemistry taking place in the dark zone [3, 4]. An interior ballistic flamespreading code (IBF) capable of modeling the physiochemical processes taking place in the dark zone is under development at ARL. Scientists at ARL have been asked to provide a simplified chemical-kinetic mechanisms of sufficiently small size for use in IBF. These simplified kinetic mechanism must be able to reproduce important aspects of dark zone chemistry predicted by detailed chemical-kinetic models. The problem of deducing simplified chemical-kinetic mechanisms from detailed mechanisms is addressed here.

The theoretical calculation of ignition delay is performed using a homogeneous, time-dependent chemistry. The ignition delay time (τ_{ig}) for any reactive mixture is defined in this

work as the delay time from the initiation of the reaction (time zero) to the time of maximum heat release associated with the thermal runaway. A detailed chemical-kinetic mechanisms comprising 189 elementary reactions among 41 species was developed at ARL to describe the structure of the dark zones of double base and nitramine propellants. The ignition delay times calculated using this detailed chemical-kinetic mechanism was found to agree reasonably well with experimental measurements for double base and nitramine propellants.

Skeletal chemical-kinetic mechanisms comprising 22 elementary reactions among 15 species and 23 elementary reactions among 17 species were used to calculate the structure of the dark zone of double base and nitramine propellants, respectively. These skeletal mechanisms were derived from the detailed mechanism developed at ARL after removing those reactions found to have negligible influence on the calculated values of the ignition delay times. Values of τ_{ig} calculated for double base and nitramine propellants using the skeletal mechanism were in good agreement with those of the detailed mechanism. The skeletal mechanisms were used in the development of the reduced mechanisms.

The skeletal mechanisms for double base and nitramine propellants contain 15 and 17 species, respectively. Because both mechanisms involve four elements, eleven independent species balance equations can be written for double base propellants and thirteen for nitramine propellants [5]. Therefore, the skeletal mechanism for double base and nitramine propellants are equivalent to reduced chemical-kinetic mechanisms having 11 and 13 overall steps, respectively. The skeletal chemical-kinetic mechanisms were reduced by introducing steady-state approximations for a number of species. For any species, the time derivative of its concentration is the difference between production and consumption rates for that species. A steady-state approximation is justified if either the species' production or consumption rate, which of course are nearly equal at steady-state, is much larger than the time derivative of its concentration. This criteria was employed to determine species for which steady-state approximations can be introduced.

For double base propellants steady-state approximations were introduced for eight species which provided eight nonlinear algebraic equations for calculating the concentration of the steady-state species. Because eight species are placed in steady-state, the reduced system now has three independent species balance equations and four element conservation equations. The source terms of the species which are not in steady state are rearranged and collected in three groups such that each group represents the rate of one of the three overall steps of the reduced chemical-kinetic mechanism, which is written as:

$$\begin{aligned} 2\,NO + H_2 &\rightleftharpoons N_2O + H_2O, && \text{I} \\ N_2O + H_2 &\rightleftharpoons N_2 + H_2O, && \text{II} \\ CO + H_2O &\rightleftharpoons CO_2 + H_2. && \text{III} \end{aligned}$$

The rates of the overall steps w_k, k = I, II, III were expressed in terms of the rates of the elementary reactions.

Reduced chemical-kinetic mechanisms for nitramine propellants were obtained using the same procedure employed for double base propellants. Steady-state approximations were introduced for seven species. With seven species held in steady-state, the reduced system now has six independent species balance equations and four element conservation equations. The reduced mechanism has six overall steps which can be written as:

Table 1: Comparison of the values of the ignition delay times τ_{ig} calculated using the various mechanisms for double base propellants. The initial mole fractions of NO, CO, H_2, N_2, H_2O and CO_2 are set equal to 0.24, 0.33, 0.08, 0.04, 0.20, and 0.10 respectively.

initial conditions	detailed mech. (41 sp., 189 r.)	skeletal mech. (15 sp., 22 r.)	reduced mech. (3 steps)
1 atm, 1000 K	42.28 s	41.35 s	40.4 s
1 atm, 1400 K	1.260 s	1.278 s	1.274 s
1 atm, 1800 K	$4.145 \cdot 10^{-4}$ s	$4.276 \cdot 10^{-4}$ s	$4.105 \cdot 10^{-4}$ s
5 atm, 1000 K	6.511 s	6.295 s	6.006 s
5 atm, 1400 K	$1.449 \cdot 10^{-1}$ s	$1.466 \cdot 10^{-1}$ s	$1.460 \cdot 10^{-1}$ s
5 atm, 1800 K	$9.188 \cdot 10^{-3}$ s	$9.591 \cdot 10^{-3}$ s	$9.426 \cdot 10^{-3}$ s
10 atm, 1000 K	3.138 s	3.028 s	2.868 s
10 atm, 1400 K	$5.66 \cdot 10^{-2}$ s	$5.709 \cdot 10^{-2}$ s	$5.678 \cdot 10^{-2}$ s
10 atm, 1800 K	$4.397 \cdot 10^{-3}$ s	$4.613 \cdot 10^{-3}$ s	$4.536 \cdot 10^{-3}$ s
30 atm, 1000 K	1.016 s	0.983 s	0.923 s
30 atm, 1400 K	$1.299 \cdot 10^{-2}$ s	$1.304 \cdot 10^{-2}$ s	$1.291 \cdot 10^{-2}$ s
30 atm, 1800 K	$1.261 \cdot 10^{-3}$ s	$1.334 \cdot 10^{-3}$ s	$1.316 \cdot 10^{-3}$ s

$$
\begin{aligned}
2\,NO + 2\,H_2 &\rightleftharpoons N_2O + 2\,H + H_2O, && \text{I}\\
H_2O + HCN &\rightleftharpoons H_2 + HNCO, && \text{II}\\
N_2O + 2\,H_2 &\rightleftharpoons N_2 + 2\,H + H_2O, && \text{III}\\
CO + H_2O &\rightleftharpoons CO_2 + H_2, && \text{IV}\\
2\,H + M &\rightleftharpoons H_2 + M, && \text{V}\\
NO + H + HNCO &\rightleftharpoons N_2O + CO + H_2. && \text{VI}
\end{aligned}
$$

The rates of the overall steps w_k, k = I-VI were expressed in terms of the rates of elementary reactions. To further simplify the mechanism, steady-state approximations were introduced for the species H and HNCO yielding four overall steps which can be written as:

$$
\begin{aligned}
2\,NO + H_2 &\rightleftharpoons N_2O + H_2O, && \text{I}'\\
NO + H_2O + HCN &\rightleftharpoons N_2O + CO + 1.5\,H_2, && \text{II}'\\
N_2O + H_2 &\rightleftharpoons N_2 + H_2O, && \text{III}'\\
CO + H_2O &\rightleftharpoons CO_2 + H_2. && \text{IV}'
\end{aligned}
$$

Computations were performed using the SENKIN computer code written at Sandia National Laboratories. A number of chemical details of the solutions from SENKIN were investigated using a post-processing code written at the Army Research Laboratory (ARL) [6]. The post-processing code was used to obtain information such as the heat release rate, predominant chemical pathways, and logarithmically normalized sensitivities of the calculated species and temperature profiles to the rate constants of the various elementary reactions.

Table 1 shows that the values of the ignition delay times calculated using the reduced three-step mechanism for double base propellants agree well with those calculated using the skeletal mechanism. The differences in the values of τ_{ig} calculated using these mechanisms are less than 10%. The values of τ_{ig} calculated using the reduced mechanism are lower than those calculated using the skeletal mechanism. If a steady-state approximation is introduced for N_2O, a reduced two-step mechanism is obtained for characterizing the structure of the dark zone of double base propellants. The value of τ_{ig} calculated using this reduced two-step mechanism at $p = 1$ atm and $T^0 = 1000$ K is found to be 50% lower than that calculated using the three-step mechanism.

Table 2: Comparison of the values of the ignition delay times τ_{ig} calculated using the various mechanisms for nitramine propellants. The initial mole fractions of NO, CO, H_2, N_2, H_2O, CO_2, N_2O and HCN are set equal to 0.13, 0.22, 0.07, 0.06, 0.20, 0.09, 0.02, and 0.22 respectively.

initial conditions	detailed mech. (41 sp., 189 r.)	skeletal mech. (17 sp., 23 r.)	reduced mech. 6 steps	reduced mech. 4 steps
1 atm, 1000 K	14.87 s	15.45 s	15.06 s	14.79 s
1 atm, 1400 K	$1.832 \cdot 10^{-2}$ s	$2.017 \cdot 10^{-2}$ s	$1.809 \cdot 10^{-2}$ s	$1.335 \cdot 10^{-2}$ s
1 atm, 1800 K	$2.610 \cdot 10^{-4}$ s	$2.556 \cdot 10^{-4}$ s	$2.114 \cdot 10^{-4}$ s	$1.206 \cdot 10^{-4}$ s
10 atm, 1000 K	2.153 s	1.744 s	1.678 s	1.667 s
10 atm, 1400 K	$6.256 \cdot 10^{-3}$ s	$7.183 \cdot 10^{-3}$ s	$6.567 \cdot 10^{-3}$ s	$5.476 \cdot 10^{-3}$ s
10 atm, 1800 K	$7.892 \cdot 10^{-5}$ s	$7.626 \cdot 10^{-5}$ s	$6.429 \cdot 10^{-5}$ s	$4.086 \cdot 10^{-5}$ s
30 atm, 1000 K	1.000 s	0.883 s	0.844 s	0.861 s
30 atm, 1400 K	$3.829 \cdot 10^{-3}$ s	$4.203 \cdot 10^{-3}$ s	$3.895 \cdot 10^{-3}$ s	$3.363 \cdot 10^{-3}$ s
30 atm, 1800 K	$5.806 \cdot 10^{-5}$ s	$5.684 \cdot 10^{-5}$ s	$4.870 \cdot 10^{-5}$ s	$3.171 \cdot 10^{-5}$ s

This result illustrates that a steady-state approximation for N_2O is not justified.

Table 2 compares the values of the ignition delay times calculated using the reduced six-step and four-step mechanisms for nitramine propellants with those calculated using the skeletal mechanism. The values of τ_{ig} calculated using the reduced six-step mechanism agree very well with those calculated using the skeletal mechanism and the differences are less than 18%. However, the maximum differences in the values of τ_{ig} calculated using the reduced four-step mechanism and the skeletal mechanism are about 50%. The large differences between the values of τ_{ig} calculated using the reduced four-step mechanism and the skeletal mechanism are attributed to inaccuracies introduced by the steady-state approximations for H and HNCO.

It is hoped that these skeletal and reduced chemical-kinetic mechanisms will be suitable for use in interior ballistics calculations.

References

[1] D. E. Kooker, L. M. Chang, and S. L. Howard. Flamespreading in granular solid propellant. design of an experiment. Technical Report ARL-TR-80, Army Research Laboratory, June 1993.

[2] D. E. Kooker, L. M. Chang, and S. L. Howard. Flamespreading in granular solid propellant. initial results. Technical Report ARL-TR-446, Army Research Laboratory, June 1994.

[3] D. E. Kooker, L. M. Chang, and S. L. Howard. Flamespreading in granular solid propellant. Influence of propellant composition. In *32nd JANNAF Combustion Subcommittee Meeting*, Huntsville, Alabama, October 1995.

[4] D. E. Kooker. Private communication, 1995.

[5] K. Seshadri and F. A. Williams. Reduced chemical systems and their application in turbulent combustion. In P. A. Libby and F. A. Williams, editors, *Turbulent Reacting Flows*, pages 153–210. Academic Press, San Diego, California, 1994.

[6] W. R. Anderson, S. W. Haga, J. F. Nuzman, and A. J. Kotlar. to be published.

ANALYSIS OF ADVANCED DIRECT-INJECTION DIESEL ENGINE DEVELOPMENT STRATEGIES

(ARO Contract No. DAAH04-95-1-0430)

Principal Investigator: KT Rhee

Rutgers, The State University of New Jersey
Mechanical and Aerospace Engineering Department
Brett and Bowser Roads
Piscataway, NJ 08855-0909

OVERVIEW:

In-cylinder reactions are studied of a direct-injection Diesel engine having optical access by new quantitative imaging methods when the engine is incorporated with advanced engine strategies (AES). The present work include development of Rutgers High-speed Spectral Infrared Imaging System (or Super Imaging System, SIS), and spectrometric analysis methods to process the raw data captured by the SIS. Among the AES is the use of electronically controlled high-pressure injection system in order to help achieve a high power-density Diesel engine with low soot-emission. The main events being studied include: preflame reactions; flame propagation; formation of combustion products (water vapor and soot); and temperature distribution. The technology advancements achieved under the present work are used in engine-fuel studies in both spark-ignition (SI) and compression-ignition (CI) engine areas.

TECHNICAL DISCUSSION:

After developing the first generation Super Imaging System (SIS), several new findings were obtained by capturing qualitative imaging of both CI and SI engine processes, which will be reported at the oral presentation. In order to achieve quantitative imaging, that is to determine distributions of species and temperature in the reaction chamber at successive instants of time, two requirements were to be met: (1) Determination of digital data matrix in high dynamic resolutions by the SIS so that accurate quantitative imaging can be achieved. For this, the entirely new electronic circuit packages have been designed, and they are being fabricated at present. (2) Development of new spectrometric methods for processing the raw data captured by the SIS in order to obtain quantitative imaging. Three new methods have been developed to date and applied to in-cylinder combustion studies, which will be explained in the meeting.

In addition, during the process of engine-fuel studies, it came to recognize that the amount of information captured by the SIS is far more than being handled by the manual inspection. Consequently, a new data visualization method have been developed in order to efficiently investigate the vast amounts of both raw and quantitative imaging data. The core of the method is to animate the reaction processes.

SUPER IMAGING SYSTEM. The basic concept of SIS is to determine a set of four digital images in respective spectral bands at successive instants of time of the radiating reaction volume. For this, four units of high-speed infrared (IR) cameras are lined up to an optical package with accurate alignment (pixel-to-pixel). The spectral bands

being used at present are those at the central wavelengths of 2.2μm, 2.47 μm, 3.42 μm, and 3.8 μm. The first and the last bands are to capture radiation from reactor surface or soot, the others are for those from water vapor. Figure 1 shows a schematic presentation of the optical part of SIS, which will be further discussed in the presentation.

Since the SIS was an unconventional application, a great portion of the system was newly designed and fabricated. For example, since this system was designed to obtain a set of four matrixes (64x64) of digital data (12-bit) at a rate of near 2,000 set/sec, no reasonable memory system was available when the system design was initiated, so that a new high-speed memory package was developed in order to handle the large data volume.

SPECTROMETRIC ANALYSIS METHODS. The digital data matrixes obtained by the SIS are processed in order to achieve quantitative imaging. Three new methods were developed under the present contract. Figure 2 summarizes some previous studies together with the new methods. The key differences between the previous work and the new methods are: (1) Their methods utilized some experimental findings, while the present methods employ the IR spectral data included in the NASA IR Handbook. (2) The previous works were to obtain single-point measurements, while the present methods are to determine distributions of measurements, i.e. quantitative imaging. (3) The present methods are to simultaneously determine distributions of multiple information, e.g. those of temperature, water vapor and soot.

Although the details of new methods will be explained in the presentation, Fig. 3 shows a flow-chart of data processing in the new three band iterative-method. This method requires spectral images (data matrixes) in three respective bands. The basic idea is to determine temperature distribution by using the new band-ratio method, which employs radiation from water vapor. At this time the radiation from the soot is neglected. The initial temperature calculation is used in determining soot distribution (volume fraction), which is reflected prior to the next step of using the band-ratio method so that the temperature calculation is improved. The more accurate temperature distribution is used in the soot calculation. These steps are continued until the results converge.

SAMPLE RESULTS. Figure 4 is included in order to demonstrate the use of the new three band iterative-method. Fig. 4-(A) shows high-speed spectral IR images captured of a spray plume in three respective bands from a direct-injection CI engine cylinder, and (B) includes quantitative images obtained by processing data shown in (A). Note that the direction of spray is diagonal from the low right corner to the upper left end. The results will be also presented in an animated form in the meeting.

REFERENCES

1. Uyehara, O.A. and Myers, P.S., "Flame Temperature Measurements-Electronic Solution of the Temperature Equations," SAE Quarterly Transactions, vol. 1, No. 4, 1947.
2. Agnew, W.G., "Two-wavelength Infrared Radiation Method Measures end gas Temperatures near their Peaks," SAE Journal, October 1960.
3. Ferriso, C.C., Ludwig, C.B., and Boynton, F.P., "A Band-ratio Technique for Determining Temperatures and Concentrations of Hot Combustion Gases from Infrared-emission Spectra," 10th Symp. (Int'l) on Combustion, 161, The Comb. Institute, 1965.
4. Ludwig, C.B., Malkmus, W., Reardon, J.E., Thomson, J.A.L., Handbook of Infrared Radiation from Combustion Gases," NASA SP-3080, 1973.
5. Chang, C., Clasen, E., Song, K., Campbell, S., Jiang, H., Rhee, K.T., "Quantitative Imaging of In-cylinder Processes by Multispectral Methods," SAE Paper-970872, 1997.

Rutgers Super Imaging System (Optical)

Fig. 1

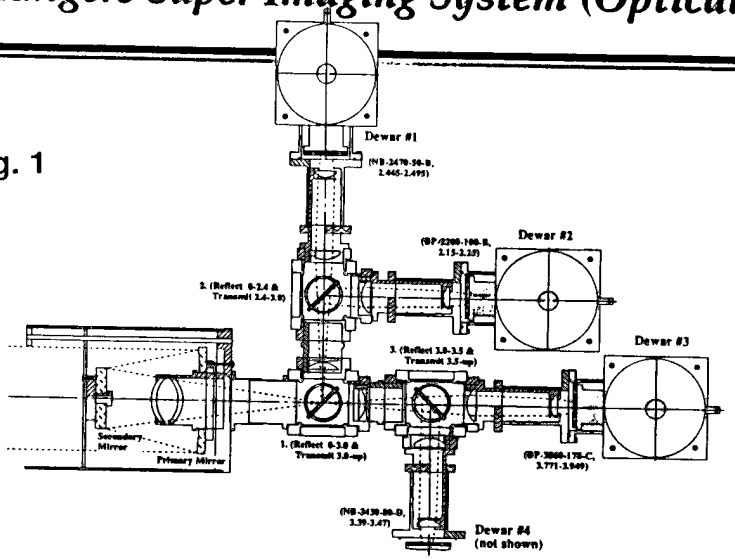

Fig. 2

Multi-band Spectral Methods

[1947]	**Two-color Method** (Uyehara and Myers)	Univ. of Wisc.	(Point-Temperature)
[1960]	**Ratio Method** (William Agnew)	General Motors	(Point-Temperature)
[1965]	**Band Ratio Technique** (Ferriso, et al.)	Genral Dynamics	(Point-Temperature)
[1973]	**Handbook of IR Radiation from Combustion Gases** (Ludwig, et al.)	NASA	(IR Data and SLG Model)
	Rutgers Super Imaging System		
[1993]	**Dual-band Mapping Method** (Jiang & Rhee)	Rutgers Univ.	(Distributions of Temperature and Water-vapor)
[1996]	**New Band-ratio Method** (This work)	Rutgers Univ.	(Distributions of Temperature and Water-vapor)
[1996]	**Three Band Iteration Method** (This work)	Rutgers Univ.	(Distributions of Temperature Water-vapor, and Soot)

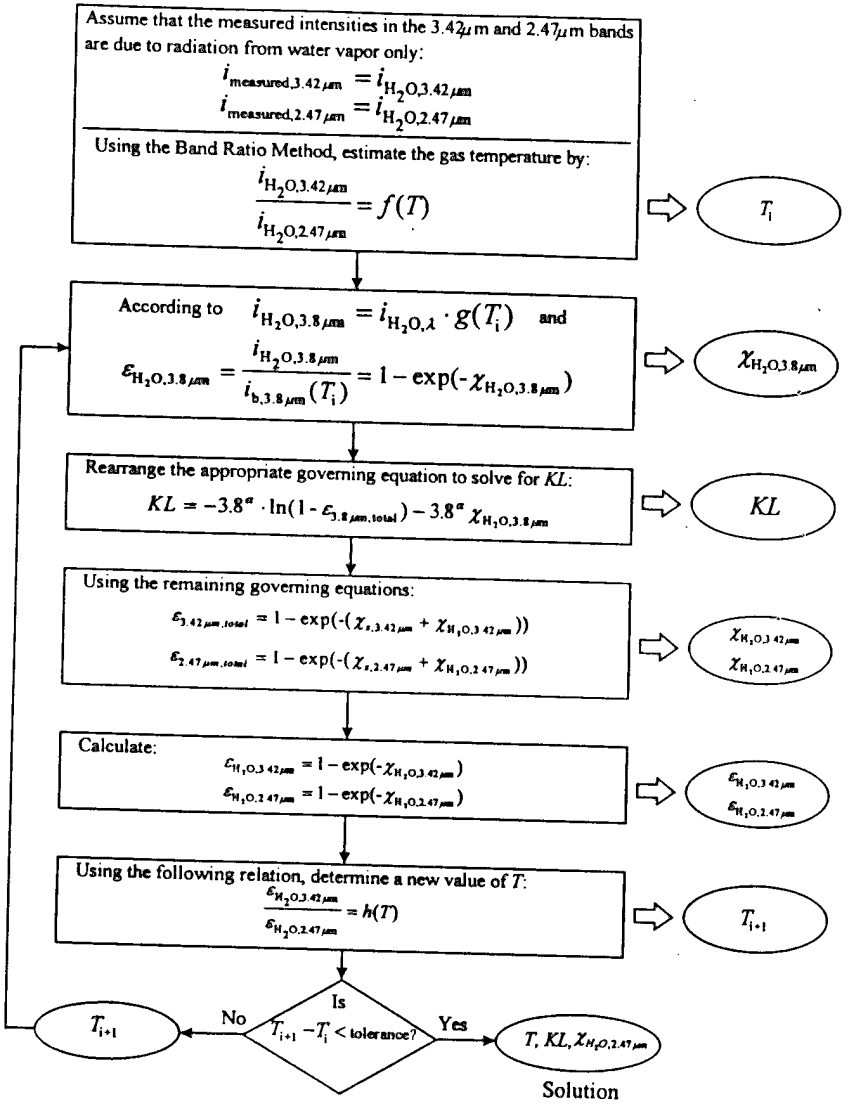

Fig. 3

Quantitative Imaging of CI Combustion

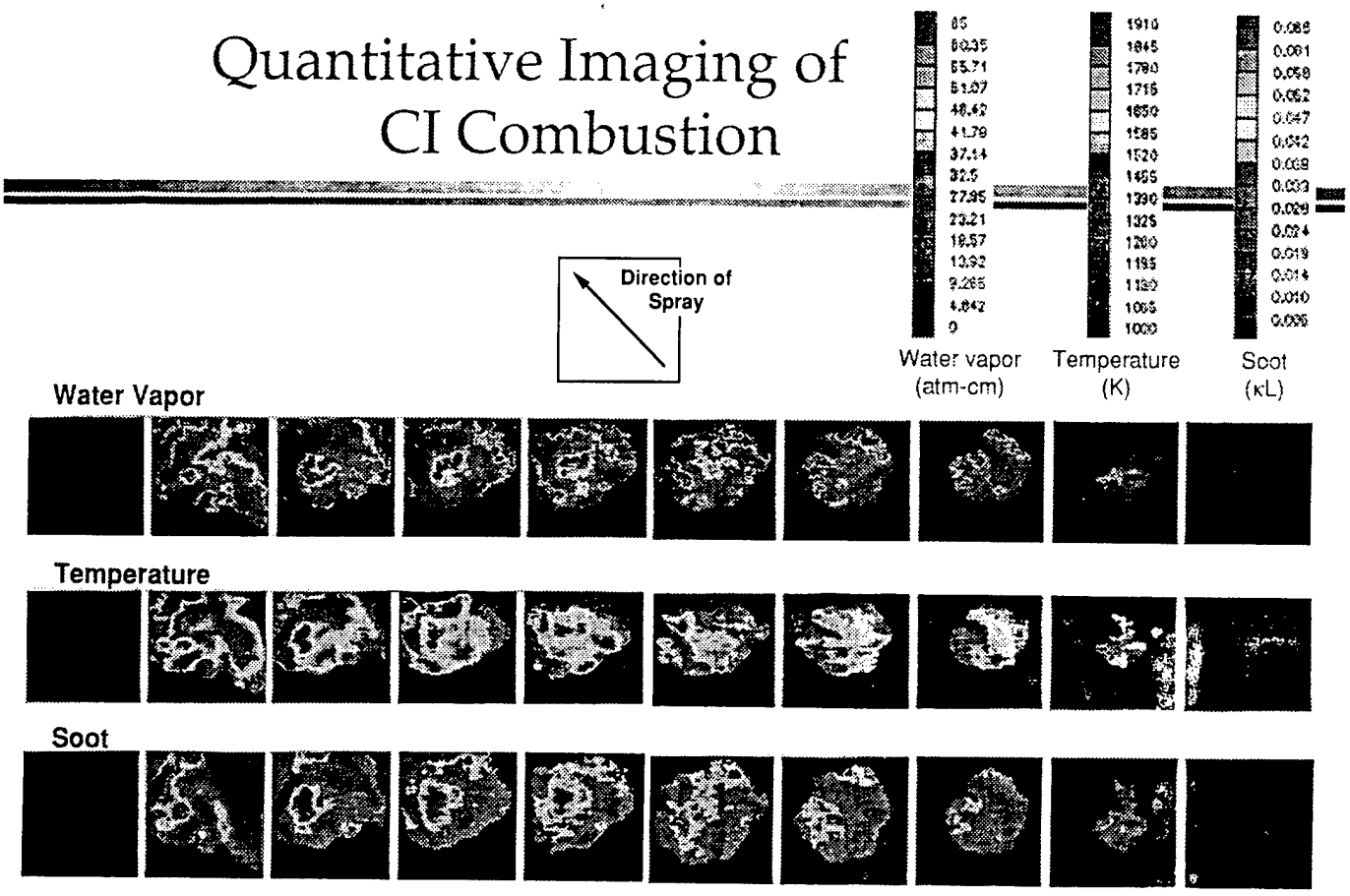

Fig. 4-(B)

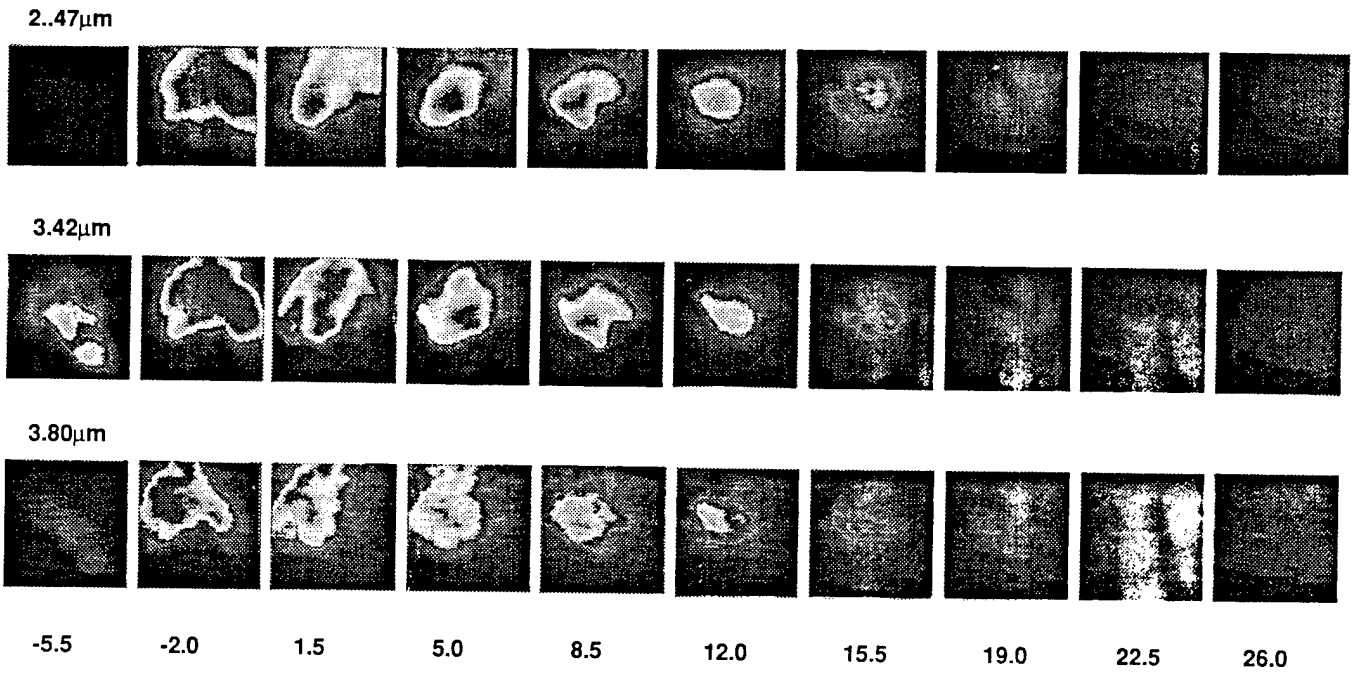

Fig. 4-(A)

VISUALIZATION OF HIGH-POWER-DENSITY DIESEL ENGINE COMBUSTION

Ming-Chia Lai and Naeim A. Henein
Mechanical Engineering Department
Center for Automotive Research
Wayne State University

Abstract:

The superior efficiency and fuel tolerance of diesel engines make them the preferred power plant for many U. S. Army propulsion and power generation needs. A compact high power diesel (HPD) engine is of particular interest to the U. S. Army, because of its wide variety of applications in tanks, armored personnel carriers, standby power generations, and other compact high-energy-density powerplant applications. The advanced military HPD engine must utilize recent available technologies, such as turbo-charging/intercooling, ultra-high fuel injection pressure, multiple injection and enhanced mixing, and low-heat rejection ceramic parts.

Direct visualization, when combined with other cylinder pressure, heat release and fuel injection measurements, provides the most detailed description of the combustion processes. Therefore, direct visualization of the combustion process is greatly needed to provide fundamental understanding to guide the design of this type of engines. In this presentation, the current development and initial testing of the experimental setup is described. The fuel injection systems being implemented include high-pressure common rail and unit injector systems, which are capable of multiple injection and shaping of injection rate. The High-speed visualization and characterization of the spray and combustion processes inside a modified "see-through" engine using both analog and digital cameras aided by high-speed laser strobes.

⇒

LARGE EDDY SIMULATIONS OF DIESEL COMBUSTION CHAMBERS

ARO Grant No.: DAAH04-96-1-0196

I. B. Celik, W. S. Lewellen, J. M. Kuhlman
E. Amin, A. Gel, D. C. Lewellen, J. Smith, I. Yavuz

Department of Mechanical and Aerospace Engineering
West Virginia University
Morgantown, WV

1.0 SUMMARY/OVERVIEW

The objective of this project is to accurately predict turbulence phenomena in diesel combustion chambers using large eddy simulation (LES) techniques, with sufficient resolution to capture the most important features of the flow which influence the combustion process and emissions formation. Relatively simple but well-tested subgrid-scale (SGS) models will be implemented to account for the SGS turbulence. Some of the issues regarding the application of LES to diesel engine combustion will be resolved. The LES model will be used to generate reliable numerical data for the turbulence characteristics within the flow process. Both time averaged and cycle averaged quantities will be computed and the differences between the two will be elucidated. Cycle-to-cycle variations within the engine cylinder will be investigated. The LES data generated can be used for refinement of traditional turbulence models.

2.0 TECHNICAL DISCUSSION

2.1 Background

Accurate prediction of turbulence is one of the outstanding obstacles in realistically simulating and predicting the mixing and combustion phenomenon inside diesel engines. Many of these issues can be resolved if large eddy simulations (LES) can be utilized to bring a new generation of realism to turbulence phenomenon in combustion chambers. The LES approach requires an accurate numerical model with sufficient resolution to resolve the most important features of the flow processes. For this purpose a combination of the existing KIVA II&III family of codes originated from Los Alamos National Labs (Amsden, 1993) which were designed specifically for internal combustion engines, and a WVU/LES code (Lewellen et al., 1997; Lewellen and Lewellen, 1996) developed for modeling atmospheric turbulence are being utilized. The 3-D, unsteady KIVA code is currently being modified to run as an LES code. The WVU/LES will be used as a guide in determining the required modifications to KIVA for relatively simple swirling flow configurations. We will then gradually make the problem more realistic as we increase complexity and resolve some of the issues regarding the application of LES to diesel engine combustion. Our ultimate goal is to simulate at least several cycles of a three-dimensional, unsteady, turbulent reacting flow in a typical engine cylinder with a simple geometry, and make an assessment of cycle-to-cycle variations versus turbulent fluctuations within the cycle. In what follows accomplishments to date are presented along the way towards a "truly" large eddy simulation of flow inside diesel combustion chambers.

2.2 Capacity Building:

Since ours is an EPSCoR project partially funded by WV State, capacity building is an important component. We have increased our computer capabilities from a very limited level to a level where we can run locally the new multi-block version of the KIVA code with 2.0×10^5 nodes. Without any optimization or improvement, the performance including 89 real and 7 integer array variables is approximately 100 user CPU seconds per time step. The runs we have made on CRAY C90 at Pittsburgh Super Computer Center (PSC) show that the CPU time per cycle reduces more than a factor of two. With some improvements in the computational efficiency, and computer power (mainly RAM) it should be possible to make runs with half a million grid nodes locally. Our present estimates indicate that this should give us sufficient resolution with appropriate grid stretching and distribution, and using wall functions. If more resolution is needed, we would seek other alternatives such as parallelizing some parts of the code. Some production runs could also be made on C90 at PSC or at the ARO High Performance Computing Center. Purchasing of a fast workstation is also among our plans. In addition, progress has been made

on the development of a non-intrusive, two-component Doppler Global Velocimeter (DGV) system (primarily funded by a separate AFOSR EPSCoR grant) with accuracies measured to within a few percent.

2.3 Assessment of Turbulence Scales:

A literature survey on the measured turbulence quantities has been completed and the most relevant ones are reported in a publication (Celik and Yavuz, 1997a). Axisymmetric computations were performed on a typical engine using the standard k-ε model to investigate the variations of turbulence quantities during the compression and expansion strokes. Some results are presented in Figure 1 where various time and length scales of turbulence are depicted as a function of the crank angle for a representative point inside the piston bowl. These results when compared to experiments indicate that the standard models can predict the trends qualitatively, and the order of magnitude of the turbulence scales can be predicted. In particular, the calculated dimensionless length scales are consistent with the data of Fraser et al. (1986) for a motored engine. It should be possible then to estimate the degree of grid and time resolution necessary for the LES simulations using the results of these simpler models as a guide. It seems that a grid resolution as small as one millimeter and a time resolution of one millisecond are desirable for accurate LES simulation of the flow field inside a typical automotive engine cylinder. For more details see Celik and Yavuz (1997a &b).

2.4 Three-Dimensional, Unsteady Runs:

We have performed some preliminary runs in 3-D unsteady mode to mimic LES using fairly coarse grids. We would like to emphasize that these are <u>not</u> LES runs, however the results show how KIVA responds to the subgrid-scale specifications, and they are being used to assess our needs both in terms of computer power, and necessary modifications to be made to the code. The current SGS model in KIVA is a two-equation k-ε model (here k is the turbulent kinetic energy, and ε is the dissipation rate of k) where the modeled transport equations for both of these quantities are solved with a cut-off point prescribed by $\varepsilon_{min} = \text{const}\ (k^{3/2})/L_{SGS}$ where L_{SGS} is a sub-gird parameter. Here we take L_{SGS} equals to $(\Delta x\ \Delta y\ \Delta z)^{1/3}$, where Δx, Δy, and Δz are the representative grid sizes in the three coordinate directions. When the dissipation rate calculated from the transport equation is less than ε_{min} , it is replaced by ε_{min} thus constraining the turbulence length scale to be less than or equal to L_{SGS}. A diesel engine which has been studied experimentally by Arcoumanis et al., (1994) has been simulated. The engine has a bore of 7.95 cm, a stroke of 9.55 cm, compression ratio of 20.5, and a five hole direct injection nozzle. The engine speed was 1000 RPM. The grid used was essentially a uniform grid with 30x20x30 grids in the x- , y-, and z-(axial) directions, respectively. Only the compression and expansion strokes of the engine cycle are considered. Some results of the computed flow field variables are depicted in Figure 2. When the SGS model is imposed the dissipation rate increases, this in turn, causes the turbulent kinetic energy to decrease, hence leading to a much lower eddy viscosity. The turbulent kinetic energy with the SGS model is about half of the values seen with the standard k-ε model. If this trend continues, then the contribution from the SG scales should reduce as we make the grid finer and finer. Whether the resolved portion of k increases by the same amount remains to be shown. An important consequence of these observations is that the truncation errors are not excessively large in these computations. If they were so, we should not have seen much difference between the two cases, for then the numerical diffusion would have smeared the results making almost no difference between the two models. In fact, another simulation of the same case with no turbulence model revealed that the flow field was significantly different than the ones shown in Figure 2 which is another indication that the truncation errors were not large. Future work includes doubling the number grids for this case and assessing the quality of the simulations in comparison with experiments. The assessment will be based on several methods to assure that we are resolving sufficient details of the turbulence field. We will ensure that truncation error goes to zero faster than the SGS contribution.

2.5 Subgrid-Scale- Models:

Modifications are underway to include wall effects (i.e. length scale being proportional to the normal distance from the wall) in the SGS model. We will consider using one equation models with an empirical parameterization of the length scale. The parameterization will include rotational effects as well as rapid dilation effects (see e.g. Canuto, 1994; Lesieur and Metais, 1996). An algebraic relation derived by Canuto et al. for the dissipation rate (which essentially determines the length scale) by reduction of Reynolds-stress model which retains the effects of rotation, and the structure function model (SFM) suggested by Lesieur and Metais both seem to capture the primary effects of rotation. Another model developed partially under this grant and implemented in the WVU/LES code includes the rotational effects via an additional constraint on L_{SGS}. It restricts L_{SGS} to be less than a constant times $k^{1/2}/S$ where S is a measure of locally computed rotational frequency. The primary influence of the new

modification is to reduce the small scale turbulent diffusion in any coherent vortex core. These models will be implemented in the KIVA code and the results will be tested against experimental data from the literature. The experimental data of Wahiduzzaman and Ferguson (1986), Sommerfeld et al. (1992) and Johnston et al., 1972 are being considered for validation of rotational effects in SGS model. We anticipate presenting the results of simulation of the Wahiduzzaman and Ferguson experiments. Future work will also include selection and implementation of a SGS model for combustion. For this the linear-eddy model pioneered by Kerstein (1988), and the pdf model suggested by Frankel et al (1993) will be used as a guide.

REFERENCES

Amsden, A.A. (1993) "KIVA-3: A KIVA Program with Block-Structured Mesh for Complex Geometries," Los Alamos National Laboratory, Los Alamos National Laboratory Report LA-12503-MS, UC-361, Los Alamos, New Mexico 87545.

Arcoumanis, C., Whitelaw, J.H., Hentschel, W. and Schindler, K-P (1994) "Flow and Combustion in a Transparent 1.9 Liter Direct Injection Diesel Engine," IMechE 1994, Part D: Journal of Automobile Engineering, Proc. Inst. Mech. Engrs., Vol. 208, pp. 191-205.

Canuto, V. (1994) "large Eddy Simulation of Turbulence: A Subgrid Scale Model Including Shear, Vorticity, Rotation, and Buoyancy," The Astrophysical Journal, Vol. 428, pp 729-752.

Celik, I. and Yavuz, I. (1997a) "Turbulence Scales in IC Engines Implied by the K-Epsilon Model," Proceedings of 7th International KIVA Users Meeting, at the SAE Congress, Feb. 23, Detroit (USA).

Celik, I. and Yavuz, I. (1997b) "An Assessment of Turbulence Scales Relevant to IC Engines," Proceedings of the ASME ICE Division 1997 Spring Engine Technology Conference, Fort Collins, Colorado, April 27-30.

Frankel, S.H., Adumitroaie, V., Madnia, C.K., and Givi, P. (1993) "Large Eddy Simulation of Turbulent Reacting Flows by Assumed PDF Method," in Engineering Applications of Large Eddy Simulations, ASME Publication No. FED-Vol. 162, editors: S.A. Ragab and U. Piomelli, pp. 81-101.

Fraser, R.A., Felton, F.G., Bracco, F.V. and Santavicca, D.A. (1986) "Preliminary Turbulence Length Scale Measurements in a Motored IC Engine," SAE Technical Paper Series #860021.

Johnston, J., Halleen, R., and Lezius, D. (1972) "Effects of Spanwise Rotation on the Structure of Two-dimensional Fully Developed Channel Flow," JFM, Vol. 56, pp 533-558.

Kerstein, A.R. (1988) "Linear-Eddy Model of Turbulent Scalar Transport and Mixing,", Comb. Sci. and Tech. Vol. 60, pp. 391-421.

Lesieur, M. and Metais, O. (1996) "New Trends in Large-Eddy Simulations of Turbulence," Annu. Rev. Fluid Mechanics, Vol. 28, pp 45-82.

Lewellen, D.C., and Lewellen, W.S. (1996) "Large-Eddy Simulations of Vortex-Pair Breakup in Aircraft Wakes," AIAA J. Vol. 34, pp. 2337-2345.

Lewellen, W.S., Lewellen, D.C., and Sykes, I.R. (1997) "Large-Eddy Simulation of a Tornado's Interaction with the Surface," J. Atmospheric Sciences, Vol. 54, pp. 581-605.

Moin, P. and Pierce, C.D. (1996) "Large Eddy Simulation of Coaxial Jet Combustors," Paper presented at the AFOSR Contractors and Grantee Meeting on "Turbulence and Internal Flows", Westin Peachtree Plaza Hotel, Atlanta, Georgia, Sept. 4-6.

Sommerfeld, M., Ando, A., and Wennerberg, D. (1992) "Swirling, Particle-Laden Flows Through a Pipe Expansion," JFE, Vol. 114, pp 648-656.

Wahiduzzaman, S., and Ferguson, C. (1986) "Convective Heat transfer from a Decaying Swirling Flow within a Cylinder," Eight International Heat Transfer Conference, paper No. 86-IHTC-253.

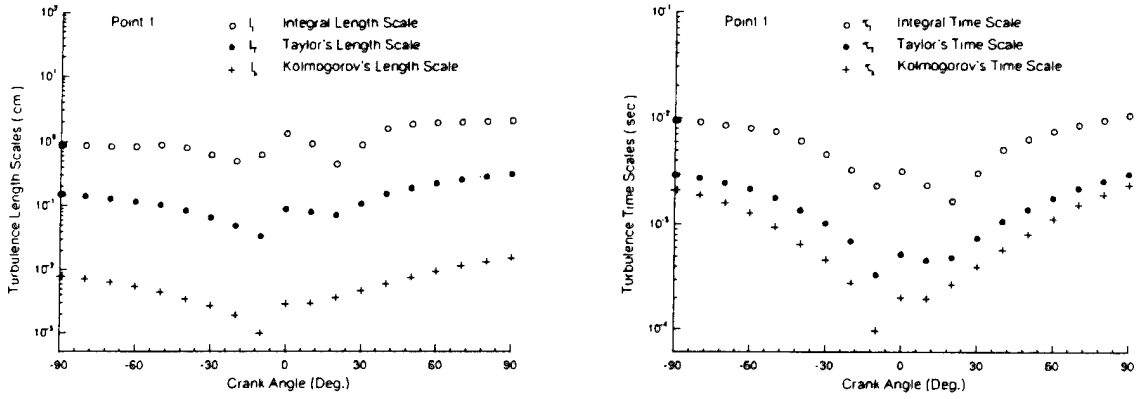

Figure 1 Calculated turbulence scales

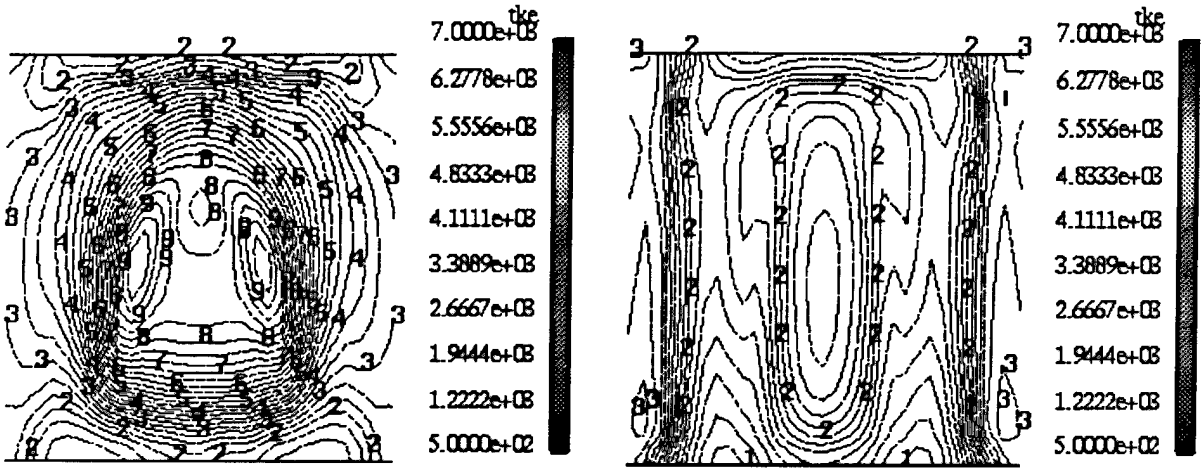

a) b)

Figure 2 Distribution of turbulent kinetic energy k(cm^2/s^2) at 120° ATDC obtained from KIVA-3
a) with standard k-ε model, b) with SGS model

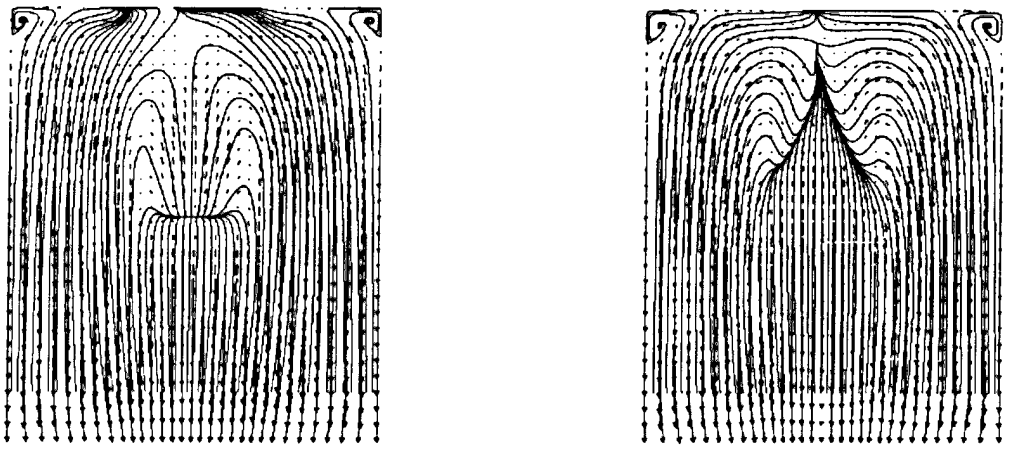

a) b)

Figure 3 Distribution of velocity vectors (cm/s) and instantaneous 2-D streamlines at 120° ATDC obtained from KIVA3 a) with standard k-ε model, b) with SGS model

A UNIVERSITY RESEARCH INITIATIVE PROGRAM FOR ADVANCED DIESEL ENGINE RESEARCH

ARO contract DAAL03-92-G-0122
ARO grant DAAH04-94-G-0328

Principal Investigators: Mike Corradini, Pat Farrell, Dave Foster, Jaal Ghandhi, Jay Martin, Rolf Reitz, Chris Rutland, Emeritus Professors: Gary Borman and Phil Myers

Engine Research Center
1500 Engineering Drive
Madison, WI 53706

OVERVIEW:

The Engine Research Center at the University of Wisconsin - Madison is the U.S. Army's Center of Excellence for Advanced Propulsion. It is a cooperative effort which has the objectives of providing knowledge and research tools for solution of long range problems of special interest and importance to mobility needs and identifying new technologies important to mobility and studying those technologies in a research environment. This effort is primarily conducted through the education of graduate student researchers. The current focus of research efforts are the fundamental phenomena associated with increasing power density, air utilization and fuel conversion efficiency of combustion propulsion systems.

TECHNICAL DISCUSSION

The Engine Research Center at the University of Wisconsin - Madison is a multi-investigator cooperative effort performing research on the fundamental aspects of advanced propulsion systems addressing unique needs of the Army. The research effort is a parallel development of experimental investigations on state of the art engines using advanced diagnostics and sophisticated 3-D model development. This effort currently includes approximately 70 graduate students working on MS and Ph.D. degrees.

This presentation will be in three parts. First, a very brief introduction to the Engine Research Center will be given which will be followed by highlights of both computational and experimental efforts addressing fundamental aspects of fuel sprays. The fuel injection system and process is arguably the most important component and process of the diesel engine. The fuel injection system is responsible for the establishing the droplet size distribution, the air entrainment rates, the distribution of the fuel throughout the combustion chamber and influences the mixing rates between the fuel and the air during the later stages of combustion. It is likely that through the use of electronic control of the injection parameters the fuel spray can be manipulated to significantly improve the performance of the engine. These improvements can be assessed as improved air utilization, higher power density, better fuel economy or lower emissions.

Three aspects of the spray research effort within the Engine Research Center will be highlighted:

Comparison between the predictions of an upgraded spray break-up model and measured in-engine, liquid, fuel, and vapor penetration and equivalence ratio distributions.

Modeling of Multi-Component Fuels Using Continuous Distributions

Collisional Behavior of Hydrocarbon Droplets at High Impact Weber Numbers

As part of the continuing effort to include the appropriate physics within the spray break-up model the ERC has developed a new break-up sub-model for implementation into our KIVA engine simulation. The new model predicts the droplet size distribution using both Kelvin-Helmholtz and Rayleigh-Taylor break-up phenomena. To facilitate reasonable computational times the processes are split up. It is assumed that the initial break-up, close to the nozzle tip, is controlled primarily by Kelvin-Helmholtz instabilities. Then, after a user prescribed distance, the model starts to consider both Kelvin-Helmholtz and Rayleigh_Taylor mechanisms for predicting the break-up. This new model has recently been compared to the experimental data obtained Dr. John Dec on a Cummins optical access engine at Sandia. The results of the comparisons of the liquid spray penetrations between the predictions of the simulation and the experimental data are shown in Figure 1.

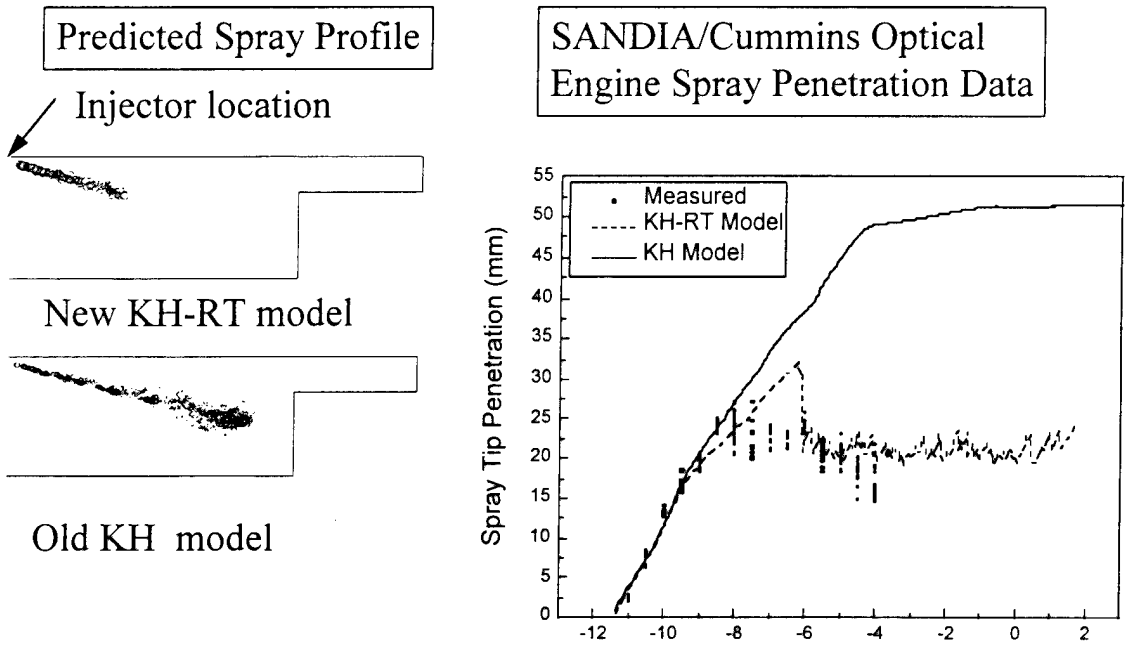

Figure 1 Comparison of Sandia/Cummins optical engine spray penetration data and the predicted profiles using the Advanced Kelvin Helmholtz/Rayleigh-Taylor spray model.

As can be seen in the figure, the new KH-RT model predicts liquid spray penetrations that are in good agreement with the measurements in the Sandia engine. It is also apparent that the model using only the Kelvin-Helmholtz break-up mechanism does not predict liquid penetration similar to that measured in the experiment. In addition to measuring the liquid spray penetration the measurements at Sandia also included an assessment of the fuel vapor distribution. Figure 2 shows a comparison between the predicted vapor distribution and the measurements reported by Dec for the same engine. It is very encouraging that the new spray model agrees quite well with the trends observed in the Sandia engine.

Previous work at the ERC has indicated the including multi-component vaporization in the simulation could be important for correctly predicting Diesel engine cold start and cold operation characteristics. The previous multi-component vaporization model considered a two component fuel and included spatial resolution within the vaporizing droplets. This approach was computationally too intensive for the current simulation. In a continuing effort to develop a computationally more streamlined sub-model, we are attempting to represent vaporization of a multi-component fuel droplet using a continuous distribution function, assuming no spatial composition gradients within the droplet and assessing vapor diffusion away from the droplet surface with global diffusion coefficients.

An evaluation of the impact of using global diffusion coefficients versus spatially resolved gas phase diffusion was performed by comparing the predicted lifetimes of gasoline and Diesel fuel droplets between the new ERC model with those published by Tamim and Hallet. Table 1 shows the results of this comparison. The predicted lifetimes were different by approximately 30 percent. However the temporal droplet composition and its temperature were similar between the two models. Figure 3 shows the predicted droplet temperature, mean

molecular weight, the boiling temperature and mass of liquid vaporized for a Diesel fuel droplet using the new continuous model.

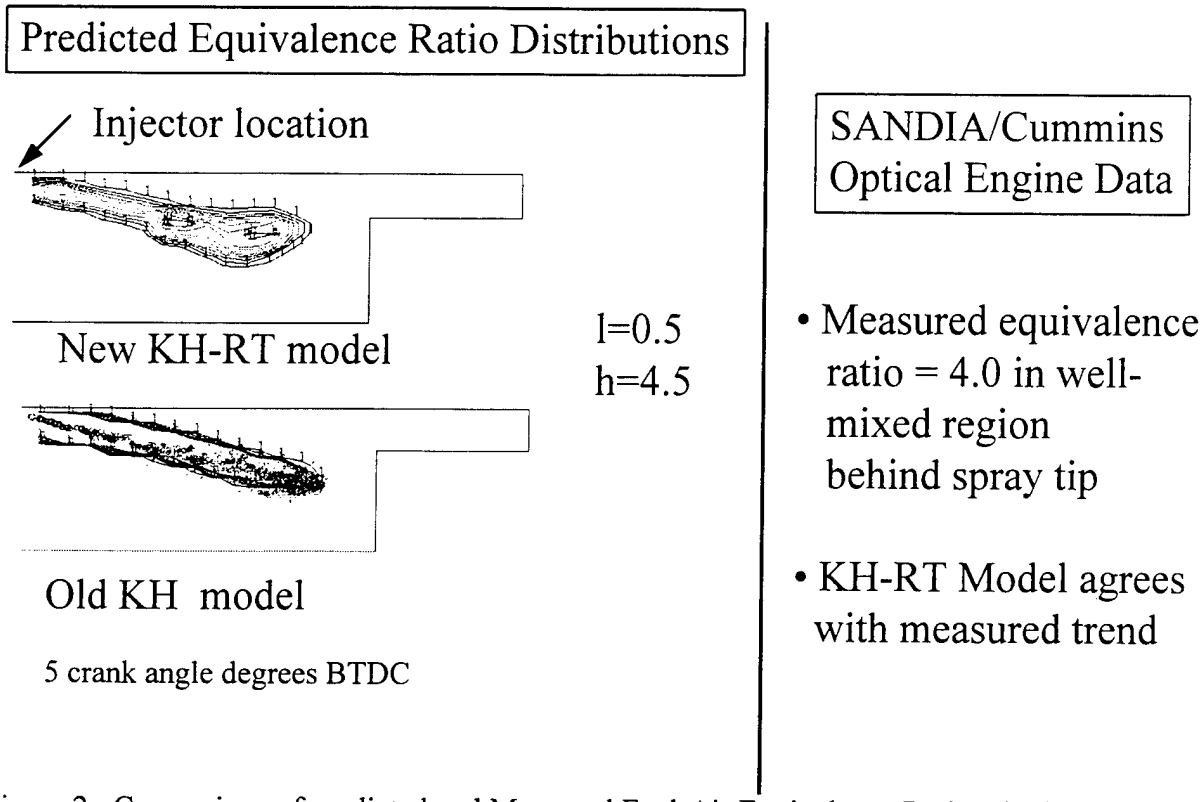

Figure 2: Comparison of predicted and Measured Fuel-Air Equivalence Ratio Distributions

Table 1 Comparison of Droplet Lifetimes

	Tamim and Hallett Model	Present Model
Gasoline	50 msec	33 msec
Diesel	56 msec	41 msec

In addition to the spray break-up and vaporization processes additional work on the effect of intra-spray droplet collisions, at high collisional Weber number and collision angles is underway. Using two approximately monodisperse droplet streams and a phase Doppler particle analyzer changes in droplet size and velocities are being measured for impacting droplets. The results show a significant decrease in the droplet diameter distribution as a result of these high impact Weber number and collision angle impacts. These results are shown in Figures 4 and 5. Figure 4 shows the droplet size distribution of the fuel stream issuing from a sapphire nozzle and Figure 5 shows the resulting droplet size distribution after collision with an identical second stream at a collision angle of 20 degrees.

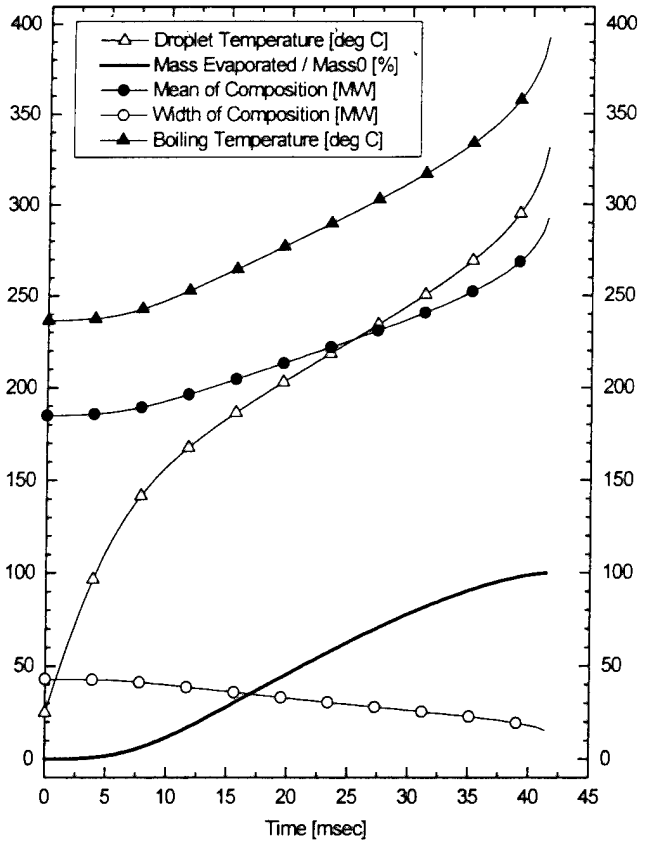

Figure 3. Predictions of a 100 μm multi-component diesel droplet vaporization history for conditions of P=101.3 kPA and T=973 K

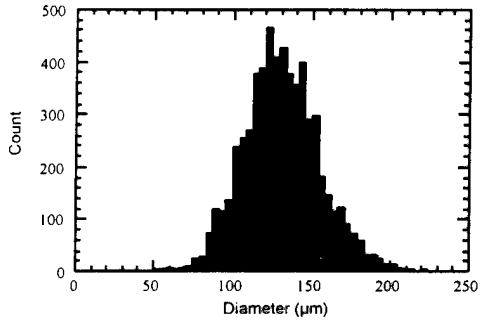

Figure 4. Droplet Diameter histogram from the nozzle

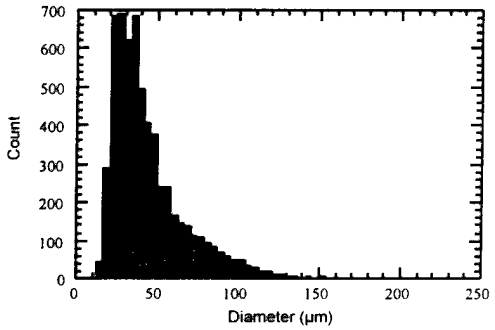

Figure 5. Droplet diameter histogram for a collision angle of 20°.

References

Dec, J., "A Conceptual Model of DI Diesel Combustion Based on Laser-Sheet Imaging," SAE 970873

Tamin, J. and Hallet W.L.H., "Continuous Thermodynamics Model for Multicomponent Vaporization," *Chem Engr. Sci*, Vol 50, No. 18, 2933-2942, 1995

RESEARCH INSTRUMENTATION AND COLLABORATIVE RESEARCH IN DIESEL ENGINE COMBUSTION

David E. Klett, North Carolina Agricultural
and Technical State University

Abstract not available at the time of printing

ENGINEERING MODEL DEVELOPMENT FOR DIESEL PERFORMANCE AND EMISSIONS

ARO Contract No. DAAH04-94-G-0236

Principal Investigators:

A.M. Mellor, Vanderbilt University

R.J. Tabaczynski, Ford Motor Co.

S.L. Plee, Motorola, Inc.

OVERVIEW:

The specific aim of the research is to develop a characteristic time model (CTM) for Diesel engine emissions. In the model, expressions describing the spatial and temporal fuel/air mixing and kinetic aspects of the combustion process are sought which, when combined in the appropriate manner, correlate the steady-state soot and NOx emissions from direct injection Diesel engines. Experimental work on a high speed direct injection Diesel is ongoing at Ford Motor Co. to acquire data for CTM model validation. Collaborative efforts are underway at both Ford and the University of Wisconsin-Madison to use CFD to model the engine intake and compression stroke air and fuel motion. Present and future efforts include utilizing the above information to better understand the Diesel fuel/air mixing and combustion process and implementing it into the CTM. One eventual end product will be an engineering model to predict trends in the major legislated emissions from Diesel engines for changes in both design and operating conditions.

TECHNICAL DISCUSSION:

Initial program plans were to focus on the mixing aspects of the CTM since an original premise of the program was that earlier work by one of the co-principal investigators on global NOx and soot kinetics based on pollutant emissions dominated by diffusion flame contributions had elucidated the kinetic aspects of the model. In particular, the original Diesel NOx kinetic characteristic time of Plee et al. (1981a,b) suggested that the effect of changes in EGR on the *net* NOx emissions could be correlated with a single activation energy deduced from a single characteristic stoichiometric flame temperature. In terms of the model, this was represented as the net kinetic time for NOx emissions incorporating both the formation and decomposition processes. However, the emphasis in the present program has been, by necessity, redirected towards the chemical kinetic aspects of the model since preliminary analysis of literature data for modern engines yielded different results from this global kinetic model. A series of experiments on a Ford 2.2L engine was thus designed to explore reasons for these differences.

Exhaust gas recirculation variations from zero to maximum level possible were performed for parametric variations in the engine operating conditions as follows: engine speed from 1000-2500 rpm; injection pressure from 56-133 MPa; start of combustion timings of -5,TDC,+5, +10; and load from 200-800 kPa BMEP. The computed variations in the stoichiometric flame temperature were used in Arrhenius plots to determine the activation temperatures for NOx and soot, and typical values for NOx were significantly lower than the previously accepted value. Changes in speed, injection pressure and start of combustion timing were found to have negligible effect on the computed activation temperature for NOx or soot. However, changes in engine load led to appreciable differences in both of these values.

Here the formation and decomposition processes are modeled independently, so that the NOx emissions index is proportional to the ratio of kinetic times $\tau_{no,decomp}$ to $\tau_{no,form}$. These are Arrhenius expressions $\tau_{no,form} \sim \exp(E_{form}/RT_{\phi=1})$ and $\tau_{no,decomp} \sim \exp(E_{decomp}/RT_{decomp})$ where $E_{form}/R \cong 68000$ K is the activation temperature for NO formation from the extended Zeldovich mechanism based on conventional gas turbine emissions (Derr and Mellor, 1990), and $T_{\phi=1}$ is the stoichiometric flame temperature evaluated at manifold-

influenced TDC conditions for the Diesel engine. The activation temperature for NO decomposition must be determined from the experimental Diesel data once a suitable temperature (T_{decomp}) is chosen. The data indicate that T_{decomp} should be a measure of engine load.

Consider a dual (limited pressure) thermodynamic cycle where processes 2-3a and 3a-3b are the constant volume and constant pressure combustion portions of the cycle, respectively. bmep (load) is defined as the net specific work per cycle (w_{net}) divided by the cylinder specific volume displaced per cycle, and from the First Law of Thermodynamics with the assumption of constant specific heats:

$$bmep \sim w_{net} \sim q_{net} \sim q_{in} = c_v (T_{3a}-T_2) + c_p(T_{3b}-T_{3a}) = c_pT_{3b} - RT_{3a} - c_vT_2$$

T_{3b} is the peak burned gas temperature and is directly proportional to engine load.

The NO decomposition process occurs in the bulk gases after peak combustion temperatures and during the expansion stroke. Since T_{3b} is representative of the bulk end of combustion gas temperature ($T_{decomp} = T_{3b}$) it possibly could be used as a surrogate temperature for determining NO decomposition similar to the manner in which an estimated end of combustion temperature is used to correlate soot emissions by others (Primus, 1995).

A fuel-air cycle analysis using the chemical equilibrium code STANJAN (Reynolds, 1987) was performed to calculate values for T_{3b}. In accordance with the dual cycle analysis, it is assumed that first one-half mol of fuel (in essence, the premixed burn fraction = 0.5) is mixed with air at the overall equivalence ratio and EGR at state 2 conditions (from polytropic compression). These reactants undergo constant volume, constant internal energy combustion to yield products (constrained to O_2, N_2, CO_2, H_2O) at state 3a. When the products are allowed to dissociate in the calculation, the mol fractions of the additional species (CO, NO, OH, etc.) are negligible. Including these species results in a less than one Kelvin change in T_{3b}. The other half mol of fuel is then mixed with the products remaining in the cylinder at state 3a conditions. Finally, these reactants undergo constant pressure, constant enthalpy combustion to state 3b. Dissociation is included in this last step.

Data from the previously mentioned parametric variations were analyzed to determine the activation temperature for NO decomposition. Arrhenius plots were constructed as follows. Since the NOx emissions index is postulated as proportional to the ratio of $\tau_{no,decomp}$ to $\tau_{no,form}$, the slope of a graph of $\ln[NOxEI \exp(68000/T_{\phi=1})]$ versus $1/T_{3b}$ is the activation temperature for NO decomposition, E_{decomp}/R. If T_{3b} is the proper correlation temperature, and if the NO decomposition kinetics can be modeled as global, then the slope will be constant irrespective of operating conditions.

As EGR rate increases, the stoichiometric flame temperature decreases as expected, and the computed bulk end of combustion temperature (T_{3b}) increases due to the increase in both inlet manifold temperature and equivalence ratio. At the highest EGR rates the computed end of combustion temperatures approach but are lower than the stoichiometric flame temperature evaluated at TDC conditions.

A sample Arrhenius plot for eight parametric variations is given in Fig. 1. It is clear that a unique NO decomposition activation temperature exists, independent of speed, injection pressure, SOC timing and load. An average value of 45216 K is obtained by weighting the number of data for each curve. Future efforts include completing the calculations for the remaining parametric variations and using the premixed burn fractions computed for the experiments instead of assuming a 50% split. In addition the generality of the above finding of a unique NO decomposition activation temperature will be further investigated by analyzing data from several additional sources encompassing a range from a small HSDI Diesel to a large, stationary power generation DI Diesel.

Another opportunity to explore the failure of the original choice of activation temperatures by Plee and co-workers for soot and NOx emissions from modern engines is afforded by the recent study of Mitsubishi (Kohketsu et al., 1996) in which a unique, hybrid nozzle capable of injecting stratified fuel-water-fuel mixtures was characterized for exhaust emissions (Psota et al., 1997). Figure 2, taken from the latter paper, shows the ratio of NOxEI with water injection to dry NOxEI versus the water-to-fuel flow rate ratio by mass. Three sets of Mitsubishi data are shown, corresponding to three different injection timings. Represented by the lines are calculated NOx reductions based on limiting cases for a water injection model for gas turbine engines developed by Newburry and Mellor (1996), modified here for the Mitsubishi Diesel engine. The solid model lines ignore residual gas, and the two dashed lines below the solid cases show the normalized computed effects of 5 and 10% residual gas, respectively (see Psota et al., 1997).

The limiting cases correspond to uniform water injection throughout the cylinder (expected to represent intake manifold water injection), denoted $T_{\phi=1,unif}$, and best-case reduction, in which all water is injected only into stoichiometric eddies surrounding the spray plume, labeled $T_{\phi=1,all}$. The latter situation is deemed hypothetical because of the impossibility of matching all of the water locally with each and every stoichiometric eddy.

The salient point is that these model curves were computed using the Zeldovich activation temperature of 68000 K, in contrast to the Plee et al. value of 35000 K. The traditional Zeldovich value ignores decomposition of NO, and comparison of the measurements with the model lines in Fig. 2 suggests that at low water-to-fuel ratios, because less reduction is observed than for uniform water injection, the Mitsubishi injector does not operate as effectively as would intake manifold injection (since these relatively small amounts of water remain localized within the stoichiometric contour). In contrast, for larger water-to-fuel ratios and depending on injection timing, water injection via the stratification induced by the hybrid nozzle increases in effectiveness over uniform injection to a degree similar to that observed in fielded combustion turbines (see Newburry and Mellor, 1996, and Psota et al., 1997). Psota et al. discuss reasons for this increase in effectiveness, including both enhanced penetration of the water to the time-mean stoichiometric contour and beneficial effects of increased dwell due to split fuel injections obtained with the Mitsubishi design.

Another possibility is that the value of activation temperature used in Fig. 2 is incorrect for Diesel engines. Based on Fig. 1 and the discussion of the effect of load on NO activation temperature for the Ford data, one could argue that the 35000 K value is the appropriate value for the Mitsubishi Diesel. However, the largest water-to-fuel measurements demonstrate NOx reductions greater than the theoretical maximum based on the Plee et al. activation temperature, which shows that the choice of a one-step global activation temperature equal to 35000 K for these cases is also invalid. Consequently, the approach outlined previously, to break the one-step global characteristic kinetic time for NOx emissions into a two-step formation, then decomposition model, is our next approach to the analysis of the Mitsubishi NOx data.

This hybrid injector is of particular interest because it can simultaneously reduce both NOx and particulate emissions. The latter observation is thought to reflect the beneficial effect on the formation of soot of water injection directly into the interior of the spray plume, although injection pressure is increased somewhat with increased water-to-fuel ratio. Consequently, we are now using selected soot emissions data reported by Kohketsu et al. (1996) to develop a two-step soot formation/oxidation model very similar to that discussed in the previous section for NOx emissions. The temperature characteristic of soot formation is presently evaluated as the arithmetic average of the fuel 50% recovery temperature and the ϕ=2 flame temperature evaluated at TDC. Thus, the original one-step global kinetics based on the stoichiometric flame temperature, as developed by Plee and co-workers, will be replaced by two-step global kinetics representing both the formation and destruction of NO and soot in the engine and based on different surrogate temperatures characteristic of the Diesel combustion process.

REFERENCES

Derr, W.S. and Mellor, A.M. (1990), "Recent developments," Design of Modern Turbine Combustors, Academic Press, London, pp. 474-544.

Kohketsu, S., Mori, K. and Sakai, K. (1996), "Reduction of exhaust emission with new water injection system in a Diesel engine," SAE Paper 960033.

Newburry, D.M. and Mellor, A.M. (1996), "Semiempirical correlations of NOx emissions from utility combustion turbines with inert injection," AIAA J. Propuls. Power 12, 527-533.

Plee, S.L., Ahmad, T. and Myers, J.P., (1981), "Flame temperature correlation for the effects of exhaust gas recirculation on diesel particulate and NOx emissions," SAE Paper 811195.

Primus, R. (1995), Cummins Engine Co., Personal Communication.

Psota, M.A., Easley, W.L., Fort, T.H. and Mellor, A.M. (1997), "Water injection effects of NOx emissions for engines utilizing nonpremixed combustion," SAE Paper 971657.

Reynolds, W.C. (1987), STANJAN Version 9.3, Dept. of Mech. Eng., Stanford Univ.

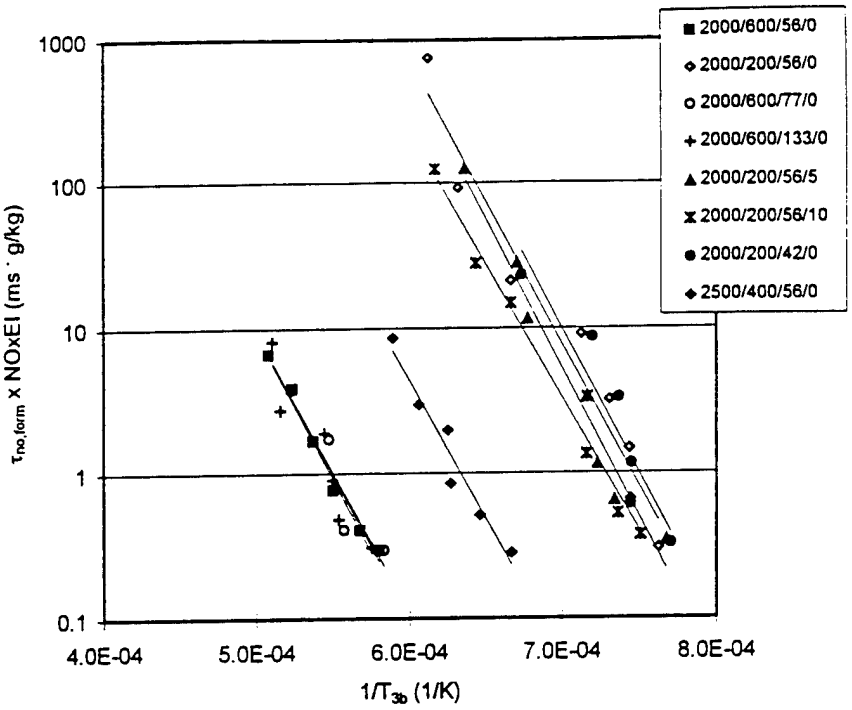

Figure 1 - Arrhenius plot used in determination of NO decomposition activation temperature. Lines represent least squares fits of data. Legend numbers are speed (rpm), bmep (kPa), injection pressure (MPa) and start of combustion timing (degrees), respectively.

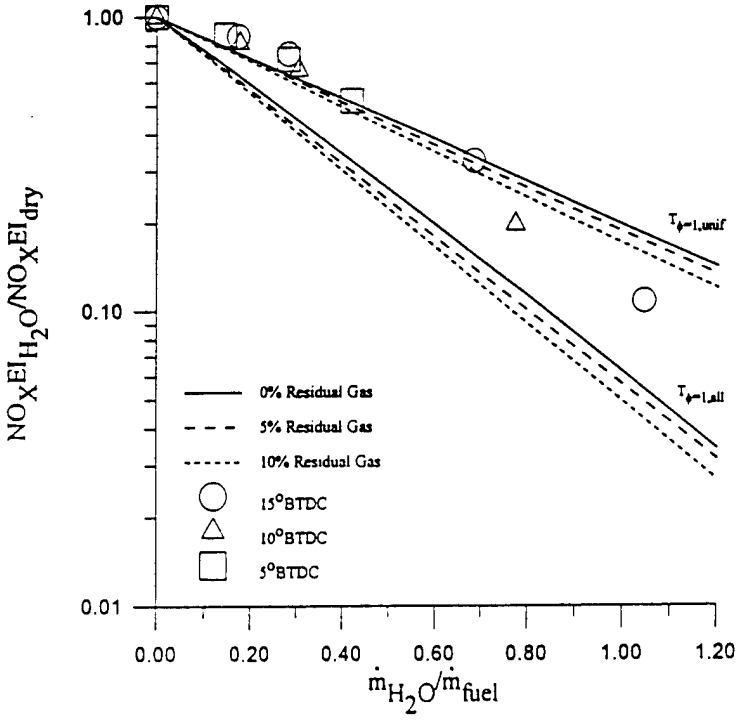

Figure 2 - Linear representation of normalized NOx emissions index reduction as a function of water to fuel mass ratio. E/R of 68000 K is used (from Psota et al., 1997).

HIGH PRESSURE PREIGNITION CHEMISTRY OF HYDROCARBONS AND HYDROCARBON MIXTURES

Contract No's. DAAH04-93-G-0042 and DAAH04-93-G-0145
Reference No's. 30782-EG and 31270-EG-AAS

N.P. Cernansky and D.L. Miller

Department of Mechanical Engineering and Mechanics
Drexel University, Philadelphia, PA 19104

PROGRAM OVERVIEW

A research program to investigate the high pressure oxidation and ignition characteristics of hydrocarbon fuels has continued, and includes efforts under an associated AASERT Award. The objectives of this program are to develop the kinetic and mechanistic information in the low and intermediate temperature regimes (650-1000 K) and at elevated pressures (up to 20 atm) which will be useful to understand the oxidation of pure hydrocarbons, determine the synergistic and antagonistic effects for binary and ternary mixtures of full boiling range fuel components, and formulate hypotheses on ignition mechanisms. Efforts are directed towards experimental investigation of the oxidation of pure hydrocarbons and hydrocarbon blends, prediction and validation of mechanisms relevant to preignition chemistry of hydrocarbons and hydrocarbon mixtures, and development of in situ measurement techniques using degenerate four-wave mixing (DFWM) and Cavity Ringdown Laser Absorption Spectroscopy (CRLAS).

In our experimental work, pure neat fuels, their simple blends and full boiling range fuels are being examined using static, flow reactor and engine systems under a wide range of temperature and pressure. Detailed product distributions and/or time-resolved profiles have been collected. Over the last year, our pressurized flow reactor (PRF) facility has been upgraded to reach higher reaction temperature and to enhance its liquid fuel metering capacity. Also, we continued to refine and extend both our detailed and reduced kinetic mechanisms. In our related AASERT work, we are exploring the possibility of infrared detection of polyatomic molecules (CO_2, H_2O, HO_2, etc.). In conjunction with Sandia National Laboratory, we detected methyl radical (CH_3) in a low pressure laminar flat flame using Infrared Cavity Ringdown Laser Absorption Spectroscopy (IR-CRLAS).

Specific work is reviewed in the following sections.

STUDIES IN STATIC AND PRESSURIZED FLOW REACTOR

Experimental investigation of the oxidation of 1-pentene and a blend of n-pentane and 1-pentene in our static reactor system was completed. The results of n-pentane experiments identified the important steps controlling product formation. Neat 1-pentene experiments were conducted at temperatures spanning the negative temperature coefficient regime (573 to 773 K), at both lean and rich equivalence ratios (0.8 and 1.3), and at pressures in the range 200 to 400 torr. Induction time profiles indicated the presence of a negative temperature coefficient (NTC) region between 615 and 665 K. Changes in product distribution indicated a transition in the chemistry between the low and intermediate temperatures in the region of the NTC behavior; this was interpreted using a mechanism which describes the main reaction paths and shifts. Studies of a n-pentane / 1-pentene blend indicated that in a mixture the two components reacted intramolecularly through a common pool of small labile radicals such as OH, H and HO_2. At low temperatures, the alkene preferentially reacted with the radicals and diverted the reaction into the slower alkene chain, reducing the reactivity of the alkane. In the region of NTC and just beyond, where the alkane is relatively unreactive, the n-pentane acted as a radical trap for some of the radicals formed in the alkene reaction chain, thereby retarding the activity of the alkene.

As the logical follow-up work, we conducted experimental studies of n-pentane and 1-pentene oxidation utilizing the PFR facility. These studies were done in the low temperature and

NTC regimes (600 to 825 K) and at elevated pressures (4 to 12 atm) under dilute, lean conditions ($\phi \sim 0.3$). Strong NTC behavior was observed with both fuels, and is attributed to the same shifts in radical dominance as occurs with the smaller alkanes. Very high yields of oxygenated hydrocarbons were observed in the NTC region with both fuels (e.g., propionaldehyde with 1-pentene), primarily as a result of secondary oxidation of C5 alkenes. Also, formaldehyde and carbon monoxide formation exhibited a significant pressure effect, possibly due to enhanced importance of the "Waddington" mechanism with increasing pressure. n-Pentane was consumed faster with increasing pressure, while 1-pentene consumption was unaffected by pressure.

In order to cover the full range of low and intermediate temperature, the PFR facility has been upgraded by adding a second stage air heater. The new heater has been installed and its operation was verified. The reactor can reach temperatures in excess of 1000 K (the previous limitation was 850 K). Verification experiments using n-pentane have been completed. Comparing with previous results, the current reactivity map reproduces the NTC phenomena and the profile of CO formation [Figure 1]. With this background work completed, the proposed experimental studies of neo-pentane oxidation have been initiated. Considering the low boiling point of neo-pentane, the liquid flow controller has been also updated to meter and direct the fuel into the pressurized flow reactor.

In related research work, we began to extend our studies to examine the preignition reactivity of full boiling range industry standard fuels (ISF). We have mapped the reactivity of Indoline and Auto-Oil fuels, RFA and RFB, as a function of inlet manifold temperature in our research engine under motored engine conditions. Results have been compared with those of primary reference fuels (PRF's) and a simple fuel mixture of an aromatic, an olefin and saturates (92 ON MIX), blended to match the overall composition of the ISF's. All these fuels show similar reactivity behavior [Figure 2]. We concluded that a simple fuel mixture can be a good surrogate for full boiling fuels, thereby supporting the relevance of our studies with simple fuels and blends. In parallel, we are initiating work to generate comparable reactivity maps with ISF's in the well characterized thermal and fluid mechanical environment of our PFR. In addition, product distributions will be collected for further kinetic modeling work.

REDUCED AND DETAILED MECHANISM

The detailed species evolution profiles generated by our experimental studies are being used extensively in the development and validation of autoignition models incorporating low temperature and NTC chemistry. In conjunction with William Pitz and Charles Westbrook at Lawrence Livermore National Laboratories (LLNL), a detailed chemical kinetic model for propane oxidation, incorporating the low temperature and negative temperature coefficient chemistry, was developed based upon our experimental species evolution profiles and our reevaluation of the relevant thermochemistry. The detailed model can match the experimental results very well [Figure 3]. Key features new to this model include: propyl radical and hydroperoxy-propyl radical reactions with O_2 proceeding primarily through thermalized adducts, not chemically activated channels; and many propylperoxy radical reactions attaining partial equilibrium at 10-15 atm. These features represent a fundamental change in our understanding of such systems. Since we have generated product profiles of various fuels, more efforts will be made to develop detailed kinetic mechanism of hydrocarbon oxidation.

A reduced chemical kinetic model for predicting the preignition oxidation behavior of primary reference fuels (PRF's) at low and intermediate temperatures was developed. It can predict ignition delay, preignition heat release, and the behavior of key chemical species including consumption of the fuel, formation of CO as a major oxidation product, and production of other species classes. The predicted oxidation behavior is in fairly good agreement with experiments. Using the experimental data from n-butane and its blends with iso-butane, under skip fired engine conditions, we extended the reduced model to the butanes. As was the case for PRF's, the model appears to be able to satisfactorily predict the major preignition oxidation behavior at low and intermediate temperatures for different fuels and under various engine condition, with appropriate adjustments to the fuel specific rate parameters. We continue to explore the breadth of applicability of the model with the available experimental results and those to be generated.

LASER DIAGNOSTIC ACTIVITIES

We continue in our efforts to develop in-situ laser diagnostics to detect radical species generated in our various reactor systems. We have applied degenerate four-wave mixing (DFWM) to detect OH via the $A\ ^2\Sigma^+ - X\ ^2\Pi$ system near 308 nm in a variety of experimental systems, including flames and supersonic jet expansions. To our knowledge, this was the first detection of OH via DFWM in a free jet expansion. This work was followed by an attempt to improve DFWM sensitivity by using a tilted backward pump beam DFWM geometry. This allows for increased signal collection (by placing the signal-collecting beamsplitter with a mirror) and a significant decrease in background noise reaching the detector. This improvement in S/N allowed for the detection of the cyano (CN) radical in the $B\ ^2\Sigma^+ - X\ ^2\Sigma^+$ band in a C_3H_8 / O2 / N2 atmospheric pressure flat flame doped with nitric oxide. Relative concentration profiles have been measured for ten premixed flames at various equivalence ratios. It was found that the CN concentration profile is strongly dependent on equivalence ratio with a maximum amount produced for an equivalence ratio of 1.73.

We have been collaborating with David Rakestraw's group at Sandia National Laboratory (SNL) to study the feasibility of measuring radical polyatomic species in high temperature/low pressure laminar flat flames using a more sensitive laser absorption-based technique, namely Cavity Ringdown Laser Absorption Spectroscopy (CRLAS). Absolute absorption profiles were calculated for a number of radicals, including HO_2, HCO, CH_3, CH_2, and C_3H_3. We concluded that CRLAS, with a detection limit of approximately 10 ppm, has the potential of measuring HCO and CH_3 under these conditions, but not the other radicals in the flames studied. However, DFWM, with a less sensitive detection limit, has no apparent potential of measuring such weakly absorbing species in high temperature systems.

Based on the above calculations, we successfully employed Infrared Cavity Ringdown Laser Absorption Spectroscopy (IR-CRLAS) to detect the methyl radical (CH_3) in a low pressure laminar CH_4 / O_2 / N_2 flat flame, the first measurement of a combustion-generated polyatomic radical in the infrared. Roughly half of the known methyl transitions in this region were found to be totally obscured by much larger absorption features, numerous in this spectral region, some of which were identified (with the aid of the USF HITRAN-PC database) to be due to CH_4, H_2O, C_2H_2, CO_2 and OH. The spectral congestion in the mid infrared was found to be significant and may also preclude the measurement of other weaker polyatomic radicals such as HO_2 and C_3H_3.

Consequently, the dependence of the height-above-burner (HAB) absorption profile was determined for 37 torr CH_4 / O_2 / N_2 flat flames of two different equivalence ratios (Φ = 1.0 and 1.6) [Figure 4]. The flame temperature profile was also measured using N_2 coherent anti-Stokes Raman spectroscopy (CARS) and a spectral fitting code developed at SNL. The HAB absolute concentration profiles were then compared to that predicted by the Miller-Bowman mechanism. The comparison was favorable for stoichiometric conditions. But, for the fuel-rich case, the model overpredicts both the amount and height of the CH3 maximum. Reasons for this discrepancy are currently being explored.

More recently, the HCO radical has also been detected in identical flames using CRLAS via the visible A - X electronic band. Our HCO HAB data compares to the predicted Miller-Bowman concentrations in a similar manner as observed with CH_3: the model overpredicts both the amount and position of maximum [HCO] for Φ = 1.6. This observation strengthens the argument that the model does not accurately predict the chemistry in rich flames, since HCO is thought to be produced from formaldehyde, a product of CH_3 reactions.

CURRENT AND FUTURE WORK

The standard Fourier Transform Infrared spectra of anticipated products from oxidation of neo-pentane are being generated for use in our qualitative and quantitative analyses. Once completed, we will conduct the proposed experimental studies of neo-pentane in the PFR, and then conduct any necessary follow-up experiments with other fuels. The associated work on reduced and detailed models will continue, as will our diagnostic development and application activities.

RELATED FIGURES

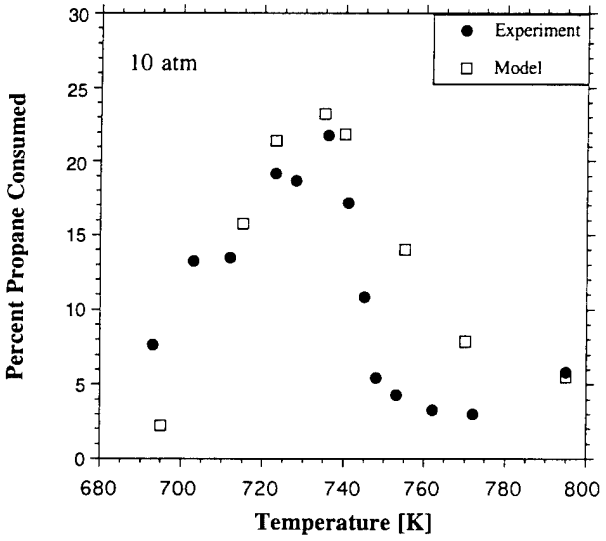

Figure 1. Comparison of experimental and detailed modeling results with propane across the NTC region. Model reproduced the characteristic shape of profiles. Both the model and experiments show a distinct NTC region.

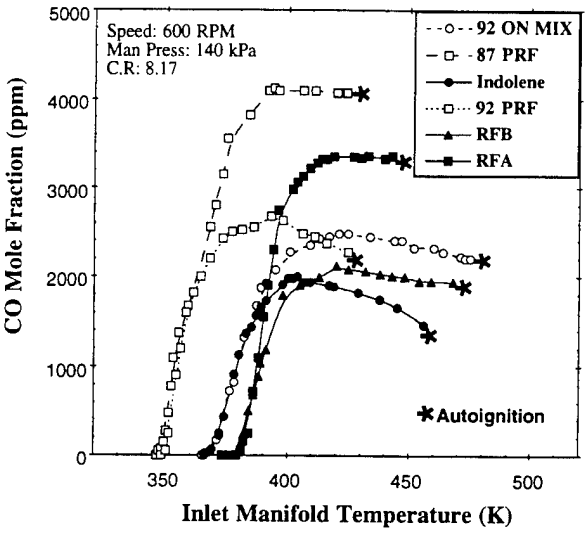

Figure 2. Reactivity map for full boiling range industry standard fuels, PRF's, and a simple mixture fuel. Reactivity maps of ISF are similar to those of PRF blend. The peak reactivity of ISF is lower and initiation of reactivity occurs at higher temperature.

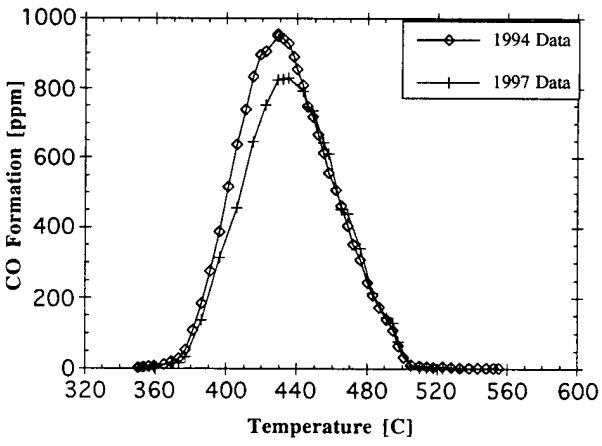

Figure 3. Comparison of recent reactivity map in modified PFR facility and previous result using n-pentane as the fuel.

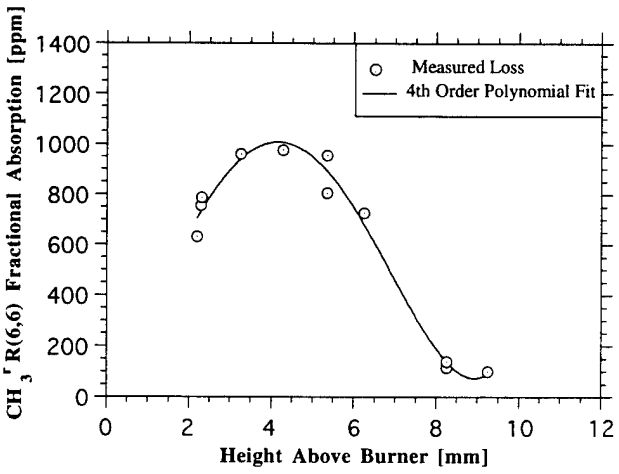

Figure 4. $CH_3{}^rR(6,6)$ Absolute Intensity vs. Height Above Burner (HAB) (in a low pressure $CH_4/O_2/N_2$ flat flame at $\emptyset = 1.6$).

IGNITION IN CONVECTIVE-DIFFUSIVE SYSTEMS

(ARO Grant No. DAAH04-94-G-0051)

Principal Investigator: Chung K. Law

Princeton University
Princeton, NJ 08544

SUMMARY/OVERVIEW

Ignition in convective-diffusive media is investigated in this program with the goal of better understanding and hence controlling the ignition event in Diesel engines. These ignition events take place in highly turbulent, non-uniform environments. As such, the transport phenomena for heat and mass are tightly coupled to the chemical kinetics and exert a strong influence on the overall ignition process. These complex interactions are studied using the well-characterized counterflow configuration, in which a cold fuel jet flows against an opposed hot air jet, and eventually ignites as the air temperature is gradually raised. The ignition response is studied experimentally, computationally, and analytically for a variety of fuels, with extensive variations of the fuel concentration, flow strain rate, and ambient pressure. During the report period we have investigated the ignition of ethane, propane, n-butane, and isobutane fuels. Specific issues addressed are the relative roles of low-to-intermediate and high temperature kinetics, their coupling at ignition with the heat release feedback, the existence of multiple ignition and mild oxidation regimes and their response to changes in the flow intensity, fuel concentration, and system pressure. In parallel, we have initiated studies on unsteady and turbulent ignition, focusing first on the reference hydrogen-air system. The computational results on unsteady ignition indicate that the system behaves quasi-steadily for low frequency imposed oscillations, whereas for high frequencies the system may persist beyond the limits of steady-state solutions. For turbulent ignition, preliminary experimental results show that the ignition temperature near the second ignition limit is remarkably insensitive to the turbulence characteristics. In addition, we have experimentally demonstrated for the hydrogen-air system the existence of triple stable stationary states for nonpremixed systems, and analyzed computationally the thermokinetic mechanisms leading to this multiplicity and to the accompanying dual-staged ignition and extinction phenomena.

TECHNICAL DISCUSSION

1. Multiple ignition, extinction, and stability of nonpremixed H_2-air flames

The interplay between thermokinetic and transport phenomena can produce complex responses even for the relatively simple system of hydrogen-air. In this system we have demonstrated experimentally for the first time the existence of three stable stationary states at the same boundary conditions, as shown by the water concentration Raman measurements plotted in Fig. 1. These three states correspond to distinct regimes of "frozen" flow, mild oxidation, and flaming combustion, which can be accessed in a dual-staged ignition sequence by increasing gradually the air boundary temperature. The first ignition is characterized by radical runaway (Fig. 2), while the second ignition is thermokinetic in nature. The first ignition leads to a mild oxidation regime characterized by minimal heat release and fuel conversion, in contrast to the flaming situation attained after the second ignition. The existence and response of these regimes to parametric changes in the pressure, flow intensity, and fuel dilution have been extensively characterized, both computationally using full and skeletal chemistry, and by experimental measurements.

2. Ignition of C_2–C_4 hydrocarbon fuels

Both ethane and propane are commonly found in natural gas blends, hence their practical importance. In addition, the ethane and propane oxidation mechanisms are essential building blocks of higher hydrocarbons mechanisms, therefore a good understanding of these subsystems is required for explaining the behavior of more complex fuels. Furthermore, n-butane and isobutane represent the lowest alkanes to exhibit isomerism, therefore their characteristics have relevance in understanding the effects of chemical structure on ignition. The ignition temperatures of C_2H_6, C_3H_8, n-C_4H_{10}, and i-C_4H_{10} were determined experimentally for a wide range of pressures, fuel concentrations and aerodynamic strain rates. In addition, ethane ignition has been simulated numerically, using detailed chemistry and transport properties. Interestingly, it has been found that all these fuels share a number of common characteristics, discussed in the following.

First, flame ignition is experimentally found to be preceded by chemiluminescent emission from excited formaldehyde and OH, over wide ranges of the system parameters (Fig. 3). Numerical modeling of ethane ignition indicates a sequence of kinetic acceleration followed by thermokinetic ignition, both dominated by high temperature branching. These two transitions show different sensitivity to changes in the external parameters, as shown by the variation of the associated air boundary temperatures with fuel concentration (Fig. 3) or flow strain rate (Fig. 4). Specifically, flame ignition is found to be more sensitive to these changes, as would be expected considering the amplifying effect of thermal feedback.

Second, the ignition temperature variation with fuel concentration is similar for the fuels investigated, as typified by ethane ignition in Fig. 3. In the limit of low concentrations the ignition temperature increases sharply with decreasing fuel content, whereas for concentrations in excess of 20–30% it remains essentially constant. The calculated results, shown in Fig. 3 with solid lines, agree qualitatively with the experimental findings. The quantitative disagreement, however, suggests that further scrutiny of the kinetic model is required.

Third, the ignition response to strain rate is also similar for these fuels, in that the ignition temperature increases monotonically with increasing strain rate (Fig. 4). This response can easily be understood recognizing that increasing strain rate increases the rates of convective and diffusive loss of both radicals and heat, hence the requirement for higher ignition temperatures.

Finally, similarity is also apparent in the response to pressure changes, in that the increase in pressure facilitates ignition throughout the ranges investigated (0.1–8 atm). This generic dependence on pressure is seen in Fig. 5 which plots the p-T ignition boundaries for n-butane. Qualitative differences exist, however. In the limit of high pressures the C_4 alkanes possess a distinct regime of insensitivity to pressure variation, that is, the system ignites single-staged at approximately the same temperature, despite the continuous pressure increase. The abrupt transition to this regime seen in Fig. 5 is reminiscent of the transition to a low temperature branching mode observed in homogeneous systems.

Differences in the diffusive ignition characteristics exist not only when using fuels with different chemical composition, but also when the fuel *structure* is varied. An example is n-butane versus isobutane. Isobutane is found to ignite at consistently higher temperatures than n-butane, although the overall response is similar. The interpretation of these results, as well as the relation of the first ignition to cool-flame behavior, is a subject of ongoing research.

3. Additive enhancement of nonpremixed ignition

The addition of highly diffusive molecular hydrogen was found in our previous studies to reduce drastically the temperatures required for ignition in the methane-air system. An even more dramatic effect of hydrogen addition was found computationally concerning the ignition of CO-air flames. We have confirmed experimentally this effect during the reporting period (Fig. 6). In addition, flame ignition is found to be preceded by excited CO_2 chemiluminescence, except at high fuel concentrations, as seen in Fig. 6.

4. Unsteady and turbulent ignition

Regimes of minimal effects of transport on ignition were identified in our previous work, in particular near the H_2-air second ignition limit which was shown to be dominated entirely by radical runaway. This suggests that situations exist where *turbulent* ignition is also governed by chemistry, in which case modeling might be significantly simplified by decoupling the temperature and major species equations from the relations governing the minor species evolution. Our exploratory investigation of turbulent ignition in the H_2-air system supports this hypothesis, as plotted in Fig. 7, which shows that the ignition temperature is relatively insensitive to strain variation over a wide range of the strain rate (500–2000 s^{-1}) and turbulence intensity (0–13%).

The effects of sinusoidal velocity oscillation on the ignition of hydrogen were computationally investigated with detailed descriptions of chemistry and transport. Results show that ignition basically behaves quasi-steadily for low frequency oscillations in that transient ignition occurs once the instantaneous strain rate falls below the steady-state ignition strain rate (Fig. 8). For ignitable systems subjected to high frequency oscillations, increasingly larger amplitudes are needed to effect ignition as the frequency increases. In particular, for sufficiently rapid oscillations the system may not have enough time to be ignited before the flow condition again becomes unfavorable for ignition, and as such with increasing frequency a system can persist beyond the regime in which steady-state solutions do not exist.

MAJOR PUBLICATIONS

[1] "A flame-controlling continuation method for generating S-curve responses with detailed chemistry," by M. Nishioka, C. K. Law, and T. Takeno, *Combust. Flame* 104:328–342 (1996).

[2] "Ignition in nonpremixed counterflowing hydrogen versus heated air: computational study with detailed chemistry," by T.G. Kreutz and C.K. Law, *Combust. Flame* 104:157–175 (1996).

[3] "Ignition in the supersonic hydrogen/air mixing layer with reduced mechanisms," by H. G. Im, B. T. Helenbrook, S. R. Lee, and C.K. Law, *J. Fluid Mechanics*, 322:275–296 (1996).

[4] "Ignition of hydrogen and oxygen in counterflow at high pressures," by B.T. Helenbrook and C.K. Law, *Twenty-Sixth Symposium (International) on Combustion*, The Combustion Institute, Pittsburgh, PA, pp. 815–822 (1996).

[5] "Ignition of counterflowing methane versus heated air under reduced and elevated pressures," by C.G. Fotache, T.G. Kreutz and C.K. Law, *Combust. Flame*, 108:442–470 (1997).

[6] "Theory of radical-induced ignition of counterflowing hydrogen versus oxygen at high temperatures," by B.T. Helenbrook, H. G. Im and C.K. Law, *Combust. Flame*, in press.

[7] "Ignition of hydrogen-enriched methane by heated air," by C.G. Fotache, T.G. Kreutz and C.K. Law, *Combust. Flame*, in press.

[8] "Ignition in nonpremixed counterflowing hydrogen versus heated air: computational study with skeletal and reduced chemistry," by T.G. Kreutz and C.K. Law, submitted.

[9] "Mild oxidation regimes and multiple criticality in nonpremixed hydrogen/air counterflow," by C. G. Fotache, C. J. Sung, C. J. Sun, and C.K. Law, *Combust. Flame*, in press.

[10] "Ignition of oscillating counterflowing nonpremixed hydrogen against heated air," by C. J. Sung and C.K. Law, submitted.

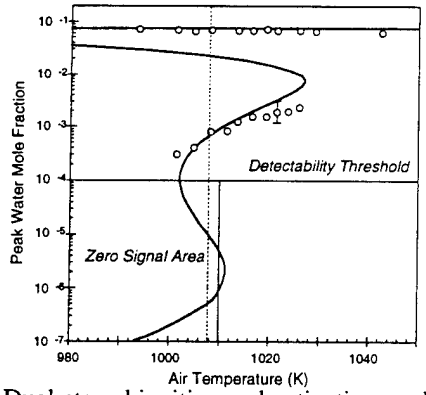

Fig. 1: Dual-staged ignition and extinction, and triple stable stationary states in the H_2-air system.

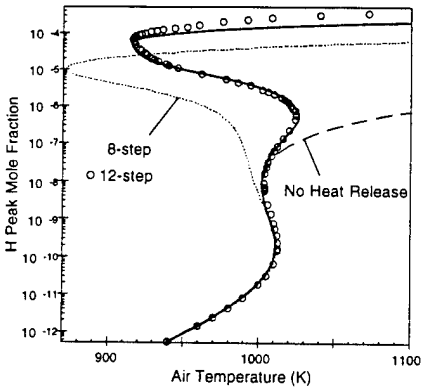

Fig. 2: System response curves with full and skeletal chemistry, with and without heat release.

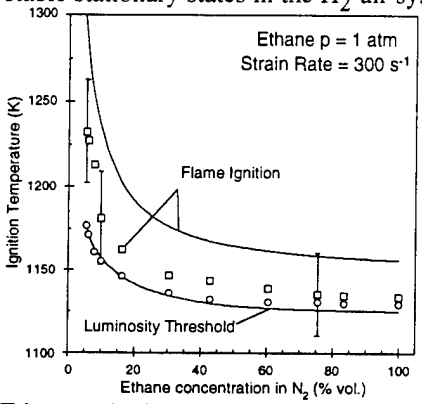

Fig. 3: Ethane ignition temperature vs fuel concentration.

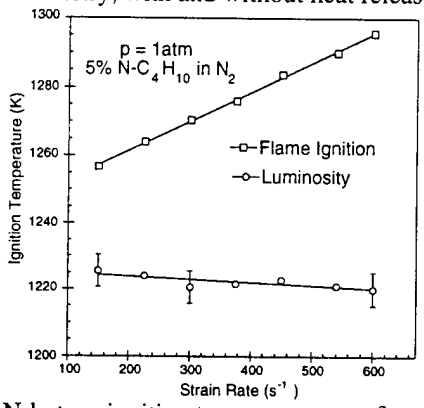

Fig. 4: N-butane ignition temperature as a function of the flow strain rate. Lines are data curve fits.

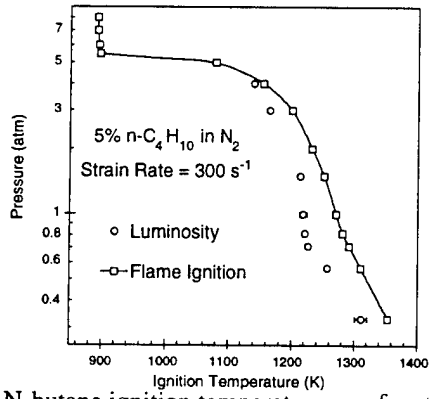

Fig. 5: N-butane ignition temperature as a function of system pressure. Solid line is a data curve fit.

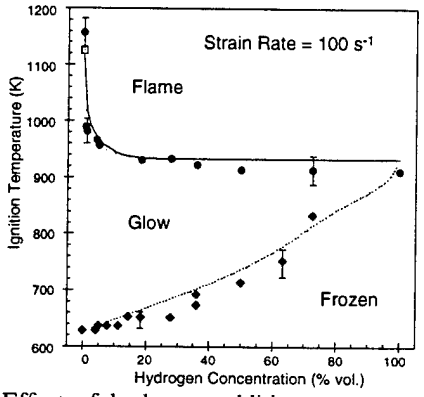

Fig. 6: Effect of hydrogen addition on nonpremixed ignition in the CO/H_2-air system.

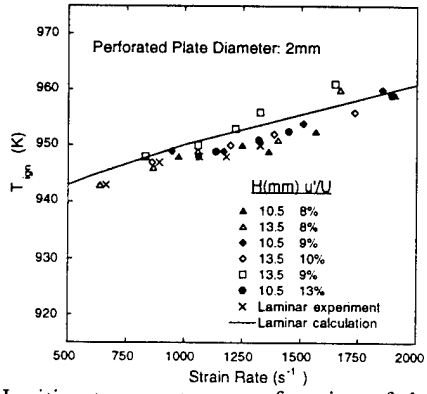

Fig. 7: Ignition temperature as a function of the flow strain rate and turbulence intensity (H_2-air).

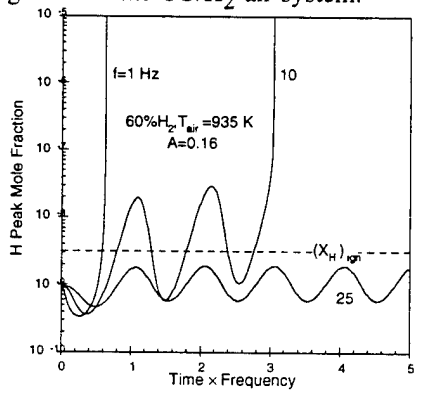

Fig. 8: Simulated effect of imposed flow oscillations on H_2-air ignition.

STUDIES ON HIGH PRESSURE AND UNSTEADY FLAME PHENOMENA

(AFOSR Grant No. F49620-95-1-0092)

Principal Investigator: Chung K. Law

Department of Mechanical and Aerospace Engineering
Princeton University, Princeton, NJ 08544

SUMMARY/OVERVIEW

The objective of the present program is to study the structure and response of steady and unsteady laminar premixed and nonpremixed flames in reduced and elevated pressure environments through (a) non-intrusive experimentation, (b) computational simulation using detailed flame and kinetic codes, and (c) multiple-expansion asymptotic analysis with large activation energy. During the reporting period progress has been made in the following projects: (1) An experimental and computational study of the response of counterflow premixed and diffusion flames to strain rate variations at reduced and elevated pressures. (2) An analytical, computational, and experimental study of the structure and propagation of premixed flame in nozzle-generated counterflow. (3) A computational study on the effects of pulsating instability on the fundamental flammability limit of rich hydrogen/air flames.

TECHNICAL DISCUSSIONS

1. Response of High-Pressure Counterflow Premixed and Diffusion Flames

Our previous studies on the response of the flame structure subjected to strain rate (κ) variations at atmospheric pressure showed that it is remarkably insensitive. Since many practical combustion processes take place under elevated pressures, it is compelling that the investigation be extended to include the effects of pressure on the flame response. Conceptually, since the burning rate and thereby thicknesses of laminar flames have been shown to vary quite substantially with pressure through chemical kinetic effects, and since these two quantities in turn yield the flame time and thereby the intensity of flame stretch, the chemical and transport processes are intrinsically coupled. As such, it is necessary to assess the extent of structural sensitivity for a range of system pressures, especially for non-equidiffusive flames whose responses are expected to be more sensitive, and for diffusion flames whose scaling with the strain rate may depend on pressure.

The computed and experimental results of lean propane/air premixed flames, with ϕ=0.7 and p=5 atmosphere are plotted in Fig. 1(a). The good agreement between the computed and experimental results suggests the adequacy of the C_3 scheme used herein for the description of the thermal structure.

Based on the computational results, for κ = 113 to 293 s^{-1}, the maximum temperatures of the strained flames are 25 to 35 K smaller than those of the unstrained flame. This is expected because the effective Lewis number is greater than unity. A prominent observation of Fig. 1(b) is the nearly invariant thermal structure of the strained flames. This is to be contrasted with the previous results at atmospheric pressure, which showed a more substantial decrease in the maximum flame temperature with increasing strain rate as compared to the near-equidiffusive flames. This reduced sensitivity at elevated pressures is due to the reduced flame thickness and hence the influence of stretch.

For diffusion flames, experiments were conducted at four pressures, 0.6, 1, 3, and 5 atmospheres, with the mass flow rates for both the fuel and oxidizer sides being fixed. Accordingly, the flames studied are characterized by constant density-weighted strain rates,

$\rho_u\kappa \approx 380$ kg/(sec–m^3), where ρ_u is the density of the oxidizer freestream. The experimental and computed results are shown in Fig. 2. It is seen that, regardless of the change of pressure, and hence κ, by a factor of 8.3, the temperature profiles collate with each other fairly well by using the density-weighted strain rate, except for the peak values whose differences reflect different extent of reactant leakage. Thus it is the density-weighted strain rate, instead of the strain rate alone, that is the relevant parameter representing the intensity of stretch for situations in which the freestream density changes in the investigation.

Regarding the comparison between the experimental and computed results, we found good agreements for p = 1, 3 and 5 atmospheres. Figure 2(b) shows the comparison for p = 5 atmosphere. A significant discrepancy, however, occurs at 0.6 atmosphere in that while the flame can be experimentally sustained at $\rho_u\kappa \approx 380$ kg/(sec–m^3), numerical calculation predicts flame extinction at $\rho_u\kappa = 170$ kg/(sec–m^3). This result is consistent with the underprediction of laminar flame speeds by the GRI mechanism at reduced pressures. Similar results were also found by using a different chemical mechanism. Thus there appears to be a severe inadequacy in the prediction of extinction limits. Further study on this issue is merited.

This work is reported in Publication No. 1.

2. Propagation of Nozzle-Generated Counterflow Premixed Flame

The accuracy of the counterflow, twin-flame technique for the determination of laminar flame speeds was examined analytically, numerically and experimentally. The analysis was conducted by using multiple-expansion, large activation energy asymptotics while the numerical simulation incorporated detailed chemistry and transport. In both approaches the solutions were obtained in a finite domain and with plug flow boundary conditions in order to better simulate the actual experiments. Results show that linear extrapolation of the minimum velocity to zero stretch over-estimates the true laminar flame speed. This over-estimate, however, can be reduced by using larger nozzle separation distances. The theoretical results were further confirmed by experimental measurements for methane/air flames with various stoichiometries and nozzle separation distances. The numerical and experimental results indicate that for atmospheric methane/air flames, nozzle separation distances in excess of about 2 cm yield laminar flame speeds, obtained by linear extrapolation, accurate to within the uncertainty range of the experiment. The results obtained herein thus provide further support for the viability of the counterflow technique, when the influence of the nozzle separation distance is properly accounted for. This work is reported in Publication No. 2.

3. Unsteady Ignition of Counterflowing Nonpremixed Hydrogen Against Heated Air

Flows within practical combustors are highly transient and turbulent, and therefore involve additional time scales which must be considered. In the present investigation we have therefore extended our previous *steady-state* ignition studies to the ignition of a laminar counterflowing fuel/air system when it is subjected to periodic flow straining, which not only provides a well-defined characteristic transient time scale, but it also simulates the fluctuating influence of turbulent eddies. In addition, the unsteadiness of the flow field has been found to significantly modify the behavior of laminar flames from their steady-state responses. To assess such an effect on ignition, it is appropriate to analyze how laminar ignition is modified by unsteadiness arising from a monochromatic oscillating flow field.

To assess the influence of the amplitude of oscillation, A, we first note that, for a given frequency or response time, quasi-steady ignition is expected to be promoted for larger A. It is seen from Fig. 3 that as A is increased from 0.10 to 0.20, the system behavior (e.g. the peak mole fraction of the hydrogen radical, X_H^*) changes from permanent oscillation, to ignition after increasingly smaller number of cycles, to ignition within one cycle. Transient ignition is possible only for A exceeding a value between 0.15 and 0.16, which implies that the minimum cycle strain rate is now much smaller than the steady-state ignition value. In addition, the system is now able to continuously oscillate without ignition, sustained at this state beyond the steady-state ignition condition, with the transient strain rate being smaller than κ_{ign} and the transient X_H^* much larger than $(X_H)_{ign}$.

Furthermore, it is found that there exists a critical frequency beyond which transient ignition is not possible by increasing the amplitude of oscillation alone. This cut-off frequency governing transient ignition is slightly larger than that determining the system responsivity.

Results for the oscillation frequency higher than the cut-off frequency demonstrate that unlike the ignitable situations, the mean peak mole fraction of the hydrogen radical as well as the overall system reactivity decrease with increasing amplitude of oscillation such that the system is not ignitable. To demonstrate the progressively weakened reactivity with increasing amplitude for high frequency oscillations, Fig. 4 plots the temporal variation of X_H^* for various amplitudes at f=100 Hz. It is seen that the peak and mean values of X_H^* decrease with increasing amplitude, which exhibits disparate behavior from those of "low" frequency oscillations (e.g. Fig. 3).

This work is reported in Publication No. 3.

4. Pulsating Instability in the Fundamental Flammability Limit of Rich Hydrogen/Air Flames

The fundamental flammability limit is traditionally defined by the failure of a one-dimensional planar flame to propagate *steadily* through a doubly-infinite domain with radiative heat loss. However, for near rich limit hydrogen/air flames, in which the Lewis number is greater than unity, pulsating instability has been observed to take place at fuel concentrations slightly below that of the rich limit. This study numerically investigates the unsteady behavior of these flames using detailed chemistry and transport descriptions, both with and without radiative heat loss. Adiabatic flames with equivalence ratios up to 7.3 were found to propagate steadily. In mixtures with equivalence ratios (ϕ) between 7.4 and 7.7, the flame propagates in an oscillatory manner, with period doubling at higher values of ϕ. Beyond this range, the flame exhibits long periods of substantially diminished reactivity, being separated by short intervals of high reactivity (see Fig. 5). When radiative heat loss was considered, the limit for the onset of oscillatory propagation did not appear to be affected. However, the flame was found to extinguish at $\phi = 7.8$ (see Fig. 6). Heat loss also increases the intensity of oscillation, while leaving the frequency unchanged. Steady solutions for the radiative flame produced a turning point at $\phi = 10.22$, which is well beyond this oscillatory extinction limit. Thus, the flammability range of a mixture is narrowed when the intrinsic oscillatory nature of its flame propagation mode is properly taken into account.

A unified explanation concerning the nature of this pulsating instability was proposed. Both a large Lewis number and a large overall activation energy through the competition of the chain-branching and chain-terminating reactions were found to be necessary conditions for oscillations to develop. A preliminary version of this work was presented at the 1997 Spring Technical Meeting of the Western States Section of the Combustion Institute.

MAJOR PUBLICATIONS (April, 1996 – March, 1997)

1. "Response of counterflow premixed and diffusion flames to strain rate variations at reduced and elevated pressures," by C. J. Sun, C. J. Sung, D. L. Zhu, and C. K. Law, *Twenty-Sixth Symposium (International) on Combustion* , pp. 1111-1120 (1996).
2. "Structure and propagation of premixed flame in nozzle-generated counterflow," by B. H. Chao, F. N. Egolfopoulos and C. K. Law, *Combustion and Flame*, in press.
3. "Ignition of oscillating counterflowing nonpremixed hydrogen against heated air," by C. J. Sung and C. K. Law, submitted.
4. "Further studies on effects of thermophoresis on seeding particles in measurements of strained flames," by C. J. Sung, J. S. Kistler, M. Nishioka and C. K. Law, *Combustion and Flame*, Vol. 105, pp. 189-201 (1996).
5. "Response of counterflow premixed flames to oscillating strain rates," by H. G. Im, J. K. Bechtold and C. K. Law, *Combustion and Flame,* Vol. 105, pp. 358-372 (1996).
6. "Extinction of counterflow diffusion flames under velocity oscillations," by J. S. Kistler, C. J. Sung, T. G. Kreutz, C. K. Law and M. Nishioka, *Twenty-Sixth Symposium (International) on Combustion* , pp. 113-120 (1996).
7. "The role of chain mechanisms in some fundamental combustion phenomena," by C. K. Law, *Physical and Chemical Aspects of Combustion*, in press.
8. "On the aerodynamics of flame surfaces," by C. K. Law, C. J. Sung and C. J. Sun, Annual Review of Heat Transfer, Vol. VIII, in press.

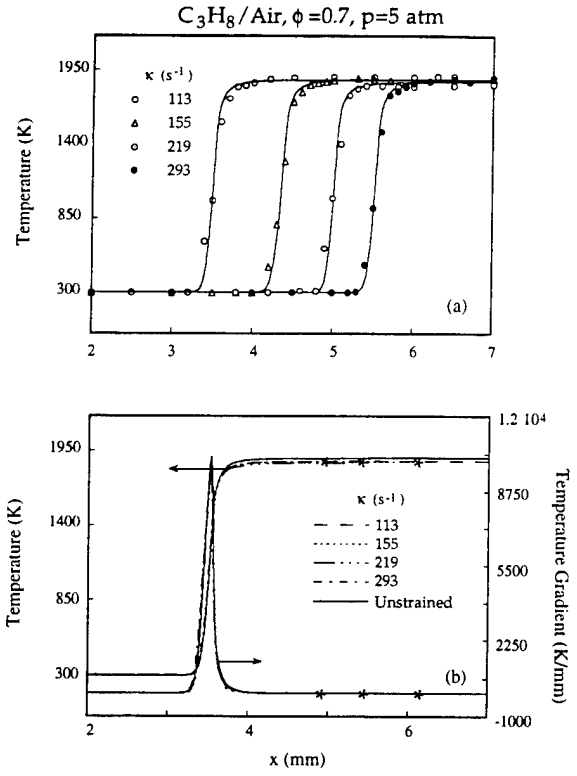

Figure 1

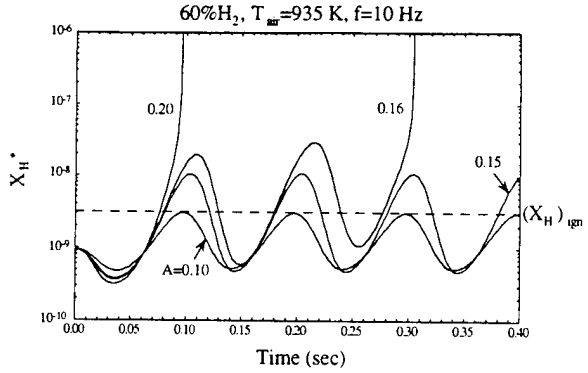

Figure 3

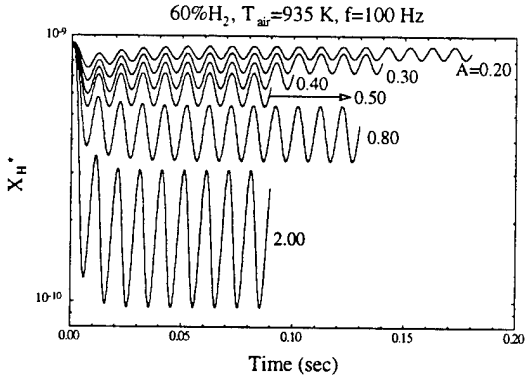

Figure 4

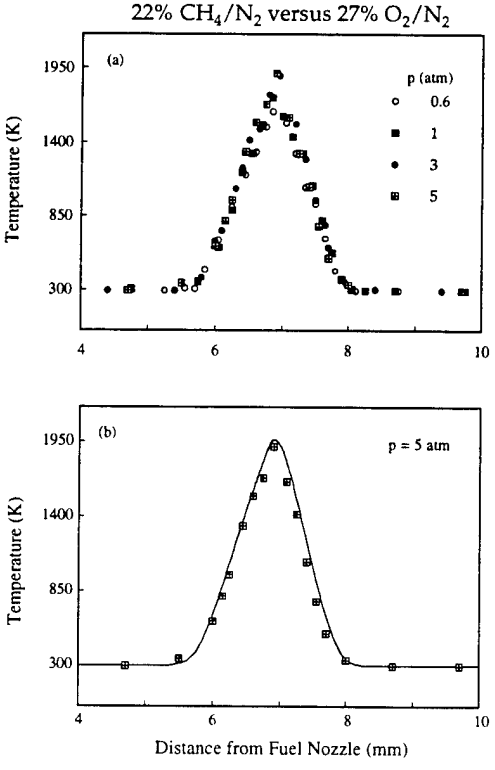

Figure 2

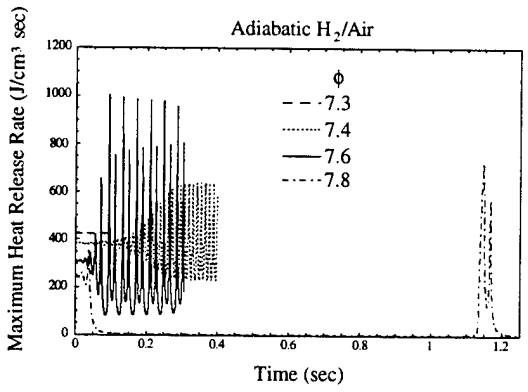

Figure 5

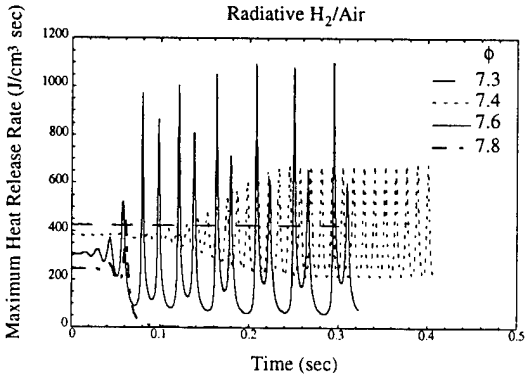

Figure 6

FLAMELET SURFACE DENSITY AND BURNING RATE INTEGRAL IN PREMIXED FLAMES

ARO Grant # DAAH04-95-1-0109

Principal Investigator: F. C. Gouldin

School of Mechanical and Aerospace Engineering
Cornell University
Ithaca, NY 14853

SUMMARY / OVERVIEW

Our research objective is the development of expressions for mean chemical reaction rates in practical combustion systems. We are studying premixed flames for conditions under which chemical reaction is confined to thin sheets and reaction rates are proportional to the area of these sheets. In turn, the area of these sheets is being determined by measuring the distribution of surface orientation using a new crossed-plane laser tomography technique developed at Cornell and an average value of the area via conditional flow velocity measurements leading to the determination of the burning rate integral which, in turn, is proportional to the average area. Ours are the first fully three dimensional flamelet orientation measurements and provide unique data for this important quantity. Relevant evidence indicates that available turbulent burning velocity data significantly exaggerate the effects of turbulence on combustion rates.

TECHNICAL DISCUSSION

Introduction.

Premixed turbulent combustion occurs in many practical devices, and for an important range of conditions chemical reaction is confined to thin sheets or interfaces separating reactants from products - the flamelet regime. In this regime the mean flamelet surface density or surface to volume ratio, $\bar{\Sigma}$, is proportional to the mean chemical reaction rate. A widely used expression for the mean rate of production formation is $\langle w \rangle = \rho_r u_L I_0 \bar{\Sigma}$, where ρ_r is the reactant gas density, u_L is the laminar burning velocity of the mixture, and I_0 is a correction term to account for the effects of flamelet curvature, stretch and transients on the mean flamelet reaction rate per unit surface area.

In previous Cornell work, it has been shown that $\bar{\Sigma} = \langle 1 / | \underline{N} \cdot \underline{n}_y | \rangle n_y$ [1] and, to reasonable approximation, that $n_y = N_c \langle c \rangle (1 - \langle c \rangle)/l$ [2]. In the first expression $\underline{N}$ is the flamelet surface normal; $\underline{n}_y$ is a unit vector with arbitrary orientation; and n_y is the mean flamelet crossing density on a line parallel to $\underline{n}_y$. In the second expression $\underline{n}_y$ is no longer arbitrary but is locally normal to mean progress variable, $\langle c \rangle$, constant surfaces; y is a coordinate parallel to $\underline{n}_y$; N_c is the mean number of flamelet crossings on y across the turbulent flame; and finally, l is a measure of the flame brush thickness. A major goal of the current research is to measure $\underline{N}$ and N_c for V- and Bunsen flames.

B_T, the burning rate integral defined as the integral of $\langle w \rangle$ along y across the turbulent flame brush, has been suggested as a well-defined and more appropriate measure of mean combustion rate or intensity than the ill-defined turbulent burning velocity [2, 3]. A specific definition for B_T has been proposed for flames of general geometry [3];

$$B_T = \int_{-\infty}^{\infty} \langle w \rangle h_x h_y h_z \, dy \; / \; h_x^* h_z^* ,$$

where h_x, h_y and h_z are the scale factors of an appropriately defined orthogonal curvilinear coordinate system and * denotes values on a <c> constant plane where the mean mass flux per unit area equals B_T. A second objective of our research program is to measure B_T for a variety of conditions using methods based on integral and control volume analyses.

Crossed-Plane Imaging Tomography

While there are several reports in the literature of flamelet normal measurements, in no case is the full three-dimensional quantity measured directly; instead it is inferred from partial data. Here we report a new, fully three-dimensional method for measuring $\underline{N}$ based on laser tomography in which a laser beam is split to form two perpendicularly aligned sheets of illumination and pairs of images of light scattering from an oil mist marking reactants are obtained by photography. From each image, the line separating reactants from products is determined and is a line on the flamelet surface. The two lines so defined from each pair of images intersect each other in physical space at least once along the line of intersection of the two planes illuminated by the laser sheets. At these points of intersection, vectors in the illumination planes and tangent to the two interface lines are also tangent to the flamelet surface, and hence, their cross product is aligned with the flamelet normal at the point(s) of intersection (see Fig. 1).

As a first step in applying this method to turbulent flames, we have performed measurements on a laminar V-flame perturbed by the vortex street of a cylinder placed upstream in the reactant flow and aligned parallel to the flame stabilizing rod. Since the flame sheet perturbations are predominantly two-dimensional, the perturbed flame sheet normal can be measured easily by single plane tomography for comparison with $\underline{N}$ data obtained using the crossed-plane method. Fig. 1 shows a schematic of the V-flame burner and crossed-plane tomography configuration used in these measurements. Results for measured flamelet normal are shown in Fig. 2 as a scatter plot of the $\underline{N}(\theta, \phi)$ vector tips (above) and (below) as pdf's of the angles θ (the polar angle of $\underline{N}$ relative to an axis both perpendicular to the intersection of the two illumination planes and parallel to the vortex generator) and ϕ (the corresponding azimuthal angle of $\underline{N}$). If the flame surface perturbations are 2-dimensional and aligned with the vortex generator, then $P(\phi) = \delta(\phi - \pi/2)$, a delta function. The results shown in Fig. 2 are quite encouraging and indicate that the angles ϕ and θ can be measured with a $\pm 5°$ uncertainty or less.

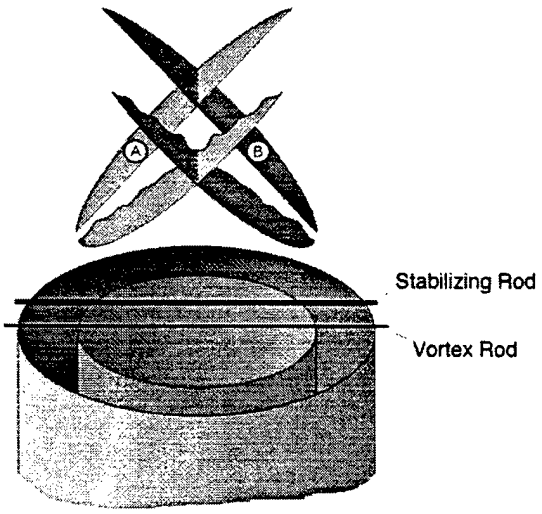

Fig. 1. Schematic of crossed-plane configuration and V-flame burner.

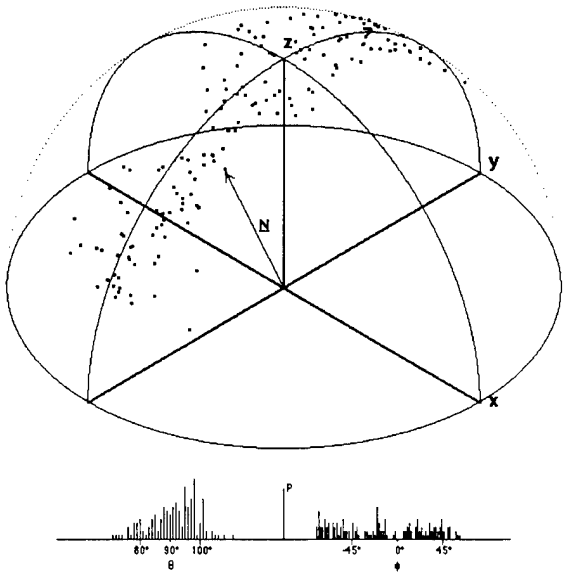

Fig. 2 $\underline{N}$ data from perturbed V-flame measurements.

It should be noted that this method can be extended to measure scalar gradients (and surface curvature) in flows using planar imaging (e.g., planar laser induced fluorescence) in the crossed-plane configuration. On pairs of planar images obtained from synchronized measurements, lines of constant scalar quantity, C, can be defined and where these lines intersect with the two illumination planes, the C constant surface normal can be obtained as described above. Furthermore, in each image plane the corresponding component of the scalar gradient ∇C_i can be determined. This component is related to the gradient, ∇C, by $|\nabla C_i| = |\underline{n}_i \bullet \nabla C|$, where $\underline{n}_i$ is the unit vector normal to the C constant line and in the ith image plane at a point of intersection of the two planes. Since there are two illumination planes, a redundant measurement is possible.

Determination of $< 1/ | \underline{N} \bullet \underline{n}_y | >$

In the expression for $\bar{\Sigma}$, n_y is the average number of flamelet crossings of a line y per unit length of that line. In turn, $< 1 /| \underline{N} \bullet \underline{n}_y | >$ is proportional to the mean flamelet area per such a crossing contained in a small differential right cylinder having its axis on y [1]. Hence, the average is a crossing weighted average. We show here that the weighting factor is simply $|\underline{N} \bullet \underline{n}_y|$, the magnitude of the cosine of the angle between $\underline{N}$ and $\underline{n}_y$.

This can be seen by considering an ensemble of surfaces and dividing each surface of the ensemble into small, planar differential segments of equal area and orientation $\underline{N}$. Let $P(\theta,\phi)d\Omega$ be the probability of finding an area segment with $\underline{N} = \underline{N}(\theta,\phi)$ and θ and ϕ in the differential solid angle $d\Omega$. Then focus on a small volume V, such that $P(\theta,\phi)$ and the distribution of segments are statistically uniform over V. For a line in V of length dy and orientation $\underline{n}_y$, the probability that an area segment is pierced by dy is proportional to the segment area projected normal to dy which, in turn, is proportional to $| \underline{N} \bullet \underline{n}_y |$. It follows then that, $| \underline{N} \bullet \underline{n}_y |$ is the weighting factor and that for $P(\theta,\phi)$ normalized,

$$< \frac{1}{| \underline{N} \bullet \underline{n}_y |} > = 1 \Big/ \int_0^{\pi} \int_0^{2\pi} | \underline{N} \bullet \underline{n}_y | \, P(\theta,\phi) \sin\phi \, d\phi \, d\theta.$$

Shepherd [4] has expressed concern with the relationship for $\bar{\Sigma}$ introduced above because of contributions from segments aligned perpendicular to y for which $| \underline{N} \bullet \underline{n}_y | = 0$. The weighting required to find $< 1 / | \underline{N} \bullet \underline{n}_y | >$ removes this problem and leads to a well defined average.

As a check of the preceding expression for $< 1 / | \underline{N} \bullet \underline{n}_y | >$, one may consider a corrugated surface with a square wave corrugation of unit amplitude and wavelength 2. The area of this surface in a rectangular volume of 2 units (1 unit height and depth and 2 units of width) is 4, and therefore the surface to volume ratio is 2. $P(\theta,\phi)$ for this surface reduces to three delta functions at $\theta = -\pi/2, 0, \pi/2$; ϕ is not a variable; and $d\Omega$ reduces to $d\theta$.

$$P(\theta) = (1/4)\,\delta(\theta + \pi/2) + (1/2)\,\delta(\theta) + (1/4)\,\delta(\theta - \pi/2).$$

Furthermore, $n_y = 1$. Evaluating the appropriate integral one finds that $< 1 / | \underline{N} \bullet \underline{n}_y | > = 2$, the correct value. While this result does not validate the expression in general, it does demonstrate that it works in a situation where a large portion of the surface is oriented such that $| \underline{N} \bullet \underline{n}_y | = 0$.

The Burning Rate Integral

As noted we define the burning rate integral to be a measure of the overall mean combustion rate in a volume segment of a turbulent flame that spans the flame brush. In previous work we have argued that the turbulent burning velocity is an ill-defined quantity and that values of this quantity reported in the literature are consequently misleading and in some cases overestimate mean combustion rates by considerable amounts [3]. On the other hand, the burning rate is

unambiguously defined and clearly is a measure of the mean combustion rate. An important practical problem with the use of B_T as the gauge of combustion intensity is the difficulty one encounters in measuring it.

So far we have investigated two approaches to measuring B_T that require extensive velocity measurements for each flame condition; the amount depending on the overall symmetry of the flame [2, 3]. Other than the amount of data required to evaluate B_T, a second problem has been made clear by our work. To find B_T we need to measure the mass flux and not the velocity. If flamelets are vanishingly thin, simply-conditioned velocity measurements which distinguish measurements in reactants and from those in products would be sufficient. The density field in this limit is bimodal with reactants having one density and products another. Unfortunately, in most experiments the flamelet is not vanishingly thin, and the proportion of velocity measurements made in the presence of a flamelet is not negligible in determining B_T. Therefore to measure mass flux, we are now setting up for simultaneous velocity and temperature measurements. The temperature measurement will be made with compensated fine-wire thermocouples using the compensation method we have been working on and verified in measurements on perturbed laminar flames [5, 6, 7].

Finally, note that the burning rate integral is related to an integral of $\bar{\Sigma}$ over the flame brush.

$$B_T = \int_{-\infty}^{\infty} \rho_r u_L \, I_o < \frac{1}{| \underline{N} \cdot \underline{n}_y |} > n_y \, h_x h_y h_z \, dy \, / \, h_x^* h_z^* = \rho_r u_L < I_o < 1 / | \underline{N} \cdot \underline{n}_y | >_B > N_c,$$

where B denotes an average over the flame brush and the scale factors have been suppressed for clarity. If flame stretch effects are not large this expression reduces to

$$B_T = \rho u_L << 1 / | \underline{N} \cdot \underline{n}_y | >>_B N_c$$

($I_o = 1$), and flamelet normal data along with N_c data (both are measurable with our new crossed-plane tomography method) can be used to estimate B_T or visa versa

Summary

Our research has as its goals the measurement of flamelet surface normal $\underline{N}$ and the burning rate integral B_T. A method for measuring $\underline{N}$ has been proposed and demonstrated in perturbed laminar V-flame measurements. It will now be used to make the first direct measurements of this quantity in turbulent premixed flames. An extension of the method to measuring scalar gradients has been proposed. B_T data for different flames is to be determined through velocity and temperature measurements and from flamelet surface normal measurements. B_T data are needed to provide a data base for mean combustion rates in premixed turbulent flame. Burning velocity data, previously used for this purpose, are discredited because of ambiguity in the definition of the burning velocity.

REFERENCES

1. Gouldin, F.C., *Analysis of Certain Closure Models for Premixed Turbulent Combustion*, in *Physical and Chemical Aspects of Combustion: A Tribute to Irvin Glassman*, R.F. Sawyer and F.L. Dryer, Editors. 1997, Gordon and Breach Science Publishers: Newark, NJ.
2. Gouldin, F.C. and P.C. Miles, Combustion and Flame, 1995. **100**: p. 202 - 210.
3. Gouldin, F.C., pp. 381 - 388 in the **26th Symposium (International) on Combustion**, Combustion Institute, 1996.
4 Shepherd, I., pp. 373 - 379 in the **26th Symposium (International) on Combustion**, Combustion Institute, 1996.
5. Miles, P.C. and F.C. Gouldin, Combust Science and Tech, 1993. **89**: p. 181 - 199.
6. Tacke, M.M. and F.C. Gouldin, *Evaluation of Compensated Thermocouple Measurements in Premixed Flames*, AIAA 95-0142, presented at the 33nd Aerospace Sciences Meeting, Reno Nevada, January 9-12, 1995.
7. Rog, D. and Gouldin, F. C. *One and Two Point Temperature Measurements with Compensated Thermocouples*, 1996 Fall Technical Meeting of the Eastern States Section of the Combustion Institute, Hilton Head, SC, December 9-11, 1996.

TURBULENCE–CHEMISTRY MODELS FOR HIGHLY TURBULENT FLAMES

AFOSR Contract F49620–94–C–0020

Iris Z. Hu and Sanjay M. Correa
General Electric Corporate Research and Development Center
Schenectady, New York, 12301

SUMMARY: OBJECTIVES AND PRIOR RESULTS

The practical objective of turbulent combustion modeling is to increase engineering productivity and hence the rate of technological innovation, by contributing to design codes for the prediction of flame stability, flow/temperature fields and emissions from air–breathing combustors. The specific objective of this research program is to develop and assess models for turbulence–chemistry interactions in highly turbulent flames.

Prior results include:
(i) PDF/CFD An "elliptic" 2D axisymmetric CFD code was combined with the joint velocity–composition pdf model. A 2–variable partial equilibrium scheme was used for CO/H_2–air chemistry [1]. A 4–step 5–variable scheme was used for CH_4–air chemistry [2]. In each case, the calculations compared favorably with Raman data (mixture fraction, major species, and temperature). Hence this approach is being used in design codes. However, the work also indicated inadequacies in the physical and chemical sub–models.
(ii) PaSR To address some of the latter inadequacies in greater detail, the Partially Stirred Reactor (PaSR) model was developed. We have used the PaSR to study premixed CO/H_2 flames with full or partial equilibrium chemistry [3]; CH_4 flames with full and 25–step or 4–step reduced chemistry schemes [4]; alternate methods for computational "parallelization" of particle–tracking algorithms [4]; comparison of the Curl, modified Curl and IEM mixing models in the context of full chemistry [5]; the effect of the level of initial unmixedness on autoignition delay time (including comparison with premixed data in the baseline case of zero initial unmixedness) [6]; and to test a global three–variable chemistry scheme for kerosene [7].

PROGRESS MADE OVER THE PAST YEAR

Given the complexity of the phenomena and fuels of interest, full rather than reduced chemistry schemes will probably be required. In principle, the laminar flamelet model (LFM) is available [8]. In the context of intensely turbulent combustion, the LFM breaks down because the reaction zone is not thin and the fluctuation of mixture fraction in the reaction zone is not small [9]. Here, an alternative to the LFM is developed.

Model for Non–Premixed Flames Based on PSR Microstructure and Full Kinetic Schemes

In the proposed model, the turbulent mixing–scale structure of the flame is assumed to be in the "distributed reaction zone" regime. In the non–premixed case, it is assumed that fluctuations in the mixture fraction ξ and the scalar dissipation rate χ are statistically independent, i.e., their joint pdf $P(\chi,\xi)$ is separable, $P(\chi,\xi)=P_1(\chi)P_2(\xi)$. Following [10], the pdf of scalar dissipation $P_1(\chi)$ is taken to be log normal with a mean related to the local turbulence kinetic energy k, the local dissipation rate ε, and the local mean scalar variance, $\overline{g}$, viz., $\overline{\chi}=C_{g2}\,(\varepsilon/k)\,\overline{g}$, where C_{g2} is a constant in the k–ε–g model.

The residence time "τ" in the mixing scales is related to the dissipation by $\tau = C\,\overline{g}/\chi$, where C is a constant in the model. The pdf of the residence time in the mixing scales is therefore $P(\tau)= \chi^2 P_1(\chi)/(C\overline{g})$. Note that this differs from Magnussen et al. [11], who ascribed a single residence time $(\nu/\varepsilon)^{1/2}$ to the mixing scales.

Calculations were compared with Raman data from two turbulent non–premixed flames:
(i) a non–premixed bluff–body stabilized $CO/H_2/N_2$–air flame, and
(ii) a non–premixed bluff–body stabilized CH_4/H_2–air flame.

Details of these comparisons were discussed in the 1996 Abstract and are available in Ref. 12.

Model for Premixed Flames Based on PSR Microstructure and Full Kinetic Schemes

In the case of premixed flames, there is no need to carry the mixture fraction as a variable and the thermochemical properties become a function of residence time alone. The pdf $P(\tau)$ is needed throughout the flow field. Since the mixture fraction is uniform in a premixed flame, calculation of $P(\tau)$ cannot depend on the scalar variance $\overline{g}$ as in the non–premixed case. Instead, an analogous approach is developed in which the local k and ε are used to form the residence time $\tau = C\, k/\varepsilon$, where C is a coefficient which can be adjusted, and ε is the instantaneous turbulence dissipation rate instead of the mean quantity. Similarly to the non–premixed case, the pdf of τ can be obtained from the pdf of ε by assuming a log–normal distribution for the latter [12].

Hence, in this approach, the calculation of a turbulent premixed flame involves solving the continuity equation, the momentum equations, the two equations for k and ε and a one–dimensional convolution of $P(\tau)$ over a range of τ to obtain the mean thermochemical properties.

Ref. 13 describes the premixed CH_4–air flame, which is depicted in Fig. 1. Premixed CH_4 and air at an equivalence ratio of 0.586 (corresponding to an equilibrium flame temperature of 1641K) flow over an axisymmetric conical flame holder oriented with its vertex pointing upwind. The base diameter of the cone is 44.45 mm, the tunnel is 80 cm x 80 cm, and the average premixture velocity upstream of the flame–holder is 14.46 m/s.

Calculations are compared with Raman data at two axial locations x/d=0.1 and x/d=0.6, where d is the base diameter of the cone. The calculated mean temperature profiles agree extremely well with the Raman data at both locations (Fig. 2), although the fairly featureless uniformity of the mean temperature is not a severe test of the model. The excellent agreement on mean CO at x/d=0.1 (Fig. 3) in terms of both the magnitude and shape of the profile is a much more severe test, because of the competing production–destruction paths involved in the determination of CO in methane flames. The model captures the pronounced non–equilibrium effects in the high shear region. The agreement on CO at x/d=0.6 is as good in the outer (shear layer) part of the flame, but the model significantly overpredicts the CO along the centerline: the model calculates a greater departure from equilibrium than is apparent from the data. Lastly, comparisons of the calculated mean NO with Raman data at both x/d=0.1 and x/d=0.6 (Fig. 4) indicate agreement to within a factor of two or better.

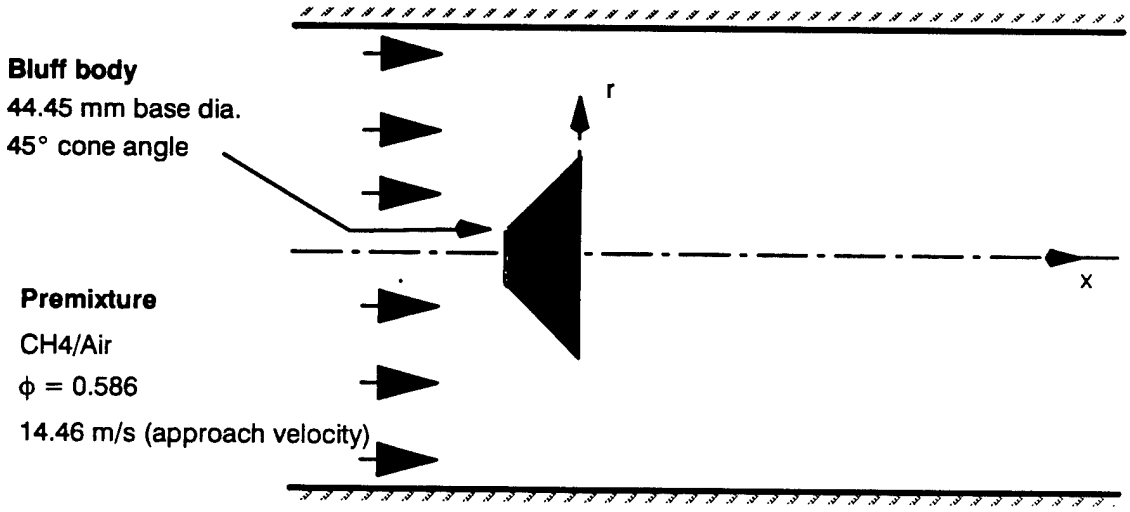

Figure 1. The premixed CH_4–air flame [Ref. 13].

Based on assessment in three quite different flames, the PSR–microstructure model appears to be adequate for calculating the mean fields, at least, of turbulent flames.

Kinetic Schemes for Complex Fuels

Since aeropropulsion gas–turbine engines burn fuels such as kerosene, (i) appropriate (full or reduced) kinetic schemes are needed and (ii) combustion models must be able to accommodate the schemes. Ref. 7 describes prior work on a simple three–variable reduced scheme, which has been applied in the context of the 3D CFD/particle–tracking PDF transport approach to a gas–turbine combustor [14]. The same model has also been used with the four–variable scheme of Ref. 15. These reduced schemes, to date, have not produced acceptable results on temperature/velocity flowfields and CO *at low power* (where it is an issue). Work is in progress to determine whether the errors are caused by the fluid mechanical or the chemical parts of the model.

If reduced schemes prove to be inadequate, the PSR–microstructure model described above is capable of including full chemical kinetic schemes at the very modest computational cost of *a priori* PSR calculations for look–up tables in mixture fraction and residence time, followed by $k-\varepsilon-g$ flowfield calculations.

REFERENCES

1. Correa, S.M. and Pope, S.B., Twenty–Fourth Symposium (International) on Combustion, The Combustion Institute, Pittsburgh, PA, pp. 279–285, 1992.
2. Correa, S.M., Gulati, A., and Pope, S.B., Twenty–Fifth Symposium (International) on Combustion, The Combustion Institute, Pittsburgh, PA, pp. 1167–1173, 1994.
3. Correa, S.M., *Comb. and Flame,* 93, pp. 41–60, 1993.
4. Correa, S.M. and Braaten, M.E., *Comb. and Flame,* 94, pp. 469–486, 1993.
5. Correa, S.M., *Comb. and Flame,* 103, pp. 194–206, 1995.
6. Correa, S.M. and Dean, A.J., Twenty–Fifth Symposium (International) on Combustion, The Combustion Institute, Pittsburgh, PA, pp. 1293–1299, 1994.
7. Correa, S.M., *J. Prop. Power,* Vol. 11, No. 3, pp. 448–455, May–June, 1995.
8. Peters, N., Twenty–First Symposium (International) on Combustion, The Combustion Institute, Pittsburgh, PA, pp. 1231–1250, 1988.
9. Bilger, R.W., Twenty–Second Symposium (International) on Combustion, The Combustion Institute, Pittsburgh, PA, pp. 475–488, 1988.
10. Liew, S.K., Bray, K.N.C., and Moss, J.B., *Comb. and Flame* 56, pp. 199–213, 1984.
11. Magnussen, B.F., Hjertager, B.H., Olsen, J.G., and Bhaduri, D., Seventeenth Symposium (International) on Combustion, The Combustion Institute, Pittsburgh, PA, pp. 1383–1393, 1979.
12. Hu, I.Z. and Correa, S.M., Twenty–Sixth Symposium (International) on Combustion, The Combustion Institute, Pittsburgh, PA, pp. 307–313, 1996.
13. Nandula, S.P., Pitz, R.W., Barlow, R.S., and Fiechtner, G.J.,"Rayleigh/Raman/LIF Measurements in a Turbulent Lean Premixed Combustor," Paper AIAA 96–0937, 34th AIAA Aerospace Sciences Meeting, Reno, NV, January 15–18, 1996.
14. Tolpadi, A.K., Hu, I.Z., Correa, S.M., and Burrus, D.L.,"Coupled Lagrangian Monte Carlo PDF–CFD Computation of Gas–Turbine Combustor Flow Fields with Finite–Rate Chemistry," 41st ASME Turbo Expo, Birmingham, UK, June 10–13, 1996.
15. Chen, J.–Y., and Kollmann, W., Twenty–Second Symposium (International) on Combustion, The Combustion Institute, Pittsburgh, PA, pp. 645–653, 1988.

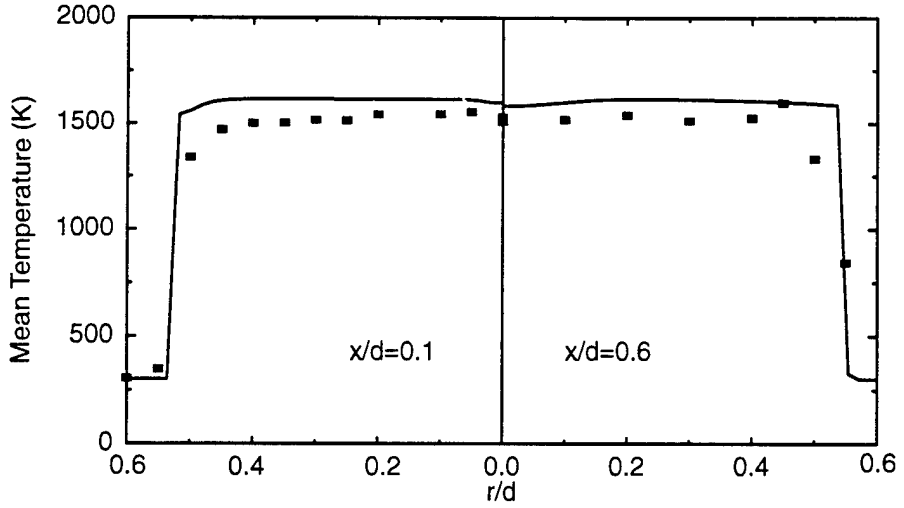

Figure 2. Comparison of calculated temperature with Raman data in premixed CH_4–air flame.

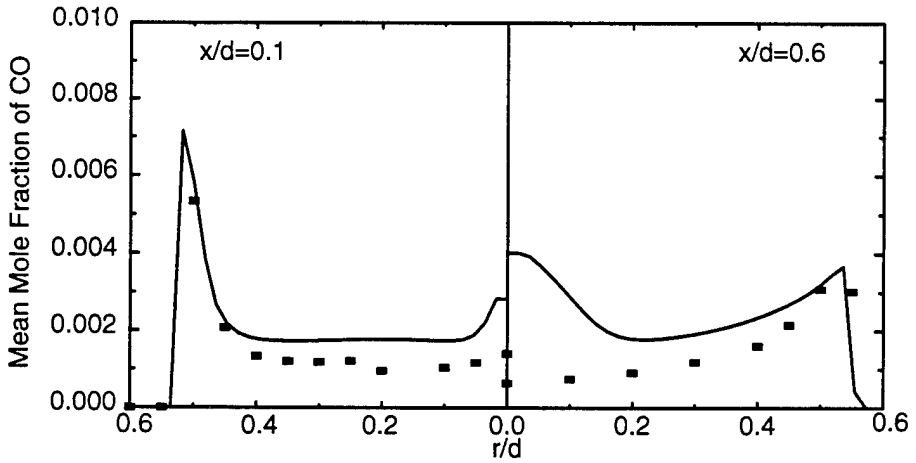

Figure 3. Comparison of calculated CO with Raman data in premixed CH_4–air flame.

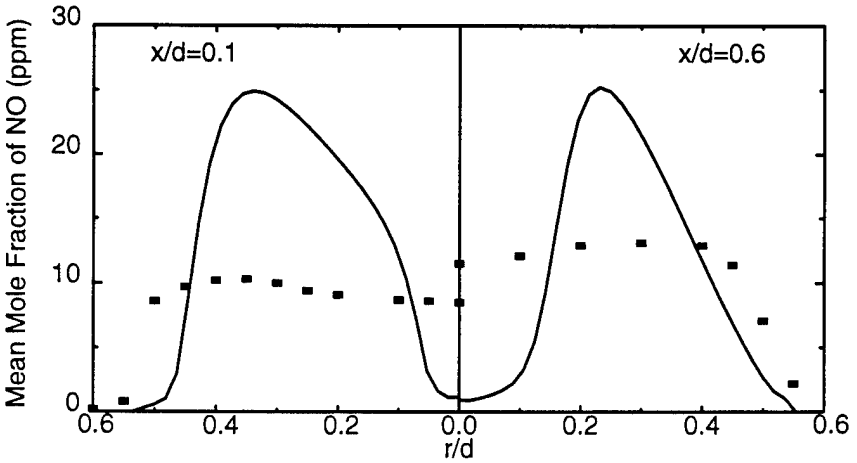

Figure 4. Comparison of calculated NO with Raman data in premixed CH_4–air flame.

TWO- AND THREE-DIMENSIONAL MEASUREMENTS IN FLAMES

AFOSR Grant No. 94-1-0135
Principal Investigator: Marshall B. Long

Yale University
Department of Mechanical Engineering and Center for Laser Diagnostics
New Haven, Connecticut 06520-8284

SUMMARY/OVERVIEW

Laser-based imaging techniques are being developed and applied to the study of turbulent reacting flows. These techniques incorporate a variety of light scattering mechanisms to allow the measurement of the spatial distributions of quantities such as temperature, species concentration, velocity, and mixture fraction. The data provided by these measurements can afford a better understanding of the interaction of turbulence and chemistry in turbulent flames and thus aid in the modeling of this interaction. During the past year, our work on simultaneous scalar and velocity imaging in turbulent premixed flames has been published[1] and we have continued to analyze and present the results from our mixture fraction imaging experiments in nonpremixed flames.

TECHNICAL DISCUSSION

The mixture fraction (ξ) and its gradient are important parameters in the modeling of turbulent nonpremixed flames, and the experimental determination of mixture fraction over a wide field is essential for testing these models. We have been collaborating with Dr. Sten Stårner and Prof. Robert Bilger at the University of Sydney to develop and apply a two-scalar approach to mixture fraction imaging. The method assumes unity Lewis number, equal diffusivities, and a simplified one-step reaction between fuel and oxidizer. It has been shown previously that the measurement of fuel concentration and Rayleigh scattering is sufficient to determine the mixture fraction.

In our recent mixture fraction imaging experiments, the fuel concentration has been obtained using Raman scattering from the fuel. The use of Raman scattering to determine the fuel concentration allows the use of chemically simple fuels such as methane and hydrogen, which are reasonably consistent with the one-step chemistry assumptions implicit in the technique. Earlier experiments using fluorescence from more complex hydrocarbons provided good signal/noise, but suffered inaccuracies in the derived mixture fraction due to loss of parent fuel.

Experiments were performed in a variety of nonpremixed flame configurations, including a lifted methane diffusion flame. This work (described in last year's annual report) has since been published.[2] Data sets were also obtained for piloted methane/air flames and an unpiloted hydrogen flame. In the methane/air flames, the methane was diluted with air (70% by volume) to eliminate soot, and resulted in a stoichiometric mixture fraction of $\xi = 0.29$. The premixed annular pilot flame was a stoichiometric mixture of acetylene, hydrogen, and air, which insured a steadily burning main flame without significant local extinction. The fuel jet issued from a nozzle of diameter 6.1 mm into a filtered, vertical, coflowing 7.0 m/s air stream. For the hydrogen flame, the same flow arrangement was used, but without the pilot. Data were taken at Reynolds numbers of 10,100; 14,300; 21,300; and 31,000 for the methane/air flames and at a Reynolds number of 13,500 for the hydrogen flame.

The experiments were performed using a novel intra-cavity technique, in which the laser sheet was formed within the laser cavity of a flashlamp-pumped dye laser.[3] This configuration resulted in a sheet energy of roughly five times that of a more conventional setup. The scattered Raman and Rayleigh light were detected with two intensified CCD cameras located on opposite sides of the laser sheet. The imaged region was selected so that each shot included the coflow air on one side. Since the conditions were known in this area, the Rayleigh image contained all the information needed to correct both images for variations in the laser sheet intensity-distribution, as well as shot-to-shot energy fluctuations. The images obtained were transferred to a computer for storage and processing. Once in the computer, the two images were scaled, rotated and cropped to allow comparison on a pixel-by-pixel basis. After this matching, each pixel corresponded to a volume of 0.06 x 0.06 x 0.56 mm^3, with the largest value being the sheet thickness.

In order to further increase the signal/noise ratio in the Raman data, some degree of smoothing is desirable. Because the Raman and Rayleigh images are highly correlated in the regions where the Raman signal is non-zero, the Rayleigh image can be used to optimize the smoothing of the Raman image. By performing smoothing of the Raman image along constant intensity contours derived from the Rayleigh image, we have shown that it is possible to increase the signal/noise by a factor of 10, while retaining the gradient information.[4]

A set of 100 image pairs was recorded for each Reynolds number of the flames noted above. Each image pair was processed to obtain the mixture fraction and temperature using an iterative data reduction scheme. Once the mixture fraction is obtained, two components of the scalar dissipation (χ) can be calculated. An example of the temperature, mixture fraction and scalar dissipation from the methane/air flame (Re = 21,300) is shown in Fig. 1.

In addition to providing insight into the spatial structure of the mixture fraction and scalar dissipation fields, this collection of images can be used to statistically characterize these quantities. The temperature, mixture fraction, and fuel mass fraction derived from the images were found to be in general agreement with single-point data from similar flames obtained by others. The aspect of the current work that is most unique is the ability to determine the scalar dissipation rate, which cannot be derived from single-point measurements and is of particular interest to modelers. Analysis of the data shows that the probability density of scalar dissipation in these flames differs from that in isothermal flows. This appears to be associated with the heat release associated with combustion, which reduces the local turbulence Reynolds number and increases the integral length scale around the stoichiometric contour (see Fig. 2). In modeling turbulent nonpremixed flames, considerable simplification results if the mixture fraction and scalar dissipation are assumed to be statistically independent. Our measurements indicate that this assumption is not fully justified. The complete results of this analysis have been submitted to *Combustion Science and Technology*.[5]

REFERENCES

1. J.H. Frank, K.M. Lyons, and M.B. Long, "Simultaneous Scalar/Velocity Field Measurements in Turbulent Gas-Phase Flows," *Combust. Flame* **107**, 1, (1996).
2. S.H. Stårner, R.W. Bilger, J.H. Frank, D.F. Marran, and M.B. Long, "Mixture Fraction Imaging in a Lifted Methane Jet Flame," *Combust. Flame* **107**, 307 (1996).
3. D.F. Marran, J.H. Frank, M.B. Long, S.H. Stårner, and R.W. Bilger, "An Intracavity Technique for Improved Raman/Rayleigh Imaging in Flames," *Opt. Lett.* **20**, 791 (1995).
4. S.H. Stårner, R.W. Bilger, and M.B. Long, "A Method for Contour-Aligned Smoothing of Joint 2D Scalar Images in Turbulent Flames," *Combust. Sci. Tech.* **107**, 195 (1995).
5. S.H. Stårner, R.W. Bilger, M.B. Long, J.H. Frank, and D.F. Marran, "Scalar Dissipation Measurements in Turbulent Jet Diffusion Flames of Air Diluted Methane and Hydrogen," submitted to *Combust. Sci. Tech.*

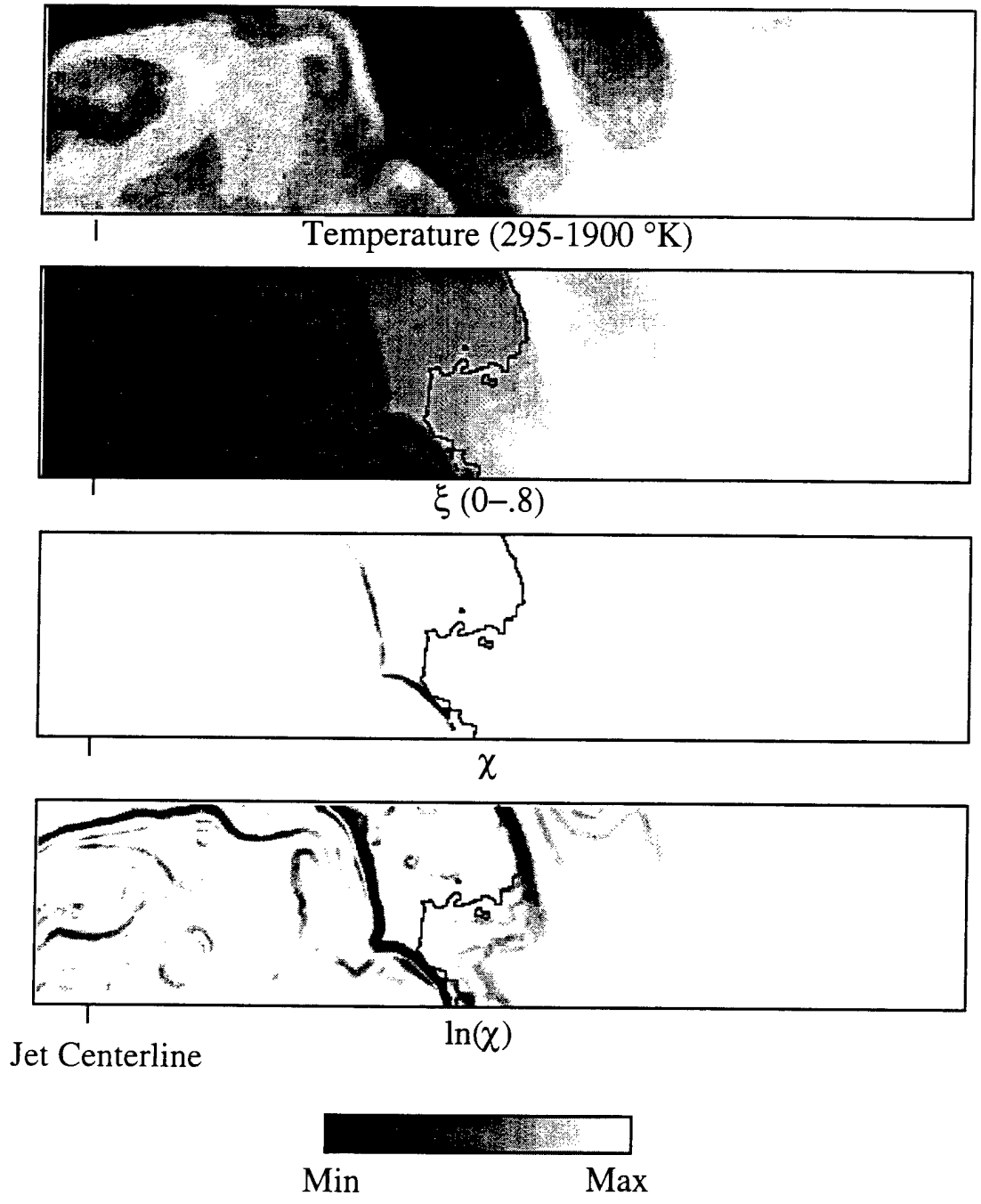

Figure 1. The temperature, mixture fraction (ξ), scalar dissipation (χ), and the log(χ) obtained in a turbulent nonpremixed methane/air flame (Re = 21,300). The image is centered 25 diameters downstream of a 6.1 mm nozzle. The imaged region corresponds to 6.5 mm in the axial direction by 30 mm in the radial direction. The stoichiometric contour at $\xi = 0.29$ is shown in black.

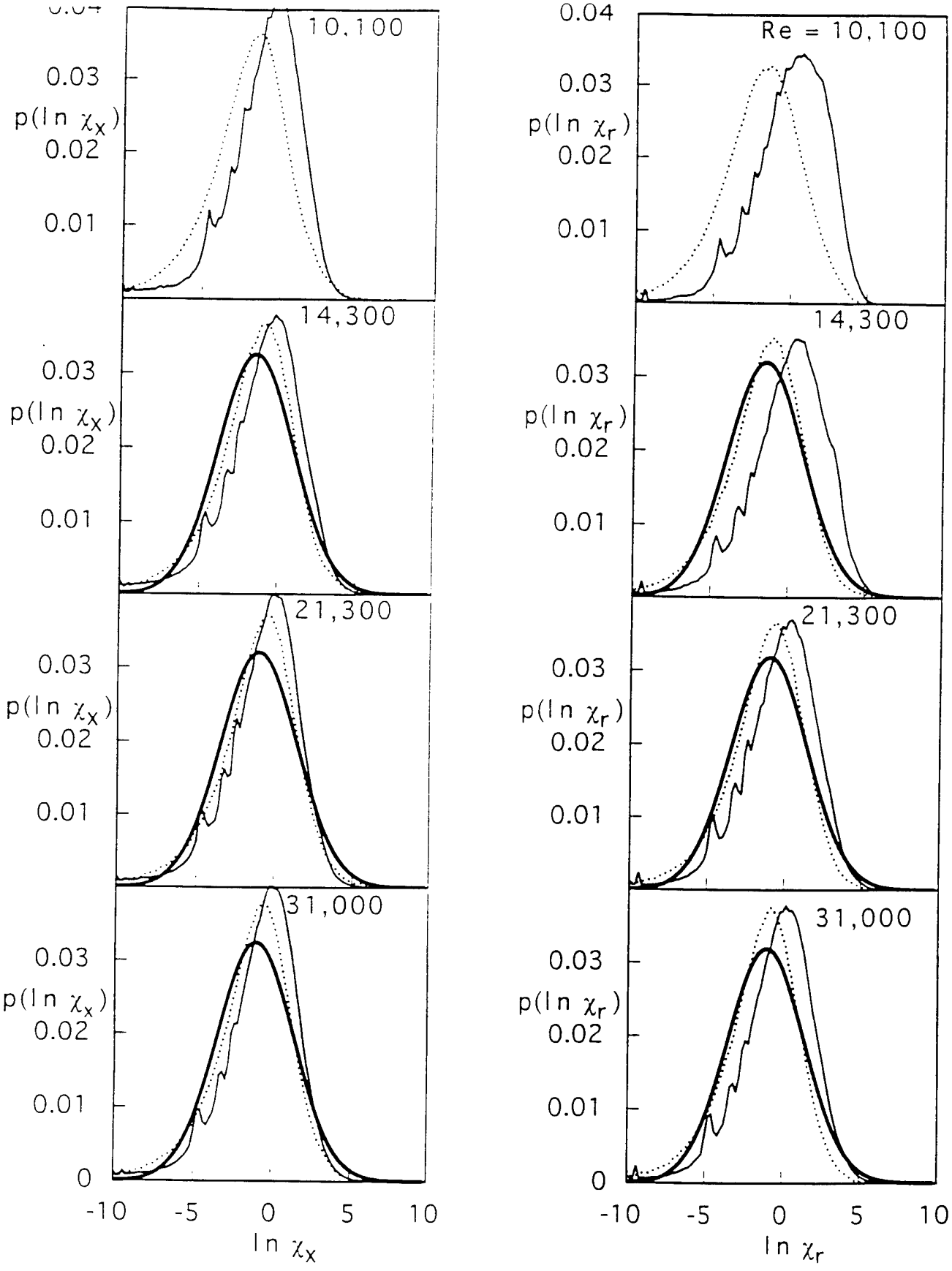

Figure 2. Probability density of axial (left) and radial (right) components of the scalar dissipation, χ, for four different Reynolds numbers from the methane/air flame. The solid line corresponds to values taken from the jet centerline, and the dotted line was from values taken in the shear layer. The dark solid line shows a log normal distribution with the same mean and rms as for the data on the centerline.

MODELLING MIXING AND REACTION IN TURBULENT COMBUSTION

AFOSR Grant F-49620-97-1-0126

Principal Investigator: S. B. Pope
Mechanical & Aerospace Engineering
Cornell University
Ithaca, NY 14853

SUMMARY

PDF methods are increasingly being used in universities and in industry to make calculations of flows involving turbulent combustion. In the last few years, there have been significant advances in the physical and chemical submodels, as well as in the numerical algorithm used to solve the modelled PDF equations. The objectives of the research are to make accurate calculations of turbulent flames for which there are reliable experimental data, and thereby to quantify the capabilities of the models.

RECENT ADVANCES

Some of the important recent advances in the PDF methodology are:

1. the *in situ* adaptive tabulation method (ISAT, Pope 1997) for the efficient implementation of combustion chemistry, which allows the incorporation of detailed chemistry in PDF calculations

2. the Euclidean minimum spanning tree (EMST) mixing model (Subramaniam & Pope, 1997), which overcomes serious deficiencies of other mixing models

3. the wavevector/velocity model (Van Slooten & Pope 1997), which provides a sounder physical basis for the modeling of complex flows: it is exact in the limit of rapid distortion of homogeneous turbulence

4. the extension to high-speed flows (Delarue & Pope 1996)

5. the extension to near-wall flows (Dreeben & Pope 1997)

6. the use of the PDF methodology for sub-grid scale modeling in large eddy simulations (Colucci et al., 1997).

PILOTED JET DIFFUSION FLAME

Work is currently in progress of making PDF calculations of piloted jet diffusion flames, for comparison with the experimental data (see Masri, et al., 1988). The model equation solved is for the joint PDF of velocity, turbulence frequency and composition, using the EMST mixing model. The chemistry in this methane-air flame is described by a skeletal mechanism involving 16 species and 41 reactions, and is implemented using the ISAT algorithm.

As preliminary results, Fig. 1 shows some calculated mean mass fractions compared to the experimental data. (These are Monte Carlo calculations of moderate accuracy, and the statistical fluctuations in the results may be observed.) The chemistry is described in some detail, and so much more information than means can be extracted. For example, Fig. 2 shows a scatter plot of O_2 versus CO.

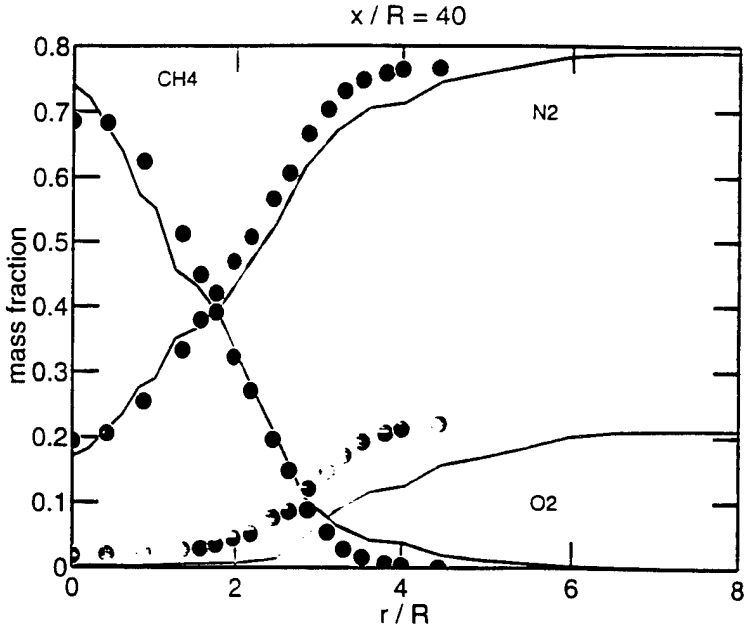

Fig. 1: Mean mass fractions in a piloted methane-air jet diffusion flame. Symbols, experimental data of Masri, et al. (1988). Lines PDF calculations of Saxena & Pope (1997).

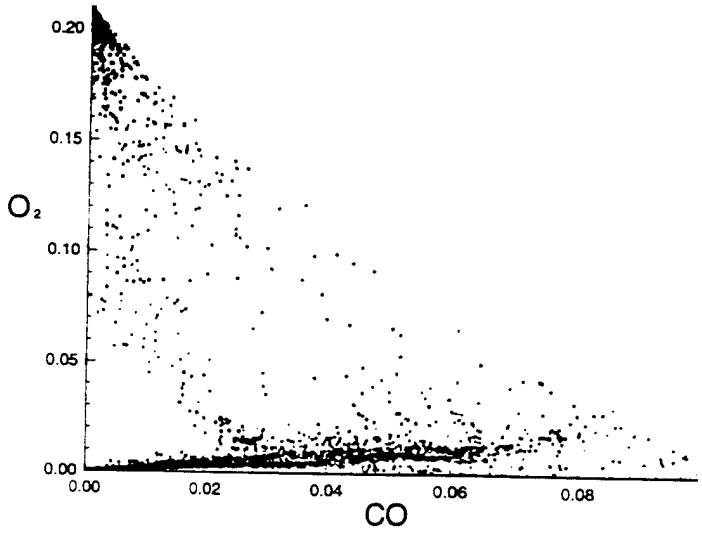

Fig. 2: Scatter plot of instantaneous mass fractions of O_2 and CO. From PDF calculations of piloted methane-air jet diffusion flames (Saxena & Pope, 1997).

EXTINCTION

The drive to make combustion chambers as compact as possible inevitably leads to operating conditions that can be close to extinction. A known deficiency of the popular IEM mixing model is that it incorrectly predicts extinction for non-premixed combustion at very high Damkohler numbers. The EMST mixing model is motivated by the need to overcome this deficiency.

To test the efficacy of different models, the test case of "periodic reaction zones" has been studied (Subramaniam & Pope, 1997). In this problem the parameters are the Damkohler number Da, and the reaction zone thickness parameter $F \equiv \xi_R/\xi'$ (where ξ_R is the reaction zone thickness in mixture fraction space, and ξ' is the r.m.s. mixture fraction). For given F, there is a minimum value of Da for stable combustion, below which extinction occurs. This value of the critical Damkohler number according to different models is shown in Fig. 3. The smallest value of F ($F \approx 0.3$) corresponds to the flamelet regime. It may be seen that the EMST model and the conditional moment closure (CMC) yield comparable predictions. But IEM incorrectly predicts a value of Da larger by a factor of a thousand.

These results, together with those of Masri, et al. (1996), confirm the advantages of the EMST model.

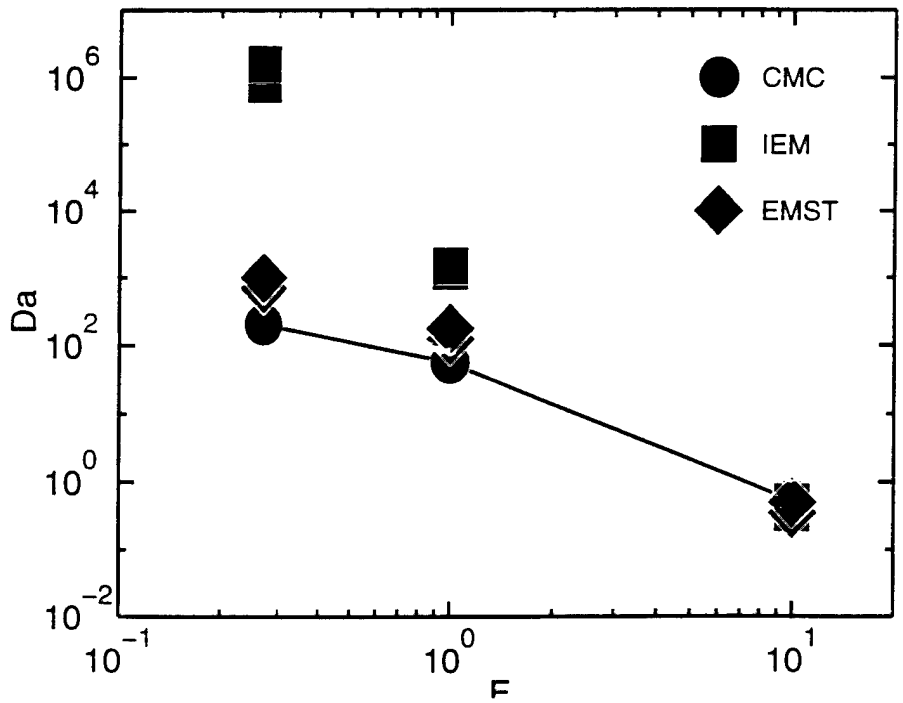

Fig. 3: Predictions of critical Damkohler number for extinction against reaction zone thickness parameter $F = \varepsilon_R/\varepsilon'$ for different models (from Subramaniam & Pope, 1997).

REFERENCES

P.J. Colucci, F.A. Jaberi, P. Givi and S.B. Pope (1997) "Filtered Density Function for Large Eddy Simulation of Turbulent Reacting Flows," Physics of Fluids, (submitted).

B.J. Delarue and S.B. Pope (1996) "Application of PDF methods to compressible turbulent flows," Physics of Fluids, (submitted).

T.D. Dreeben and S.B. Pope (1997) "Probability density function and Reynolds-stress modeling of near-wall turbulent flows," Physics of Fluids, **9**, 154–163.

T.D. Dreeben and S.B. Pope (1997) "Wall-function treatment in PDF methods for turbulent flows," Physics of Fluids, (to be published).

T.D. Dreeben and S.B. Pope (1997) "PDF/Monte Carlo simulation of near-wall turbulent flows," J. Fluid Mech., (to be published).

A.R. Masri, R.W. Dibble, and R.W. Bilger, (1988) "Turbulent Nonpremixed Flames of Methane Near Extinction: Mean Structure from Raman Measurements", Combust. Flame 71:245–266.

A.R. Masri, S. Subramaniam and S.B. Pope (1996) "A mixing model to improve PDF simulation of turbulent diffusion flames," Twenty-Sixth Symp. (Int'l) on Combust., pp. 49–57.

S.B. Pope (1997) "Computationally Efficient Implementation of Combustion Chemistry using In Situ Adaptive Tabulation," Combustion Theory and Modelling, **1**, 41–63.

S.B. Pope (1996) "Diffusion by continuous movements: implications for turbulent mixing and the scalar flux," Journal of Fluid Mechanics, (submitted).

V. Saxena and S.B. Pope (1997) "PDF calculations including detailed chemistry for piloted jet flames of methane" (in preparation).

S. Subramaniam and S.B. Pope (1997) "Comparison of PDF mixing models for nonpremixed turbulent reacting flow" Cornell University report FDA 97–03.

P.R. Van Slooten and S.B. Pope (1997) "PDF modeling of inhomogeneous turbulence with exact representation of rapid distortions," Physics of Fluids, **9**, 1085–1105.

EVALUATION OF CLOSURE MODELS OF TURBULENT DIFFUSION FLAMES

AFOSR Contract/Grant No. F49620-97-1-0092

Principal Investigators: G. Kosály and J. J. Riley

Department of Mechanical Engineering
University of Washington, Seattle, Washington 98195

SUMMARY/OVERVIEW

The large eddy simulation of turbulent reacting flows requires the use of sub-grid scale modeling. This abstract reports on a new sub-grid scale model based on the flamelet approximation. The model is tested against 256^3 direct numerical simulations. Practical flamelet modeling predicts that the dependence of the average mass fractions on molecular properties is exclusively related to viscosity dependence of turbulent mixing. Direct numerical simulation results are shown to illustrate this point.

TECHNICAL DISCUSSION

Large eddy simulation of turbulent combustion. The Large Eddy Laminar Flamelet Model (LELFM)

Let $\phi_i(\mathbf{x}, t)$ be physical quantities in a turbulent flow. The goal of the LES (Large Eddy Simulation) is to derive and solve equations for the resolved components of the physical quantities ($\overline{\phi_i}$) defined by a filtering operation that removes the contribution of the small scale dynamics. Due to filtering the equations have unclosed terms that require sub-grid scale modeling (SGS). Our approach to the SGS modeling of species mass fractions expands on an earlier effort by Cook and Riley (1994) who used the equilibrium chemistry approach for closure (Equilibrium Chemistry Limit, ECL). The present starting point is the flamelet approximation introduced by Peters (1983) and Kuznetsov (1982). In this approximation the mass fraction of the i-th specie satisfies the local equation

$$-N\frac{\partial^2 Y_i}{\partial Z^2} = \dot{w}_i. \tag{1}$$

Here Z is the mixture fraction variable and $N = \mathcal{D}\nabla Z \cdot \nabla Z$, the local scalar dissipation rate. The boundary conditions are standard. To evaluate the filtered mass fractions we take steps analogous to the ones taken to compute the ensemble averages. By solving Eq. (1), a flamelet library ($Y_i = Y_i(Z, N)$) can be obtained, whence the i-th filtered mass fraction is

$$\overline{Y_i} = \int_0^\infty \int_0^1 Y_i(Z, N)\overline{P}(Z, N)dNdZ. \tag{2}$$

The weight factor in Eq. (2) is the joint large eddy pdf of Z and N (Gao and O'Brien, 1993). Following an approximate step introduced by Kuznetsov (1982), Eq. (2) can be written as

$$\overline{Y_i} = \int_0^1 Y_i(Z, \overline{N|Z})\overline{P}(Z)dZ. \tag{3}$$

Here $\overline{N|Z}$ is the filtered average of the scalar dissipation rate conditioned on the mixture fraction. Using, e.g., an assumed beta-function for $\overline{P}(Z)$, the filtered mass fractions can be tabulated as functions of the

filtered average and sub-grid variance of the mixture fraction ($\overline{Z}$, Z_v) and the filtered average of the scalar dissipation rate ($\overline{N}$):

$$\overline{Y_i} = f_i(\overline{Z}, Z_v, \overline{N}). \tag{4}$$

In deriving Eq. (4) we have assumed that $\overline{N|Z}$ can be parameterized by $\overline{N}$. The evaluation of the filtered species mass fractions requires the modeling of $\overline{Z}$, Z_v and $\overline{N}$. Equation (4) is the LELFM (Large Eddy Laminar Flamelet Model) expression to be used to compute the filtered mass fractions. The expectation is that the LELFM result becomes more valid at higher Damköhler numbers. Recent comparisons to laboratory data provide encouraging results regarding the applicability of the flamelet model in hydrogen-air and syngas-air flames (Buriko *et al.*, 1994; Lentini, 1994; Sanders *et al.*, 1997). The approximation used to arrive at Eq. (3) from Eq. (2) has been investigated recently by deBruynKops *et al.* (1997a) and was found to improve with increasing Damköhler number values. In another investigation (Cook and Riley, 1997; deBruynKops, 1997b) used data sets from 256^3 point direct numerical simulations (DNS) of incompressible, isotropic, temporally-decaying, reacting turbulence to investigate the accuracy of the LELFM model. In these computations a single reaction step was considered with a relatively high pre-exponential Damköhler number and different activation energy values. In order to test the model, the DNS data fields were filtered onto a 16^3 point LES mesh. First, "exact" values for $\overline{Y_p}$ (product), $\overline{w_f}$ (fuel), $\overline{Z}$, Z_v, and $\overline{N}$ were computed by averaging over the 16^3 DNS grid points in each LES grid cell. The next step was to compute the filtered mass fractions and reaction rates from $\overline{Z}$, Z_v, $\overline{N}$ via Eq. (4) and a similar expression for the filtered reaction rates. The data were taken at one eddy turnover time after scalar initialization.

Figure 1 compares the "exact" filtered product mass fractions (as computed from the DNS) to the LELFM filtered mass fraction computed from Eq. (4) and to the ones computed using the equilibrium chemistry approximation (ECL, Cook and Riley, 1994). The LELFM results are superior compared to the ECL ones, especially for large values of the activation temperature.

Our next plan is to use the LELFM formalism to the prediction of experimental data. As a first step we intend to compare the LELFM predictions to the experimental data of Bilger *et al.* (1991) and Mungal *et al.* (1985).

Reynolds number similarity of the average mass fractions.

If we replace the filtered averages on the RHS of (4) by ensemble (time) averages, the resulting equation will provide the ensemble (time) averaged species mass fraction. This equation says that, in the flamelet approximation, the average mass fractions depend on Reynolds number (viscosity) through the Reynolds number dependence of the mixing process. Since for large Reynolds number values turbulent mixing is assumed to become independent of the molecular properties (Corrsin, 1964), the flamelet expectation is that the average mass fractions are not dependent on the actual value of the viscosity, they obey Reynolds number similarity.

Figure 2 shows average fuel mass fractions versus time from a DNS. (One step, isothermal chemistry, isotropic decaying flow, Sc = 1.) The mass fractions are shown for different initial Damköhler numbers and Reynolds numbers. Curves belonging to different Re values deviate. In Fig. 3 the same mass fractions are shown as before but instead of time non-dimensionalized by the initial large eddy turnover time the characteristic mixing time $t^* = ln[\sigma(0)/\sigma(t)]$ was used ($\sigma(t)$ is the standard deviation of Z at some time t). The collapse of the curves corresponding to different Reynolds number values demonstrates that the Reynolds number dependence seen in Fig. 2 is due to the dependence of the mixing process on Re as predicted by the flamelet approximation. The expectation therefore is that at higher Re values the Re dependence seen in Fig. 2 will disappear. Note, however, that Menon *et al.* (1994) found via the linear eddy investigation of a typical "Sandia-jet" that the average OH mass fraction predictions do depend on the molecular properties used in the calculations. This finding contradicts flamelet modeling in a major way. To investigate the issue further we are presently working on new simulations that account for radical behavior (Swaminathan and Bilger, 1997).

References

Bilger, R. W., Saetran, L. R. and Krishnamoorthy, L. V. (1991) *J. Fluid Mech.*, **233**, 211

Buriko, Y. Y., Kuznetsov, V. R., Volkov, D. V., and Saitsev, S. A. (1994) *Combust. Flame*, **96**, 104

Cook, A. W., and Riley, J. J. (1994) *Phys. Fluids*, **6**, 2868

Cook, A. W., and Riley, J. J. (1997) *Comb. Flame* (in press)

Corrsin, S. (1964) *AIChE Journal*, **10**, 870

deBruynKops, S. M., Kosály, G., and Riley, J. J. (1997a) "Investigation of the Flamelet Modeling of Turbulent Combustion," Gas Research Institute, GRI-97/00319
deBruynKops, S. M., Riley, J. J., and Kosály, G. (1997b) "Large Eddy Simulation of a Reacting Mixing Layer," WSS/CI Paper 97S-051
Gao, F., and O'Brien, E. E. (1993) *Phys. Fluids A*, **5**, 1282
Kuznetsov, V. R. (1982) *Mehan. Zhidkost Gasa*, **6**, 3-9
Lentini, D. (1994) *Comb. Sci. Tech.*, **100**, 92
Menon, S., Calhoon Jr., W. H., Goldin, G., and Kerstein, A. R. (1994) Twenty-Fifth Symposium (International) on Combustion, The Combustion Institute, 1125
Mungal, M. G., Hermanson, J. C. and Dimotakis, P. E. (1985) *AIAA J.*, **23**, 1418
Peters, N. (1983) *Comb. Sci. Tech.*, **30**, 1
Sanders, J. P. H. and Gökalp, I. (1997), "Non-Equilibrium and Differential Diffusion effects in Turbulent Hydrogen Diffusion Flames," Submitted to Journal of Thermophysics and Heat transfer
Swaminathan, N. and Bilger, R. W. (1997, to appear in *Phys. Fluids*)

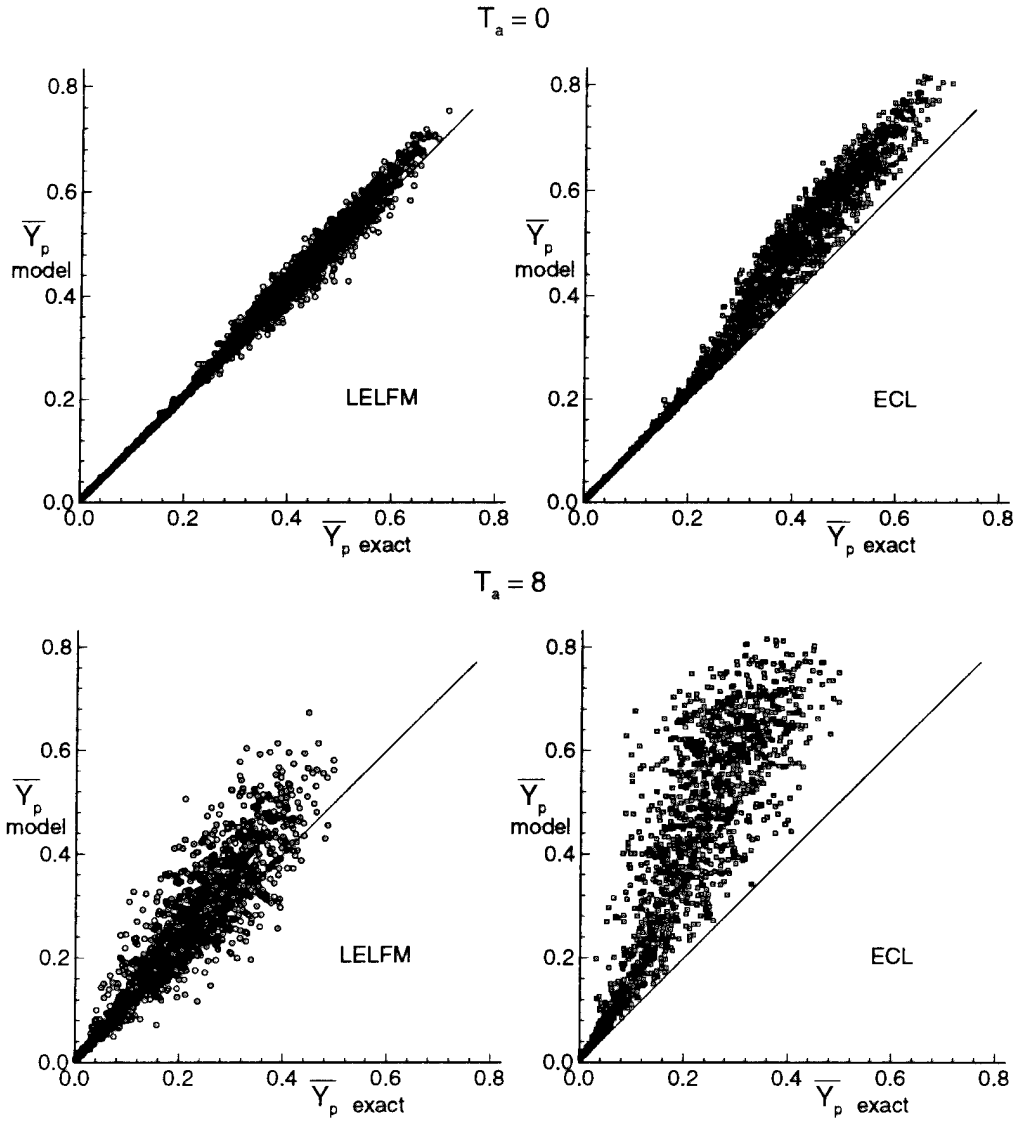

Figure 1: Correlation of exact and modeled product mass fraction for different activation temperatures.

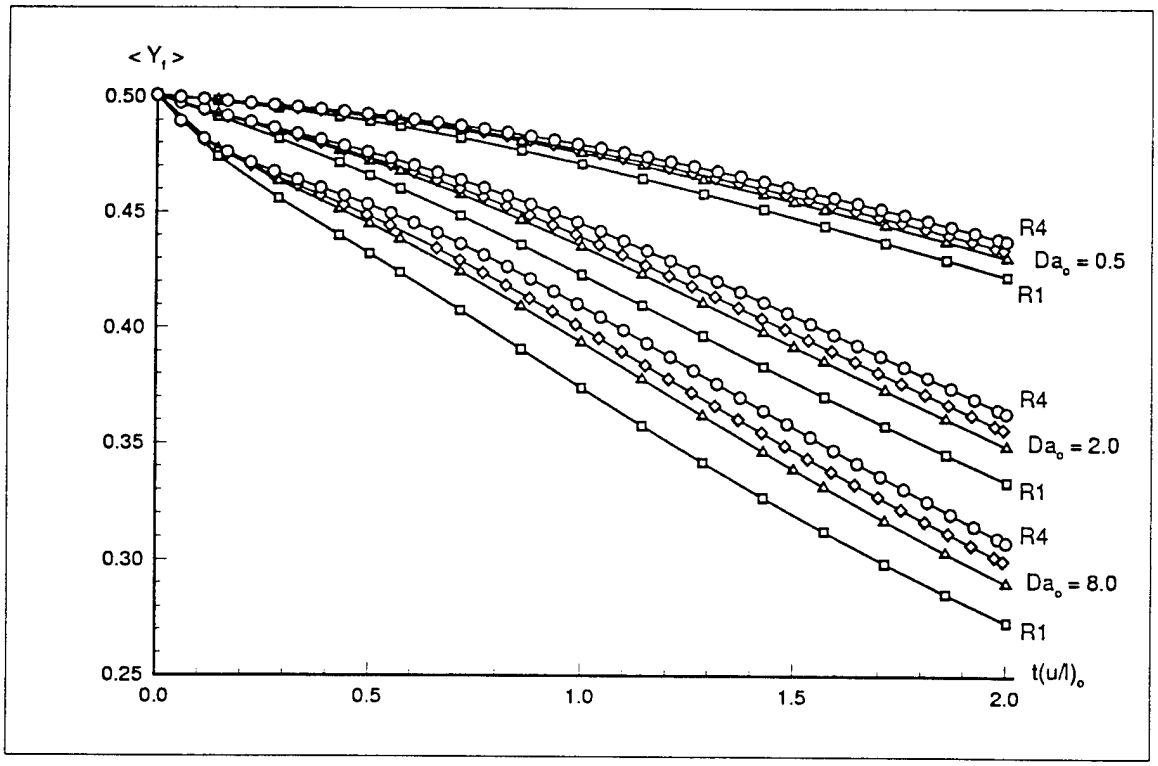

Figure 2: The average mass fraction of fuel vs. $t(u/\ell)_o$ at varying initial Damköhler and Reynolds numbers. Results for the smallest and largest Reynolds number velocity field used in the DNS are indicated as R1 and R4, respectively.

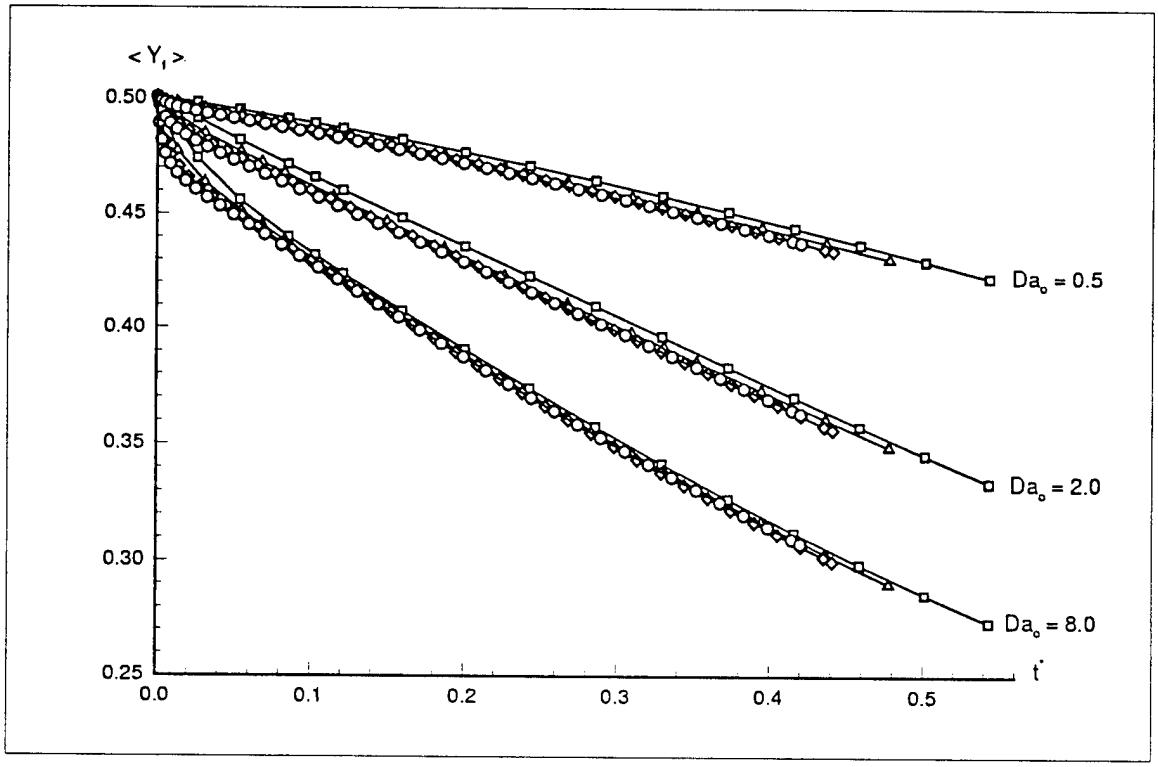

Figure 3: The average mass fraction of fuel vs. t^* at varying initial Damköhler and Reynolds numbers.

COMBUSTION RESEARCH

AFOSR: 92WL036

Principal Investigators: W. M. Roquemore, R. D. Hancock, J. R. Gord

WL/POSC Bldg 490
1790 Loop Rd N
Wright-Patterson AFB OH 45433-7103

SUMMARY/OVERVIEW

This combustion research program encompasses experimental and computational activities that range from fundamental vortex-flame interaction studies to the development of advanced gas turbine combustor concepts. Vortex-flame interactions represent the fundamental building blocks of turbulent flames, while advanced combustors depend on high levels of turbulence for proper mixing and combustion. Throughout this year we have investigated vortex-flame interactions in jet and counterflow diffusion flames. Direct numerical simulations (DNS) and extensive optical diagnostic measurements were obtained in these flames. The results indicate that the local Lewis number and thermal diffusion are important parameters in determining the local flame temperature and nitric oxide (NO) production rates. Additional work not included in this technical discussion includes the establishment of an ultrafast laser lab for combustion diagnostics, modeling of sprays, the extinction of jet diffusion flames, and the development and characterization of trapped-vortex combustion concepts for use in gas turbine combustors.

AUTHORS: R. D. Hancock, W. M. Roquemore, J. R. Gord

TECHNICAL DISCUSSION

Vortex-Flame Interactions

A flame is considered to be turbulent when its entire flame surface becomes wrinkled and bumpy (Hottel and Hawthorne, 1949). Countless photographs of jet flames indicate that these wrinkles and bumps are often caused by many small- and large-scale vortical structures that collide and interact with the flame sheet. Turbulent flames have length- and time-scales that vary over several orders of magnitude, and the gas temperature and species concentrations will vary significantly in space and time. These variations strongly affect flame temperature, combustion efficiency, and the formation of pollutants. We have chosen to study single, reproducible, vortex-flame interactions because they are representative of individual "turbulent" events. These events are extremely reproducible and have been studied extensively with a multitude of laser diagnostic techniques which include coherent anti-Stokes Raman spectroscopy (CARS), dual-pump CARS, laser-induced fluorescence (LIF), reactive Mie scattering (RMS), and OH LIF imaging.

Jet Diffusion Flames

Several experimental and computational studies have been performed simultaneously to investigate vortex-flame interactions (Hancock, 1996; Hancock et al., 1996; 1997a ,1997b; Thevenin et al., 1996; Hsu et al., 1996; Schauer et al., 1996; Katta and Roquemore, 1996, 1997; Takahashi and Katta, 1997; Grisch et al., 1996). We have studied vortices that originate on both the fuel and air sides of jet diffusion flames (Carter et al., 1995). However, this written description of jet diffusion flames is confined to a discussion of fuel-side vortex-flame interactions.

In a particular fuel-side vortex-flame interactions study, four different flames were investigated that had the same overall volumetric flow rate, but varying amounts of H_2, N_2, and He (Hancock, 1996; Schauer et al., 1996; Hancock et al., 1996). In order to investigate complex vortex-flame interactions, it was first essential that the steady jet diffusion flames be modeled accurately. Initial calculations with our DNS model showed poor agreement with the experiment in terms of the peak flame temperature and

flame location. After a thorough investigation of experimental parameters such as the fuel and co-flow velocity profiles and the chemistry model in the DNS code, we turned our attention to the diffusive transport mechanisms. By multiplying the concentration diffusion coefficient of diatomic hydrogen by a factor of 1.7, excellent agreement between the DNS code and experiment was achieved. This apparent diatomic hydrogen diffusion coefficient enhancement suggest that thermal diffusion, which acts to raise the mass flux of 'light' species such as H_2 in the direction of increasing temperature, may be an important factor in the high-temperature-gradient regions of these diffusion flames. As illustrated in Fig. 1, when thermal diffusion is included in the model the pure hydrogen flame temperature rises ~100 K to within the experimental error of the CARS temperature measurements. Because of the impact of the diffusion coefficients on the flame structure, a thorough investigation of the transport coefficients found in the literature and used in the DNS model is warranted. Furthermore, thermal diffusion must be considered for flames in which there are large molecular weight differences for the various gases involved in the combustion process.

Figure 2 is an illustration of a H_2/N_2 flame with an internally generated vortex. The left side of the figure shows the experimental image. The right side of the figure is the computational result. There are several phenomena that complement, or compete, with one another to influence the local flame temperature and chemical composition during a vortex-flame interaction. These phenomena include local Lewis number, finite-rate chemical kinetics, flame stretch and curvature, and velocity flowfield. Our direct numerical simulation (DNS) model can account for each of these complicated processes, allowing them to interact actively with one another. Extensive temperature and nitric oxide species concentration measurements were also obtained in these flames using CARS and LIF. These measurements, in combination with the DNS calculations, indicate that, for high-Damkohler-number flames like that shown in Fig. 2, the gas temperature in the positively stretched regions of the flame can actually be higher than the temperature of an unstretched flame (Hancock, 1996). Likewise, it was found that the temperature in the negatively stretched regions of the flame decreases. These results are illustrated in Fig. 3. The positively stretched region is at the bulge of the vortex and the negatively stretched (compressed) regions are upstream and downstream of the vortex.

Counterflow Diffusion Flames

Numerical studies for counterflow diffusion flames are usually conducted using a quasi-one-dimensional assumption. Despite the apparently successful comparisons with experiments, some concern has been expressed regarding this assumption. To our knowledge, no one has made a complete simulation for the counterflow diffusion flame. Such simulations not only eliminate the concerns of the quasi-one-dimensional analyses, but also provide a valuable test case for the validation of mathematical models. Furthermore, experimental studies on vortex-flame interactions in counterflow diffusion (Rolon et al., 1995) and premixed (Roberts et al., 1993) flames demand two- or three-dimensional simulations. Results for steady opposing jet flames are presented by Katta and Roquemore (1996). In this work, simulations were made for the experiments of Rolon. Vortices are forced toward the flat flame from the fuel and/or oxidizer sides by rapidly injecting a specified amount of fuel or oxidizer from the respective side of the burner. For methane flames, two interactions (one with the slowly moving vortex and the other with the fast moving vortex) were studied. In each case, the same volume of fluid was injected from the fuel- or oxidizer-sides. When the vortex strength is weak (slow-moving vortex), the flame temperature near the stagnation point decreases by ~140K and the flame returned to its unperturbed position as the vortex dissipates in time. However, in the second case (fast-moving vortex), the flame in the neighborhood of the stagnation point quenched initially, and as time passed the entire flame was quenched. It was also found that while the temperature of the flame in the neighborhood of the stagnation point decreases during the vortex-flame interaction, the concentration of certain species (i.e. CH_2O, CO) increase and certain other species (i.e. CH_3, CO_2, H_2) decrease. Calculations performed for vortex-flame interactions in hydrogen flames resulted in a very interesting phenomenon. Unlike methane flames, quenching of the hydrogen flame first appeared along an annular ring away from the stagnation point, i.e, not at the highest strain rate location. As illustrated in Fig. 4, these predictions were recently confirmed by the unpublished experiments of Rolon. Preliminary analyses indicates that the non-unity-Lewis numbers associated with the hydrogen flames are responsible for this behavior of extinction occurring at intermediate strain rates. These results may have a significant influence on the current practice for generating flamelet libraries.

We have recently completed the fabrication of a counterflow diffusion flame burner similar to that used by Thevenin et al. (1996) and Rolon et al. (1995). This burner will reside at Wright Laboratory

and will be used to obtain extensive velocity flow field measurements, gas temperatures and species concentrations. These measurements, and our continued modeling work, will complement the work being done by our European counterparts.

REFERENCES

Carter, C. D., R. D. Gould, L. P. Goss, V. R. Katta, and K. Y. Hsu (1995). "The Structure of a Dynamic Nonpremixed H_2-Air Flame," Western States Section of the Combustion Institute, paper WSS/CI 95F-222, Stanford, CA.

Grisch, F., B. Attal-Tretout, P. Bouchardy, V. R. Katta, and W. M. Roquemore (1996). "A Vortex-Flame Interaction Study Using Four-Wave Mixing Techniques," Journal of Nonlinear Optical Physics and Materials **5**(3): 505-526.

Hancock, R. D. (1996). "Laser Diagnostic Investigation of the Structure of Steady and Driven Hydrogen Jet Diffusion Flames," Ph.D. Dissertation, University of Illinois at Urbana/Champaign, Aug 1996.

Hancock, R. D., F. R. Schauer, R. P. Lucht, V. R. Katta, and K. Y. Hsu (1996). "Thermal Diffusion Effects and Vortex-Flame Interactions in Hydrogen Jet Diffusion Flames," Twenty-Sixth Symposium (International) on Combustion, The Combustion Institute, Pittsburgh, PA.

Hancock, R. D., K. E. Bertagnolli, and R. P. Lucht (1997a). "Nitrogen and Hydrogen CARS Temperature Measurements in a Hydrogen/Air Flame Using a Near-Adiabatic Flat-Flame Burner," Combustion and Flame, May 1997.

Hancock, R. D., F. R. Schauer, and R. P. Lucht (1997b). "Dual-Pump Coherent Anti-Stokes Raman Scattering (CARS) Measurements of Nitrogen and Oxygen in a Laminar Jet Diffusion Flame," Accepted for publication in the August 1997 issue of Applied Optics.

Hottle J. C. and W. R. Hawthorne (1949). "Diffusion in Laminar Flame Jets," Third Symposium on Combustion, Flame and Explosion Phenomena, The Combustion Institute, Pittsburgh PA., pp. 254-266.

Hsu, K.-Y., V. R. Katta, and W. M. Roquemore (1996). "An Experimental and Numerical Investigation on Local Extinction in Jet Diffusion Flames," Presented at the 1996 Technical Meeting of the Central States Section of the Combustion Institute, 5-7 May 1996, St. Louis MO; Published in Combustion Fundamentals and Applications (The Combustion Institute, Pittsburgh PA, 1996), pp. 437-442.

Katta, V. R., and W. M. Roquemore (1996). "Extinction in Methane-Air Counterflow Diffusion Flames," Presented at the 1996 Technical Meeting of the Central States Section of the Combustion Institute, 5-7 May 1996, St. Louis, MO; published in Combustion Fundamentals and Applications (The Combustion Institute, Pittsburgh, PA, 1996), pp. 449-454.

Katta, V. R. and W. M. Roquemore (1997). "NOx Formation in a Dynamic Methane-Air Jet Diffusion Flame," Presented at the 1997 Technical meeting of the Central States Section of the Combustion Institute, 27-29 April 1997, Point Clear AL.

Roberts, W. L., J. F. Driscoll, M. C. Drake, and L. P. Goss (1993). "Images of the Quenching of a Flame by a Vortex-To Quantify the Regimes of Turbulent Combustion," Combust. Flame **94**: 58-69.

Rolon, J. C., F. Aguerre, and S. Candel (1995). "Experiments on the Inteaction between a Vortex and a Strained Diffusion Flame," Combustion and Flame **100**: 422-429.

Schauer, F. R., R. D. Hancock, R. P. Lucht, and V. R. katta (1996). "Thermal Diffusion and Nonunity Lewis Number Effects in Hydrogen Jet Diffusion Flames," Presented at the 1996 Technical Meeting of the Central States Section of the Combustion Institute, 5-7 May 1996, St. Louis MO; published in Combustion Fundamentals and Applications (The Combustion Institute, Pittsburgh PA, 1996), pp. 97-102.

Takahashi, F. and V. R. Katta (1997). "A Numerical Investigation of the Stabilizing Mechanism of Methane jet Diffusion Flames," Presented at the 35th Aerospace Sciences Meeting and Exhibit, Reno NV, Paper AIAA 97-0251.

Thevenin, D., J. C. Rolon, R. H. Renard, D. W. Kendrick, D. Veynante, and S. Candel (1996). "Structure of a Non-Premixed Flame Interacting with Counterrotating Vortices," Twenty-Sixth Symposium (International) on Combustion, The Combustion Institute, Pittsburgh PA.

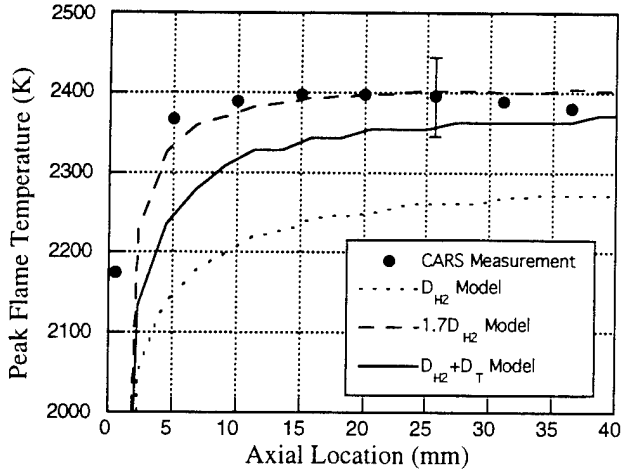

Figure 1. Measured and modeled peak flame temperatures from a pure hydrogen diffusion flame. Model results shown for three hydrogen diffusion formulations.

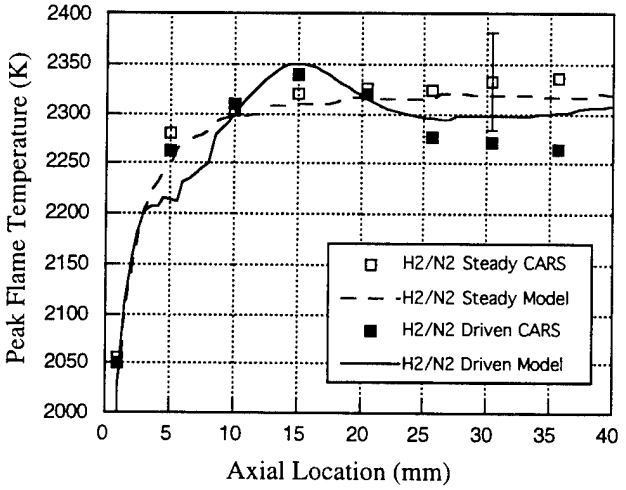

Figure 3. Measured (CARS) and modeled peak flame temperatures for steady and driven jet diffusion flames. $1.7D_{H2}$ diffusion formulation used in model.

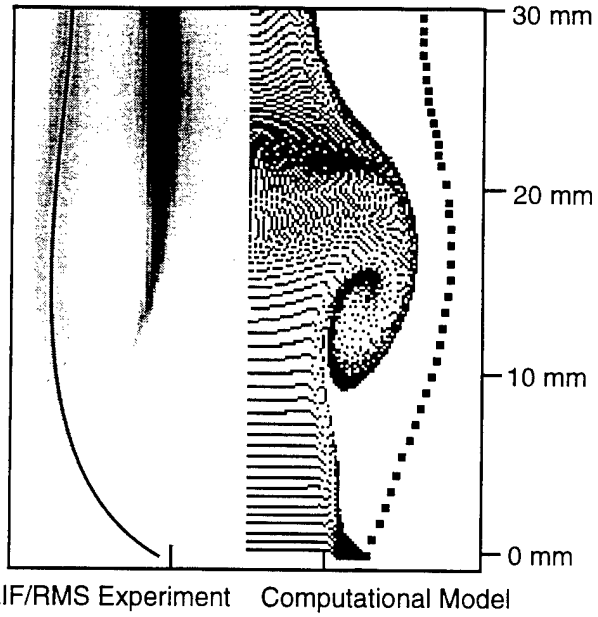

Figure 2. Comparison of experimental and computational images of a vortex-flame interaction in a H_2/N_2 jet diffusion flame.

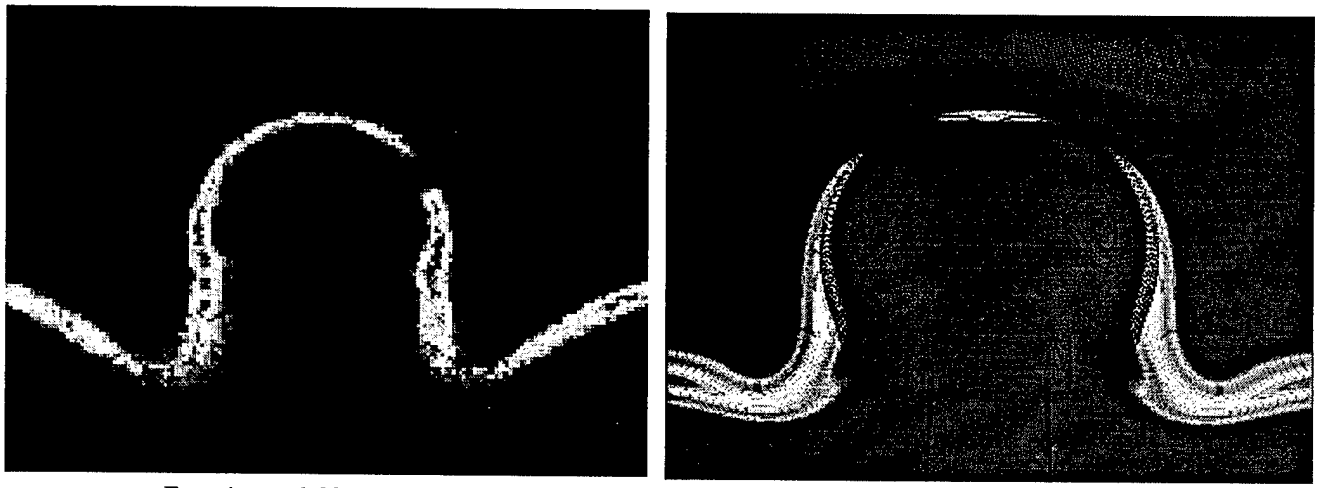

Experimental OH LIF Image
J. C. Rolon

Numerical Simulation
V. R. Katta

Figure 4. Vortex-flame interaction in opposing jet flames. Extinction does not occur first in the highly stressed region.

AFOSR RESEARCH ON STRUCTURAL CERAMICS FOR EXTREME TEMPERATURES AND ENVIRONMENTS

Dr. Alexander Pechenik
Program Manager

AFOSR/NA
110 Duncan Avenue, Suite B115
Bolling AFB, Washington, D.C. 20332-0001

SUMMARY: This talk will outline the program of basic research sponsored by the Air Force Office of Scientific Research in the area of structural ceramic materials. Structural ceramic materials offer unique opportunities for the designers of future propulsion systems. Some monolithic ceramics are capable of performing structural functions at extremely high temperatures and in a variety of corrosive environments. Ceramic composites, when carefully designed for a specific application, can provide toughness and reliability necessary for advanced propulsion systems. Materials designers and system designers must work together to solve the immensely complex problems arising from the development of future propulsion systems. This talk will concentrate on the fundamental phenomenology of materials functioning at extremely high temperatures and in very corrosive environments.

TECHNICAL DISCUSSION: The Air Force basic research program on structural ceramics and nonmetallic structural materials and composites is managed under the auspices of the Office of Scientific Research (AFOSR), which is the organization managing all basic research for the US Air Force. All projects related to structural ceramics are located in the Directorate of Aerospace and Materials Sciences headed by Dr. C.I. Chang. Two programs, Mechanics of Materials, managed by Dr. W.F.Jones, and Ceramic and Nonmetallic Materials, managed by Dr. A.Pechenik, deal with structural ceramics. The scopes of the two programs complement each other, the former emphasizing mechanics-related issues and the latter concentrating on materials science issues, such as

microstructure development, processing, thermodynamic stability, and diffusion. For example, research projects on ceramic matrix composites (CMCs) dealing with mechanics of brittle-matrix composites and fracture mechanics are supported by the Mechanics of Materials program, whereas those addressing high-temperature properties of fibers and fiber-matrix interfaces, or the issues related to environmental stability of composites, are sponsored by the Ceramic and Nonmetallic Materials program.

The general objective of the Air Force structural ceramic and nonmetallic materials program is to provide scientific background for the current and future applications of ceramics, ceramic-matrix composites, and carbon-based materials in flight-related systems and structures. The main driving force behind the introduction of ceramic-based materials into the Air Force systems is the high-temperature capabilities of ceramic materials combined with their high specific strength, stiffness, and excellent wear and corrosion resistance. Major improvements in performance of air-breathing and rocket engines, and hot sections of airframes are expected from the introduction of ceramic materials. Some near-term applications of ceramic materials, that are of particular importance and promise to the Air Force, include ceramic-metal and full ceramic bearings for turbine engines, CMCs for engine hot exhaust sections, and thermal barrier coatings for superalloys and intermetallics used in engines. For these applications to become a reality, a scope of fundamental issues is being addressed by the AFOSR. Some of these issues are outlined below.

The AFOSR structural ceramics program can tentatively be subdivided into six areas of concentration. These areas are: ceramic-matrix composites, carbon/carbon composites, ceramic toughening, very high temperature ceramic behavior, advanced processing, and coatings. These research areas are emphasized because of their importance for the applications that are currently being developed by the Air Force Wright Laboratory and related industries. Program managers of the AFOSR maintain close scientific interactions with the applied efforts of the Wright Laboratory and the in-house scientists have a significant input into the process of selection of proposals and development of scientific directions for the AFOSR.

Currently and in the near future, the major research effort in structural ceramics is concentrated in the areas related to ceramic-matrix composites. The main factors important for successful application of CMCs in Air Force systems and structures are: reliability, dimensional stability under a variety of thermo-mechanical loads, environmental stability, and, last but not least, affordability.

One of the important components of the research on CMCs is understanding high-temperature strength and creep-resistance of ceramic materials on atomic and microscopic levels. This basic knowledge is necessary for the development of high-strength, creep resistant, and affordable fibers and matrixes for CMCs capable of very high-temperature applications. Of particular interest are creep-resistant oxide materials, such as yttrium aluminum garnet (YAG), alumina, and zirconia. In addition, silicon nitride, silicon carbide, and other refractory non-oxide ceramics are considered for applications at extremely high-temperatures (above 1500 °C). It is generally accepted, that, currently, the crucial issue for successful development of all CMCs is the development of thermally-stable, oxidation-resistant, mechanically-controlled interfaces between fibers and matrixes. The problem of developing such "optimized" interfaces is approached in this program from many directions. Theoretical studies emphasize thermodynamic stability and atomic structure of interfaces, whereas experimental work is directed toward developing new coatings for ceramic fibers that prevent chemical reactions between fibers and matrixes.

Another important part of the program is the design of microstructure of monolithic ceramics. One of the major detriments in using monolithic ceramics for structural applications, such as bearings, is their brittleness. The issue of reducing or controlling brittleness of monolithic ceramics is addressed in this program in three ways: (1) study of the influence of ceramic microstructure on fracture, fatigue, and flaw-tolerance of monoliths; this approach provides criteria for predicting performance of ceramics under a variety of conditions; (2) evaluation of various means of toughening of brittle materials, such as martensitic transformations, flaw- and stress-induced toughening; and (3) layering and particulate reinforcements. The scientific issues comprising this part of the program range from grain size optimization for martensitic transformations to elucidating the effects of the R-curve behavior on tolerance of surface damage. Texturing and surface strengthening of monolithic ceramics are also of interest since these techniques likely to play a significant role in the development of ceramic bearings and other tribological parts.

Advanced processing is a very important part of the program. Generally speaking, "processing" research projects that are of interest to this program fall into two categories, those dealing with fundamentally new approaches to fabricating ceramic materials, such as, for example, nano-particles or polymer pre-cursors to ceramics, and those emphasizing "intelligent", optimized processing of ceramic materials via improved modeling, process control, and utilization of in-situ, real-time sensors. Again, there is a separation of tasks between the Materials

Science program of Dr. Pechenik, which emphasizes atomistic, chemical, and thermodynamic approaches to processing and the Mechanics program of Dr. Jones, that concentrates on mathematical modeling of processing and "scale-up"-type issues.

Arguably, carbon-carbon composites can be studied in the same program as ceramics, due to the fact that mechanical properties of these structural materials are similar. Thus, traditionally, AFOSR structural ceramics program includes basic research on carbon materials. Light-weight, high-temperature resistant carbon/carbon composites are increasingly used as structural elements for hypersonic aircraft and space structures. To facilitate their use, resistance to oxidation of these materials must be improved. To this end, this program seeks to elucidate oxidation mechanisms of carbon materials, with the goal of inhibiting oxidation by using dopants and surface modifiers. Also studied are carbon-like materials, such as BC_3, which resist oxidation better than carbon. In addition, new approaches to oxidation-inhibiting coatings for carbon-carbon composites are investigated.

CHEMICAL REACTIONS in TURBULENT MIXING FLOWS

AFOSR Grant F49620–94–1–0353

P. E. Dimotakis and A. Leonard

Graduate Aeronautical Laboratories
California Institute of Technology, Pasadena, CA 91125

Summary/Overview

This program is focused on fundamental investigations of mixing, chemical-reaction, and combustion processes, in turbulent, subsonic, and supersonic free-shear flows. The program is comprised of an experimental effort; an analytical, modeling, and computational effort; and a diagnostics and data-acquisition-development effort. The computational studies are focused on fundamental issues pertaining to the numerical simulation of compressible flows with strong fronts, in both chemically-reacting and nonreacting flows. Parts of this effort are cosponsored by AFOSR URI Grant No. F49620–93–1–0338.

Technical discussion

Experiments in subsonic shear layers were performed to gauge Reynolds-number effects on molecular mixing. Previous results indicated a weak Reynolds number effect (roughly 6% decrease per factor of two increase in Re).[1] Those measurements, however, were at Reynolds numbers substantially lower than ones encountered in subsequent, higher-speed, compressible shear layers, rendering it difficult to assign differences in mixing to Reynolds-, or Mach-number effects. A series of subsonic-flow experiments, extending the previous data range to $Re_\delta = \rho\,\Delta U\,\delta/\mu \simeq 7 \times 10^5$, were performed to measure the extent of molecular mixing and fill this gap. These experiments relied on fast chemical reactions and "flip" experiments to measure molecular mixing. The results are in accord with previously-documented behavior, as well as with a measurement by Clemens & Paul (1995) in a cylindrical shear layer,[2] using a very different (optical) technique. They indicate a mixed-fluid fraction, $\delta_{\rm m}/\delta_T$, where $\delta_{\rm m}$ is the molecularly-mixed fluid thickness and δ_T is the 1% chemical-product profile thickness, that slowly decreases to a nearly-constant value.

In other experimental investigations, supersonic flows were also studied in the GALCIT Supersonic Shear-Layer Facility. Data from one such experiment is presented below, recorded with a recently-developed, color-schlieren system that uses color hue and intensity to code gradient direction and magnitude. Figure 1 depicts a bi-supersonic mixing-layer formed by (laboratory-frame) bi-supersonic freestream flows: $M_1 \simeq 1.5$ [Ar] over $M_2 \simeq 1.2$ [N_2]. This flow includes some complex wave-turbulence interactions. In particular, the interaction of an intentionally-generated wave, emanating from the splitter plate tip (reflected from the upper guidewall), can be seen to interact with the turbulent layer. At these freestream conditions,

significant baroclinic vorticity is produced, that augments the primary shear-layer vorticity. This shock-wave/shear-layer interaction has a negligible effect on the large-scale growth of the layer, however, in accord with previous findings,[3] as well as with previous work at Caltech. Color-schlieren visualization improves over classical black-and-white visualization and is capable of resolving the (spanwise-integrated) two-dimensional index-of-refraction-gradient field. In a complex flowfield, such as the confined, bi-supersonic flow of Fig. 1, this additional information can alleviate ambiguities in the inferred local structure incurred by the one-dimensional "mapping" that the classical schlieren visualization registers. For example, the alternating blue-red pattern of the shock waves visible in the original color version of the upstream region of Fig. 1 is indicative of an "N-wave" structure.

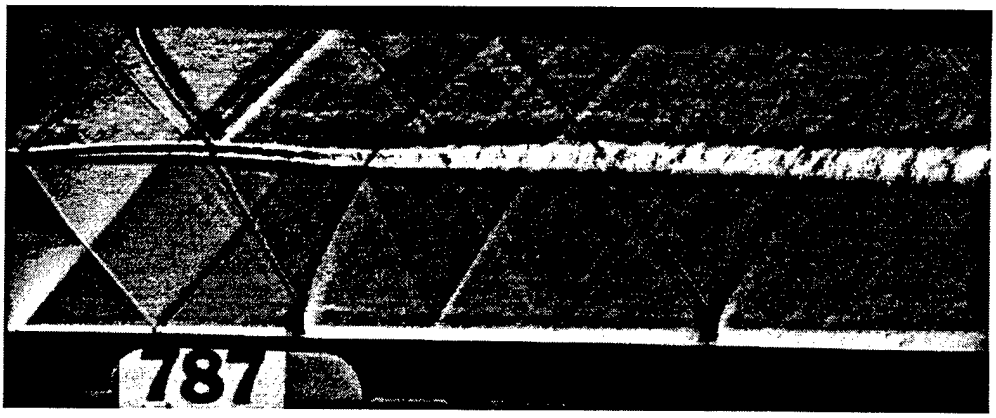

FIG. 1 B&W rendition of color-schlieren of bi-supersonic ($M_1 \simeq 1.5$ [Ar]; $M_2 \simeq 1.2$ [N_2]) mixing-layer. Flow is from left to right, with the high-speed, high-density, Ar freestream above the low-speed, lower-density, N_2 freestream.

A new framework has been developed for the study of the geometry of level sets and applied to scalar isosurfaces in turbulent-jet mixing.[4–6] Level sets are important in turbulent-mixing and combustion and can be used to express scalar transport evolution,[7] or capture the instantaneous, hydrocarbon burning (stoichiometric) surfaces.[8] In our recent work, relations between coverage (fractal) statistics and scale distributions, in general, have been derived. Reynolds-number and scalar-threshold effects were investigated, in the far field of turbulent jets, at $Re \simeq 4.5\times10^3$, 9.0×10^3, and 18×10^3. A coverage (fractal) dimension that smoothly increases with scale, from unity at the small scales, to 2 at the large scales, is indicated by the 2-D data, in accord with previous, 1-D temporal and spatial data.[9] The scale distribution was computed in terms of a multidimensional (2-D, for these data) spacing scale, defined as the size of the largest empty box (LEB), randomly located in the bounding box of the level set, that contains no part of the level set. At the inner scales, the coverage dimension and LEB-scale distribution were found to be consistent with lognormal statistics. A lognormal distribution of the sizes of individual island/lake level-set contours is indicated by the data (*cf.* Fig. 2). The LEB scale distribution was also shown to provide a dimensionless measure of the surface-volume (perimeter-area, in 2-D) ratio of the level sets, in the small-scale limit.

A more detailed description of scale distributions and their relation to (power-law or scale-dependent) fractal geometry has also recently been discussed.[10] A review of fractals in the context of turbulent mixing was recently presented in a NATO, Advanced Studies Institute lecture series.[7] Three-dimensional space-time isosurfaces are presently under investigation with analysis of the 3-D level-set geometry in progress.

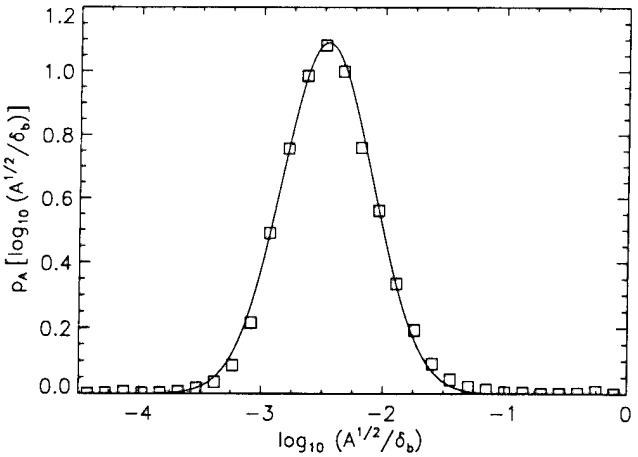

FIG. 2 Size pdf of islands and lakes in the far field of a turbulent jet ($Re \simeq 9 \times 10^3$).

A new, unsplit algorithm has been developed, for one- and multi-dimensional hyperbolic systems of conservation laws with source terms, that integrates the terms of the governing equations simultaneously, in a single, fully-coupled time-step. Conventional schemes split the temporal and spatial directions, with each term of the equations integrated in separate steps. No flux-splitting, or explicit artificial viscosity for the stabilization of discontinuities, or any of the other usual "fixes", are needed in the new algorithm. The algorithm has also been used in conjunction with Adaptive Mesh Refinement techniques.

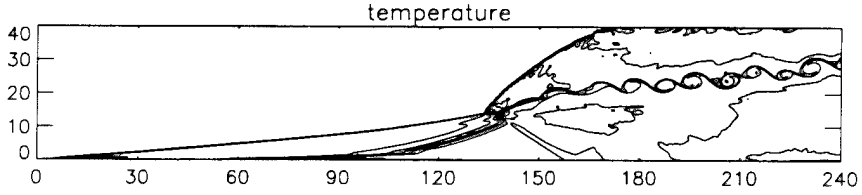

FIG. 3 Instantaneous temperature contours for a 2-D, wedge-induced detonation ($\theta = 35°$), at $t = 36.0$ ($M_\infty = 11$). Coordinates aligned with inclined wedge surface.

The algorithm has been used to investigate unsteady ZND detonations (low over-drive factor) that can result in chaotic behavior.[11] It has also been successfully used to simulate the multi-dimensional propagation of unstable 2-D ZND detonations in narrow channels and

to provide high-resolution simulations of wedge-induced detonations; a phenomenon important in some envisaged hypersonic-propulsion applications. Temperature-field contours are plotted in Fig. 3, for a wedge-induced detonation, by way of example. The freestream Mach number is $M_\infty = 11$ and the wedge angle is $\theta = 35°$. A strong explosion is initiated at the front and a strong entropy layer that generates vortices can be seen to emanate further downstream. Studies of detonations induced by projectiles of various shapes are currently under way.

Progress in other areas includes work on the effects of initial conditions in high-Re flows, work in chemically-reacting supersonic flows, Image Correlation Velocimetry investigations of the flow over an accelerating airfoil, as well as multi-dimensional and fast-imaging applications.

References

[1] Mungal, M. G, Hermanson, J. C., and Dimotakis, P. E., "Reynolds Number Effects on Mixing and Combustion in a Reacting Shear Layer," *AIAA J.* **23**, 1418–1423 (1985).

[2] Clemens, N. T., and Paul, P. H., "Scalar measurements in compressible axisymmetric mixing layers," *Phys. Fluids* , **7**(5), 1071–1081 (1995).

[3] Shau, Y. R., Dolling, D. S., and Choi, K. Y., "Organized structure in a compressible turbulent shear layer," *AIAA J.* **31**(8), 1398–1405 (1993).

[4] Catrakis, H. J., *Mixing and the Geometry of Isosurfaces in Turbulent Jets*, Ph.D. thesis, California Institute of Technology (1996).

[5] Catrakis, H. J., and Dimotakis, P. E., "Mixing in turbulent jets: scalar measures and isosurface geometry," *J. Fluid Mech.* **317**, 369–406 (1996).

[6] Catrakis, H. J., and Dimotakis, P. E., "Scale Distributions and Fractal Dimensions in Turbulence," *Phys. Rev. Lett.* **77**(18), 3795–3798 (1996).

[7] Dimotakis, P. E., and Catrakis, H. J., "Turbulence, fractals, and mixing," NATO Advanced Studies Institute series, *Mixing: Chaos and Turbulence*, GALCIT Report FM97–1 (1996).

[8] Burke, S. P., and Schumann, T. E. W., "Diffusion Flames," *Ind. Eng. Chem.* **20**(10), 998 (1928).

[9] Miller, P. L., and Dimotakis, P. E., "Stochastic geometric properties of scalar interfaces in turbulent jets," *Phys. Fluids A* **3**, 168–177 (1991).

[10] Catrakis, H. J., and Dimotakis, P. E., "Scale-dependent-fractal geometry," NATO Advanced Studies Institute series, *Mixing: Chaos and Turbulence* (1996).

[11] Papalexandris, M. V., Leonard, A., , and Dimotakis, P. E., "Unsplit Schemes for Hyperbolic Conservation Laws with Source Terms in One Space Dimension," *J. Comp. Phys.* (to appear) (1997).

COMPRESSIBLE TURBULENT REACTING FLOWS

(AFOSR Grant No. F49620-96-1-0106)

Principal Investigators: F.A. Williams, P.A. Libby and S. Sarkar

Department of Applied Mechanics and Engineering Sciences
University of California San Diego, La Jolla, CA 92093-0411

SUMMARY/OVERVIEW

The objective of this research is to advance fundamental understanding of reacting flows that are relevant to Air Force needs in high-speed airbreathing propulsion. Specific areas investigated are direct numerical simulation of compressible turbulent combustion, theory and modeling of compressible turbulent combustion, high-speed turbulent Couette flows with combustion, and combustion in turbulent counterflowing streams. The approaches involve computation, theoretical modeling and small-scale experimentation. Solutions to problems in the areas addressed should ultimately increase predictive capabilities of flows in combustion chambers, including supersonic combustion, thereby reducing needs for extensive trial and error in engine upgrades. The results could help to improve abilities to design propulsion systems that employ high-speed turbulent combustion.

TECHNICAL DISCUSSION

The evolution of turbulence and associated mixing has been studied by DNS (Direct Numerical Simulation) in three different flows. The results are summarized below.

Uniformly sheared, compressible reacting flow: Our previous simulations [1] of nonreacting, compressible flow with a uniform shear had shown that the turbulence intensities were dramatically reduced when the Mach number increases. We have performed new simulations with the inclusion of combustion to assess the additional effect of heat release on the turbulence. A single-step, infinitely fast, reaction model with large nondimensional heat release was used. Fig. 1 contrasts the evolution of the turbulent kinetic energy K as a function of nondimensional time St for a nonreacting case A3 and a reacting case A3R with high heat release $Ce = Q/C_vTO_2$=12. The intial Mach number $M_g = 0.66$ is identical between both cases and is large enough so that the asymptotic growth rate of K is a factor of 2 smaller than the corresponding incompressible value. Comparison of the evolution of K in cases A3 and A3R shows that the additional effect of heat release is small. The effect of heat release on other turbulence statistics such as dissipation rate and scalar p.d.f appear to be small as in our previous simulations of isotropic, reacting turbulence [2] in spite of density variation by a factor of 8 across the flame. Examination of the terms in the enstrophy transport equation shows that, although the baroclinic term is an order of magnitude larger because of reaction, it is still much smaller that the nonlinear vortex stretching term. Thus, the stabilizing effect of heat release that has been observed in other studies of flow instabilities may be less substantial in the case of *strongly nonlinear*, well-developed turbulence. Furthermore, the correlation between density and velocity fluctuations is small and, consequently, variable density effects in the turbulence stress transport equation are small [3].

The plane jet: The spatial evolution of the plane jet was studied using fourth-order compact derivatives in space, fourth-order Runge-Kutta time integration, grid clustering, and characteristic boundary conditions. Figs. 2-3 show results for a subsonic, M=0.4, plane jet. (Flow is from left to right in the x direction.) The contours of spanwise vorticity ω_z in Fig. 2 show the rollups of the shear layers at the jet edges and subsequent interaction of these shear layers

downstream of the potential core. The flow develops significant three-dimensionality as shown by the spanwise (z) variation of vorticity in Fig. 3. The broadband velocity fluctuations whose initial r.m.s. magnitude was approximately *3%* of the mean velocity grows by almost an order of magnitude by $x/h = 8.0$. Future simulations of the plane jet will be performed with larger domain length $x/h = 20$ and at higher Mach and Reynolds numbers. We have also performed two-dimensional simulations of shear layers and jets [4]. Although the mean velocity field and the thickness growth rate in 2-D simulations of the shear layer were in generally good agreement with experimental (3-D) observations, the profiles of fluctuation intensity differed substantially. In the case of the jet, the 2-D simulations were fundamentally different even with respect to the mean velocity field.

The shear layer: The scalar mixing in a temporally evolving shear layer has been studied for different types of initial forcing. Figs. 4-5 shows scalar isocontours in a x-y cross-section from a case where a spanwise array of streamwise vorticity is superposed on 2-D disturbances. The breakdown of the scalar isosurfaces (and consequent increase in mixing) at later time is evident from Fig. 5. Such breakdown was not observed with pure 2-D initial disturbances. It is remarkable that a single three-dimensional mode leads eventually to such large three-dimensional variation. Our future simulations will consider the evolution of finite-amplitude, three-dimensional fluctuations for a range of convective Mach numbers and with finite-rate, exothermic reaction. Mixing enhancement strategies for high-speed flows will be explored.

Reactive flows are complicated phenomena for which the interactions between the fluid dynamics and the chemistry play a fundamental role. Although the limit of infinitely large Damköhler numbers, in which all chemical processes are assumed to be infinitely fast, is useful in describing very weakly strained flows, finite-rate effects are significant under most strain conditions and must be taken into account if accurate descriptions are to be obtained. In general, different chemical processes exhibit very different time scales at the temperatures present in reaction zones, with radical-shuffling reactions typically being the fastest. Seeking simplifications that account for the disparity of the different time scales through steady-state assumptions for the radicals and through partial-equilibrium assumptions for the fast reactions has been common practice in recent years, leading to reduced chemical-kinetic mechanisms that potentially can be used in numerical calculations of complex reactive flows. In the present work, to extend the DNS formulation to account for these effects, a general three-step reduced mechanism for hydrogen-oxygen nonpremixed combustion with infinitely fast radical-shuffling reactions and finite recombination rates was developed [5], that applies under a wide range of flowfield conditions. The generalized coupling-function formalism originally developed by Liñán and Williams is employed in this work to transform the corresponding conservation equations, yielding a formulation that circumvents the stiffness of the fast radical-shuffling reactions, while accounting for the different values of the thermal and species diffusivities. The philosophy is to let the chemical simplifications dictate the conservation equations instead of trying to graft the chemistry into the equations after the fluid dynamical formulation is completed, an approach that often results in severe numerical difficulties.

The resulting formulation is somewhat too extensive to be reproduced but will be available in the publication [5]. A new kind of reaction sheet emerges from the analyses. The stoichiometry of this new reaction sheet is such that three hydrogen molecules are consumed, instead of two, for each oxygen molecule consumed. The additional hydrogen molecule generates two hydrogen atoms at the sheet, which recombine in a distributed manner throughout the Burke-Schumann diffusion zones, at a rate given by a source term that does not exhibit stiffness. The analysis thus generalizes the Burke-Schumann description not only by allowing for differing diffusivities but also by accounting for distributed recombination and the associated distributed heat release, which dominates the chemical energy liberation in the flow.

The new model provides a formulation that is well adapted to numerical treatment because it eliminates all disparate chemical time scales from the problem, removing any stiffness. The recombination time is the characteristic chemical time for the computation. This simplified

formulation is estimated to produce reasonable accuracy in describing hydrogen-oxygen diffusion flames, with nitrogen dilution, over about three orders of magnitude in a characteristic flow time, such as the reciprocal of a strain rate, whenever conditions of ambient pressure, feed-stream temperature and dilution lead to adiabatic flame temperatures between about 1000 K and 3000 K; the low-temperature limit increases gradually with increasing pressure, reaching about 1500 K at 50 atm, as determined by estimates of the crossover temperature. The formulation this is accurate over a wide range of conditions of practical interest.

One of the most attractive applications of the generalized Burke-Schumann procedure [5] is in direct numerical simulations of turbulent flows. It has proven difficult to include full hydrogen-oxygen chemistry in such simulations because of the widely differing time scales of chain-carrying and recombination steps. The generalized Burke-Schumann formulation overcomes these disparate-time complications, facilitating both computations and modeling of turbulent diffusion flames. It is intended to explore how much progress can be made in improving understanding of turbulent nonpremixed hydrogen-oxygen combustion through use of this new methodology. Work is also in progress on extending this type of formulation to methane-air flames with three-step reduced chemistry. This extension would show how to apply the procedures to hydrocarbon-air flames, in general.

Our research on turbulent Couette flow has as a goal comparison of the predictions of a Reynolds stress formulation for high speed turbulent flows with DNS results. Such a comparison should permit an assessment of the various models needed in these formulations in a convenient theoretical and computational setting. However the work we have done to date including a careful review of currently available Reynolds stress formulations has exposed significant shortcomings particularly with respect to the treatment of the energy flux equation and the pressure-velocity, pressure-rate-of-strain and pressure-enthalpy models. This has lead us to take up near term, a more modest topic, one which as far as we have been able to determine has not been treated, namely low speed Couette flow with large rates of heat transfer. In this case the variations of the viscosity coefficient and density result in nonlinear variations of the mean velocity across the central portion of the passage and in different viscous sublayers on the two surfaces. Thus this flow will resemble in these respects the high speed case to be taken up later. We intend to employ asymptotic methods which expose the essential elements of the flow. Thus we treat two viscous sublayers within which molecular and turbulent transport exchange dominance and a core flow devoid of molecular exchange.

REFERENCES

[1] S. Sarkar, "The Stabilizing Effect of Compressibility in Turbulent Shear Flow," *J. Fluid Mech.*, **282**, 163-186, 1995.

[2] G. Balakrishnan, S. Sarkar and F.A. Williams, "Direct Numerical Simulation of Diffusion Flames with Large Heat Release in Compressible Homogeneous Turbulence", AIAA Preprint No. 95-2375, 31st AIAA/ASME/SAE/ASEE Joint Propulsion Conference, San Diego, CA, July 1995.

[3] S. Sarkar, "On Density And Pressure Fluctuations In Uniformly Sheared Compressible Flow," *IUTAM Symposium on Variable Density Low Speed Flows*, Marseilles, July 1996, Kluwer Academic Publishers.

[4] S. Stanley and S. Sarkar, "Simulations of Spatially Developing Two-Dimensional Shear Layers and Jets", *Theor. Comput. Fluid Dyn.*, to appear 1997.

[5] A.L. Sánchez, A. Liñán and F.A. Williams, "A Generalized Burke-Schumann Formulation for Hydrogen-Oxygen Diffusion Flames Maintaining Partial Equilibrium of the Shuffle Reactions", Combustion Science and Technology, to appear, 1997.

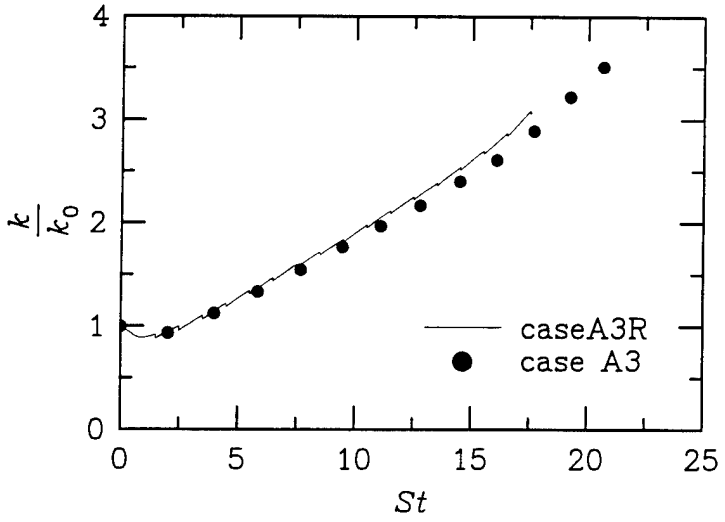

Fig. 1: The temporal evolution of turbulent kinetic energy is compared between the reacting case A3R and nonreacting case A3 (symbols) in compressible, uniform shear flow. Corresponding parameters in both cases are identical.

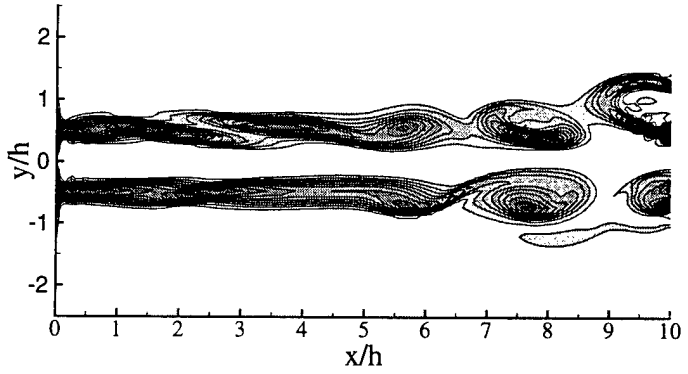

Fig. 2: Contours of z-vorticity on an xy-plane in a three-dimensional plane jet, Re_h=6000

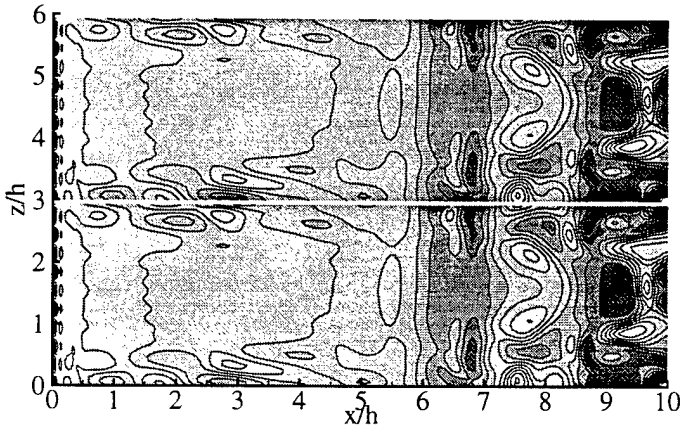

Fig. 3: Contours of z-vorticity on an xz-plane (y/h=0.5) in a three-dimensional plane jet, Re_h=6000

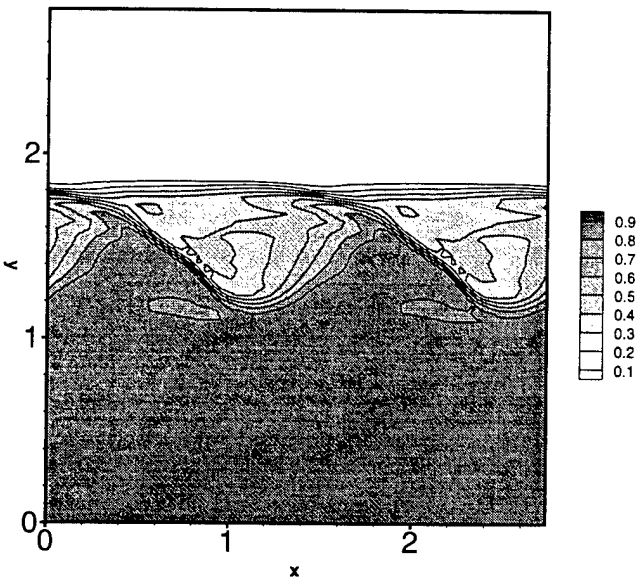

Fig. 4: Scalar isocontours in a three-dimensional, temporally evolving shear layer (t^*=12.95), Re_θ=260.

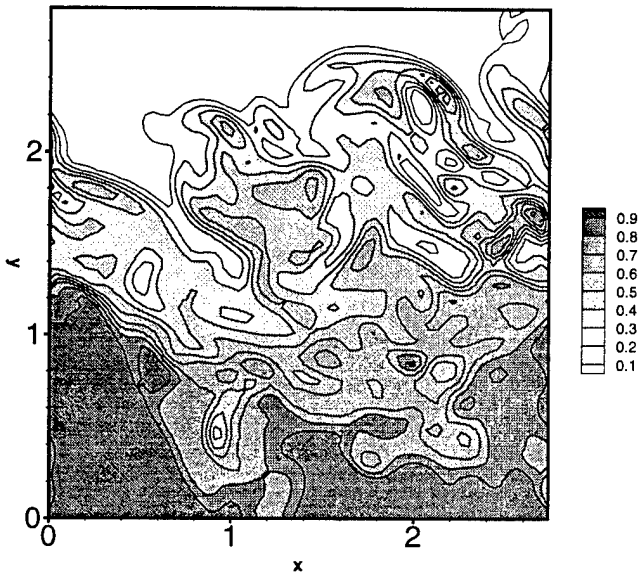

Fig. 5: Scalar isocontours in a three-dimensional, temporally evolving shear layer(t^*=25.47), Re_θ=260.

MECHANISMS OF UNSTEADY FLOW IN SCRAMJET COMBUSTORS

AFOSR Grant F49620-96-1-0435

Principle Investigators: Frank E. Marble and Edward E. Zukoski

California Institute of Technology
Pasadena, California 91125

OVERVIEW

It is suggested that unsteady scramjet disturbances of gasdynamic and combustion origin have a time scale below one millisecond and that disturbances of small magnitude and of this time scale diverge in time, leading to disgorging the inlet shock system, combustion instability, flameout and unacceptable losses due to flow separation associated with shock-boundary layer interaction. The present work is an effort to identify and characterize such small amplitude precursor phenomena.

AUTHORS: Frank E. Marble and Christopher P. Cadou

TECHNICAL DISCUSSION

There exist boundaries in the parameter space of a scramjet which, when crossed, result in gross changes of the flowfield. These boundaries in the operating envelope may be associated with i) a major reconfiguration of the combustor inlet shock structure, ii) a restructuring of the flame spreading and stabilization process that leads to flame-out, and iii) the onset and growth of combustion instability. Between the GALCIT M=2.5 wind tunnel and the Caltech Unsteady Combustion Facility we have an "experimental model" of these three main gasdynamic and combustion phenomena that establish the operating envelope of the scramjet. Since the initiation of the grant, the work has concentrated entirely on the preparation for experiments in the supersonic wind tunnel.

The tunnel working section, Figure 1, has required extensive modifications to accommodate the proposed experiments. The tunnel has a planar working section 32 inches long and 2.5 inches wide with optical side walls. The section height is 2.25 inches in the region where the experiments will be carried out. The upper wall incorporates two new features. The first is the inlet for the 0.4 inch thick low velocity layer modelling the ramp boundary layer ingested into an actual scramjet. A splitter plate separates the high speed flow in the tunnel from the subsonic stream injected parallel to the main flow. Because the tunnel working section operates at less than one tenth atmosphere, this flow may be metered from room air and the pressure at which it enters can be adjusted to minimize the disturbance to the main flow. The second feature is the disturbance generator situated 15.5 inches downstream of the splitter plate. This consists of a small shock tube normal to the wall which injects, through a 0.006 inch slot, an air pulse of controllable magnitude into the subsonic boundary layer. This device is one that we developed and used some years ago at JPL in the investigation of combustion stability boundaries. It's purpose is to provide the disturbance that will initiate the low amplitude precursor which will be measured by the array of high speed piezoelectric pressure transducers. The shock tube is 2.25 inches in diameter and has been sized to provide a pulse of approximately 1.5 ms duration. The diaphragm is a 0.005 mm mylar film which rests on a nichrome wire cross that spans the tube section. As the driving section is pressurized, the diaphragm bulges onto the wires and the tube fires.

Figure 2 shows an x-t diagram for the flow in the shock tube together with a timing diagram for the experiment. The driver section is pressureized to the desired level and the pulse is initiated by applying a voltage to the nichrome wires, rupturing the diaphragm and causing a shock wave to propagate into the tube. A zero-crossing circuit connected to the output of a piezoelectric pressure transducer at the bottom of the tube detects the shock passage and triggers the data acquisition for all pressure transducers installed in the tunnel.

Pressure data is acquired using piezoelectric (PCP Piezotronics) and strain-gauge type (Statham) transducers and two A/D boards housed in a pentium based personal computer. The high speed board (DAS50) records data from the Piezoelectric transducers at an acquisition rate of 1 Mhz. The other A/D board (DAS20) has a maximum single channel conversion rate of 100 kHz and is used to monitor signals from the strain-gauge type pressure transducers (Statham) that have slower response times. These gauges monitor pressures in the driver section of the shock tube, the stagnation chamber for the choked orifice flow meter, and the pressure in the injection port. Both boards are triggered by the output of the zero-crossing circuit.

The tunnel modifications are complete, the data acquisition system has been completed, and the complete system is awaiting its shake-down runs as this is being written.

The following Table I gives information for symbols employed in Figure 1 and Figure 2.

Table I

Instrument Designation and Description

Symbol	Description		
R1	Pressure Regulator	Shock Tube	Diaphragm
SV1	Solenoid Valve	Shock Tube pressurization	
V1	Valve	Shock Tube equalization	Ball Valve
V2	Valve	Air Injection throttling	Gate Valve
PT1	Pressure Transducer	Shock Tube - Statham PA208TC-15-350	Strain Gauge
PT2	Pressure Transducer	Choked Orifice - Statham PA208TC-15-350	Strain Gauge
PT3	Pressure Transducer	Injector entrance - Statham PA208TC-05-350	Strain Gauge
PTS	Pressure Transducers	Tunnel - 7x PCB 112A21	Piezoelectric
		Shock Tube (refl. shock) - 1x PCB 113A21	Piezoelectric
PG1	Pressure Gauge	Shock Tube pressurization	
PG2	Pressure Gauge	Injector pressure	
A/D 1	A/D converter	Tunnel piezoelectric pressure transducers	Das 50
A/D 2	A/D converter	Other pressure and temperature measurements	Das 20
Zero Cross		Zero Crossing Circuit	Custom
Choked Orifice		d = 0.324 in, 0.002 kg/s < Mdot < 0.016 kg/s	Custom
Shock Tube		d = 2.25 in, Ldriven = 9.8 in, Ldriver = 19.7 in	Custom

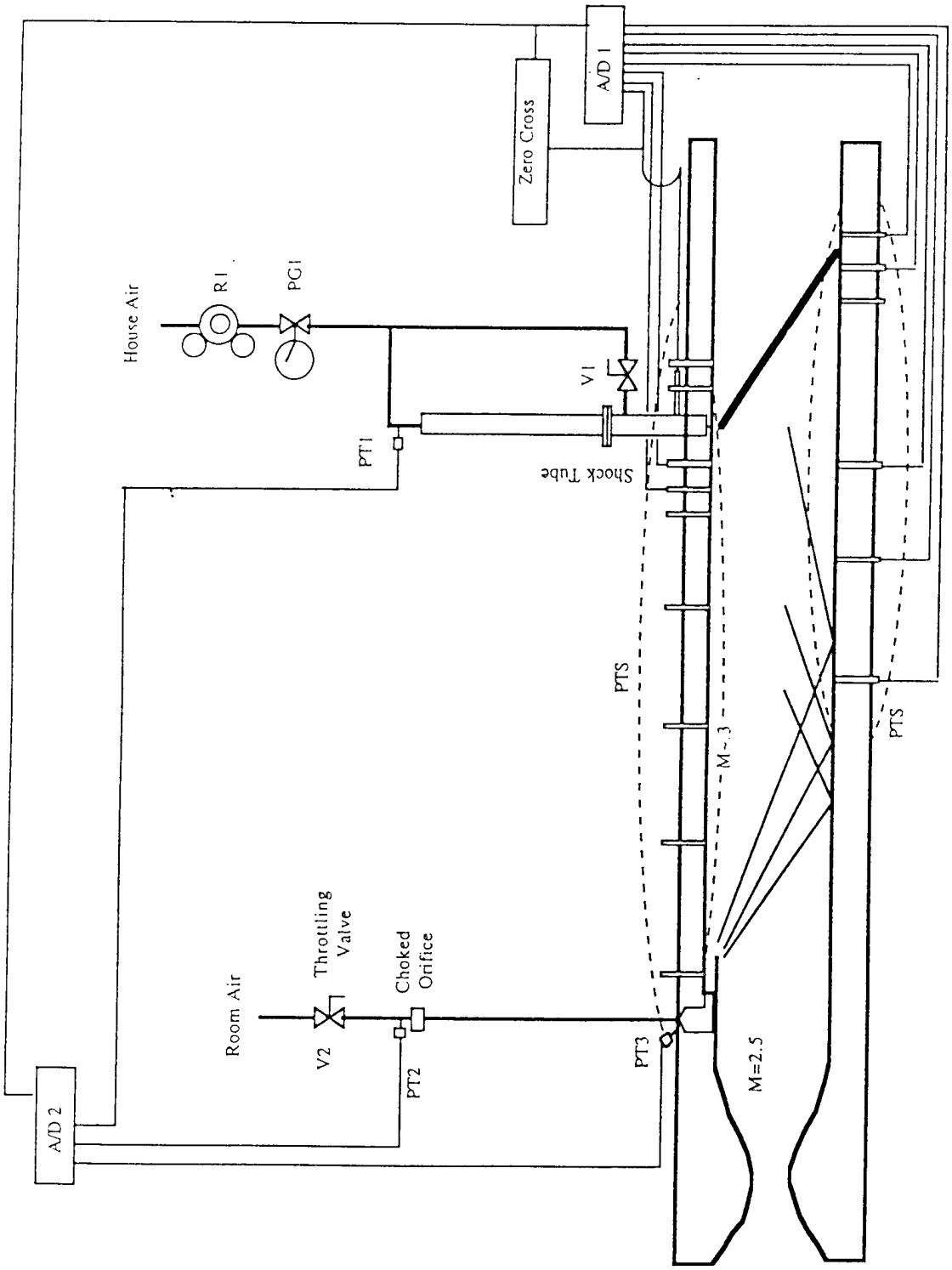

Figure 1.- Sketch of GALCIT 2.5 Mach Number Tunnel Modified for Stability Experiments

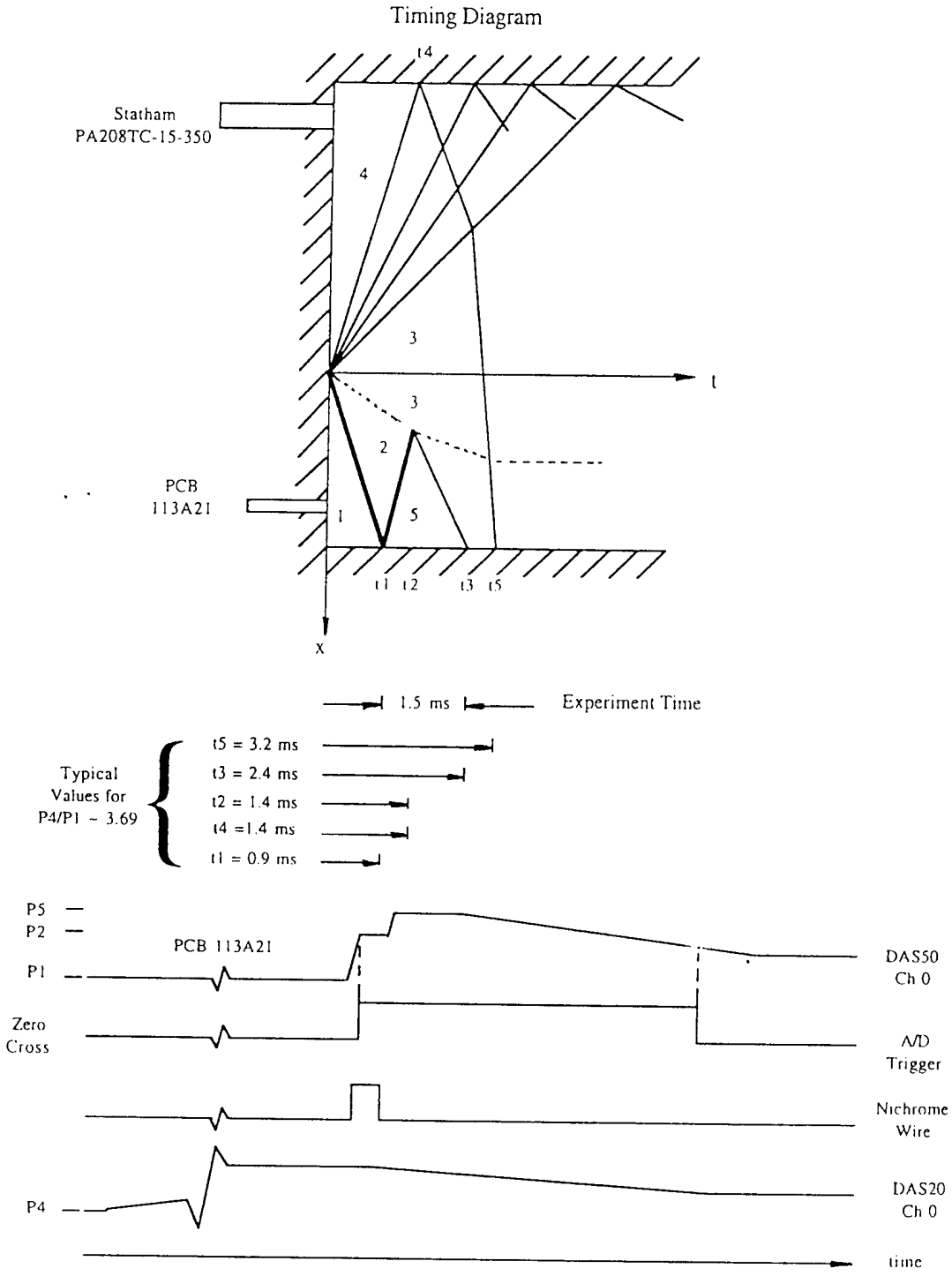

Figure 2.- X-T Diagram for Pulse Generator and Timing Diagram for Experiment

HIGH RESOLUTION MEASUREMENTS OF SUPERSONIC MIXING AND COMBUSTION IN COFLOWING TURBULENT JETS

AFOSR Grant No. F49620-95-1-0115

Werner J.A. Dahm and James F. Driscoll

Gas Dynamics Laboratories
Department of Aerospace Engineering
The University of Michigan
Ann Arbor, MI 48109-2118

Summary/Overview

Supersonic mixing and combustion in coflowing turbulent jets are being investigated and compared with results from compressible mixing layers to identify generic features of supersonic turbulent reacting shear flows. Experiments are used to investigate mixing and combustion in a turbulent fuel jet issuing into a supersonic ($M_\infty = 2.2$) coflowing air stream with stagnation temperatures as high as 600 K. Results are compared with supersonic turbulent mixing layers under investigation elsewhere to discern changes in large-scale and small-scale structure due to compressibility, and identify consequent effects on mixing and combustion properties. Such comparisons with results from compressible mixing layer studies allow identification of compressibility effects that are common to supersonic combustion in turbulent shear flows from those that are specific to the mixing layer only.

Technical Discussion

During the past year we have addressed the effects of density variations due to exothermicity and compressibility on the outer variable scalings of turbulent shear flows. This has resulted in a generalized methodology for extending the scaling laws for nonexothemic flows to account for the effects oif combustion heat release in reacting turbulent shear flows. The methodology is based on an equivalence shown in Fig. 1 between density variations due to heat release and density variations due to simple mixing in nonexothermic flows. The bilinear form of the temperature variation in an appropriately defined mixture fraction based on Cp-weighted mole fraction allows linear extrapolation of either branch past the peak temperature to yield an effective temperature for either stream. The temperature (density) on either branch is then equivalent to simple mixing between this stream at its effective temperature and the other stream at its true temperature. The approach is general and, in the absence of significant buoyancy effects, can be applied to predict the effects of heat release on the outer variable scalings in any turbulent shear flow from the scaling laws for the nonexothermic flow.

Examples comparing predictions from this methodology with data from a variety of flows are shown in Figs. 2-7. In Figs. 2-5, the scaling laws for nonexothermic jets are extended to jet flames by replacing the classical Thring & Newby (1953) and Ricou & Spalding (1961) momentum diameter d^* with the extended scaling parameter $d^+ \equiv [(T_\infty)_{\rm eff}/T_\infty]^{1/2} d^*$. This is seen to correctly predict the effects of heat release on velocity decay, entrainment, and mixing rates. In Fig. 6, the same approach predicts the effects of heat release on planar turbulent jet flames. In Fig. 7, the weak effect of heat release on mixing layer growth rate,s seen in the Hermanson & Dimotakis (1989) data, are predicted by this methodology. Moreover, Fig. 7*b* even shows that small variations that appeared to be "scatter" in these data are correctly predicted by this new scaling extension as effects of stoichiometry and flame temperature.

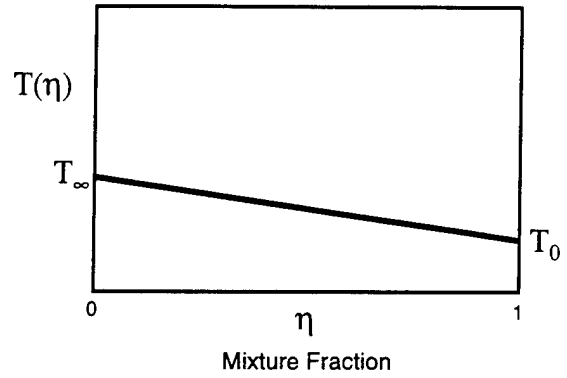

Figure 1*a*. Temperature (density) variation with mixture fraction η in any two-stream nonreacting turbulent flow, showing the linear variation required in the mixture fraction defined from Cp-weighted mole fraction. Straight-line variation such as this is characteristic of simple mixing between two fluid streams. Compare with Figure 1b below.

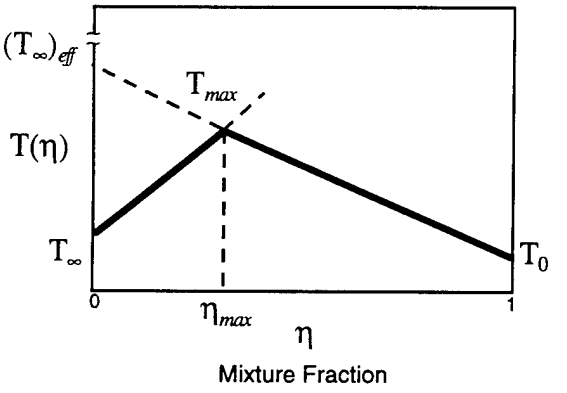

Figure 1*b*. Corresponding temperature (density) versus mixture fraction in two-stream reacting turbulent flows, showing the bilinear variation that results in the Cp-weighted mole fraction η. The linearity of either branch allows density effects on the outer scaling laws for *reacting* flows to be determined from the scaling laws for a *nonreacting* flow with an *effective* ambient fluid temperature $(T_\infty)_{eff}$, obtained by extending the linear (simple mixing) branch to $\eta = 0$ as shown.

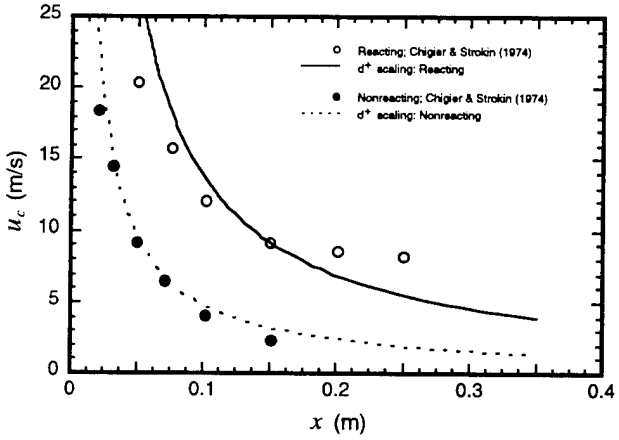

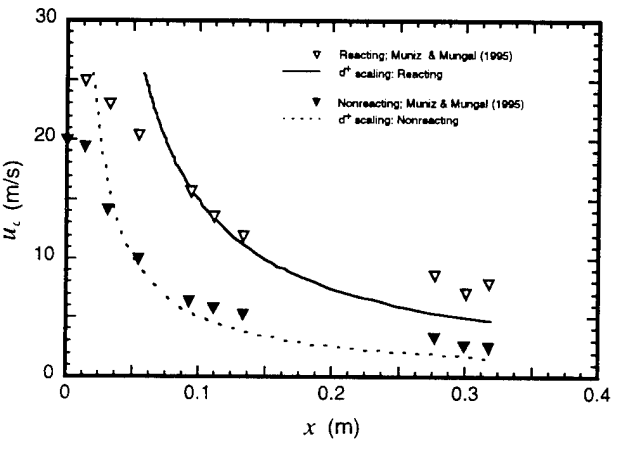

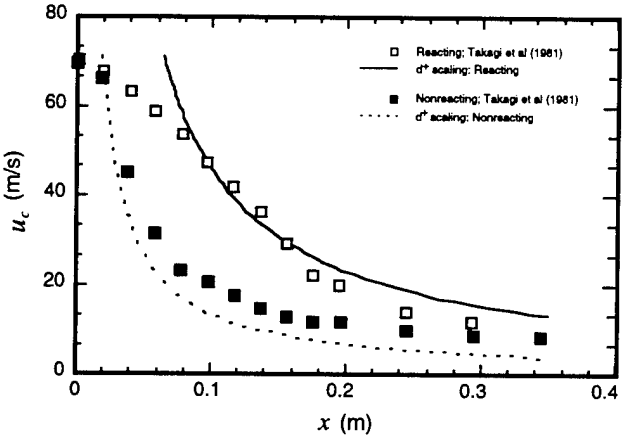

Figure 2. Verification of the extended density scaling methodology in Figure 1 and the resulting scaling parameter d^+ for axisymmetric turbulent jets. Shown are comparisons of measured and predicted centerline velocity decay for reacting turbulent jet flames and nonreacting turbulent jet flows. The resulting new parameter d^+ effectively extends the Thring & Newby (1953) and Ricou & Spalding (1961) momentum diameter d^* to account for density effects in reacting turbulent flows with exothermic heat release. See Figures 3-5 for further validations of d^+. Figures 6-7 show application of this general heat release scaling methodology to the planar turbulent jet flames of Rehm & Clemens (1996) and to the reacting turbulent mixing layer of Hermanson & Dimotakis (1989).

Figure 3. Comparison of centerline velocity decay scaling $u(x)$ for *reacting* and *nonreacting* turbulent jets in terms of the extended density scaling parameter d^+. Data from reacting jet flames are shown with open symbols, while data from nonreacting jets are shown with solid symbols. Note that reacting jet flames and nonreacting jet flows follow the *same* velocity decay scaling in the extended density scaling parameter d^+. Results for other outer flow variables are shown below.

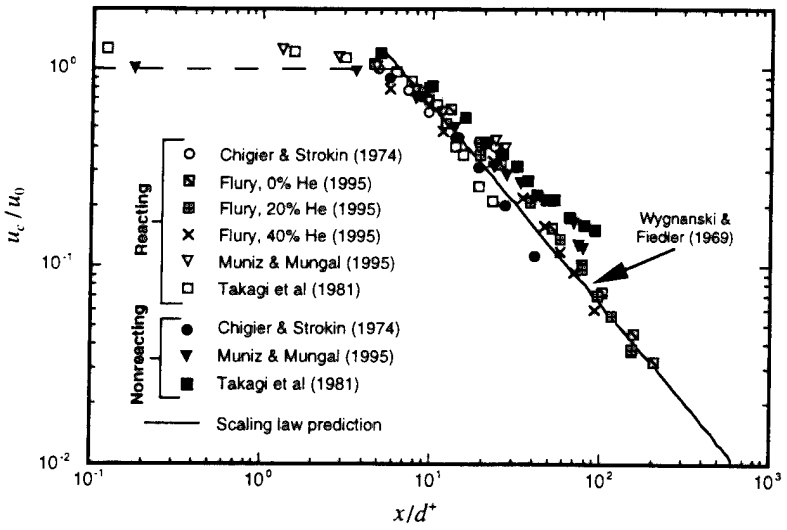

Figure 4. Comparison of outer length scaling $\delta(x)$ for *reacting* and *nonreacting* turbulent jets. Data from reacting jet flames are shown with open symbols; data from nonreacting jets are shown with solid symbols. The present scaling methodology suggests that, in the absence of buoyancy effects, reacting jet flames and nonreacting jet flows should follow the *same* scaling law for the flow width $\delta(x)$. This is confirmed by the data. Figure 5 shows corresponding results for the mixture fraction scaling.

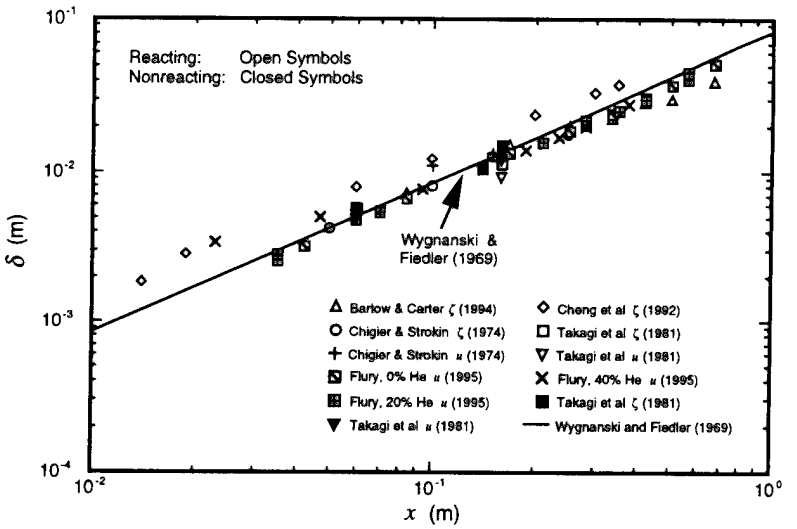

Figure 5. Comparison of centerline mean mixture fraction decay scaling $\zeta(x)$ for *reacting* and *nonreacting* turbulent jets. Data from reacting jet flames are shown with open symbols; data from nonreacting jets are shown with solid symbols. As predicted by the present extended density scaling methodology, both reacting and nonreacting flows show the same mixing rate in the density scaling parameter d^+. Analogous results for planar turbulent jets are shown in Figure 6, and for planar turbulent mixing layers in Figure 7.

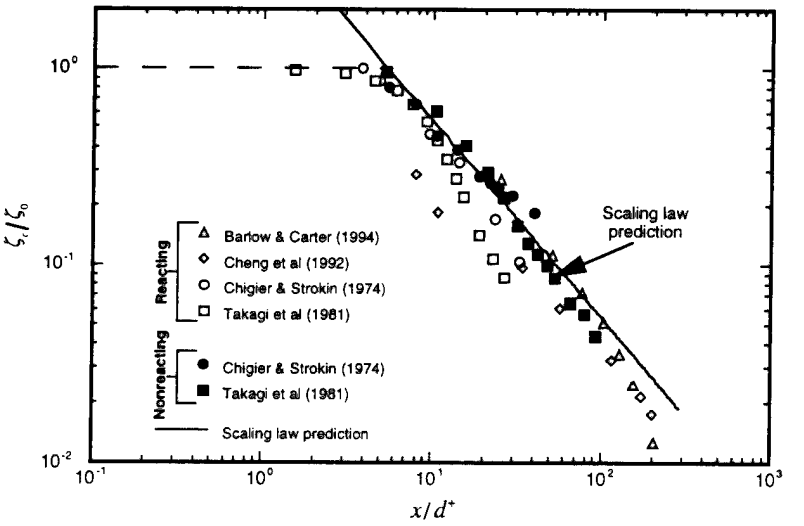

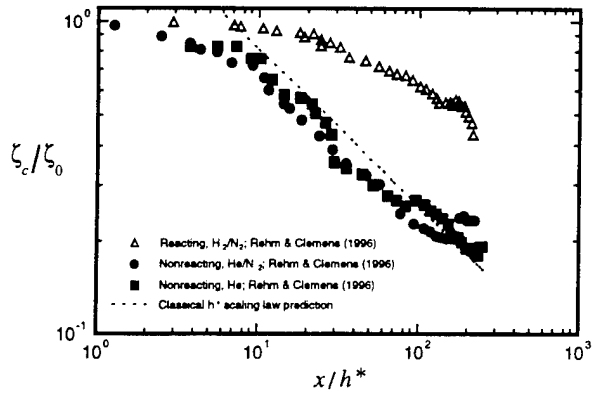

Figure 6*a*. Comparison of centerline mean mixture fraction decay $\zeta(x)$ for nonreacting and reacting *planar* turbulent jets in terms of the classical Thring & Newby (1953) and Ricou & Spalding (1961) density parameter h^*. As can be seen, the classical scaling accounts for density effects in flows without exothermicity, but does not account for density effects due to reaction heat release. The same data (from Rehm & Clemens 1996) are shown below in the present extended density scaling parameter h^+.

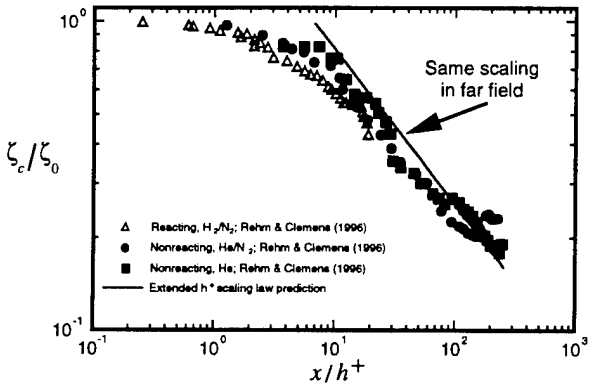

Figure 6*b*. Same data as in Figure 6*a* but plotted in the extended density scaling parameter h^+. Note that, as suggested by the equivalence in Figure 1 *b* on which the present generalized scaling methodology is based, the data from exothermic reacting planar jet flames follow the same scaling, when normalized by h^+, as in nonreacting jets.

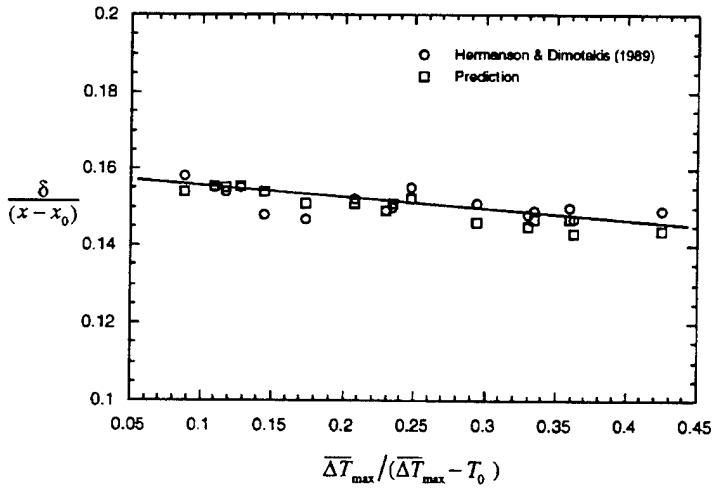

Figure 7*a*. Effects of exothermic heat release on outer flow width scaling $\delta(x)$ in planar turbulent mixing layers. Shown are data [circles] of Hermanson & Dimotakis (1989) compared with predictions [squares] from the present generalized scaling methodology. The extended density ratio parameter s^+ based on the effective high-speed stream temperature $(T_1)_{eff}$ is used in the Dimotakis (1986) scaling laws for nonreacting mixing layers. See also comparisons below.

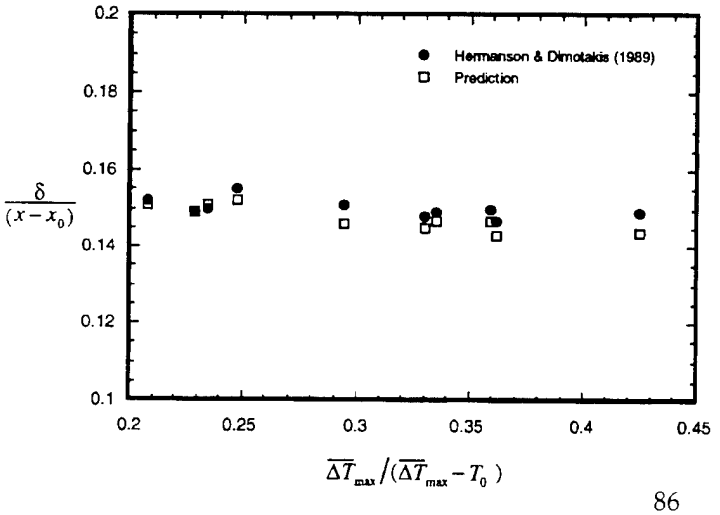

Figure 7*b*. Detailed comparison of predicted outer flow width scaling $\delta(x)$ from the present generalized methodology [open squares] with the mixing layer data of Hermanson & Dimotakis (1989) [solid circles]. Note that the present methodology not only predicts the overall slight reduction in growth rate as seen in Figure 7 *a*, but also predicts the "scatter" seen in the data. This "scatter" is found to result from variations in stoichiometry and maximum flame temperature among the various experimental cases.

Fuel Injection and Mixing in Supersonic Flows

AFOSR TASK 2308BW

Principal Investigators Abdollah S. Nejad
Mark R. Gruber
Raymond P. Fuller

Advanced Propulsion Division
Aero Propulsion and Power Directorate
Wright-Patterson AFB Ohio 45433-7251

SUMMARY/OVERVIEW:

Flush wall sonic injection of fuel into supersonic crossflow is a viable fuel injection technique in scramjet combustors. We have established a research program to study the effects of flow compressibility, injector shape, and geometry on mixing and mixing enhancement in supersonic flows. The objective is to find techniques for mixing enhancement without incurring adverse flow losses. In the first phase of our studies, temporally correlated Rayleigh/Mie scattering images were used to examine the convective characteristics of the large-scale vortex structures associated with sonic transverse fuel injection through circular and elliptic fuel nozzles into a Mach two crossflow. Both compressibility and injector geometry were found to have significant influences on the convective characteristics of the large eddies. The second phase of our effort centered around an experimental program for comparing mixing characteristics of a novel nine-hole injector array and a, ubiquitous NASP driven technology, compression ramp injector. Conventional probing techniques, including species composition sampling, were employed to interrogate the flowfield at several downstream locations. The results indicate that mixing characteristics of the nine-hole array was similar to that of the compression ramp with better total pressure recovery.

TECHNICAL DISCUSSION:

A schematic of the time-averaged transverse injection flowfield appears in Figure 1. This illustration shows the qualitative features of the flowfield in a plane through the jet longitudinal centerline including the three-dimensional bow shock, the separation shock, the jet shock structure, and the upstream and downstream separation zones. The large-scale vortices that are the subject of the present investigation reside at the upper jet boundary. Key participants in the mixing processes that occur in this flow are these large-scale eddies that initiate the turbulent energy cascade which proceeds down to the molecular scales. These large-scale motions are considered important because they actively entrain large quantities of one fluid into another. They also enhance the interfacial strain until the length scales of the motions reach the Kolmogorov scale (Broadwell and Mungal 1991) given by

$$\lambda_\kappa \approx \delta_\omega / \mathrm{Re}^{3/4} \qquad (1)$$

where the local Reynolds number is computed using

$$Re = (\delta_\omega \cdot \Delta U \cdot \rho)/\mu . \qquad (2)$$

Most planar visualization techniques only examine the instantaneous vortex structure of the flowfield. Knowledge of the temporal development of the eddies produces important information about the evolution of these features including their convection characteristics. Fric and Roshko (1989) conducted an experimental study using the smoke-wire visualization technique to examine the development of large-scale structures in the flowfield created by a jet injected into a low speed crossflow. Their photos illustrate the emergence of four types of vortical structures near the injector including vortices that form in the upper edge shear layer. These eddies oriented themselves in such a way as to roll up into the freestream fluid indicating that, in the region near the injector exit, the injectant fluid moved with a higher velocity tangent to the interface than the freestream fluid. However, to date the convective characteristics of these features have not been reported. The large-scale eddies in a planar turbulent shear layer have been studied recently by Bunyajitradulya and Papamoschou (1994) and Papamoschou and Bunyajitradulya (1995) using a two laser/single camera

technique. The authors used planar laser-induced fluorescence (PLIF) of acetone to discern the mixing layer structure. The temporal characteristics of the structures were captured by placing two laser sheets side by side in the flow direction and imaging the fluorescence from both sheets onto a single detector. Measurements of convective velocity were obtained and compared to theoretical predictions. Results from several cases showed significant deviations from theory with the measured convective velocity tending toward the velocity of one of the freestreams. The main problem with this technique is the relatively long time delay (~35-65 ms) between the two laser sheet pulses. This long delay allows the structures to change shape making measurements of displacement somewhat arbitrary.

The momentum thickness variation around the circumference of a small aspect ratio elliptical nozzle produces an asymmetric instability leading to the development of asymmetric vortices (Ho and Gutmark 1987 and Schadow, et al. 1987). The resulting spreading characteristics associated with the major and minor axes develop quite differently and at some point an axis-switch is realized (Gutmark, et al. 1987 and Schadow, et al. 1989). That is, the spread in the minor-axis plane overtakes the spread in the major-axis plane. Previous work by Gruber, et al. (1995) has shown that the axis-switch phenomenon persists in the transverse injection flowfield. It is therefore expected that some structural differences between the circular and elliptical jet plumes are present in the transverse injection cases of this study. The objective of the present work is to gain a better understanding of the temporal characteristics of the large-scale eddies that exist along the jet/freestream interface in the flowfields created by sonic transverse jets injected into a supersonic crossflow. Temporally correlated image pairs are obtained by illuminating the seeded flowfield with two coincident laser sheets and collecting the scattered light onto two intensified charge coupled device (ICCD) cameras, each synchronized to and gated around one of the sheets. The laser sheets are separated by a fixed time difference so that obtaining the structural displacement from one image to the other leads directly to a measurement of the velocity with which the structure convects. Four cases are investigated using two injector geometries (circular and elliptical) fueled by helium and air. These two injectant gases allow the examination of the effects of compressibility on the convection of the large-scale interfacial structures. The experiments were conducted in the supersonic research facility located at the Aero Propulsion and Power Directorate. For the present study, two separate injector geometries were incorporated into the removable test inserts housed within the bottom wall of the test section. The details of the injector designs appear elsewhere (Gruber, et al. 1995 and 1996); Table 1 summarizes the important geometric features of each injector including the eccentricities (e), and the semi-major (a) and semi-minor (b) axes. Each injector was placed at the same streamwise location to ensure that the approaching turbulent boundary layer would be of the same thickness for each case. At the injector location, the ratio of boundary layer thickness-to-effective jet diameter is approximately $d/d_{eff} = 1$. Figure 2 illustrates the double-pulsed imaging system used in these experiments. Two Spectra Physics Nd:YAG lasers (a DCR-4 and a GCR-170) provided the two pulsed laser beams required. The output of these lasers passed through second harmonic generators to produce vertically polarized beams of light at 532 nm (approximately 400 mJ/pulse). This allowed both beams to be combined on a 50% beam splitter optic so that a single optical train could be used to produce the two coincident laser sheets required. A combination of mirrors, prisms, and lenses (150 mm cylindrical and 500 mm biconvex) produced the collimated laser sheets used for illuminating the transverse injection flowfield. The sheets entered through the top window of the test section. Each laser sheet was roughly 50 mm wide and about 200 mm thick at the long focal waist (measured using a photodiode and an oscilloscope).

Two independent camera systems were placed on opposite sides of the test section to collect the scattered light. Each imaging system was composed of a single Princeton Instruments ICCD camera (384 x 578 pixel array) and image acquisition system (controller model ST-130). The cameras were water-cooled and purged with nitrogen to reduce dark current noise. A Nikon UV-Nikkor 105 mm f/4.5 telephoto lens placed in front of each pixel array improved the resolution associated with the pixel area. Careful adjustments of the cameras using a common transparent target led to identical imaging areas with identical resolutions. Each camera was gated around a single laser pulse so that two temporally correlated images of the injector flowfield could be obtained. The time delay between the arrival of the first and second laser sheets was set using a custom built delay controller coupled with a pulse generator. Two 486-based computers running the CSMA image acquisition software collected the images. Further analysis of the images was performed on a Power Macintosh.

The seed particles introduced into the flowfield must rapidly adjust to the turbulent fluctuations so that the collected images may be accurately interpreted. Samimy and Lele (1991) found that accurate particle response for Mie scattering images requires a Stokes number, defined as the ratio of the particle response time scale to the characteristic fluid dynamic time scale, of less than about 0.5. The Stokesian drag law of Melling (1986) and the large-eddy rollover time provide

estimates of the particle response and fluid dynamic time scales, respectively. These estimates are computed as follows:

$$t_p = (1 + 2.76 \cdot Kn) \cdot \rho_p d_p^2 / (18\mu) \quad (3)$$

$$t_{\delta_\omega} = \delta_\omega / \Delta U . \quad (4)$$

Maxwell's relation, given by

$$\ell \cong 1.5\mu / (\rho a), \quad (5)$$

allows estimation of the mean free path and thus calculation of the Knudsen number, assuming a nominal particle diameter is available.

Combustion of silane (SiH_4) injected into the freestream air upstream of the settling chamber was used to produce the particles required for imaging the jet/crossflow interaction. Silane burns with oxygen to form primarily solid silicon dioxide (SiO_2), water, and hydrogen. In lean reactions (less than 30% silane), Hartman, et al. (1987) found that the reaction stoichiometry took the form

$$3\ SiH_4 + 7\ O_2 \rightarrow 3\ SiO_2 + 6\ H_2O + O_2 . \quad (6)$$

Rogers, et al. (1994) characterized the silicon dioxide particle sizes using an electron microscope and found the particles to be in the 0.2 mm diameter range. Using the specific gravity of silicon dioxide (SG ≈ 2.2) along with the expected operating conditions of the jet and freestream flows then yields an estimate of the Stokes number as approximately 0.09. However, this seeding technique did not provide adequate signal levels for acceptable data quality. Thus, the SiO_2 seeding technique was supplemented by operating the facility at ambient temperatures so that the naturally occurring water vapor in the freestream air condensed around the SiO_2 particles. A separate examination of particle size in this combined seeding arrangement using horizontally polarized laser light indicated that the particles were in the Rayleigh scattering regime. Since the incident wavelength in these experiments was 532 nm, an upper bound on the particle diameter resulting from the combined seeding technique is ~0.5 μm yielding a Stokes number of ~0.38. This suggests that even particles with this upper bound diameter accurately follow the turbulent fluctuations.

Estimates of large-scale convection velocity (U_c) and structure convection angle (f) were determined from approximately 30 instantaneous eddies in each case, see Figure 3. It should be emphasized that these measurements are instantaneous in nature (i.e., not ensemble-averaged); thus, scatter in the data is expected, although general trends may be observed. Both of the measured quantities are functions of the streamwise and transverse positions of the individual structure; however, the results that follow are only plotted against the streamwise coordinate. This gives some indication of the behavior of the interfacial eddies as the jet is turned downstream. Figure 4 presents the results of analyzing the image pairs of an air jet issuing from the circular injector. Large-scale convection velocities appear in Figure 4a. This plot contains two velocity reference lines that indicate both the crossflow air velocity (u_∞ = 516 m/s) and the velocity of the sonic air jet at its exit ($u_{e,j}$ = 317 m/s). Also note that error bars are included on all of the measured values of U_c. In this case, the ± 1 pixel uncertainty in the structure's position translates into a convection velocity measurement uncertainty of ± 47 m/s. Initially, near the jet exit (i.e., x/d_{eff} = 0), the eddies that form at the jet/freestream interface convect with velocities that are larger than the exit velocity of the jet. This phenomenon results from the fact that the jet is underexpanded and, as it expands out of the nozzle, the velocity of the jet fluid increases. As the jet turns toward the downstream direction, the convection velocities of the structures generally increase toward the freestream velocity. Several eddies, however, move with velocities close to the jet exit velocity downstream of x/d_{eff} = 1. The estimates of convection angle to the eddy position measurements are presented in Figure 4b. In this plot, the crossflow direction is represented using a solid line at f = 0°. The circles that indicate the actual measured convection angles are bounded by error bars that correspond to the ± 1 pixel accuracy of the measurements. As the air jet exits the circular nozzle, the structural convection angle is relatively high as evidenced by the values plotted near x/d_{eff} = 0. This is expected since the jet's momentum is originally perpendicular to the flow direction of the approaching freestream. With increasing streamwise position, the eddies begin to move at shallower angles to the crossflow direction. At the farthest downstream measurement station, however, the structure convection angles generally remain greater than zero suggesting that the transverse penetration of the jet fluid is still increasing.

Table 1 Injector Geometries

Injector	a (mm)	b (mm)	d_{eff} (mm)	e
Circular	3.18	3.18	6.35	0
Elliptical	6.25	1.63	6.35	0.97

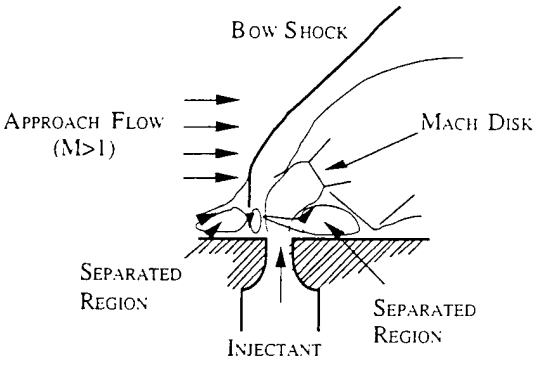

Fig. 1 Transverse injection flowfield schematic

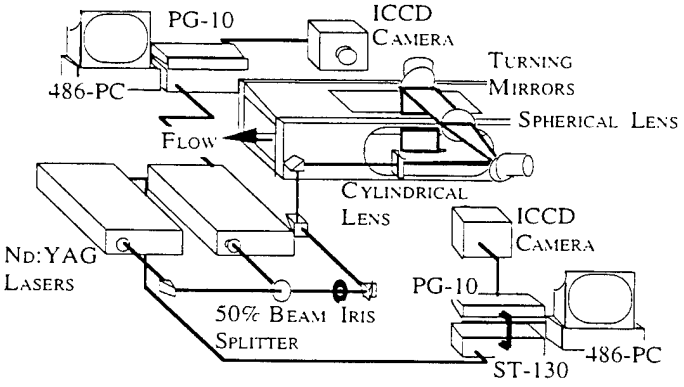

Fig. 2 Schematic of double-pulsed Rayleigh/Mie scattering optical arrangement

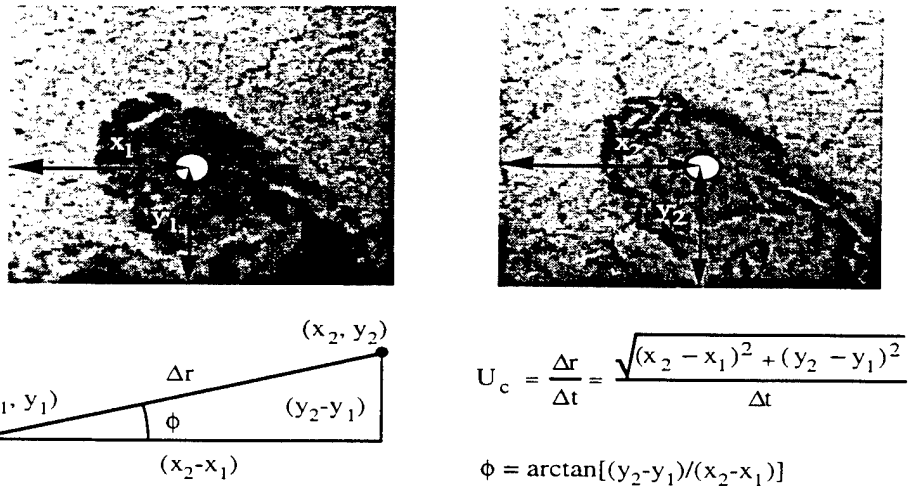

Fig. 3 Large-scale convection velocity and structure convection angle determination

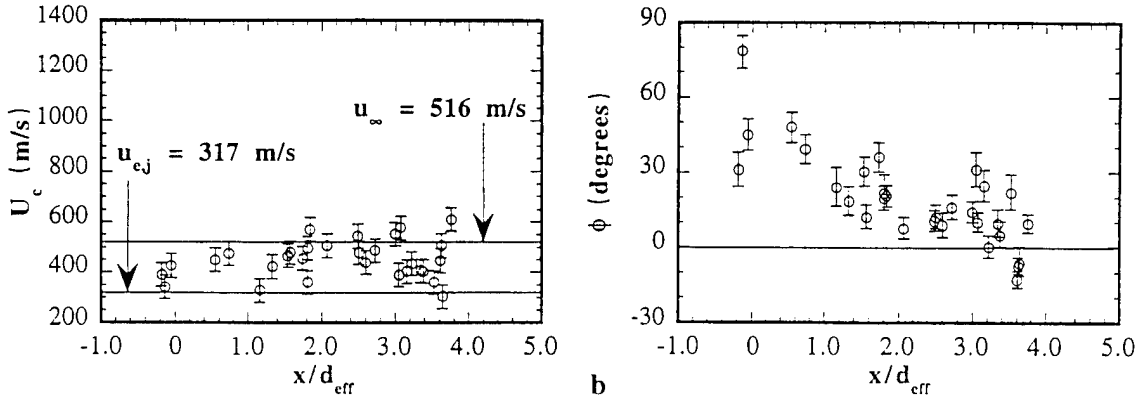

Fig 4. Results for circular injection using air, a) Convection velocity, b) Convection angle distribution

ABSTRACTS OF WORK UNITS NOT PRESENTED AT THE MEETING

MODELING STUDY TO EVALUATE THE IONIC MECHANISM OF SOOT FORMATION

(AFOSR CONTRACT No. F49620-94-C-0014)

Principal Investigator: H. F. Calcote

AeroChem Research Laboratories, Inc.
P O. Box 12 , Princeton NJ 08542

SUMMARY / OVERVIEW

The objective of this program is to examine the role of ions in soot nucleation by modeling the process of ion growth and comparing the results with experiments. Thermochemical and reaction kinetic databases have been completed and are being prepared for submission for publication Some problems with the computer code were identified and corrected. Comparison of characteristic times for soot formation by the ionic and neutral mechanisms shows that the choice of the correct mechanism is important for modeling soot formation in turbulent flow. Consideraton of why a sharply defined soot threshold should exist has led to examination of the cause of the dramatic change in cations at soot threshold. These are the only property of the flame that changes at soot threshold. To date, the best explanation is that soot particles attach electrons, decreasing the rate of cation decay. This still leaves the question: what initiates soot formation at soot threshold.

COMPARISON OF MODEL WITH EXPERIMENT

Problems in the manner in which the computer code handled cation-electron recombination, electron diffusion, electron attachment, and cation-anion recombination have been corrected. Complications with neutral mechanisms in the computer model have been avoided by inputting some experimentally measured neutral species profiles. Because the concentration profile of the initial cation, HCO^+, is unavailable in flames of interest, the chemiionization step $CH^* + O \Rightarrow HCO^+ + e^-$ has been handled by inventing a profile of CH*, chosen to give agreement with experiment. This is the only adjustable parameter. Including a correction for nozzle cooling on measured concentrations limits the portion of the experimental ion profiles that can be analyzed because when the correction is applied upstream of where the ions are formed it interferes with their diffusion, which is greater than originally anticipated. Downstream of where the ions are formed this complication is less critical. Thus to obtain the true ion concentrations the mass spectrometer data are corrected downstream of where the ions are formed and it is assumed that the calculated values are correct upstream, if they agree with mass spectrometer measurement downstream.

The experimental and calculated comparisons at 10 and 15 mm from the burner are compared in Figs. 1 and 2, respectively. At 15 mm the maximum cation concentration has fallen by almost two orders of magnitude and some of the larger cations have begun to level off in concentration. The maximum CH* concentration assumed for this calculation was $1x10^{-6}$ mol fraction and to occur at 8.5 mm above the burner, the width at two decades down was 2.5 mm.

TURBULENCE, SOOT, IONS AND NEUTRALS

Model predictions of soot formation in turbulent combustion will depend strongly on the ratio of the characteristic turbulent times to characteristic chemical times. If the characteristic chemical times for individual steps in the ionic and the neutral mechanisms are grossly different then the choice of mechanism will be critical. That is, the choice of mechanism will determine whether the Damkohler number, D, is <1 or >1. Since soot formation is a complex process, involving a series of events, e.g. formation of precursors, nucleation, growth, and coagulation, each of these characteristic times must be considered with respect to the characteristic time of the relevant elements of the turbulent field. The question must then be raised as to the continuity requirements for soot formation. For example, if D<1 and a chemical soot formation series of events is not completed, will that terminate the soot formation process, or, when that element of flame finds itself in a more favorable environment, will the process continue from where it left off.? The magnitude of the differences between the two basic mechanisms is demonstrated in Table 1 for an acetylene / oxygen flame at 2.67 kPa, equivalence ratio = 3.0..

One observation is that the time to initiate the chemiionization process is much longer than for the neutral process, but that for all other times the ionic process is faster than the neutral process. Thus the ionic mechanism would lend itself to a one or two step simplified mechanism more readily than the neutral mechanism. Clearly, until the appropriate mechanism is better defined, it is necessary to pursue both mechanisms.

SOOT THRESHOLD

In a recent Poster [1] we demonstrated, by a review of the literature, that the only flame characteristics that correlate with the soot threshold are ion concentration and more dramatically the ion identity. There are two questions: are the changes in ion concentration a cause or effect of soot formation, and why does the ion identity change so dramatically? We are considering these questions. Because ionic growth reactions are strongly inversely proportional to temperature, we considered this possibility, because the adiabatic flame temperature, with the exception of acetylene flames, decreases with increasing C / O. A major complication has to be recognized: the flame on which most studies have been is an acetylene flame where soot first appears at C / O =1.0, where it is expected to appear on stoichiometric / thermochemical grounds [2] and where the soot concentration observed is actually less than predicted by thermochemistry. Not only does the adiabatic flame temperature remain essentially constant with C / O for the acetylene flame, but the measured temperature does also, both showing only a small drop at soot threshold. Examination of other flame systems [2] demonstrate that the experimental flame temperature is considerably less than the adiabatic temperature but are also non-variant through the critical C / O for soot formation. No other mechanisms could be dreamed up, except maybe the source of chemiionization, CH*, decays rapidly through soot threshold There seems to be no data available on this point.

It has been proposed previously by a number of people that the change in ions at soot threshold is due to the formation of ions from soot particles. This scenario has now been rejected [3] as unrealistic because of energetic considerations. The possibility that anions were formed at soot threshold removing electrons and thus reducing the rate of cation decay was examined. The concentration of large PCAH is too small and the electron are also too small. We then considered

how electron attachment to soot particles - from heaven (more likely hell) might affect the cation composition. If one could accept the neutral mechanism, that could of course be the source of the soot particles. A recent paper [4] should make acceptance of the neutral mechanism more difficult.

The removal of electrons from a combustion plasma by the addition of particles is a well known process [5], considered e.g. for reducing radar attenuation in rocket exhausts [6] To estimate the possibility that soot particles may remove electrons by electron attachment, thus decreasing the rate of cation - electron recombination, and thus increasing the number of positive ions, the number of electrons attached to soot particles was estimated. The same principles determining the wall potential of a Langmuir probe were used. The rate of electron and cation collision with the particle were calculated, accounting for repulsion of electrons by a negatively charged particle, and the charge on the particle was determined when the two rates were equal. Using available data and estimating it when necessary, the results were as reported in Fig. 3. For all cases, all of the electrons were removed. Thermoelectric emission was not considered, this might change the result a little. With all the of the electrons removed, recombination of cations can now only occur with charged particles and will thus be orders of magnitude slower than with electrons. Soot particles will reduce the rate of cation decay, so that the concentration does not decay as rapidly. This, however does not account for the sudden increase in cation size at soot inception. The cause of a sharp soot threshold is still not defined, but the effect of particle accumulation of electrons must be considered.

ACKNOWLEDGMENTS

Dr. D. G. Keil's contribution to this program is gratefully acknowledged.

REFERENCES

1. Calcote, H. F.and Keil, D. G. "Why a Sharp Soot Threshold" Poster, Twenty Sixth Symposium on Combustion, Milan, Italy 1996, Eastern States Meeting of the Combustion Institute, October 1995

2. Calcote, H. F. and Keil, D. G.,"Thermodynamic Considerations of Soot Formation", Appendix B. AeroChem TP-531, AFOSR Final Report, July 1994

3. Gerhardt, Ph, and Homann, K. H. "Ions and Charged Soot Particles in Hydrocarbon Flames 2. Positive Aliphatic and Aromatic Ions in Ethyne/Oxygen Flames", J. Phys. Chem. 94: 5381-5391 (1990)

4. Calcote, H. F. "In Defense of The Ionic Mechanism of Soot Formation" Eastern Sates Meeting of The Combustion Institute, Hilton Head, South Carolina, December 1996

5. Bradley, D. and Jamel, M. A. M., "Attachnebt if Flame Chemielectrons to Inert, Fine Particles" Comb. Flame 58: 115-124 (1984)

6. Sodha, M. S., Palumbo, C. J. and J. T. Daley "Effect of Solid Particles on Electromagnetic Properties of Rocket Exhausts" Brit. J. Aool. Phys. 14: 916-919 (1963)

Table 1, Comparison Of Characteristic Times for Neutral and Ion Mechanisms For Soot Formation

	Neutral	Ion
To add one carbon atom, μs	2.0	0.67
Number reactions to add 10 Carbon Atoms	11	5
Average time/step, μs	2.3	1.3
Time per step, Min./Max., μs	0.04/11	0.5/4
Initial Step, μs		
$C_3H_3 + C_3H_3 \Rightarrow C_6H_6$	7	
$CH^* + O \Rightarrow HCO^+$		600

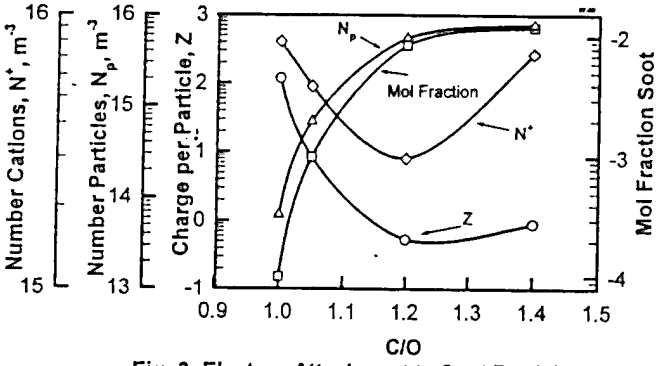

Fig. 3, Electron Attachment to Soot Particles

All Scales are logarithmic

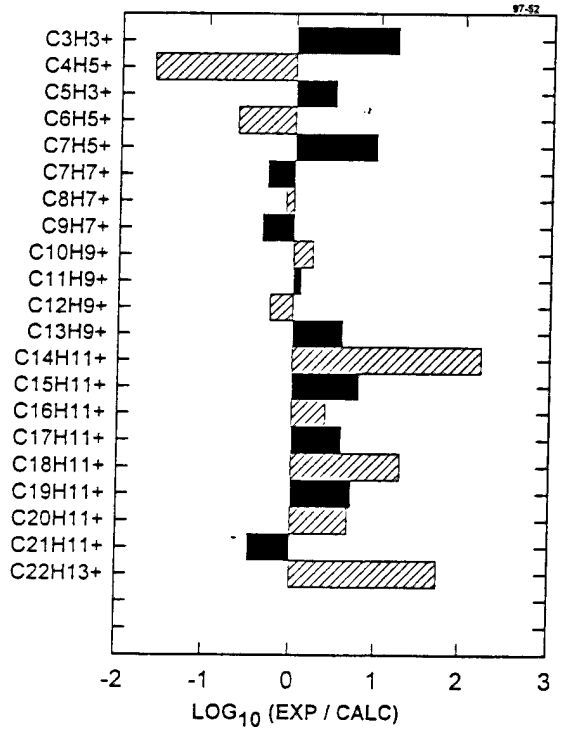

FIG. 1 Comparison of experimental (EXP) and calculated (CALC) Cation Concentrations 10 mm above the burner.

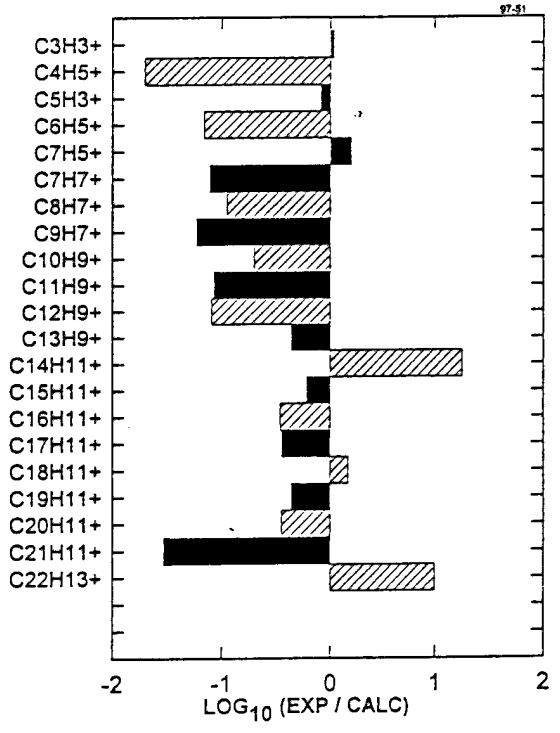

FIG. 2 Comparison of experimental (EXP) and calculated (CALC) Cation Concentrations 15 mm above the burner.

MECHANISMS CONTROLLING SOOT FORMATION IN DIFFUSION FLAMES

AFOSR Contract F49620-94-C-0059

Principal Investigators: Meredith B. Colket and Robert J. Hall

United Technologies Research Center
Silver Lane, E. Hartford, CT 06108

SUMMARY/OVERVIEW:

The overall objectives from this work are to (1) refine and update a pyrolytic model which describes PAH formation; (2) modify and validate an opposed jet diffusion flame code which includes soot formation and radiation and then extend model predictions over a range of flame parameters, and (3) with assistance from Prof. M. Smooke, incorporate the soot formation and radiation models into a code for a coflow laminar, diffusion flame. Experiments and modeling on aromatics will help to minimize discrepancies between known PAH formation rates and those required to explain particle inception rates in flames. Validation (and modification, as necessary) of the flame codes with data from laboratory flames will increase their reliability in predicting sooting characteristics of other hydrocarbon fuels and with varying inlet conditions.

PAH Formation and Modeling

The rate of soot inception has been modeled[1-3] as the rate of formation of selected PAHs. To minimize CPU time, these formation rates are calculated via steady-state expressions based on temperatures and concentrations of selected species. An alternate sequence based upon Refs. 4-5 considers the roles of sequential methyl and propargyl addition to aromatics:

$$C_6H_6 + CH_3 \Leftrightarrow C_7H_8 + H$$
$$C_7H_8 \Leftrightarrow C_7H_7 + H$$
$$H + C_7H_8 \Leftrightarrow C_7H_7 + H2$$
$$C_7H_7 + C_3H_3 \Rightarrow C_{10}H_8 + 2H$$

The advantages of this sequence are that an H-atom does not have to be stripped from the benzene ring to initiate the process and the radical 'recombination' involves resonantly stabilized molecules whose concentrations attain virtually comparable levels of their parents (allene and toluene, respectively) in flames. This sequence has been tested for ethylene flames where its contribution appears to be small. We plan to investigate its possible role in the methane flames in which the concentrations and relative roles (in ring formation) of methyl and propargyl radicals are much greater.

Modeling of Soot Formation in Diffusion Flames

In addition to our ongoing work[1-2] in modeling opposed jet diffusion flames, significant accomplishments in modeling of a coflow, laminar diffusion flame model have been achieved[3]. Most studies in which detailed chemical kinetics are coupled with detailed soot models have been focused on one-dimensional problems. A few recent efforts[6,7] have focused of laminar jet diffusion flames using monodisperse soot formation models with skeletal reaction mechanisms. In this program, we have modified the sectional soot formation model[1,2] for incorporation into a laminar, axisymmetric, diffusion flame in which a cylindrical fuel stream is surrounded by a coflowing oxidizer jet. Computationally, we employ a velocity-vorticity model[8] in which the governing conservation equations are solved with detailed transport and finite rate chemistry submodels to predict local temperatures, species mass fractions, and velocity fields. Appropriate sectional equations are included for describing the different particle size classes with a chemical, diffusive, and convective production balance. These equations, along with surface growth, oxidation, and radiation (from both gas and particulate species) are fully integrated with the governing equations. A discrete solution is obtained on a two dimensional grid by employing Newton's method with adaptive mesh refinement. Unlike some models, in which diffusion in the axial direction is neglected, we considered the fully elliptic problem. Solutions were compared to an experimental study[9] on a methane coflow flame. GRIMech 2.11, with its related thermodynamics but with all NO related reactions deleted, was used for the computations. Benzene formation and destruction steps as previously outlined[1] were added to this kinetic set.

After some examination of initial conditions and the sensitivity of the solution to parameters such as initial fuel and air temperature, local heating near the fuel tube exit, etc., solutions compared well to the general shape and structure of the flame. Temperature is perhaps the single most parameter to model accurately, since it has a direct influence on virtually all other flame properties, i.e., flame width, height, species concentration, soot, etc. A close comparison of our solutions indicates noticeable uncertainties in the temperature predictions, e.g., underprediction by about 100K at nearly all locations along the centerline of the flame. In addition, while the magnitude of peak temperatures are well described, the predicted peak locations were shifted slightly (away from the centerline) compared to the experimental data. Also, the laboratory flame closes to the centerline a few millimeters sooner than the model flame. We believe most of these uncertainties are due to the inability to match the inlet/boundary conditions, although one possible explanation of the low temperatures along the centerline is the lack of including absorption by methane of the energy radiated from the flame front. The inaccuracies in predicted temperatures while relatively small can have a significant effect in predicting other flame properties, particularly soot. Nevertheless, the general agreement overall is good enough that detailed comparisons and interpretations are worthwhile.

Overall, soot volume fractions are underpredicted when using either our soot formation/growth model or that of Ref. 10 by approximately a factor of three. A two dimensional plot of the soot volume fraction is shown in Fig. 1. Inception in our model occurs predominantly along the outer wings, low in the flame, and surface mass growth dominates elsewhere in the flame. In the Fairweather model, significant contributions of acetylene also occur in the top, central portion of the flame where large concentrations of acetylene exist. Benzene concentrations also are large in this region of the flame as seen in Fig. 2. Oxidation occurs both by hydroxyl radicals and by molecular oxygen, but the model indicates that the former by far dominates the oxidation process

Figure 1

Figure 2

Figure 3

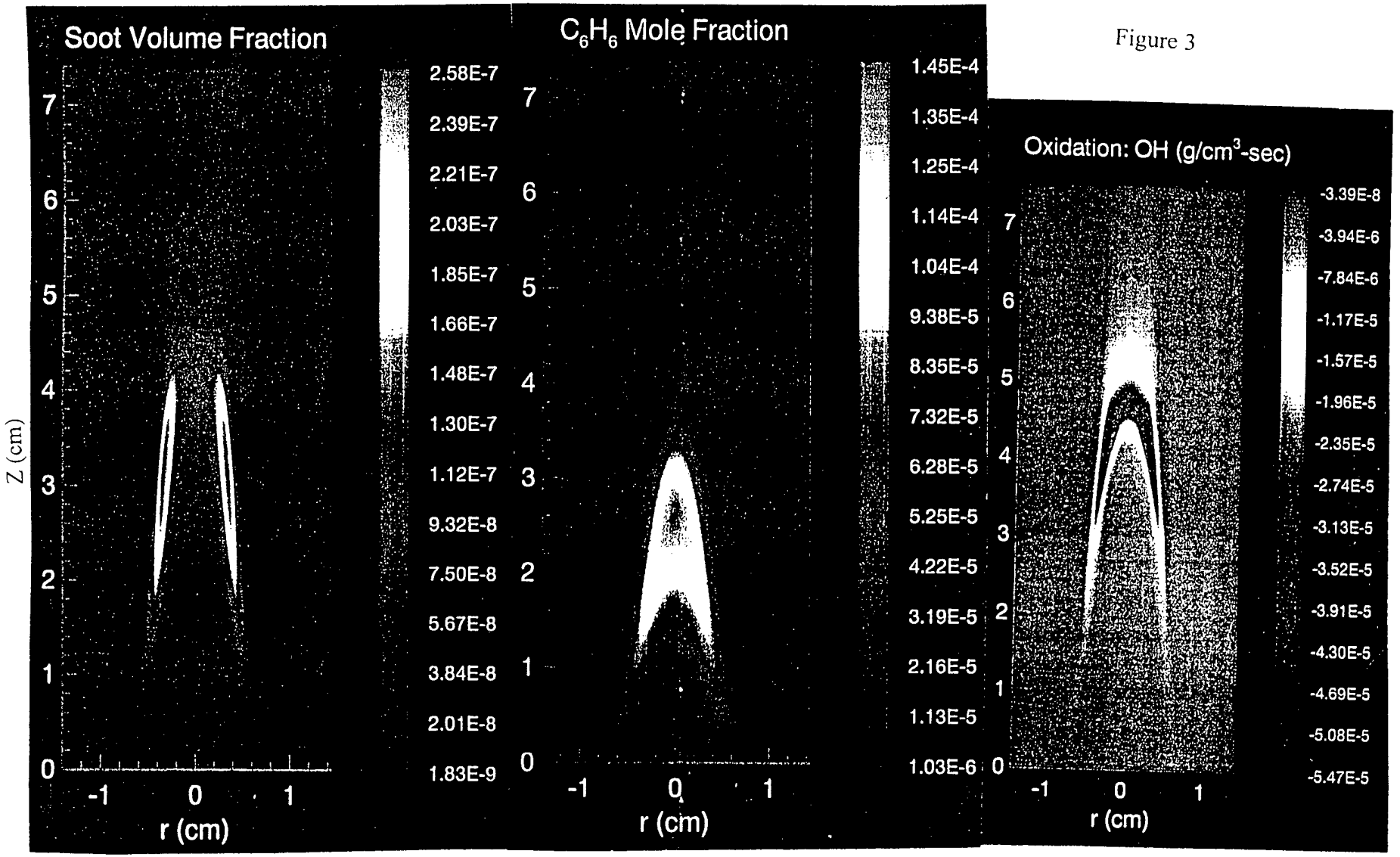

in this methane coflow flame. A plot of the oxidation rate by OH is shown in Fig. 3. This result is consistent with results of Refs. 7 and 11 and cast significant doubt on models which neglect the role of oxidation by OH in such flames. The importance of OH is enhanced in these flames due to superequilibrium levels. In Fig. 4, the calculated OH concentration at a height of 4 cm relative to OH calculated based on several 'equilibrium' or partial equilibrium methods is plotted as a function of radius from the center of the flame. This height and the radial location of about 0.35 cm coincides with the region in which OH oxidation is contributing very significantly to soot destruction. The superequilibrium levels on the order of 10 are clearly dramatic. An analysis assuming local equilibrium conditions could easily lead to a false impression of the relative importance of oxidation by OH.

References

1. R. Hall, M. Smooke, and M. Colket, "Predictions of Soot Dynamics in Opposed Jet Diffusion Flames", Combustion Science and Technology Book Series (1997).
2. M. Smooke, R. Hall, and M. Colket, "Application of Continuation Methods to Soot Formation in Diffusion Flames," to be submitted to Comb. Theory and Modeling, (1997).
3. M. Smooke, C. S. McEnally, L. D. Pfefferle, R. Hall, and M. Colket, "Computational and Experimental Study of a Sooting, Coflow, Laminar Diffusion Flame", submitted (1997).
4. M. Colket, "Rapid Naphthalene Production from Allene and Toluene," presentation to the Eastern States Section of the Combustion Institute, Oct. 16-18, 1995.
5. M. Colket and D. Seery, Twenty-Fifth Symposium (International) on Combustion, The Combustion Institute, Pittsburgh, p. 883 (1995).
6. C. R. Kaplan, C. R. Shaddix, and K. C. Smyth, Combust. Flame, **106**, 392 (1996).
7. I. M. Kennedy, D. R. Rapp, R. J. Santoro, and C. Yam, Combust. Flame, **107**, 386 (1996).
8. A. Ern, C. C. Douglas, and M. D. Smooke, Int. J. of Supercomputer Appl. **9**, 167 (1995).
9. C. S. McEnally and L. D. Pfefferle, Comb. Sci. Tech., **116-117**, 183 (1996).
10. M. Fairweather, W. Jones, and R. Lindstedt, Comb. Flame, **89**, 45 (1992).
11. A. Garo, G. Prado, and J. Lahaye, Combust. Flame, **79**, 226 (1990).

Figure 4. Super-Equilibrium OH in Methane Coflow Flame

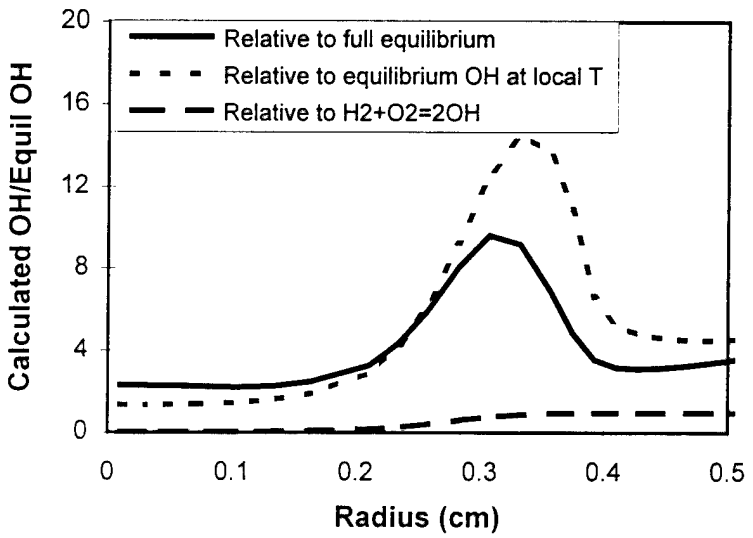

THEORETICAL AND COMPUTATIONAL STUDIES OF NUCLEATION IN SUPERCRITICAL FUELS

(AFOSR GRANT F49620-96-1-0169)

Principal Investigator: Pablo G. Debenedetti

Department of Chemical Engineering
Princeton University
Princeton, NJ 08544-5263

SUMMARY/OVERVIEW

The objective of this research is to improve the basic understanding of how thermodynamics and nucleation kinetics influence the deposit of pyrolytic products from supercritical fuels. To this end, we analyze the equilibrium phase behavior and map the retrograde regions of hexacene and picene in supercritical methylcyclohexane. We also calculate the solid-phase compositions that result from the partial expansion of supercritical methylcyclohexane containing small amounts of dissolved picene and hexacene along both adiabatic and isobaric paths, both in the limit of instant precipitation and taking nucleation kinetics into account. The results suggest that small improvements in the fuel's thermal stability can lead to significant changes in the amount of deposits that can form along fuel transfer lines.

TECHNICAL DISCUSSION

The Statistical Associating Fluid Theory (SAFT) is used to model the fluid-phase equilibria of picene and hexacene in methylcyclohexane (Huang and Radosz, 1990). The semi-empirical SWAP correlation is used to estimate the vapor pressures of picene and hexacene (Smith *et al.*, 1976). An expression based on classical nucleation theory with due account for fluid-phase non-ideality is used to calculate the deposition rate of picene and hexacene from methylcyclohexane (Debenedetti, 1990). A modified MacLeod-Sugden correlation is employed to estimate the surface tension between supercritical methylcyclohexane and picene or hexacene (Rasmussen *et al.*, 1992). Steady, one-dimensional, friction-driven, adiabatic expansions are described by coupling mass, momentum, and energy balances with the SAFT equation of state (e.g., Lele and Shine, 1992; Tom et al., 1994).

Retrograde solubility is a characteristic feature of the phase behavoir of non-volatile solutes dissolved in supercritical solvents (Debenedetti and Kumar, 1988). In the vicinity of the solvent's critical point, the decrease in density upon heating overwhelms the corresponding increase in the solute's vapor pressure, causing the equilibrium solubility to decrease upon isobaric heating (Chimowitz and Pennisi, 1986). This fluid-phase non-ideality can influence the deposition of pyrolytic products from a supercritical fuel.

The retrograde regions of picene and hexacene in supercritical methylcyclohexane are displayed in Figure 1a. Inside the retrograde regions, the solubility of each compound increases

with decreasing temperature. Isobaric cooling trajectories are also depicted. Notice that the cooling trajectories at 110 and 50 bar are respectively above and below the retrograde regions. The 80 bar trajectory passes through both retrograde regions, while the 95 bar trajectory intersects only the hexacene retrograde region. Mixed solute precipitation along each isobar is profoundly affected by the cooling path relative to the boundaries defining the retrograde regions. This is shown in Figure 1b, which illustrates the cumulative composition of solid-phase picene and hexacene precipitating upon isobaric cooling from initially saturated methylcyclohexane. The kinetics of homogeneous nucleation is incorporated into this calculation. The solid-phase composition curves correspond to the isobars depicted in Figure 1a. The non-monotonic composition curve results from the 95 bar trajectory crossing the retrograde boundary of hexacene. This calculation is illustrative of the effects of fluid-phase non-idealities and nucleation kinetics upon the precipitation of solutes from a near-critical solvent.

The situation is quite different when the expansion is adiabatic. In this case, changes in temperature and pressure inside the retrograde region have competing effects: depressurization favors precipitation, but cooling favors dissolution. Both equilibrium and kinetic calculations, however, show that during adiabatic expansions through the retrograde region, depressurization overwhelms cooling. Thus, in contrast to the dramatic effect of retrograde behavior on mixed-solute precipitation and solid-phase composition during isobaric cooling, retrograde effects are negligibly small during adiabatic expansions.

Figure 2a shows attainable nucleation rates of picene from an adiabatically-expanding, one-dimensional flow of supercritical methylcyclohexane. The fluid-phase concentration of picene in methylcyclohexane at the onset of adiabatic expansion is varied from saturation to 60% of saturation. Decreasing the mole fraction of picene in methylcyclohexane prior to adiabatic expansion lowers the supersaturation and results in a significant decrease in the nucleation rate. For example, lowering the starting picene mole fraction from saturation to 90% of saturation yields a four-order of magnitude decrease in the nucleation rate at the outlet of the expansion device. Using the nucleation rates displayed in Figure 2a, the cumulative moles of picene that precipitate during the adiabatic expansion are calculated and shown in Figure 2b. A decrease in the starting picene mole fraction of just 10% (from saturation to 90% of saturation) lowers the amount of precipitated picene by a factor of 400. This result suggests that slight improvements in the thermal stability of fuels may significantly lower the deposition of pyrolytic deposits.

Figure 3 shows the calculated cumulative solid-phase composition during the mixed precipitation of picene and hexacene from adiabatically-expanding methylcyclohexane. Hexacene nucleation generally dominates the solid-phase deposition despite the presence of greater amounts of picene in methylcyclohexane; equilibrium calculations predict that the solubility of picene is 10 times greater than that of hexacene. If the initial amount of hexacene in solution is varied as in Figure 2b, the ratio of solid-phase picene to hexacene changes dramatically. For example, by lowering the starting hexacene mole fraction to 50% of its saturation value, the ratio of solid-phase picene to hexacene increases by almost 8 orders of magnitude.

Both the equilibrium and kinetic aspects of mixed-solute precipitation from a near-critical solvent have been modeled under conditions relevant to the deposition of pyrolytic products from a supercritical fuel, methylcyclohexane. Pronounced changes in the composition of the solid deposit result from small changes in the mixture's initial composition. This suggests that small improvements in the fuel's thermal stability can profoundly influence the formation of deposits.

REFERENCES

Chimowitz, E. H., Pennisi, K. J. (1986) *AIChE Journal*, 32, 1665.

Debenedetti, P. G., Kumar, S. K. (1988) *AIChE Journal* , 34, 645.

Debenedetti, P. G. (1990) *AIChE Journal*, 36, 1289.

Huang, S. H., Radosz, M. (1990) *Ind. Eng. Chem. Res.*, 29, 2284.

Lele, A., Shine, A. D. (1992) *AIChE Journal*, 38, 742.

Rasmussen, D. H., Liang, M. -T., Esen, E., Abbleby, M. R. (1992) *Langmuir*, 8, 1868.

Smith, G., Winnick, J., Abrams, D. S., Prausnitz, J. M. (1976) *The Canadian Journal of Chemical Engineering*, 54, 337.

Tom, J.W., Debenedetti, P.G., Jérome, R. (1994) *J. Supercrit. Fluids*, 7, 9.

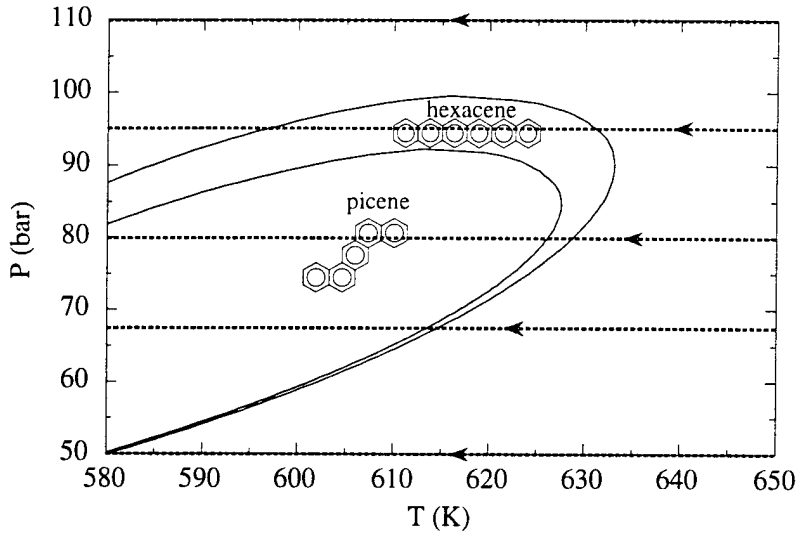

Figure 1a: Retrograde regions of hexacene and picene in supercritical methylcyclohexane. Inside the retrograde region, the solubility decreases with increasing temperature at constant pressure. Also shown are several isobaric cooling paths.

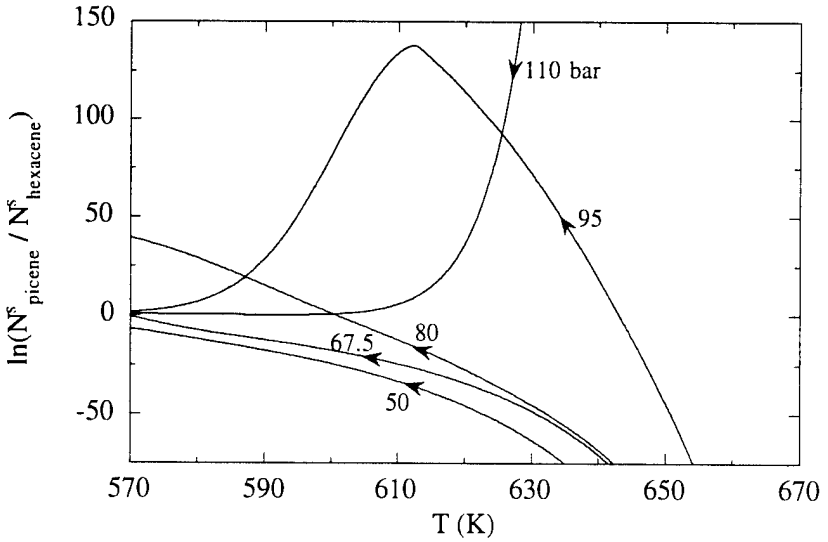

Figure 1b: Calculated cumulative solid-phase compositions (N_s = number of moles in the solid) corresponding to the cooling paths shown in Figure 1a, for initially saturated solutions.

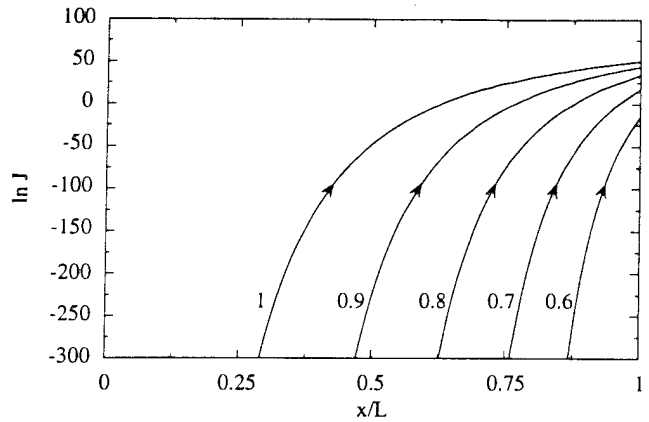

Figure 2a: Attainable picene nucleation rate profiles during partial adiabatic expansions of methylcyclohexane in one-dimensional, choked flow (L/D = 400). J is the nucleation rate (nuclei/m^3· sec). Initial conditions: 610 K, 90 bar. Labels on the curves indicate the ratio of actual-to-equilibrium mole fraction of picene in the starting solution.

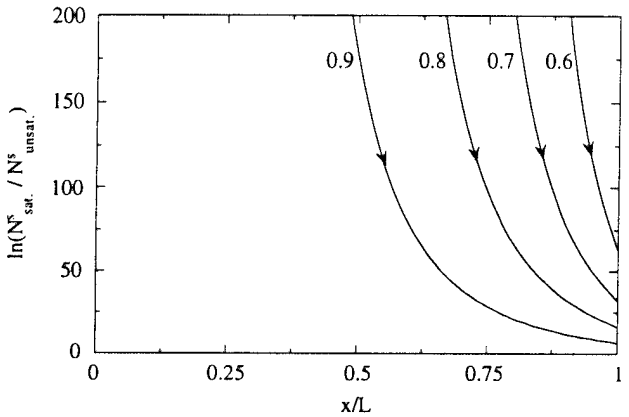

Figure 2b: Cumulative moles of picene that precipitate during partial adiabatic expansions of methylcyclohexane as per Figure 2a. Ratio of precipitated material when the starting mixture is saturated [N_s(sat.)] to that which precipitates when the ratio of actual to saturated mole fraction of picene in methylcyclohexane at the start of the expansion is the number on the curves [N_s(unsat.)].

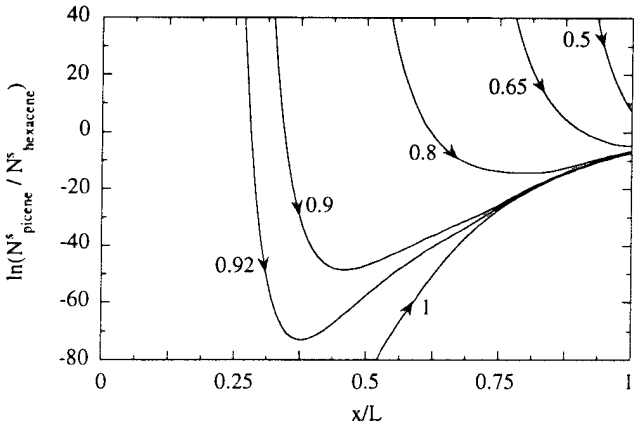

Figure 3: Cumulative composition of solid-phase picene and hexacene formed during partial one-dimensional adiabatic expansions of supercritical methylcyclohexane initially at 610 K and 90 bar, in an expansion device with L/D = 400. The initial mixture is saturated with picene, and the initial ratio of actual-to-equilibrium mole fraction of hexacene is indicated on each curve.

ADVANCED SUPERCRITICAL FUELS

AFOSR Task # 93WL002

Principal Investigators: Tim Edwards, Jim Gord, Mel Roquemore

USAF Wright Laboratory
WL/POSF Bldg 490
1790 Loop Rd N
Wright Patterson AFB, OH 45433-7103

SUMMARY/OVERVIEW:

Increases in aircraft and engine performance are increasing the heat load being transferred into an aircraft's primary coolant--the fuel. This research is aimed at understanding the limitations of operation of fuel heated to 480 °C (900 °F) and beyond. Important issues are expected to be thermal stability, heat transfer/flow instabilities, and injection/combustion properties.

TECHNICAL DISCUSSION

One of the most significant barriers to the successful use of high temperature fuels is expected to be thermal stability. For fuels heated to temperatures in excess of 1000 °F, thermal stability is defined as the tendency to avoid fuel system deposits from both oxidative and pyrolytic reactions [1]. Much of the effort in the first part of this research focused on thermal-oxidative deposition, where advances in understanding of thermal stability could be directly transitioned to the 6.2 JP-8+100 program [2,3]. The understanding of thermal-oxidative fuel behavior has come about through experimental efforts in several research devices: the Quartz Crystal Microbalance (QCM) [4-7], the Near-Isothermal Flowing Test Rig (NIFTR) [8-12], and the Phoenix Rig flow reactor [13-15]. Diagnostic research has also been performed, resulting in a better understanding of fuel oxidation and deposition processes [16]. Fiber-optic probes have been partially successful in Raman probing of high temperature fuels. In ultrafast laser probing of reactions in supercritical solvents, the effects of local density augmentation were very system dependent [17,18]. Using these devices to understand fuel oxidation and deposition behavior has led to the development of improved models for these processes in fuels [19-22,15]. Notable work has been done on understanding how additives modify the oxidation processes in a manner that reduces deposition

The study of pyrolytic deposition has become a recent focus of this research [1]. A general understanding of the effects of fuel type, temperature, and residence time has been obtained. Fuel/material compatibility is also being studied under pyrolytic conditions [23]. The pyrolytic behavior of fuel, where cracking reactions have altered the character of the fuel itself, has some interesting parallels to soot formation. As shown in Figure 1, cracking of the fuel at high temperatures and pressures produces light gases such as hydrogen, methane, ethylene, etc. As shown in Figure 2 (from Lefebvre), the conventional model for soot formation involves fragmentation of fuel molecules as well as condensation to form larger hydrocarbons. Note the

similarity between this process and the processes that occur in a high temperature fuel system. In this second case, as shown in the bottom half of Figure 2, the soot precursor reactions are proceeding inside the fuel system itself, prior to injection into the combustor. Note the differences in conditions: combustor--pyrolysis proceeds in an oxidizing atmosphere at temperatures up to ~2700 °F, high temperature fuel--pyrolysis proceeds in the absence of oxygen ($\Phi=\infty$) at temperatures of 1000-1500 °F. There has been considerable progress in chemical kinetic modeling of soot formation recently, partially funded by AFOSR. It seems like an opportune time to look for the synergies that could come from applying these soot models to fuel system precombustion reactions. Indeed, a relationship between fuel pyrolysis, PAH formation, and fuel system deposits have been described by workers at Princeton [24], as well as Wright Laboratory. A complete model would include fuel system catalytic endothermic reactions [25], as well as detailed kinetic modeling of the combustor [26]. This general fuel "combustion" model, that includes fuel system reactions as well as combustion, seems a reasonable goal for the AFOSR research community.

The combustion behavior of high temperature fuels is also an issue, especially for hypersonic vehicles [27,28]. At WL, the Well-Stirred Reactor [29] is being used to examine the effect of fuel cracking processes on blowout behavior. Initial indications are that cracking the fuel improves its blowout performance, relative to the original fuel. Ignition delay is also important.

REFERENCES

[1]. Edwards, T., Atria, J., "Thermal Stability of High Temperature Fuels," prepared for ASME Turbo Expo, Orlando, FL, June 1997.

[2]. Heneghan, S. P., Zabarnick, S., Ballal, D. R., Harrison, W. E., "JP-8+100: Development of a Thermally Stable Jet Fuel," ASME Journal of Energy Resource Technology, Vol. 118, pp. 170-179, 1996.

[3]. Heneghan, S. P., Zabarnick, S., Ballal, D. R., "Designing High Thermal Stability Jet Fuels for the 21st Century," Proceedings of the 31st Intersociety Energy Conversion Engineering Conference, pp. 486-493, 1996.

[4]. Zabarnick, S., Zelesnik, P., Whitacre, S. D., "Silver Corrosion and Sulfur Detection Using a Quartz Crystal Microbalance with Silver Electrode Surfaces," Ind. Eng. Chem. Research, Vol. 35(8), pp 2576-2580, 1996.

[5]. Zabarnick, S., Whitacre, S., "Aspects of Jet Fuel Oxidation," prepared for ASME Turbo Expo, Orlando, FL, June 1997.

[6]. Zabarnick, S., Zelesnik, P., Grinstead, R. B., "Jet Fuel Deposition and Oxidation: Dilution, Materials, and Oxygen Effects," ASME Journal of Engineering for Gas Turbines and Power, Vol. 188, pp. 271-277, 1996.

[7]. Beaver, B., DeMunshi, R., Heneghan, S. P., Whitacre, S. D., "Model Studies Directed at the Development of New Thermal Oxidative Stability Enhancing Additives for Future Jet Fuels," Energy & Fuels, Vol. 11, pp. 396-401, 1997.

[8]. Pickard, J. A., Jones, E. G., "Kinetics of the Autoxidation of Jet A Fuel," Energy & Fuels, Vol. 10, pp. 1074-1077, 1996.

[9]. Jones, E. G., Balster, L. M., "Impact of Additives on the Autoxidation of a Thermally Stable Aviation Fuel," Energy & Fuels, Vol. 11, May-June 1997

[10]. Jones, E. G., Balster, L. M., Balster, W. J., "Thermal Stability of Jet A Fuel Blends," Energy & Fuels, Vol. 10, pp. 509-515, 1996.

[11]. Balster, L. M., Balster, W. J., Jones, E. G., "Thermal Stability of Jet Fuel/Paraffin Blends," Energy & Fuels, Vol. 10, pp. 1176-1180, 1996.

[12]. Balster, W. J., Jones, E. G., "Effects of Temperature on Formation of Insolubles in Aviation Fuels," prepared for ASME Turbo Expo, Orlando, FL, June 1997.

[14]. Ervin, J. S., Williams, T. F., Heneghan, S. P., Zabarnick, S., "The Effects of Dissolved Oxygen Concentration, Fractional Oxygen Consumption, and Additives on JP-8 Thermal Stability," ASME 96-GT-132, June 1996, to be published in ASME Journal of Engineering for Gas Turbines and Power, 1997.

[15]. Ervin, J. S., Williams, T. F., Katta, V. R., "Global Kinetic Modeling of Aviation Fuel Fouling in Cooled Regions in a Flowing System," Industrial and Engineering Chemistry Research, Vol. 35, pp. 4028-4032, 1996.

[16]. Vilimpoc, V., Sarka, B., "Application of Photon-Correlation Spectroscopy and Quartz-Crystal Microbalance to the Study of Thermally Stressed Jet Fuel," Industrial and Engineering Chemistry Research, Vol. 36, pp. 451-457, 1997.
[17]. Bunker, C. E., Rollins, H. W., Gord, J. R., Sun, Y.-P., "Efficient Photodimerization Reaction of Anthracene in Supercritical Carbon Dioxide," submitted to Journal of Physical Chemistry.
[18]. Bunker, C. E., Sun, Y.-P., Gord, J. R., "Time-Resolved Studies of Fluorescence Quenching in Supercritical Carbon Dioxide: System Dependence in the Enhancement of Bimolecular Reaction Rates at Near-Critical Densities," submitted to Journal of the American Chemical Society.
[19]. Ervin, J. S., Zabarnick, S., Williams, T. F., "Modeling of Jet Fuel Oxidation at Low Temperatures," AIAA Paper 97-0272, Jan. 1997
[20]. Zabarnick, S., "Chemical Kinetic Modeling of Antioxidant Chemistry for Jet Fuel Applications," submitted to Industrial and Engineering Chemistry Research.
[21]. Ervin, J. S., Heneghan, S. P., "The Meaning of Activation Energy and Reaction Order in Autoaccelerating Systems," prepared for ASME Turbo Expo, Orlando, FL, June 1997.
[22]. Ervin, J. S., Zabarnick, S., "Computational Fluid Dynamic Simulations of Jet Fuel Oxidation Incorporating a Pseudo-Detailed Chemical Kinetics Model," submitted to Industrial and Engineering Chemistry Research, May 1997.
[23]. Edwards, T., "Research in Hydrocarbon Fuels for Hypersonics," paper presented at 1996 JANNAF Propulsion and Joint Subcommittee Meeting, Dec. 1996.
[24]. Stewart, J. F., Brezinsky, K., Glassman, I., "Formation of Polycyclic Aromatic Hydrocarbons in Supercritical Methylcyclohexane," paper presented at 11/96 AIChE Annual Meeting, Chicago, IL, Nov. 15, 1996. See also AFOSR Contractor's Meeting abstracts.
[25]. Zhou, N., Krishnan, A., "A Numerical Model for Endothermic Fuel Flows with Heterogeneous Catalysis," AIAA Paper 96-0650, Jan. 1996.
[26]. Lindstedt, R. P., Maurice, L. Q., "A Detailed Chemical Kinetic Model for Practical Aviation Fuels," AIAA Paper 97-2836, July 1997.
[27]. Tishkoff, J. M., Drummond, J. P., Edwards, T., Nejad, A. S., "Future Direction of Supersonic Combustion Research: Air Force/NASA Workshop on Supersonic Combustion," AIAA Paper 97-1017, Jan. 1997.
[28]. Edwards, T., "Combustion Challenges of High Temperature Jet Fuels," paper 204a presented at AIChE Annual Meeting, Nov. 15, 1996, Chicago, IL.
[29]. Blust, J. W., Getz, M. G., Zabarnick, S., "Probe Design Optimization for the Well-Stirred Reactor," AIAA Paper 97-0907, Jan. 1997

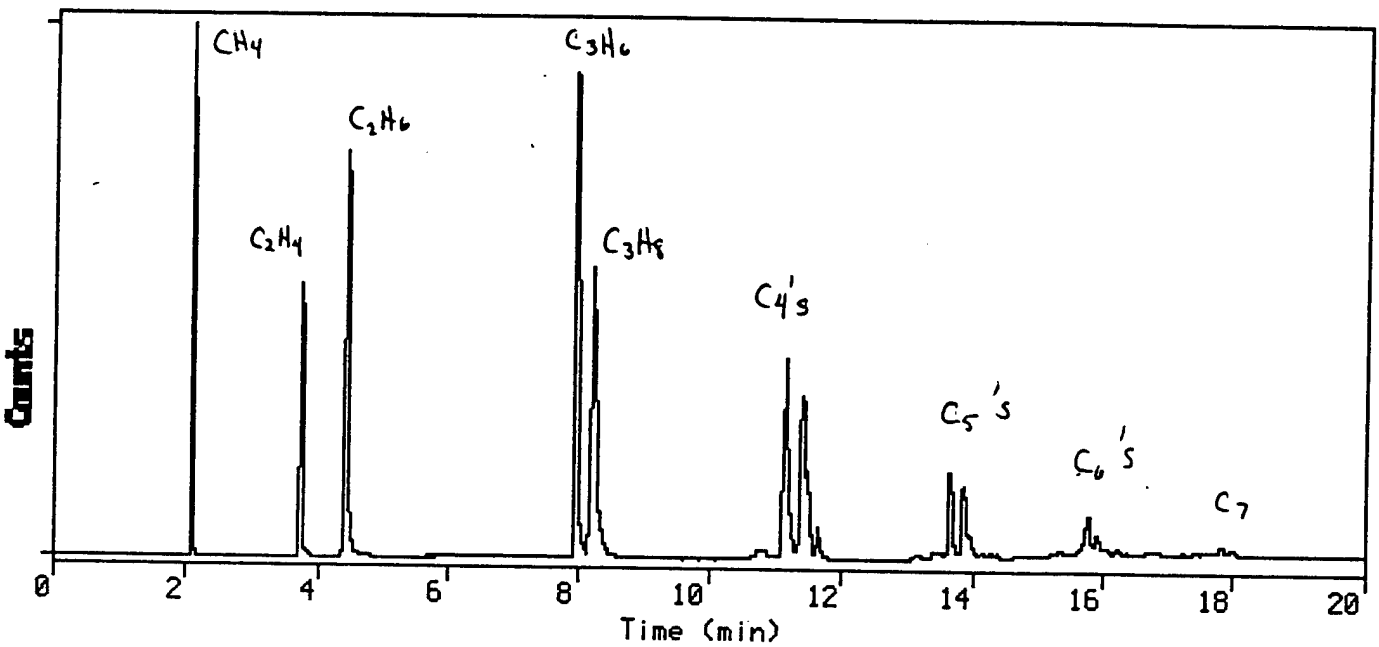

Figure 1. Analysis of light gases from fuel cracking at 560 °C. Concentrations range from 18 mol% CH_4 and C_2H_6 down to 0.1% C_7, with 2.7% H_2 measured separately.

Soot - Fuel System Deposit Analogy

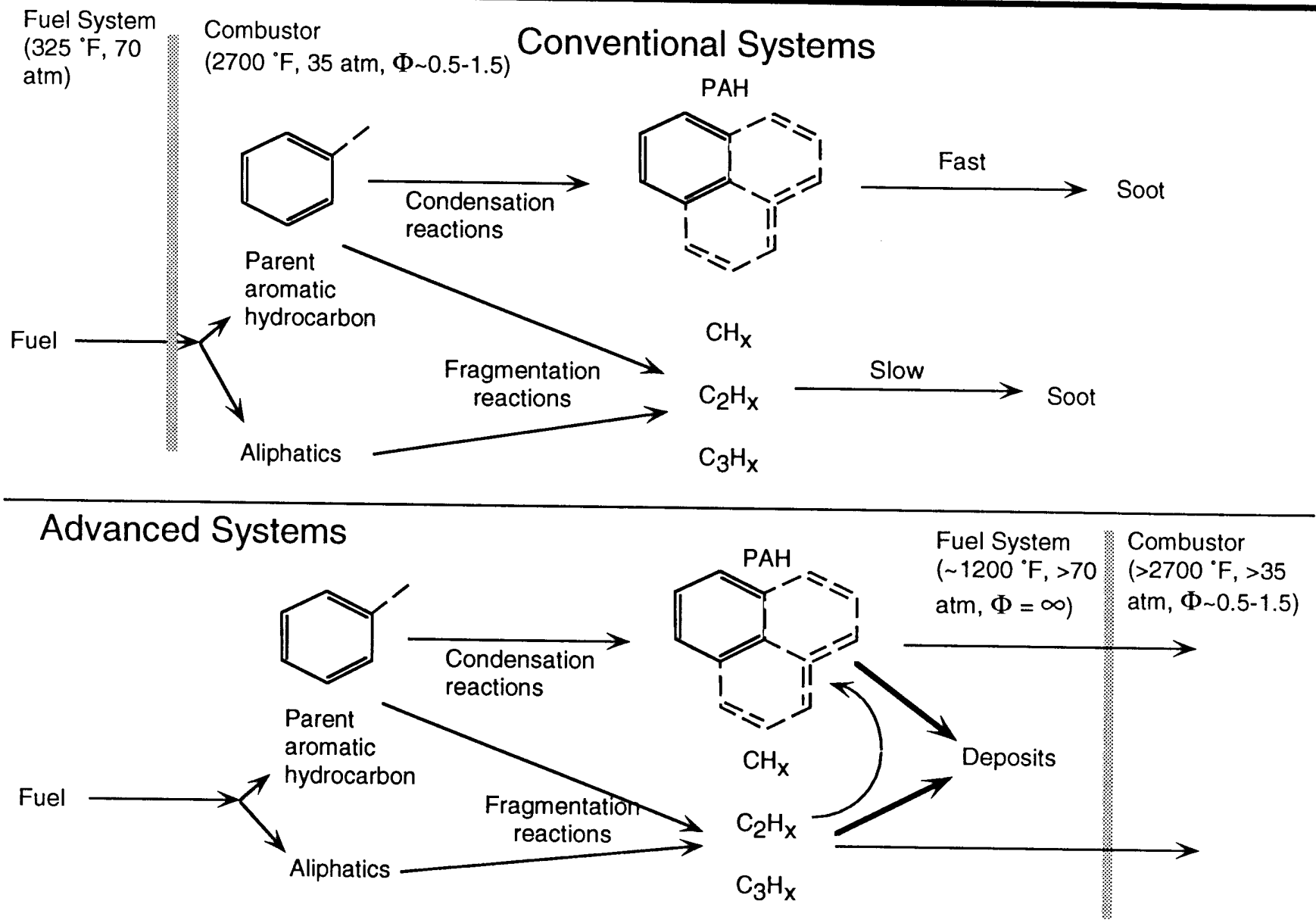

SECONDARY BREAKUP AND TURBULENCE INTERACTIONS OF DROPS

(AFOSR Grant No. F49620-95-I-0364)

Principle Investigator: G.M. Faeth

Department of Aerospace Engineering
3000 FXB Building
The University of Michigan
Ann Arbor, Michigan 48109-2118

SUMMARY/OVERVIEW:

Secondary breakup and turbulence interactions of drops are being studied because they are important phenomena of dense sprays. Past work on secondary drop breakup has yielded information about the regimes and outcomes of drop deformation and breakup when effects of liquid viscosity are small; current work is addressing secondary drop breakup as a rate process and effects of liquid viscosity, both of which become important for practical combusting sprays at elevated pressures. Measurements are made using pulsed holography of drops during breakup caused by shock-wave disturbances.

Work on turbulence interactions of drops is concentrating on effects of turbulence generation when relative velocities between the drops and the continuous phase are large because these conditions generally are encountered in practical sprays. Past studies suggest that particle-generated turbulence involves a stochastic combination of randomly-arriving drop (particle) wakes and have resolved some features of wakes. Current work is emphasizing direct measurements of turbulence generation properties in homogeneous particle-laden flows as well as measurements of particle wake properties in turbulence generated by homogeneous particle-laden flows.

TECHNICAL DISCUSSION:

Introduction. Past work has demonstrated the importance of secondary drop breakup and turbulence generation in sprays (Faeth 1990, 1995, 1996, 1997; Ruff et al. 1989, 1991, 1992, 1995; Tseng et al. 1992a, b, 1996; P.-K. Wu and coworkers 1991, 1992, 1993, 1995, 1995a, b); therefore, these phenomena are being studied as discussed in the following:

Secondary Drop Breakup. Studies of liquid atomization have shown that drops produced by primary breakup are unstable to secondary breakup; therefore, secondary breakup is being studied during this part of the investigation. Findings during the first phase of the investigation established the drop size and velocity distributions as jump conditions after secondary breakup but also highlighted the need to treat secondary breakup as a rate process. In view of these findings, current work is emphasizing the properties of secondary breakup as a rate process, see Chou et al. (1997a, b) for initial results.

Measurements began with the shear breakup regime for conditions where effects of liquid viscosity are small, e.g., Weber numbers, We=80-800 and Ohnesorge numbers, Oh<0.1. It was found that shear breakup involved transient and steady-state regimes. Then information about drop formation rates, drop sizes and drop velocities as a function of time during shear breakup was measured and successfully correlated using phenomenalogical theories (Chou et al. 1997a, b).

Subsequent attention turned to the bag breakup regime for conditions where effects of liquid viscosity are small, e.g., We=15-30 and Oh<0.1. It was found that roughly 44% of the initial drop mass became part of the bag with the remainder forming the basal ring at the upstream end of the bag. Drops resulting from breakup of the bag are nearly monodisperse and have diameters of roughly 0.42% of the initial drop diameter while drops formed from the basal ring are more variable in size due to the presence of node drops and have average diameters of roughly 30% of the initial drop diameter. The net effect of this behavior is for drop sizes after bag breakup to satisfy the universal root normal distribution with an SMD of 36% of the initial drop diameter. Thus, an early correlation of bag breakup properties based on extending shear breakup results by Hsiang and Faeth (1992) proves to be simply fortuitous over a narrow test range as illustrated in Fig.1. Other measurements established drop velocities and rates of drop breakup as a function of time during bag breakup, results for the rate of drop breakup are illustrated as a function of time, normalized by the characteristic breakup time, t/t^*, in Fig. 2. In this case, breakup of the bag occurs by progressive Rayleigh breakup over a short period of time while breakup of the basal ring occurs abruptly due to passive Rayleigh breakup. Similar to shear breakup, the temporal properties of bag breakup were successfully correlated based on phenomenalogical theories.

Current work is addressing two issues concerning the temporal properties of secondary breakup: (1) the properties of the multimode breakup regime at low Ohnesorge numbers, We=30-80 and Oh<0.1, and (2) the properties of secondary breakup at larger Ohnesorge numbers, which is important for combusting sprays at elevated pressures.

Turbulence Generation. Turbulence generation by drops controls the turbulence properties of dense sprays (Faeth 1990, 1995, 1996; Ruff et al. 1991, 1992). Drop-generated turbulence differs from conventional turbulence because mean velocity distributions in randomly-arriving drop wakes contribute to the velocity field of the turbulence; however, stochastic analysis seems promising for describing this flow (Parthesarathy and Faeth 1990; Mizukami et al. 1992). Past work has developed information about particle wake properties at large turbulence intensities and has demonstrated promising agreement with existing measurements of turbulence generation properties (J.-S. Wu and Faeth 1993, 1994, 1995). Current work is emphasizing turbulence generation by particles in gases, and particle wake properties in low relative turbulence intensity particle-generated turbulence, in order to address conditions representative of practical spray combustion processes.

A major problem of past measurements of turbulence generation has been limited accuracy due to very large turbulent intensities because the measurements were carried out in nearly stagnant baths. Thus a new counterflow wind tunnel illustrated in Fig. 3 was developed to avoid this problem. The arrangement consists of upflowing air with a large contraction ratio to yield a low turbulence intensity flow, and down flowing particles through a series of dispersing screens to provide controlled levels of particle-generated turbulence. Flow properties are measured using high-and low-resolution laser velocimetry for gas and particle velocities, respectively.

The test apparatus has been developed successfully and measurements of turbulence generation properties are currently in progress. Some typical results are illustrated in Fig. 4, where turbulence intensities normalized by the relative velocities of the particles are plotted as a function of the dissipation factor (a dimensionless parameter proportional to the rate of dissipation of kinetic energy due to particle motion). In addition to present measurements at different upflow velocities, U_u, and a particle diameter, d=1.0 mm, the earlier measurements in stagnant baths of Mizukami et al. (1992) and Parthesarathy and

Faeth (1990) are shown. The agreement between the three sets of measurements is excellent and supports stochastic predictions of flow properties based on Campbell's theorem that suggest relative turbulence intensities are proportional to the square root of the dissipation factor but are relatively independent of particle size.

Current work is undertaking measurements of turbulence generation properties (e.g., moments, probability density functions, correlations, spectra and integral scales) for various particle sizes and dissipation factors, and using these results to evaluate the stochastic turbulence-generation theory.

REFERENCES:

Chen, J.-H. and Faeth, G.M. (1997) 36th Aero. Sci. Meeting, submitted.
Chou, W.-H., Hsiang, L.-P. and Faeth, G.M. (1997a) Int. J. Multiphase Flow, in press.
Chou, W.-H., Hsiang, L.-P. and Faeth, G.M. (1997b) AIAA Paper No. 97-0709.
Faeth, G.M. (1990) Twenty-Third Symposium (International) on Combustion, The Combustion Institute, Pittsburgh, 1315-1352.
Faeth, G.M. (1995) Proceedings of the Second International Conference on Multiphase Flow (A. Serizawa, T. Fukano and J. Bataille, ed.), Kyoto University, Kyoto, Vol. 1, CO-1 to CO-16.
Faeth, G.M. (1996) Twenty-Sixth Symposium (International) on Combustion, The Combustion Institute, Pittsburgh, 1593-1612.
Faeth, G.M. (1997) Proceedings of the Workshop on Fuels with Improved Fire Safety, National Academy of Sciences, Washington, in press.
Faeth, G.M., Hsiang, L.-P. and Wu, P.-K. (1995) Int. J. Multiphase Flow, 21, 99-127.
Hsiang, L.-P. and Faeth, G.M. (1992) Int. J. Multiphase Flow, 18, 635-652.
Hsiang, L.-P. and Faeth, G.M. (1993) Int. J. Multiphase Flow, 19, 721-735.
Hsiang, L.-P. and Faeth, G.M. (1995) Int. J. Multiphase Flow, 21, 545-560.
Mizukami, M., Parthasarathy, R.N. and Faeth, G.M. (1992) Int. J. Multiphase Flow, 18, 397-412.
Parthasarathy, R.N. and Faeth, G.M. (1990) J. Fluid Mech., 220, 485-537.
Ruff, G.A., Sagar, A.D. and Faeth, G.M. (1989) AIAA J., 27, 901-908.
Ruff, G.A., Bernal, L.P. and Faeth, G.M. (1991) J. Prop. Power, 7, 221-230.
Ruff, G.A., Wu, P.-K., Bernal, L.P. and Faeth, G.M. (1992) J. Prop. Power, 8, 280-289.
Ruff, G.A., and Faeth, G.M. (1995) Prog. Astro. Aero., 166, 263-296.
Tseng, L.-K., Ruff, G.A. and Faeth, G.M. (1992a) AIAA J., 30, 1537-1544.
Tseng, L.-K., Wu, P.-K. and Faeth, G.M. (1992b) J. Prop. Power, 8, 1157-1166.
Tseng, L.-K., Ruff, G. A., Wu, P.-K. and Faeth, G.M. (1996) Prog. Astro Aero, 171, 3-30.
Wu, J.-S. and Faeth, G.M. (1993) AIAA J., 31, 1448-1455.
Wu, J.-S. and Faeth, G.M. (1994) AIAA J., 32, 535-541.
Wu, J.-S. and Faeth, G.M. (1995) AIAA J., 33, 171-173.
Wu, P.-K. and Faeth, G.M. (1993) Atom. Sprays, 3, 265-289.
Wu, P.-K. and Faeth, G.M. (1995) Phys. Fluids A, 7, 2915-2917.
Wu, P.-K., Ruff, G.A. and Faeth, G.M. (1991) Atom. Sprays, 1, 421-440.
Wu, P.-K., Tseng, L.-K. and Faeth, G.M. (1992) Atom. Sprays, 2, 295-317.
Wu, P.-K., Miranda, R.F. and Faeth, G.M. (1995a) Atom. Sprays , 5, 175-196.
Wu, P.-K., Hsiang, L.-P. and Faeth, G.M. (1995b) Prog. Astro. Aero., 169, 247-279.

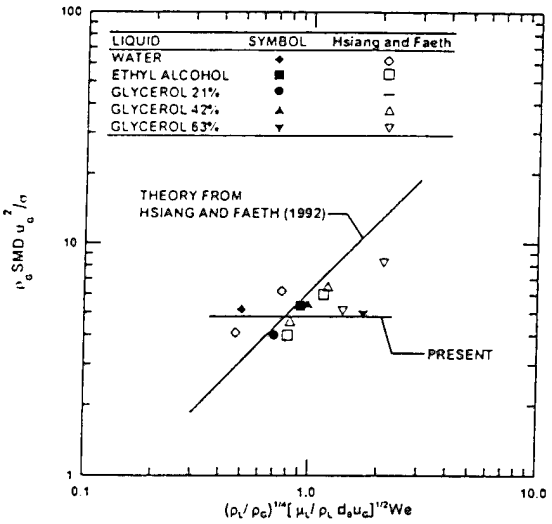

Fig.1 Correlation of SMD for bag breakup.

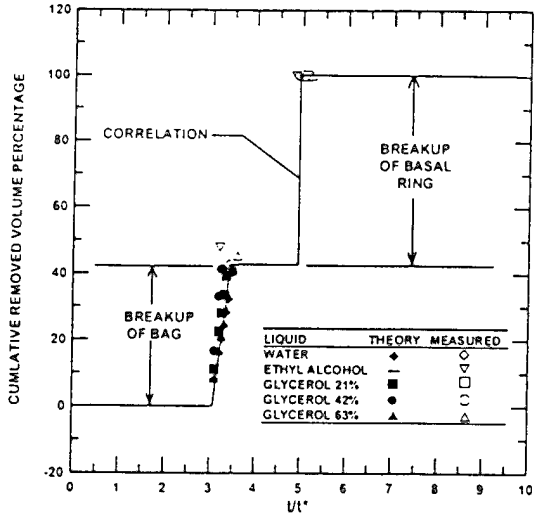

Fig.2 Mass removed as a function of time for bag breakup.

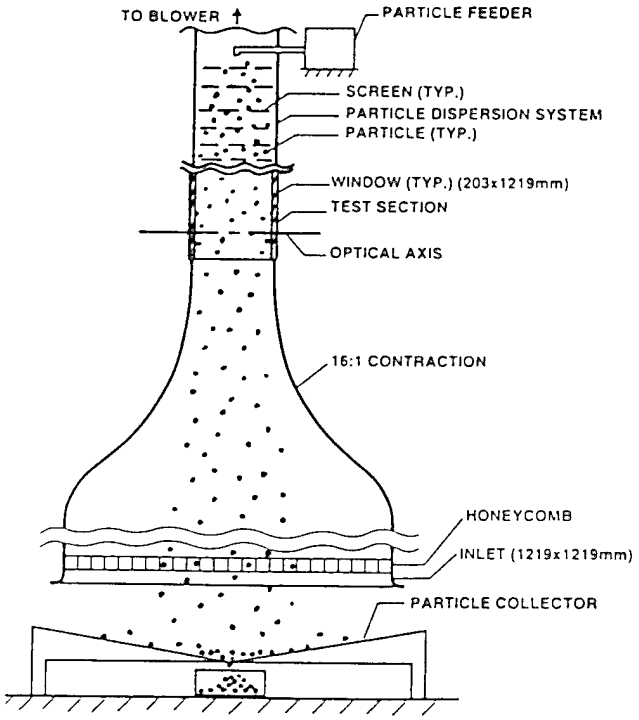

Fig.3 Apparatus for turbulence generation studies.

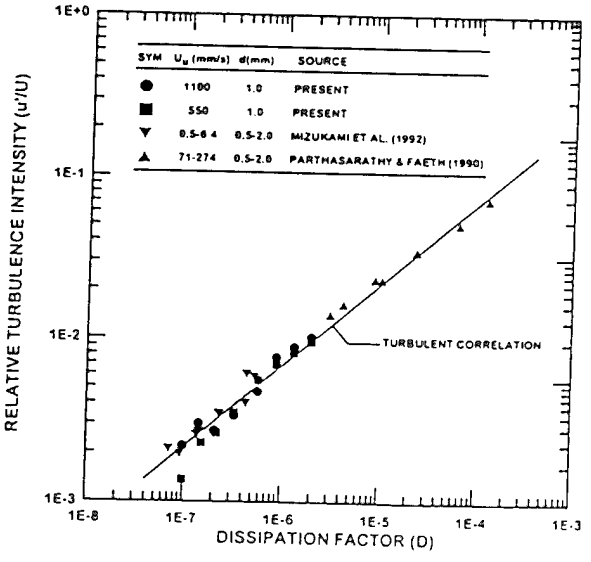

Fig.4 Turbulence generation in homogeneous particle flows.

EXPERIMENTAL STUDIES ON SUPERCRITICAL FLOWS

(AFOSR Contract F49620-97-C-0002)

Principal Investigator: Gregory W. Faris

SRI International
Molecular Physics Laboratory
Menlo Park, California 94025

SUMMARY/OVERVIEW

We are studying supercritical fluids using stimulated Rayleigh, Brillouin, and Raman scattering. New diagnostics are needed in the supercritical regime because low pressure diagnostics do not work well. From our measurements we can determine thermal, compressional, and compositional properties of supercritical fuels. These techniques should improve our knowledge of fluid properties in the supercritical state.

TECHNICAL DISCUSSION

Objectives

The objectives of this research are to develop stimulated scattering as a diagnostic for supercritical fluids, and use this technique to improve our understanding of fluids in the supercritical state.

The study of supercritical fluids and flows requires new diagnostic techniques. Currently available techniques such as laser-induced fluorescence (LIF) and coherent anti-Stokes Raman scattering (CARS) are complicated by increased molecular interactions, leading to stronger quenching, larger absorption and refractive index, and incomplete understanding of the influence of local conditions on spectroscopic parameters such as linewidths, nonresonant background contributions, and quenching rates. We believe that stimulated scattering techniques hold great promise for studying supercritical fluids.

Stimulated Scattering

Rayleigh, Brillouin, and Raman scattering occur commonly as spontaneous scattering. These scattering processes arise from natural oscillation modes of materials and can be used to determine the physical parameters responsible for those oscillations. When these collective modes are excited with a powerful laser, the mode oscillations can be driven so hard that they grow exponentially. In this case, the oscillations cause stimulated scattering. The dominant advantage of stimulated scattering is that the scattered signal can be made arbitrarily large; otherwise, these processes produce extremely weak signals. By using a probe to measure the induced amplification, we can obtain very good quantitative results. This technique is distinct from the stimulated scattering that builds up from noise, in which case quantification is very difficult.

The large signals from stimulated scattering are particularly helpful for investigating Rayleigh and Brillouin scattering, where the weak signals available from spontaneous scattering are difficult to discriminate from background excitation light. Other advantages of stimulated scattering include exceptional temporal resolution, and improved spectral resolution and signal-

to-noise ratio. Furthermore, the use of two laser beams allows spatial registration and point measurement of local conditions.

With a single detection system, all three processes—Rayleigh, Brillouin, and Raman—can be measured. These processes together provide measurements of a wide range of material properties. Rayleigh scattering provides information on thermal properties, Brillouin scattering on compressional or elastic properties, and Raman scattering on chemical and compositional properties, density, and temperature. While spontaneous Brillouin[1] and Raman[2-4] scattering have been applied to supercritical fluids, the use of stimulated scattering for supercritical fluids is new.

Research Plan

The first phase of our work will be primarily measurements of the properties of bulk supercritical materials in static or flowing cells. This work will allow measurements of the physical properties of supercritical fuels, including compressibility, speed of sound, thermal diffusivity, and chemical composition, density, and temperature. This phase is significant, because current work on supercritical fuels is limited to measurements performed after returning the fuels to ambient conditions, rather than in the supercritical state. With experience gained from measurements on uniform supercritical fluids, we expect that we will then be able to apply these techniques to supercritical mixing and combustion.

Stimulated scattering measurements are performed by producing strong scattering interactions using a pump laser and then probing the scattering using a second probe laser. The experimental arrangement for this type of measurement is shown in Figure 1. The pump laser sets up an electric polarization oscillating at the characteristic frequency of a scattering mode of the material.[5] For strong laser driving, this polarization acts as a driving force, leading to amplification of both the material oscillation and a scattered optical wave. The optical amplification is detected as a gain or loss on the probe beam. Spatial resolution is determined by the overlap volume of the pump and probe beams.

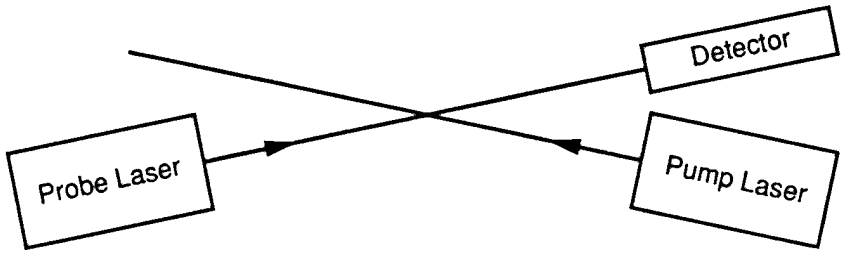

Figure 1. Experimental arrangement for stimulate scattering measurements.

Our measurements will be performed in a simple, high pressure cell of the type used for studies of supercritical water oxidation currently being performed at SRI International. This cell consists of a piece of high pressure tubing with diamond windows clamped to opposite sides. The window apertures of about 1 mm are more than adequate to perform our stimulated scattering measurements. We expect that this cell design should be applicable to supercritical fuels without any significant alteration.

Because stimulated scattering measurements are nonresonant, they can be performed at any wavelength for which the medium is transparent. Much of our previous measurements were performed at 532 nm.[5-7] The pump beam was the second harmonic of an injection-seeded Nd:YAG laser. The probe beam was produced with a cw dye laser pumped by an argon ion laser. Recent advances in diode laser technology allow use of a tunable diode laser as the probe laser. This avoids the large operating costs for the argon laser as well as reduces the amount of time required for keeping the argon and dye lasers in good operation. We plan to perform these measurements at 1.06 μm, using the Nd:YAG laser fundamental as the pump radiation and a diode laser as the probe laser.

The optical properties of the fuels in the supercritical state are an important consideration for this work on fuels. Currently, fuels taken to supercritical conditions are found to be black on returning to ambient conditions.[8] It is not known what the optical properties of the fuels are while they are still at supercritical conditions. We have measured the transmission of thermally stressed JP7 fuel and found that while it is highly absorbing in the visible, it is transparent in the near infrared, where we plan to perform our measurements. Any more severe material blackening may be reduced by using a flowing cell to heat the fuel rapidly just before performing optical measurements, since fuel conversion appears to be due more to the temperature dependence of chemical reactions than the phase of the fuel.[9]

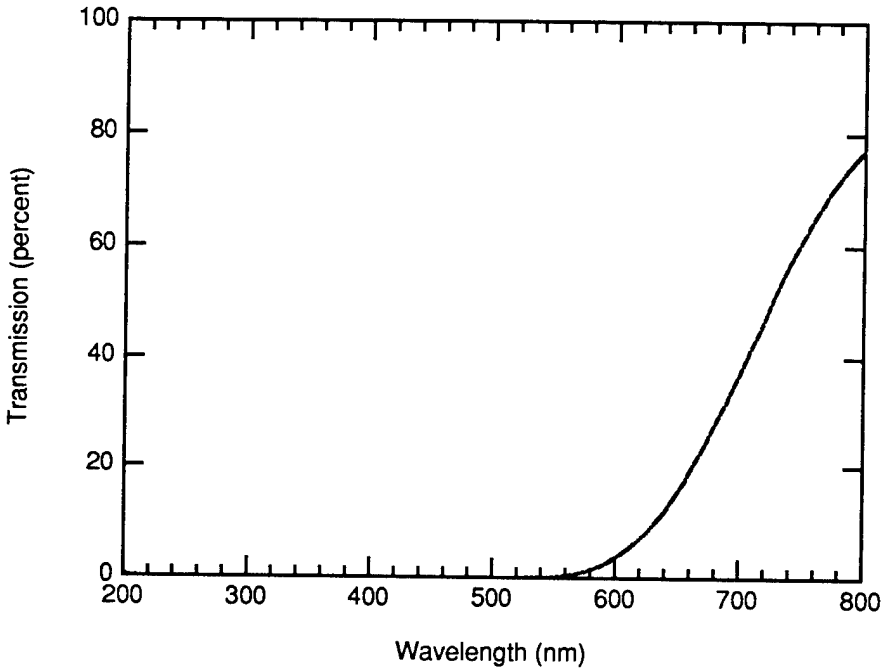

Figure . Transmission through 1 cm of JP7 fuel, thermally stressed to 1200° F.

Extraction of certain information from stimulated scattering requires knowledge of the refractive index of the material. For example, determining of thermal diffusivity from Rayleigh scattering and the speed of sound from Brillouin scattering requires use of the refractive index. We plan to measure the refractive index either interferometrically or through use of Fresnel reflections. Most refractive index measurements attempt four significant figures of accuracy. To determine thermal diffusivity and speed of sound, we require only two significant digits from our refractive index measurements, which simplifies the measurements.

Stimulated scattering measurements are performed by scanning the probe laser over spectroscopic features caused by material oscillations: thermal waves for Rayleigh scattering, sound waves for Brillouin scattering, and vibrational or rotational modes for Raman scattering. From measurements of parameters such as linewidths, line shifts, and line strengths, underlying physical parameters are determined using well defined theory.[5,10] We will measure stimulated scattering features for supercritical fluids including jet fuels or simulants under a variety of conditions and in either static or flowing cells. These measurements will be used to calculate thermal, compressional, and compositional parameters under each condition.

We will determine what limitations exist for application of stimulated scattering to supercritical fluids in terms of accuracies for physical parameters, limitations on applicability to certain situations, and experimental requirements. For the work performed on jet fuels or simulants, we will interact with personnel at Air Force laboratories to transfer information in both directions on relevant material properties and experimental procedures and difficulties. Parameters currently of interest to the Air Force include particle size and concentration,

compressibility, sonic velocity, density and phase, and chemical composition.[8] We expect that we can provide information on these parameters through stimulated scattering. Some information on particle size and concentration can be obtained through the thermal variants of Rayleigh and Brillouin scattering, perhaps supplemented with ordinary scattering measurements. The other parameters can be extracted from stimulated scattering measurements.

REFERENCES

1. R. W. Gammon, H. L. Swinney, and H. Z. Cummins, Phys. Rev. Let **19**, 1467 (1967).

2. M. S. Brown and R. R. Steeper, "CO_2-Based Thermometry of Supercritical Water Oxidation," Appl. Spectroscopy **45**, 1733 (1991).

3. W. Kohl, H. A. Lindner, and E. U. Frank, "Raman Spectra of Water to 400°C and 3000 Bar," Ber. Bunsenges. Phys. Chem. **95**, 1586 (1991).

4. R. D. Woodward and D. G. Talley, "Raman Imaging of Transcritical Cryogenic Propellants," 34 Aerospace Sciences Meeting & Exhibit, Reno, NV, AIAA paper 96-0468 (1996).

5. G. W. Faris, L. E. Jusinski, and A. P. Hickman, "High Resolution Stimulated Brillouin Gain Spectroscopy in Glasses and Crystals," J. Opt. Soc. Am. B **10**, 587 (1993).

6. G. W. Faris, L. E. Jusinski, M. J. Dyer, W. K. Bischel, and A. P. Hickman, "High-Resolution Brillouin Gain Spectroscopy of Glasses and Crystals," Opt. Lett. **15**, 703 (1990).

7. G. W. Faris, M. J. Dyer, and A. P. Hickman, "Transient Effects on Stimulated Brillouin Scattering," Opt. Lett. **17**, 1049 (1992).

8. T. Edwards, USAF Wright Laboratory, personal communication, 1996.

9. T. Edwards, "USAF Supercritical Hydrocarbon Fuels Interests," 31st Aerospace Sciences Meeting & Exhibit, Reno, NV, AIAA paper 93-0807 (1993).

10. W. Kaiser and M. Maier, "Stimulated Rayleigh, Brillouin, and Raman Spectroscopy," in *Laser Handbook*, F. T. Arecchi and E. O. Schulz-Dubois, Eds. (North-Holland, Amsterdam, 1972), Vol. 2, pp. 1077-1150.

FUELS COMBUSTION RESEARCH
(AFOSR GRANT F49620-95-1-0016)
Principal Investigator: I. Glassman
Department of Mechanical and Aerospace Engineering
Princeton University
Princeton, NJ 08544

A. Summary

Progress has continued in the investigation of the thermal and combustion characteristics of fuels at conditions of special interest to the Air Force. Recent efforts have concentrated on the characteristics of endothermic fuels necessary as coolants in next generation aircraft and fuel fouling under sub- and super-critical conditions.

B. Technical Discussion

Methylcyclohexane (MCH) has long been considered as a prototype endothermic fuel for the next generation aircraft of interest to the Air Force. Thus it was chosen for study to analyze its pyrolysis characteristics under sub- and super-critical conditions in an effort to learn the chemistry of particulate formation (fouling) in fuel lines. As a coolant MCH and other endothermic fuels must eventually undergo pyrolysis and oxidation in the engine combustion chamber; therefore, gas phase kinetic studies of these compounds were also initiated. Current results of this integrated research effort are reported next as Supercritical Fuel Degradation and Endothermic Fuel Kinetics.

1) Supercritical Fuel Degradation

The high pressure plug flow reactor designed for the supercritical hydrocarbon reaction studies and the associated analysis procedures were reported in detail last year. Pressures as high as 15 MPa and temperatures as high as 860 K can be obtained in the unique overall laboratory configuration developed This configuration is shown in Fig. 1.

The conceptual approach has been to follow PAH formation during the degradation of the MCH. At a reduced pressure (P/P_C) of 1.3 (4.51 MPa)(P_C = critical pressure) and with a residence time of approximately 0.9 minutes, conditions typical of the most extreme envisioned for next-generation hypersonic aircraft, gaseous and liquid products were analyzed at temperatures from 750 to 844 K. At the lower temperatures examined, conversion of reactants to PAH was zero or negligible. At the higher temperatures, above 820 K, significant PAH formation is observed along with formation of solids. This result is, indeed, of great practical significance.

A qualitative histogram of the uncondensed (gaseous) products found at 820 K is shown in Fig. 2. Uncondensed products at 830 K were now found to be nearly identical to those found at 820 K. The uncondensed products consisted primarily of C_1 to C_4 aliphatics. The presence of these light molecules in the quenched products may suggest that at the temperature of the reaction, 820 K, a significant radical pool from these light C_1 to C_4 species existed.

A typical gas chromatogram of the condensed (liquid) products at 820 K, at a reduced pressure of 1.3 and a residence time of 0.9 minutes is shown in Fig. 3. As the chromatograph illustrates, hundreds of condensed products are formed, most in concentrations too small to be identified. The major products were identified using GC-FTIR analysis. Relative product yields were compared on the basis of percentage of the total flame-ionization detector count of all products for a given injection. In these initial studies, some quantification of product yields has been obtained, but comparison was made between relative product yields of different experiments. The quantitative yield data obtained will be reported as soon as they have been completed.

Relative yields of the major condensed products at 820 and 844 K are shown in Fig. 3. Yields of these major products increased exponentially with increasing temperature. This exponential behavior is illustrated by the relative yields of toluene as a function of temperature, as shown in Fig. 4. It is noted that benzene and cyclohexane are identified as major products, however, presently their relative yields are unknown because the two molecules could not be separated -- they co-elute from the gas-chromatograph. The overall ratio of the yields of the PAH species in the 844 K sample to those in the 822 K sample has been determined to be about 6. Further, the PAH yields at the higher temperature were possibly also slightly depressed due to the agglomeration of PAH into small amounts of solids. It is again important to note that PAH yields were nearly undetectable below 820 K.

In addition to the observation of rapidly increasing PAH yields above 820 K in supercritical methylcyclohexane, solids were also observed to form at temperatures above 820 K and at the conditions

of pressure and residence times investigated. Based on analogous gas-phase soot-formation studies, PAH were presumed to be the precursors to homogeneous solid formation (where surface effects are insignificant). The observation of homogeneous solid inception coincident with that of substantial PAH formation would appear to support this hypothesis.

To investigate the effects of pressure on PAH formation, deoxygenated methylcyclohexane was pyrolyzed at 780 K and reduced pressures from 0.5 to 2.0. This temperature was chosen in order to minimize the pronounced effects of the +/- 5 K uncertainty in temperature on the product yields at temperatures above 810 K. At these higher temperatures, a 5 K difference in temperature can result in a difference in product yield of more than an order of magnitude. However, at lower temperatures (near 780 K), variations in product yields due to the uncertainty in temperature are minimized, and effects due to the pressure variation could be isolated. It is postulated that one effect of a higher pressure on the chemistry involved in methylcyclohexane pyrolysis is due to an increased density and its corresponding effect in supercritical kinetic phenomena. Over the range of reduced pressures examined, the density increases by a factor of about 6.

Relative product yields from the investigation of changing the pressure indicated that pressure variations can have a significant impact on product distributions and yields of products observed. Increasing pressure within the range of a reduced pressure between 0.5 and 2.0 reduces the conversion of the reactant, methylcyclohexane, to products. However, while the yields of all products is reduced as a consequence of the pressure, heavier products are a greater fraction of the total yield at higher pressures than at low. At a reduced pressure of 0.5, heavy (C_7 and larger) products constitute 72% of the total yield while at a reduced pressure of 2.0 they constitute 82% of the total yield. That is, there was a shift toward heavier products at higher pressures. This result is, of course consistent with LeChatlier's principle.

To investigate the effects of molecular structure on PAH formation, preliminary experiments with three types of hydrocarbons with different molecular structures also have been performed. Pyrolysis of supercritical methylcyclohexane, toluene, heptane, and a mixture of toluene and heptane have been examined. Experiments were performed at reduced pressures of 1.3 and residence times on the order of 1 minute. Reaction temperatures in these experiments were as high as 840 K unless solid formation was observed at a lower temperature. The critical properties of these fuels and preliminary results of these experiments are summarized in Table 1.

Table 1: Critical Properties

Fuel	Critical Temperature (K)	Critical Pressure (MPa)	PAH Formation	Solid Formation
Methylcyclohexane	572.2	3.471	Yes	Yes
Toluene	540.3	2.756	No	No
Heptane	591.8	4.104	Trace	Trace
10% Heptane, 90% Toluene (Molar)	577.5	3.610	Yes	Yes

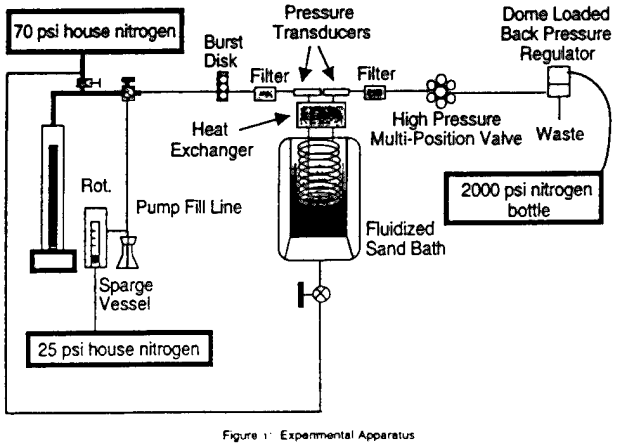

Figure 1: Experimental Apparatus

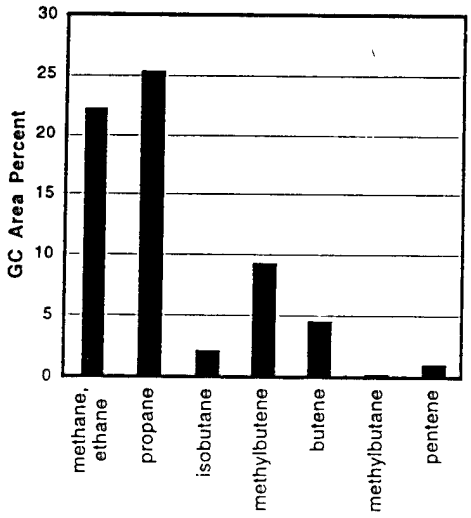

Figure 2: Major Uncondensed Products of Supercritical Methylcyclohexane Pyrolysis T=820K, Pr=1.3, Residence Time=1 minute

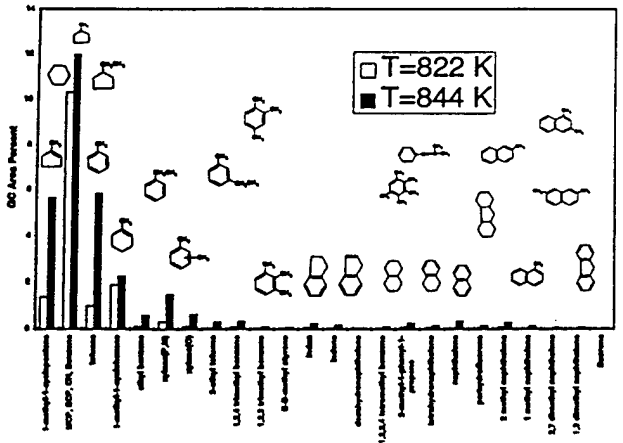

Figure 3: Methylcyclohexane Pyrolysis Major Condensed Products T=820K, 844K, Pr=1.3, Residence Time=1 minute

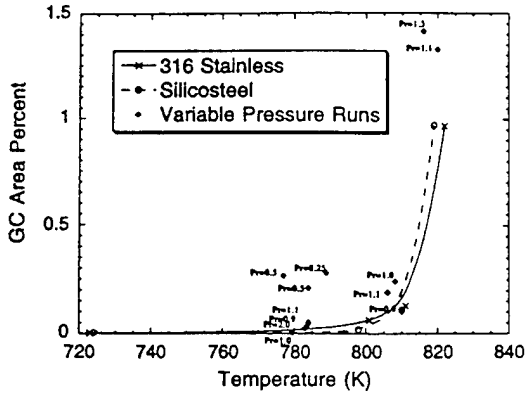

Figure 4: Toluene Yields in Methylcyclohexane Pyrolysis as a Function of Temperature and Pressure Residence Time=1 minute

2. Endothermic Fuel Kinetics

The major intermediates found during the 1 atm, gas phase MCH pyrolysis study in the Princeton flow reactor throughout the temperature range (1050-1200K) studied were ethene, 1,3 butadiene, methane and propene. Unlike the liquid-phase catalytic driven reaction reported in the literature, no toluene was formed in these gas-phase reaction studies. The assumption that the pyrolysis of the MCH occurs primarily by H abstraction and, to a lesser extent, by C-C bond homolysis, with the resulting fuel radicals decaying through β-scission of both C-C and C-H bonds, permitted an analysis which predicted formation rates of intermediates that are in reasonable agreement with the experimentally obtained reaction rates. While it is not necessary to report all the measurements taken, it is interesting to note that MCH pyrolysis decay profiles were measured (Fig. 5) as functions of time at 1 atm pressure and four temperatures (1058, 1108, 1154 and 1192K). The exponential curve fits of these data have now been calculated. When a first-order rate analysis was applied, the curves permitted the calculation of the rate constant for the overall MCH decomposition at each temperature. The experimental data, normalized by the fuel loading for each case, and the first-order curve fits are shown in Fig. 5. By linear regression of the data in this figure it was possible, of course, to determine the overall activation energy as 265 ± kJ/mol and the corresponding pre-exponential factor to be $3.7\pm0.5 \times 10^{13} s^{-1}$.

The MCH oxidation rates were found to be faster than the pyrolysis rate, but interestingly no new major intermediates were detected. Thus it was concluded that the presence of oxygen increased the rate of H abstraction from the fuel, but did not affect the β-scission paths of the radicals formed.

The results of the experiments in which MCH/toluene blends are oxidized indicated that, although the oxidation mechanisms of both fuels are unaffected by the other's presence in the reactor, the oxidation of both fuels was related to the initial MCH concentration. Increasing MCH concentrations resulted in faster decay of both component fuels. The less stable MCH produced the majority of the radical pool for both MCH and toluene attack. Complete details of this MCH effort appeared in a very recent publication (Combust. and Flame, 108, 266 (1997)).

Correspondingly to the MCH pyrolysis, studies of decalin, another endothermic fuel, have been undertaken and a pyrolysis study completed. This aspect of the research followed that of the MCH effort. Thus reported in Fig. 6 are decalin pyrolysis profiles at four different temperatures. From these data the kinetic parameters associated with the overall decay were determined to be $7.71 \times 10^{10} sec^{-1}$ and 203.9 kJ/mole for the pre-exponential and activation energy respectively. The major products formed for all temperatures considered were methane, ethene, propene, 1,3 butadiene and benzene. It is again interesting to note that whereas very little naphthalene (less than 10 ppm) was formed in these gas phase studies, naphthalene is the dominant hydrocarbon formed during the catalytic dehydrogenation of decalin. This result corresponds to that found for MCH in that there was minimal production of the primary dehydrogenation product under vapor phase conditions.

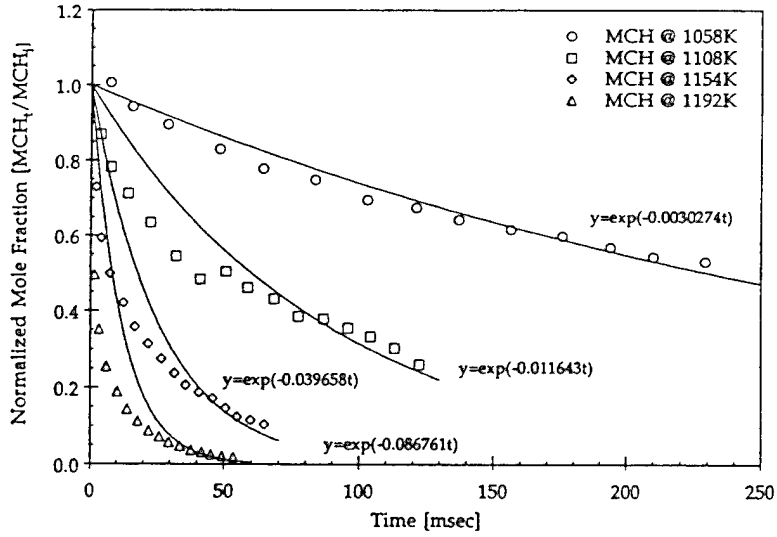

Figure 5. MCH Pyrolysis Profiles

Decalin Pyrolysis Profiles

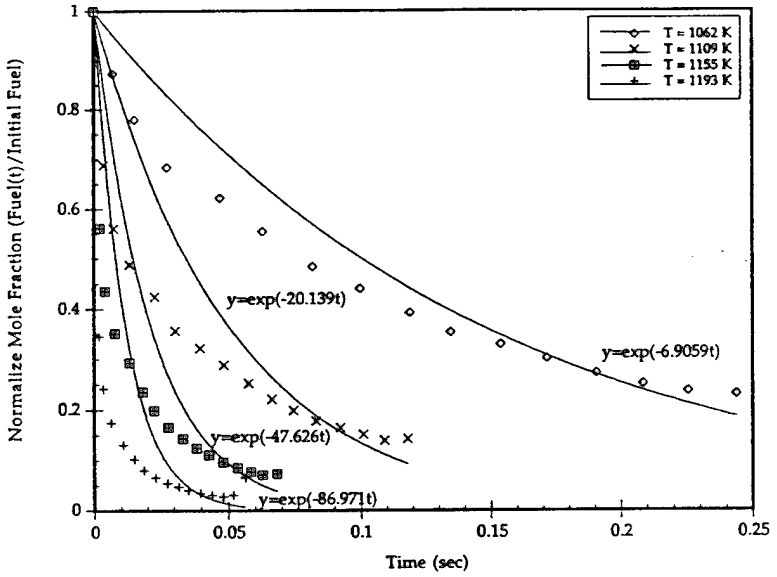

Figure 6. Decalin Pyrolysis Profiles

ADVANCED DIAGNOSTICS FOR REACTING FLOWS

AFOSR 95-1-0041

Principal Investigator: Ronald K. Hanson

High Temperature Gasdynamics Laboratory
Mechanical Engineering Department
Stanford University, Stanford, CA

SUMMARY/OVERVIEW:

This research is aimed at establishing laser-based absorption and fluorescence techniques for nonintrusive measurements in reactive gases. Significant progress was made in the development of wavelength-multiplexed diode laser absorption diagnostics for combustion sensing and control, and for measurements at high-pressures. New fluorescence strategies are reported for imaging temperature and for single-point plasma measurements.

Diagnostics for High-Pressure Gases

Progress has been made on two projects to develop high-pressure diagnostics. The first activity is aimed at monitoring H_2O and temperature at high pressures using diode laser absorption. A critical element of this work has been assembly of a code for calculation of water vapor spectra over a wide range of conditions. Example calculations of the important region between 1.3 and 1.42 microns are shown in Figs. 1 and 2; Fig. 1 illustrates the effect of temperature on the strengths and density of absorption lines, while Fig. 2 documents the role of pressure broadening, namely to eliminate regions of negligible absorption for pressures of 5 atm and higher. The latter finding invalidates the most common diode laser absorption strategy, which utilizes wavelength-scanning to record the full shape of isolated transitions.

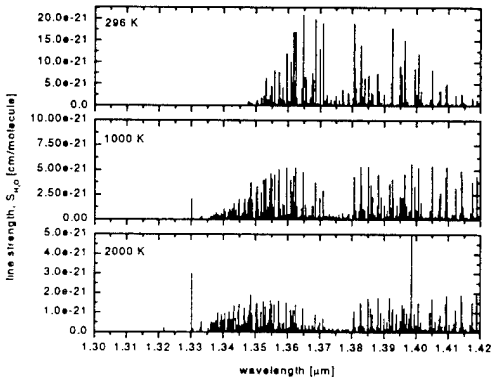

Figure 1. Line strengths (S) of H_2O transitions in the $2\nu_1$ and $\nu_1 + \nu_3$ rovibrational bands.

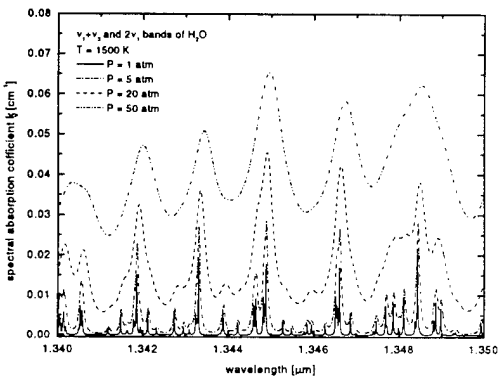

Figure 2. Calculated absorption spectrum of H_2O at various pressures for a mixture of 20% H2O, 80% N2 at 1500 K. the increasing overlap of spectral features results from collisional broadening effects at high pressures and is typical at all wavelengths.

For high pressures, we propose to utilize multiple laser sources (i.e., wavelength-multiplexing) fixed at selected wavelengths. The water vapor code has been exercised to identify optimum wavelength pairs which can be used to measure temperature (through the ratio of absorption) in cases where pressure is known, and optimized candidates for a third wavelength have been found for measurement of pressure for the general case of simultaneous monitoring of temperature, water concentration and pressure. Experiments are in progress to verify the high-pressure spectral code and the proposed fixed-wavelength diagnostic strategy.

In a separate effort, diagnostics are being developed for absorption measurements in a shock tube at pressures in the range 10 to 200 atm. At these conditions, propagation of light through turbulent, dense boundary layers causes significant beam steering and light scattering. Our approach has been to modify the conventional laser absorption arrangement to be much less sensitive to these effects. Most important has been to adopt use of an integrating sphere, rather than a small-area detector, to ensure collection of all transmitted light. Initial results with this method are very encouraging.

Diagnostics for Combustion Sensing and Control

Continued progress has been made in the development of diode-laser sensors for rapid measurements in combustion gases. A multiplexed sensor system, composed of multiple tunable diode laser sources, enables simultaneous monitoring of absorption at several wavelengths, thereby allowing simultaneous determination of multiple gasdynamic parameters and/or species concentrations. These measurements can be made remotely and at multiple measurement locations through use of fiberoptic transmission of laser light. Figure 3 illustrates the experimental arrangement employed in recent work to explore both *in situ* and fast-sampling diagnostic concepts. The *in situ* measurements employed two wavelength channels, tuned to different regions of the near-IR (1.4 microns) absorption spectrum of water vapor, so that both the temperature and concentration of water vapor could be determined from the ratio and absolute magnitude of the absorption signals. The speed of this on-line diagnostic has been improved so that temperature is inferred at 2 millisecond intervals, which is fast enough to allow near-real-time control of combustor oscillations. To demonstrate the potential for rapid control, laser-based measurements were made under oscillatory combustion conditions induced by use of a 40 cm duct above the burner, and the temperature data were used in a feedback loop (variable fuel flow rate) to minimize temperature fluctuations. Example results of the power spectra of the fluctuating temperature, before and after closed-loop control is initiated, are shown in Fig. 4.

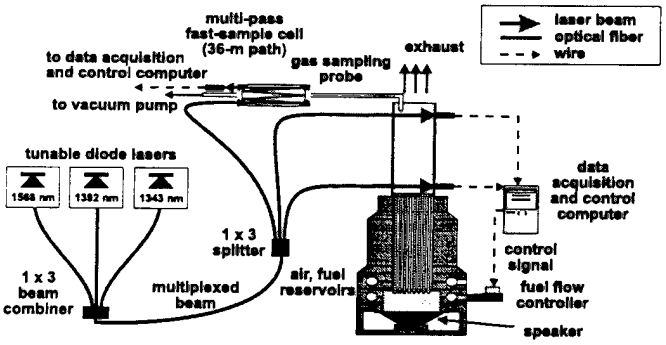

Figure 3. Schematic diagram of the multiplexed diode-laser sensor system for *in situ* and fast-sampling measurements.

In a parallel effort, we have worked to develop an ultra-sensitive species sensor based on long-path absorption in probe-sampled gases. As shown schematically in Fig. 3, the probe extracts gases well downstream of the flame zone, and these gases flow rapidly to a compact multi-pass cell (effective path length of 33 m with a volume of only 0.3 liters) where they are

analyzed by one or more diode lasers. The immediate goal has been to perform ppm level measurements of pollutants such as CO, NO and unburned hydrocarbons with a measurement time of less than 1 second. The CO system, based on detection at 1.568 microns (second

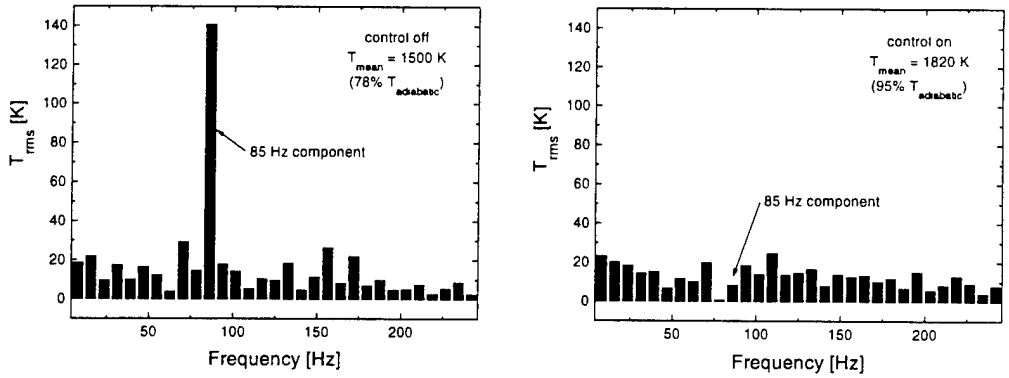

Figure 4. Measured power spectra (T_{rms} values) before (left) and after (right) initiation of closed-loop control.

overtone band), is now operating and has a detection limit of less than 10 ppm.

The availability of both types of diode laser diagnostics, fast-sampling sensors for pollutant monitoring and *in situ* sensors for near-real-time measurements, should lead to new strategies for control of combustion instabilities and overall performance. Work is in progress to monitor additional species including methane, hydrazine, nitric oxide and carbon dioxide.

Plasma Diagnostics

Work was completed on a diagnostic technique for xenon plasmas based on spectrally resolved laser-induced fluorescence of excited states. Studies were conducted in a low pressure discharge and, recently, in an ion thruster. The initial discharge experiments involved probing two 6s-6p transitions: one at 823 nm involving a metastable lower state, resulting in a lineshape dominated by Doppler broadening; and a second transition at 828 nm dominated by resonance broadening. Use of a tunable diode laser source enabled spectrally-resolved recording of the lineshapes, enabling determination of both temperature (from the 823 nm transition) and pressure (from the 828 nm transition). It was necessary to account for the complex nature of the lines resulting from multiple isotopes and complex hyperfine splitting. This diagnostic approach, combining lines with Doppler and resonance broadening, provides a new means for measurements of temperature and pressure in low pressure plasmas.

The most recent experiments were conducted in the plasma thruster fabricated by Prof. Cappelli's research group (under AFOSR support). Fluorescence excitation measurements were made of neutral xenon, using the 823 nm transition, in the exit plane of the thruster. These data enabled determination of the xenon temperature (from the lineshape) and velocity (from the Doppler shift), both of which provide critical information on the energy transfer between neutral and ionized xenon in the thruster. LIF measurements of ionized xenon (605 nm) were used to measure exit velocity (to 14 km/sec) and ion temperature.

PLIF of Acetone for Temperature Imaging

Acetone has proved to be an attractive tracer species for application of PLIF, largely because the method is simple to implement and yields large signal intensities. However, it is recognized that the acetone signal has a significant dependence on temperature and excitation wavelength (and a weak dependence on pressure). Experiments aimed at characterizing these effects have led to new strategies for temperature imaging which appear to offer important advantages relative to other schemes. For flows uniformly seeded with acetone, a simple single-wavelength approach can be used, as illustrated in Fig. 5. Here air, seeded with acetone, flows at low velocity over a heated cylinder (6 mm diameter). The single-shot results (40 mJ at 248 nm) yield accurate temperature results, with a precision of a few degrees Kelvin. Validation experiments using a dual-wavelength strategy for nonuniformly seeded flows have also been performed.

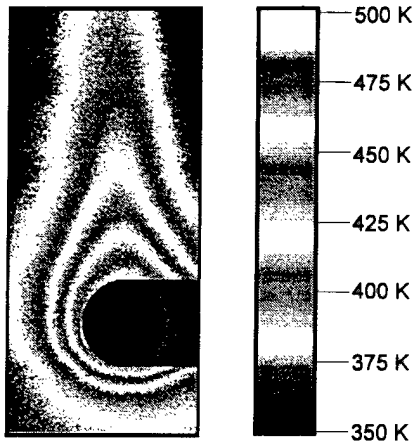

Figure 5. Single-shot temperature image in a heated cylinder flow, generated with a single-wavelength technique using 248 nm excitation. Flow is from bottom up at 6 cm/s. 40 mJ laser excitation is from left, leaving a small region unexcited.

PUBLICATIONS

D.S. Baer, V. Nagali, E.R. Furlong, R.K. Hanson and M.E. Newfield, "Scanned- and Fixed-Wavelength Absorption Diagnostics for Combustion Measurements using Multiplexed Diode-Laser Sensor System," AIAA J. **34**, 489-493 (1996).

T.C. Island, B.J. Patrie, M.G. Mungal and R.K. Hanson, "Instantaneous Three-Dimensional Flow Visualization of a Supersonic Mixing Layer," Experiments in Fluids **20**, 249-256 (1996).

R.J. Cedolin, R.K. Hanson and M.A. Cappelli, "Laser-Induced Fluorescence Measurements of Resonance Broadening in Xenon," Phys. Rev. A, **54**, 335-342 (1996).

E.R. Furlong, D.S. Baer and R.K. Hanson, "Combustion Control and Monitoring using a Multiplexed Diode-Laser Sensor System," 26th Symposium (International) on Combustion, The Combustion Inst., Pittsburgh, 1996, pp.2851-2858.

V. Nagali, S. I. Chou, D. S. Baer, R. K. Hanson and J. Segall, "Tunable Diode Laser Absorption Measurements of Methane at Elevated Temperatures," Applied Optics, **35**, 4026-4032 (1996).

J.L. Palmer, B.K. McMillin and R.K. Hanson, "Multi-Line Fluorescence Imaging of the Rotational Field in a Shock-Tunnel Free Jet," App. Phys. B, **63**, 167-178 (1996).

V. Nagali, S.I Chou, D.S. Baer and R.K. Hanson, "Diode-Laser Measurements of Temperature-Dependent Collision Widths of H_2O Transitions in the 1.4μm Region," J. Quant. Spectrosc. Radiat. Transfer, in press.

S.I. Chou, D.S. Baer and R.K. Hanson, "Diode-Laser Absorption Measurements of CH_3Cl and CH_4 near 1.65 μm," Appl. Optics, in press.

M.C. Thurber, F. Grisch and R.K. Hanson, "Temperature Imaging with Single- and Dual-Wavelength Acetone Planar Laser-Induced Fluorescence," Opt. Lett., **22**, 251-253 (1997).

PARTICLE DISPERSION IN A TURBULENT SPRAY

AFOSR Grant F49620-95-1-0276

Annual Report: 8/1/96 - 7/31/97

Principal Investigators: Ian M. Kennedy and Wolfgang Kollmann

University of California

Davis, CA 95616.

SUMMARY

The project involves an experimental component and a numerical component. The experiments are concerned with measurements of the dispersion of droplets in a turbulent spray with a view to determining the impact of the mass loading of spray on the dispersion. The diameter of droplets is also measured by a droplet lasing technique. Particle Imaging Velocimetry (PIV) has been implemented with a novel solid state high voltage switch to control the Pockel cell of a YAG laser. The PIV results show that the micro atomizers yield well behaved initial conditions for the spray. Dispersion measurements of a tagged fluorescent droplet indicate that the spray has an impact on the dispersion phenomenon. The numerical component of the project is aimed at the simulation of the jet under conditions that match the experimental conditions so that droplet dispersion and vaporization rates can be compared and correlations of drag and mass transfer evaluated. Our specific goals for the current year of the project were the implementation of the PLES method into the existing solution method for the Navier-Stokes equations and the further development of the hybrid spectral - finite difference solution procedure for the fluid phase. A semi-analytical Poisson solver was established that is accurate and fast. The PLES method showed encouraging results in jet simulations.

TECHNICAL DISCUSSION

The guiding philosophy of the experimental program has been the development of accurate data on turbulent dispersion of particles in a shear flow with well characterized initial conditions. Atomizers that are frequently used in spray research involve rather complicated geometries and initial conditions. We have striven to achieve very well defined conditions that can be implemented in a LES code for comparison. A round turbulent jet is the base flow for the experiments. The challenge has been to add a controllable spray to the flow with minimal disturbances in order to elucidate the impact of turbulence modification on the spray behavior. Initial efforts to add the spray to the base flow ended in excessive dripping of the spray from the exit of the nozzle. The current technique uses a series of micro air blast atomizers to produce a very fine aerosol close to the nozzle exit.

The air blast atomizers yield a spray with mass loadings up to 30% with the possibility of achieving higher loadings in the future. Measurements of the dispersion of the a single particle were obtained by adding a fluorescent dye to a droplet that was created by a piezo electric droplet generator. The fluorescent particle was injected along the centerline of the spray. Fluorescence that was emitted from the particle as it passed through an Argon ion laser sheet was imaged onto a position sensing photomultiplier tube. The output from the phototube was digitized and stored on a computer. Data from many particles were collected

and averaged to yield the mean square displacement from the axis, the so-called dispersion. Measurements were obtained of the dispersion of various size droplets as a function of the mass loading (mass of water per mass of air) in the spray. It was apparent that the addition of the spray had an impact on the dispersion of the tagged fluorescent particle. The *prima facie* evidence suggested that the turbulence of the base flow was modified by the liquid droplets in the flow. However, a Reynolds stress calculation of the jet flow and a stochastic calculation of the droplet motion indicated that Reynolds numbers over 100 were unlikely, too small for Hetsroni's vortex shedding mechanism to be important. A Mie scattering image (not shown) of the spray suggested an alternative explanation.

A large scale, quasi sinusoidal motion of the spray was evident in this figure. Other authors have described a similar helical mode in single phase jets in the past. It should be recalled that the exit conditions of the jet are laminar and "top hat". The amount of turbulence in the jet exit flow is small. However, jets are sensitive to small perturbations in the near field region. A potential explanation of the enhanced dispersion is suggested by this observation. That is, the stability of the jet is affected by the momentum transfer between the phases and ultimately the "helical" motion is augmented by the addition of the spray. It can also be argued that the method of spray addition contributes to additional perturbations. This question can only be answered by Planar Imaging Velocimetry (PIV) measurements at the jet exit and in the near field as the spray develops.

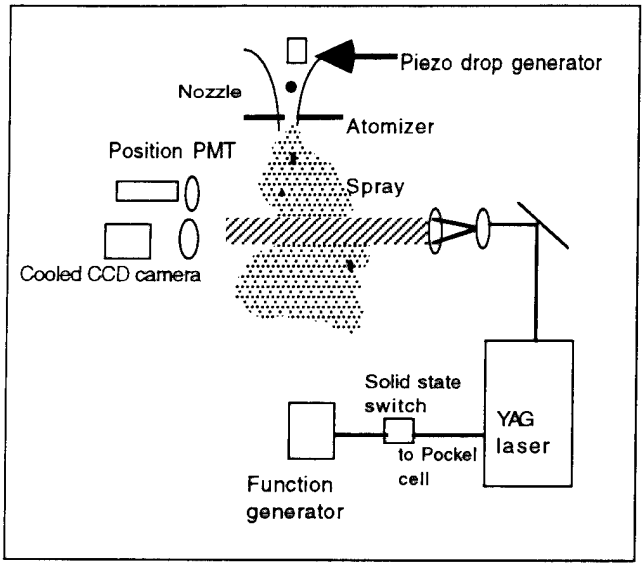

Figure 1. Schematic of spray - PIV system with solid state switch

A novel scheme has been implemented to obtain these PIV data with limited optical resources. A single YAG laser is used to generate the light sheet for the velocity imaging. A double pulse with variable timing is generated with a solid state switch that has been introduced recently to the US market. It permits switching of the 3 to 5 kV supply to the Pockel cell of the YAG laser within 10 ns, following a TTL input signal from a function generator. Hence, we do not require a Marx bank to generate the double pulse. Furthermore, the solid state switch offers flexibility in the timing as well as the possibility of using multiple pulses for Particle Tracking Velocimetry. This scheme has been successfully implemented in our spray. The strong secondary background scattering from the spray outside the laser sheet has necessitated image processing to remove noise via thresholding before a FFT analysis is carried out. The complete experimental set up is shown schematically in Figure 1.

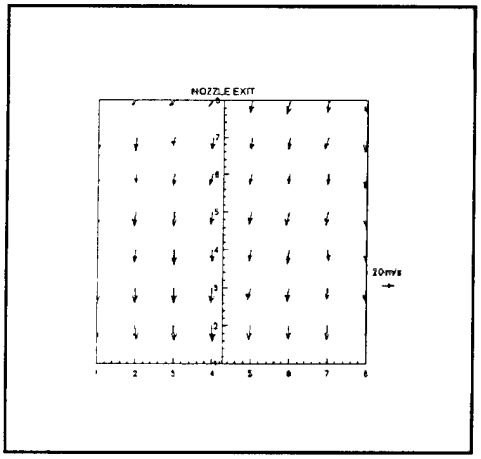

Figure 2 Velocity vectors of spray at the exit of the nozzle

Measurements of the initial velocity field of the spray are shown in Figure 2. Fifteen images were collected to form averages so that considerable statistical noise is included in the vectors that are shown in Figure 2. The mean axial velocity of the spray is about 20 m s^{-1} which is

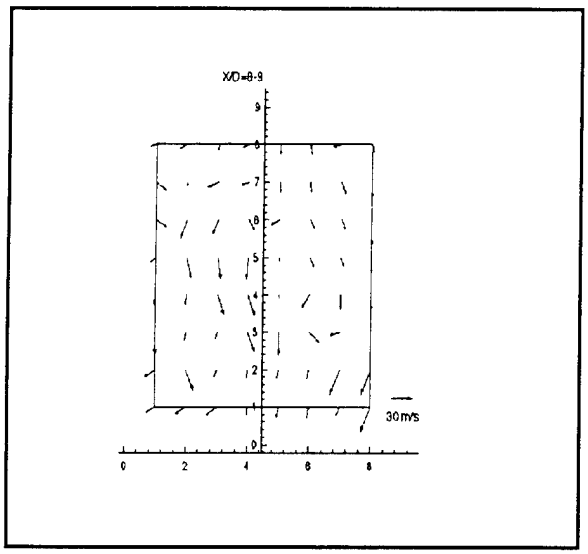

Figure 3 Instantaneous velocity vectors of spray droplets at x/d =8

approximately twice the gas phase axial velocity. The mean radial velocity of the spray is of the order of 1 m s^{-1}. The vector plot in Figure 2 indicates that the micro atomizers produce a well behaved spray with minimal radial motion and easily characterized initial conditions that can be used in the LES. PIV data were also obtained at about 8 nozzle diameters from the jet exit (see Figure 3). The instantaneous vector plot shows a large scale motion of thespray that lends credence to the notion that a helical structure may account for the increased dispersion of the tagged particle as spray is added to the jet.

Measurements of the vaporization rates of individual droplets in the spray are an integral part of the experimental program. The droplet lasing or Morphology Dependent Resonance (MDR) phenomenon is ideally suited to our experimental methodology and set up. MDR spectra will allow us to follow the diameter of an individual droplet as it changes through the flow field. Lasing spectra have been measured in ethanol/rhodamine droplets; measurements of vaporization rates of ethanol droplets are currently underway.

The computation of the turbulent flow field is based on the notion of simulating the large eddies and modelling the effect of the small and unresolved eddies on the large and resolved ones as described in the contract proposal. The LES model for the particles (PLES) developed in the previous year was implemented into the LES code for the spatially developing turbulent round jet. The PLES model treats spherical subdomains $\mathcal{D}^i(t)$ of the flow field with constant radius R containing $\mathcal{N}^i(t)$ particles as an entity (called blobs), that is governed by dynamic equations for position and velocity similar to an individual particle. These equations contain additional terms representing the effect of particle motion inside the blob and the particles leaving and entering it.

The evolution of a blob $\mathcal{D}^i(t)$ is determined by its centre location $\hat{\underline{X}}^i(t)$, the centre velocity $\hat{\underline{v}}^i(t)$ and the number of particles $\mathcal{N}^i(t)$ in the blob. The velocity of blob $\mathcal{D}^i(t)$ changes with time according to

$$d\hat{\underline{v}}^i(t) = \underline{P}^i dt + d\underline{Q}^i + d\underline{S}^i + d\left[\frac{d^2\underline{Y}}{dt^2}\right]$$

The forces acting on a blob are: $\underline{P}^i(t)$ the particle force based on the centroid properties, $\underline{Q}^i(t)$ the difference between the average acceleration and $\underline{P}^i(t)$. The third contribution is due to the motion of particles through the spherical blob boundary and the motion of particles inside the blob. Closure models have been developed for $\underline{Q}^i$, $\underline{S}^i$ and $\underline{Y}$ based on integrated white-noise processes, which can be simulated using stochastic differential equations of the Ornstein-Uhlenbeck type. Preliminary results are encouraging; the blobs follow roughly the cloud of particles they are designed to represent. The pdf of one of the Cartesian velocity components in the cross sections of a round jet at $\frac{x}{d} = 8$ is shown in Figure 4 for blobs (full line) and particles (dashed line). Each blob contains initially 100

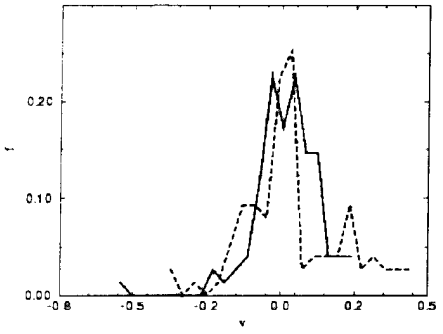

Figure 4 Pdf of blob (full line) and particle (dashed line) velocity component v at x/D = 8. Blobs and particles are released at the same locations and times.

particles, the evolution of the number $\mathcal{N}^i(t)$ is simulated as an exponential decay using a constant time scale.

The second major effort during the last year was devoted to the improvement of the numerical solution method for the fluid phase equations in cylindrical coordinates. The azimuthal direction is treated using Fourier polynomials. The radial direction is treated using a mapping of the unbounded interval $[0,\infty]$ onto $[0,1]$. Either a spectral method based on modified Jacobi polynomials or an explicit high order (at least fourth, up to eighth order) finite difference method is used for the radial direction and a high order finite difference method is applied to the axial direction.

The Poisson-Helmholtz equation

$$\frac{1}{r}\frac{\partial}{\partial r}\left(r\frac{\partial \Psi_m}{\partial r}\right) - m^2\frac{\Psi_m}{r^2} + \frac{\partial^2 \Psi_m}{\partial z^2} = R_m$$

in the semi-infinite domain $[0,\infty]x[0,1]$ arises in cylindrical coordinates for the complex-valued Fourier amplitudes $\Psi_m(\eta,z)$, where $m \geq 0$ is the (integer) circumferential wavenumber. The radial domain $[0,\infty]$ is mapped onto the unit interval and a spectral decomposition of the Galerkin equations for the Jacobi amplitudes $\hat{\Psi}_n$ leads to a decoupled system of odes

$$-\zeta_n \hat{\Psi}^*{}_n(z) + \frac{d^2\Psi^*{}_n}{dz^2} = R^*{}_n(z)$$

where $\zeta_n > 0$ (no sum over n) denotes the associated eigenvalue. This system of odes can be solved analytically using the method of variation of parameters. Dirichlet, Neumann, mixed Dirichlet-Neumann and Robin boundary conditions can be imposed and the solution is then reduced to a single quadrature for each Jacobi mode n. The Poisson solver was tested extensively and the results for the mixed Dirichlet- Neumann problem are shown in Figure 5 for an analytic test solution. The maximum norm of the absolute error for the Fourier mode$m$ = 0 and n = 51,101,201,401 (number of equidistant grid points in$z$-direction) for the fourth order accurate integration using cubic splines is plotted. The accuracy is clearly limited by the numerical integration method and the accuracy of the spectral decomposition. The error incurred by the spectral decomposition is of the order 10^{-8} for $M = 60$ Jacobi modes, hence the numerical integration procedure is the limiting factor.

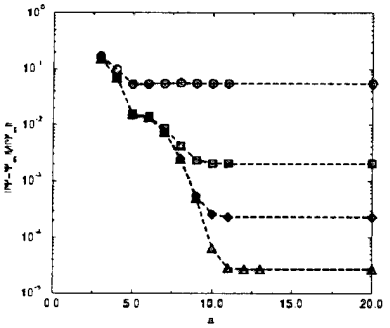

Figure 5 Maximum norm of the absolute error for the Poisson equation using the 2-parameter exponential map and $\mathcal{O}(h^4)$ spline integration for n_z=51 (circles), n_z =101 (squares), n_z =201 (diamonds), n_z =401 (triangles) grid points in axial direction.

RAPID CONCENTRATION MEASUREMENTS BY PICOSECOND TIME-RESOLVED LASER-INDUCED FLUORESCENCE

AFOSR Grant Number F49620-95-1-0218

Principal Investigators: Galen B. King and Normand M. Laurendeau

Flame Diagnostics Laboratory
School of Mechanical Engineering
Purdue University
West Lafayette, IN 47907-1288

SUMMARY/OVERVIEW

Picosecond time-resolved laser-induced fluorescence (PITLIF) is a developing technique used to probe minor-species concentrations in flames at rates sufficient for the study of turbulent fluctuations. This method has previously been applied to the measurement of CH signals in laminar and low Reynolds number turbulent diffusion flames. In the past year, LIF measurements of OH have been obtained in the same flames. The peak concentrations of the hydroxyl radical provide a signal-to-noise ratio sufficient to extend the measurements to a variety of axial and radial locations relative to the flame front. The time-series measured are used to compute power spectral densities (PSDs) which provide frequency information not previously available for minor species. These measurements provide the first known PSDs of the hydroxyl radical in a turbulent flame.

TECHNICAL DISCUSSION

Modeling of turbulent diffusion flames via the probability density function (PDF) of mixture fraction has received much attention in the literature and significant progress has been made in developing state relationships for major species[1] and in building mixture fraction PDFs[2]. However, the use of a PDF to describe turbulent fluctuations does not provide information on the frequencies of the fluctuations in the flow. This frequency information, provided by the power spectral density (PSD), has been studied extensively for non-reacting turbulent flows for which the velocity PSD is expected to have a -5/3 power law region at high Reynolds number.[3]

In this progress report, we present the first known measurements of OH time-series in a turbulent diffusion flame. From these time-series, the PSD is computed at frequencies up to 2 kHz. Previous measurements of CH time-series and PSDs in the same flame have been reported.[4] However, the hydroxyl radical is present at much higher concentrations and the resulting SNR is sufficient for measuring time-series at many locations in the axisymmetric flame. We report such measurements in a low-Reynolds number turbulent methane/air diffusion flame and discuss the possible implications of the reported PSD shapes.

---

[1] Sivathanu, Y. R. and Faeth, G. M. (1990). *Combust. Flame* **82**, 211-230.

[2] Effelsberg, E. and Peters, N. (1983). *Combust. Flame* **50**, 351-360.

[3] Tennekes, H. and Lumley, J. L. (1972). *A First Course in Turbulence*, The MIT Press, Cambridge, MA.

[4] Renfro, M. W., Klassen, M. S., King, G. B., and Laurendeau, N. M. (1997). *Opt. Let.* **22**, 175-177.

Picosecond time-resolved laser-induced fluorescence (PITLIF) was used for the hydroxyl measurements. This developing technique combines laser-induced fluorescence measurements with the capability for on-the-fly electronic quenching corrections, yielding a time-series of quantitative concentration measurements. At this time, it is not possible to correct multiple points of a time-series owing to insufficient electronics for handling the high data acquisition rate and the large data files necessary to measure the radiative lifetime (~2 ns). The correction has, however, been demonstrated for single points at times approaching the Kolmogorov scale[5] and the laser system has been upgraded to increase power and decrease noise since this previous study. Improvements to the electronics, during the next year, should eventually permit the collection of quenching independent time-series.

The laser and detection system are shown in Fig. 1. Detailed discussion of this system has been presented in the context of previous CH measurements.[4] Here, the laser is tuned to excite the relatively temperature insensitive $Q_1(8)$ line in the (0,0) band of the A^2-X^2 system of OH at 309.33 nm by tripling the output from the Ti:Sapphire laser. The temporal width of the laser beam was 18 ps, resulting in a spectral width of ~1 cm^{-1}. The beam diameter at the focus was measured to be ~100 μm FWHM, which resulted in an average laser irradiance of 1.0×10^5 mW/cm^2. The probe volume and spectral window set by the monochromator slits were ~500 μm and 26 nm, respectively.

A concentric tube burner identical to that used for the previous CH measurements[4] was used to create the diffusion flame. Methane was supplied through the central tube (5.5-mm inner diameter). The Reynolds number based on the cold methane flow rate was 2800. The relatively low Reynolds number was required to keep the flame attached to the burner.

Radial fluorescence profiles measured in the flame are shown in Fig. 2. Fluorescence detection spectra and off-resonance profiles were obtained to test for fluorescence interferences. No interferences were found below x/D=60 in this flame. Time-series measurements were made at many radial locations at heights of x/D=1, 5, 30, and 60. The PDFs and PSDs for the x/D=30 and x/D=60 cases were found to be nearly identical to each other but considerably different from the x/D=1 and x/D=5 cases. Thus, a comparison is presented for only the x/D=1, 5, and 30 cases.

Fig. 3 shows the PDFs computed at x/D=30 for several radial locations. Far off the peak ($|y|>2$), the PDF is centered near zero (no measured signal). At these locations, there is still some deviation from the zero mean as a result of flame emission. At the radial peak where the concentration is larger, the bulk of the PDF exists significantly above zero. However, even at the peak, fluctuations are large enough to cause a zero signal some of the time. The result is a bimodal PDF.

Fig. 4 shows PDFs for x/D=5 at various radial locations. On the air-side of the peak (y=0.5 mm), the PDF shows a nearly symmetric distribution toward higher and lower signals. At the peak, the PDF is again nearly symmetric. However, in this case, a long tail toward lower signals exists. A mirror image of the peak PDF occurs on the air side at y=1.0 mm. On the fuel-side, however, the distribution is non-symmetric, skewed in one direction or the other depending on the mean value. At x/D=1 (not shown) all PDFs are essentially symmetric.

Comparing the two heights, the PDF shape for x/D=30 does not significantly change from the air-side to the fuel-side. The distribution is sometimes less bimodal than at the peak (y=0) but it is always non-symmetric and all differences are likely a result of only the changing mean concentration. In contrast, the PDF shape at x/D=5 is non-symmetric on the fuel-side (similar to all PDFs for x/D=30) and symmetric on the air-side (similar to all PDFs for x/D=1). These differences cannot be described by just a change in the mean concentration and are indicative of physically different fluctuation mechanisms for regions lower and higher than x/D=5.

PSDs were also computed at each of the points corresponding to the previous PDFs. Fig. 5 shows the PSDs at x/D=30. Each PSD appears to have a two-slope structure with a linear region (log-log

[5] Reichardt, T. A., Klassen, M. S., King, G. B., and Laurendeau, N. M. (1996). *Appl. Opt.* **35**, 2125-2139.

scale) from DC to ~100 Hz and a second linear region above ~200 Hz. The second slope decays into the noise floor. Consistent with the PDFs (Fig. 3), no substantial difference is observed from the fuel to the air side. The fuel-side PSD has a slightly higher knee frequency (intersection of first and second slopes) and the transition from one slope to the next is sharper but these differences are small. From linear fits to these two slopes, the decay coefficient for the first slope varies from about -0.5 to -1.0 from the fuel to the air side, respectively. The second slope does not vary significantly from the fuel to the air side, having an average value of about -2.4.

Fig. 6 shows the same comparison of PSDs for x/D=5. At this height, significant differences are observed from the fuel to the air side, similar to the PDFs (Fig. 4). The fuel-side PSD has a two-slope structure with a sharp transition between the first and second slope. As at x/D=30, the knee frequency decreases from the fuel-side to the air-side of the flame front. The air-side PSD also has two slopes but they are so close in magnitude that the PSD visually looks like a single-slope decay. The low frequency slope varies again from about -0.5 to -1.0 from the fuel-side to the air-side, respectively. The high-frequency slope is approximately -2.2 for the fuel-side PSD, and drops to about -1.2 for the air-side PSD. In comparison, PSDs at x/D=1 (not shown) are identical from the fuel-side to the air-side, each having a single-slope structure with a slope of about -1.2.

The possible significance of a PSD slope steeper than -2 can be addressed by the relationship between velocity and fluorescence signal fluctuations. Assuming that convective fluctuations dominate the measured signals, it can be shown that the fluorescence spectrum will have an additional -2 slope imposed upon that for the velocity spectrum but will otherwise maintain the same shape.[3] If convection of the radial profile without a change in its basic shape is to be the dominant or only source of fluctuations, the slope of the PSD must be steeper than -2 at high frequencies as the velocity PSD in turbulent flames is most likely itself decaying at a significant slope. .Fluorescence PSDs with slopes steeper than -2 are very possibly dominated at high frequencies by this velocity effect, although many other physical processes are occurring such as electronic quenching, diffusion, and reaction.

For many PSDs measured in the turbulent diffusion flame (x/D≥5), the slopes are near -2.4. If the described effect were responsible, this would indicate a velocity decay with a slope of only -0.4. This is far below the Kolmogorov limited -5/3, but the Reynolds number is also very low and a strong dependence of the high frequency slope on Reynolds number has been observed in previous velocity measurements.[6] For the case of a fixed scalar profile moving across the measurement location, the PDF can be estimated from an assumed Gaussian velocity PDF and can result in a bimodal shape.[2] Furthermore, the bimodal PDFs in the current investigation coincide with PSD slopes steeper than -2 in all cases. Additional sources for these fluctuations should be examined in future work, but both the PDFs and PSDs measured high in the turbulent diffusion flame are consistent with fluctuations associated only with convection. To arrive at this simplification, the diffusion and reaction rate (w_i) terms in the species conservation equation have been neglected. Neglecting w_i is equivalent to assuming that the species concentration, Y_i, is only a function of a conserved scalar; that is, both Y_i and the mixture fraction are then governed by the same equation.

For most locations where the PDF appears Gaussian, the high-frequency slope of the PSD is around -1.2. This slope is insufficiently steep to be described solely by convection. The relevant regions are low in the diffusion flame where the flame is attached to the burner. In these regions the scalar dissipation rate is high and neglecting source terms when evaluating fluctuating species likely becomes invalid. Minor-species concentrations are not generally well described by just the mixture fraction[7] so this behavior is not surprising. The PSDs for other species and temperature (required to calculate w_i) may need to be considered to describe the OH PSDs in these regions.

---

[6] Mydlarski, L. and Warhaft, Z. (1996). *J. Fluid Mech.* **320**, 331-368.

[7] Smyth, K. C., Miller, J. H., Dorfman, R. C., Mallard, W., and Santoro, R. (1985). *Combust. Flame* **62**, 157-181.

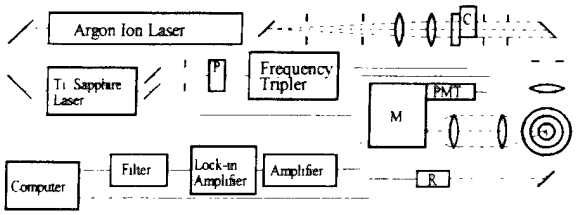

Fig. 1. Experimental setup used for the time-series measurements of OH: P, polarization rotator; C, chopper; M, 0.25-m monochromator; R, radiometer.

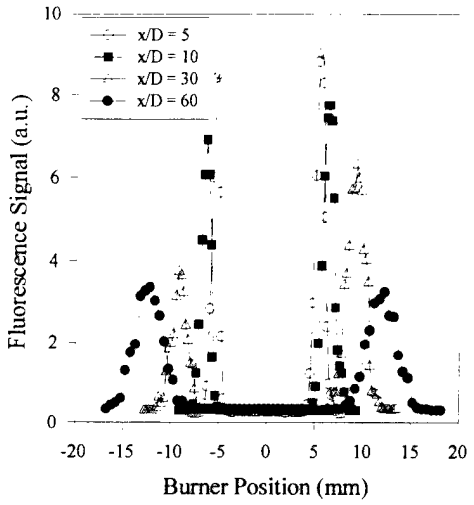

Fig. 2. Radial profiles of mean OH fluorescence signal in turbulent diffusion flame.

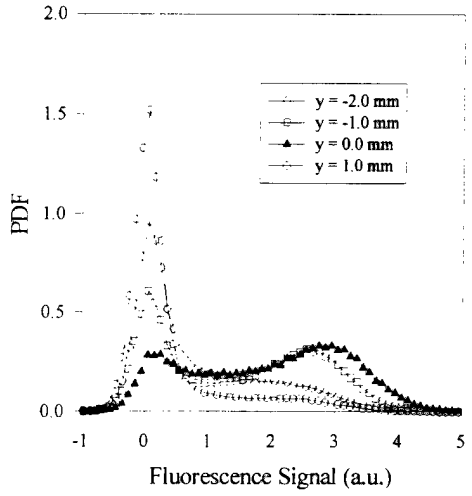

Fig. 3. PDFs measured at x/D=30 for various radial locations (y). Negative values of y are on the fuel-side of the peak (0 mm).

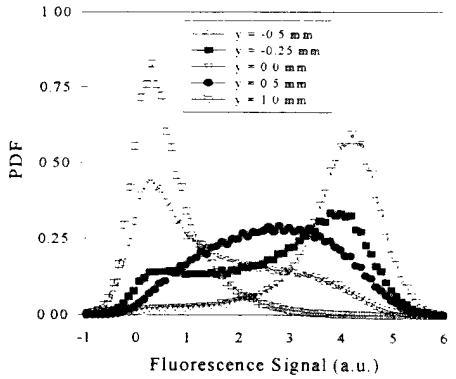

Fig. 4. PDFs measured at x/D=5 as a function of radial position (y). Negative values of y are on the fuel-side of the radial peak (0 mm).

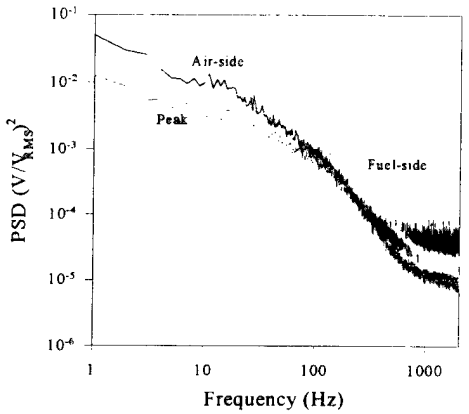

Fig. 5. PSDs measured at x/D=30. Darkest line is 1.0 mm air-side of peak, medium line is at peak, and lightest line is 1.5 mm fuel-side of peak.

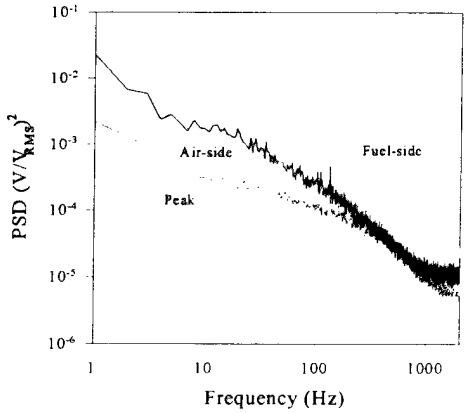

Fig. 6. PSDs measured at x/D=5. Darkest line is 0.5 mm air-side of peak, medium line is at peak, and lightest line is 0.5 mm fuel-side of peak.

FLUORESCENT DIAGNOSTICS AND FUNDAMENTAL DROPLET PROCESSES

ARO Grant DAAH04-94-G-0020

Principal Investigator: Lynn A. Melton
Co-Principal Investigator: Michael Winter*

Department of Chemistry
University of Texas at Dallas
Richardson, TX 75083-0688

SUMMARY/OVERVIEW:

This research involves the development and application of diagnostic methods which will further the understanding of the formation, evaporation, and combustion of hydrocarbon fuel sprays. This abstract will provide (1) a summary of results obtained under the title program, imaging of the transient temperature field in droplets (UTD) and imaging of internal circulation within heated droplets (UTRC) and (2) an introduction to investigations to be carried out under a new program, development of novel fluorescent diagnostics for liquid phase shear and inherent registration (UTD) and development and application of these and other diagnostics to studies of shear in liquid flows approximating realistic fuel sprays (UTRC). The diagnostics methods for liquid phase shear are expected to provide information on the processes by which bulk liquid fuel breaks up into ligaments and, ultimately, into droplets.

TECHNICAL DISCUSSION:

Current Program (UTD):

At UT-Dallas (UTD), the transient temperature field within a droplet, which has been injected as a cold droplet into high temperature nitrogen, has been imaged using combined droplet slicing imaging (DSI)/exciplex fluorescence thermometry (EFT) techniques. This work built on a succession of prior work: exciplex fluorescence thermometry (UTRC and UTD), droplet thermometry (UTD), droplet slicing imaging (UTRC), and restoration of DSI images (UTD). A room temperature decane droplet, which has been doped with the PYPYP EFT system, falls into hot (400-500 C) nitrogen. It is intercepted by a DSI laser sheet, and the resulting fluorescence is made to form two images on a CCD camera, which images are filtered to isolate two distinct wavelength regions. Restoration of both images, pixel-by-pixel ratioing of the two images, and conversion of the ratios using laboratory calibrations yields a temperature image. The images may be taken as a function of the distance the droplet has fallen since entering the high temperature region.

Images obtained with the CCD perpendicular to the DSI plane ("on axis") yield temperature information only for the interior 70% of the droplet radius; they show a rather homogeneous core temperature, which increases with droplet's fall time. Attempts to obtain images "off axis", which are predicted to give access to the "near" edge of the droplet, and consequently to "surface temperatures" have been unsuccessful, probably due to image registration problems.

The characterization of series of strongly fluorescent compounds whose total fluorescence is virtually independent of temperature and oxygen has been completed. These compounds can serve as fluorescent mass markers. However, they are relatively involatile and cannot be used for tracking the mass of automotive gasoline on engine port or cylinder walls. For some of these compounds, the fluorescent band shifts significantly with temperature and thus they can be used as thermometers. A possible application is in determining the temperature of the oil film on an engine cylinder wall.

Current Program (UTRC):

The purpose of the droplet slicing experiments carried out under this program was to investigate the shear-induced, internal motion of single fuel droplets and characterize the mass and thermal transport effects. The program utilizes 2-D imaged of laser-induced fluorescence from equatorial planes in the droplets to measure flow and temperature patterns. The slicing experiments have been performed in cold-flow, inert conditions and extended to a combustion environment with the further extension to a high pressure regime.

The nonpremixed burner, aerodynamic droplet generator and pressure vessel were described in a previous report. The flame stability has been characterized and data on the fuel/air schedule to achieve flame pressures of over 12 atmospheres has been catalogued. The data include flow rates of CH4 from 0.25 to 0.5 SLPM; air, 2.0 - 3.0 SLPM and N2 from 0 - 1.2 SLPM. Nitrogen is used as a diluent to control flame temperature and sooting.

Stable trajectories are required for reproduction of droplet position and to maintain the droplet image within the camera field of view as the droplet is tracked higher above the nozzle orifice. To date droplet injection has been achieved to 3.5 atmospheres. Motion of the droplet injector tip caused by gas flow through the nozzle is believed to limit the stability of the trajectory.

Droplet slicing experiments were performed in the inside (core region) of the non-premixed flame. Droplets were injected into the fuel flow and traveled through the flame core where they experienced a rapid temperature rise in their environment. Images of droplets from the flame at atmospheric pressure and slightly elevated pressure (1.8 atm) have been acquired. The images show subtle variations due to internal circulation. Flame conditions that might produce more pronounced circulation patterns were investigated.

New Program (UTD):

In this new program, the development and application of two new fluorescent sensors will be attempted: Microscale Unit Fluorescent Sensors (MUFS), i.e, latex spheres or other particles labelled with sensor fluorescent molecules and (2) shear sensing diagnostics.

The MUFS are a response to the request of diagnostics users for diagnostics systems with multiple capabilities, i.e, simultaneous sensing of temperature and oxygen concentration. Simultaneous sensing might be approached by adding two dopants, one optimized for oxygen sensing and one optimized for temperature sensing to the hydrocarbon liquid. In practice, this approach is likely to be unsuccessful: energy transfer between two sensor molecules which are molecularly mixed will make interpretation of the two fluorescent signals ambiguous at best. The MUFS provide a means of having the two fluorescent sensors within the same image pixel without having them mixed on a molecular level.

The 1 micron (typical) diameter of the MUFS also can make possible the development of a temperature and pressure paints with a much faster time response than is achieved with currently available pressure sensitive paints. This is in contrast to current systems in which the fluorescent sensors are encased in a thick (100 micron) layer of polymer binder and give response times on the order of seconds.

A second, and important, driving force for the MUFS systems arose from the DSI/thermometry experiments carried out at UTD and out of discussions scientists/engineers involved in wind tunnel experiments. At UTD, attempts to measure the transient temperature field within a heating droplet required ratioing of two separate images, and the exact registration of these two images proved to be quite difficult. Similar problems have been described in the use of pressure and/or temperature sensitive paints in wind tunnel tests: the images obtained under test conditions must be ratioed to initial "no flow" images, and registration is difficult (particularly so since the model may distort under aerodynamic load conditions).

The apparatus which can alleviate the registration problem is a color TV camera, in which each pixel within the camera contains three sensors (Red, Green, and Blue). There is no registration problem, because R, G, and B images are obtained simultaneously, through the same optics (and subsequently the R, G, and B images can be read out individually for further processing). However, to use such a camera, each spatial element (image pixel) on the test system (consider an airfoil in a wind tunnel as a specific example) must emit a temperature and oxygen dependent fluorescence into the RGB sensors. The experiment seems to require three fluorescent molecules: (1) a molecule whose fluorescence is independent of temperature and oxygen, (2) a molecule whose fluorescence is independent of temperature but dependent on oxygen, and (3) a molecule whose fluorescence is dependent on temperature but is independent of oxygen concentration. As noted previously, if the three fluorescent molecules are mixed on a molecular level, energy transfer effects will make the interpretation of the resulting fluorescence ambiguous. However, the key requirement is that the three emitters occupy the same spatial element on the test model. The proposed solution is then to attach the fluorescent molecules to small (typically 1 micron diameter) latex beads, one type of molecule per bead, mix the beads, and coat the beads onto the test model. Intermolecular energy transfer is eliminated, and registration and multiple parameter sensing are both achievable.

The shear sensing diagnostics are an ambitious, but probably feasible, response to the desire of scientists/engineers studying sprays to understand more clearly the breakup of the liquid into ligaments and the subsequent breakup of ligaments into droplets. If a fluorescent diagnostic becomes available which will indicate the regions of shear flow within the liquid, then shear images of sprays could be used in conjunction with other spray diagnostics and spray modeling to better understand the spray formation process.

The shear sensing diagnostics may make use of fluorescent polymers. A polymer with fluorescent chromophores attached normally exists, in a quiescent solution, as a random coil. In a shear flow, however, the coil may be distorted or even unfolded, and the fluorescence emission may change. A fluorescent system which is sensitive to these sorts of changes can provide a way to image preferentially the regions of a fuel spray in which shear flow in the liquid phase is present.

New Program (UTRC):

The purpose of the droplet slicing experiments was to investigate the shear-induced, internal motion of single fuel droplets and characterize the mass and thermal transport effects. The program utilized 2-D images of laser-induced fluorescence from equatorial planes in the

droplets to measure flow and temperature patterns. In the coming year similar methodologies will be applied to develop an understanding of strain and strain rate in the primary atomization of liquid fuel sprays.

One experimental concept relies on the principles of photoelasticty, with liquid crystals being used as the strain transducers in the liquid fuel. Phototelasticity is used extensively to measure the strain field of two dimensional solid objects by sensing the birefringence of orthogonally polarized light beams. Stress present in a normally isotropic medium causes the formation of a unique optic axis parallel to the direction of applied stress. Wavefronts that are propagated perpendicular to this optic axis are polarized into orthogonal waves with their planes of vibration parallel and perpendicular to the direction of stress. The stress produces an anisotropy in the index of refraction (birefringence) for the two polarizations and thus a relative retardation or phase shift between the waves. The retardation is proportional to the stress, cumulative over the optical path (depth of the medium) and thus is a line-of-sight technique. If the oppositely polarized waves are recombined to a single polarization upon exiting the sample, interference will be produced and can be quantitatively recorded as a fringe pattern similar to interferograms. Experimental hardware, called a polariscope, is used for this technique and includes all of the appropriate optical elements for analysis of the fringe field.

Normal liquid fuels do not have birefringent properties but the class of compounds known as liquid crystals do exhibit polarization effects when subjected to changes in their environment. The major use of these compounds has been in the field of thermometry but they are also sensitive to changes in shear stress and this property has been exploited to indicate boundary layer transition on aerodynamic surfaces. By using them as additives to the liquid fuel, an *in situ* strain transducer is produced. Special formulations have been developed by other groups that show sensitivity to shear and are independent of temperature variations. Liquid crystals are composed of long, rod-like molecules that change their orientation upon exposure to shear stress, the reorientation produces a birefringence which can be visualized with polarization sensitive optics as used in the photoelastic experiments on solids. Liquid crystals dispersed in a liquid fuel will provide sensors of the shear stress in their local region and the anisotropic refractive index will be monitored with imaging equipment. Encapsulated liquid crystals, typically used for thermometry and commercially available, do not allow the crystals to be in contact with the fuel molecules to sense the strain field. Unencapsulated liquid crystals are easily suspended in organic solvents and the experiment will depend on producing a liquid crystal formulation that is miscible in a typical hydrocarbon fuel such as decane. A simple experiment will start our investigation; injection of a sheet of liquid fuel into a fluid with different density and viscosity will establish a strain rate environment that can be analytically modelled and compared with the experimental data. Strain will be imposed on the sheet by the flow process and it can be illuminated with polarized laser light to observe intensity variations due to birefringence.

The demonstration of the utility of this new diagnostic technique will be an important step between understanding the dynamics of individual droplets and the primary atomization processes that are responsible for the droplet formation and initial spray conditions.

MOLECULAR DYNAMICS INVESTIGATION OF SUPERCRITICAL FUELS

AFOSR Grant No. F49620-97-1-0128

M. M. Micci and L. N. Long

Dept. of Aerospace Engineering
The Pennsylvania State University
University Park, PA 16802

SUMMARY/OVERVIEW:

Molecular dynamics (MD) implemented on parallel processors is being used to model supercritical fuel phenomena occurring in combustion devices. The use of molecular dynamics allows the modeling of supercritical phenomena without an a priori knowledge of the equation of state or transport properties of the individual components or the mixture. Three-dimensional supercritical oxygen evaporation into gaseous oxygen and helium using two-site Lennard-Jones potentials for the oxygen has been modeled and both the disappearance of surface tension above the critical point and the modification of the critical point for a binary mixture have been observed. Equations of state and transport coefficients for mass, momentum and energy have been calculated for supercritical argon, nitrogen and oxygen which agree with NIST values. Current work involves the modeling of hydrogen using both one and two-site potentials, calculations of equations of state and transport properties for binary mixtures, modeling of ethylene using two-site potentials and evaporation in a convective flow, all under supercritical conditions.

TECHNICAL DISCUSSION:

LOX Evaporation. The current results were obtained on either 8 or 32 nodes of IBM's Scalable Powerparallel 2 (SP-2) using the Message Passing Interface subroutine library for parallel communication. The systems consisted of roughly 20,000 molecules and the initial LOX droplet diameter was 7.7 nm. Previous work has shown that small systems accurately reproduce the results of much larger systems [1]. In order to parallelize the problem, the molecules were distributed evenly over all of the processors, regardless of their location in the computational domain. This technique, called 'atom decomposition' [2], allowed almost perfect load-balancing to be achieved. Future codes will also incorporate the 'force decomposition' technique, which parallelizes the computation of the force vectors as well. The results presented here use a common pair-wise additive intermolecular potential called the Lennard-Jones 12-6 potential. This potential contains two parameters that determine the molecular type: σ, the zero energy separation distance, and ε, the minimum energy. The gradient of this potential is used to determine the force, which is then summed over all pairs to determine the net force on a given atom. This is applied to each atom of an oxygen molecule, which is called the Lennard-Jones site-site approximation.

Although Lennard-Jones is sufficient to describe intermolecular interactions, some other method must account for constraining two oxygen atoms to be in the same molecule. Ideally, one would like to treat chemical bonds as additional terms in the potential energy equation, but this proves to be both intractable and unnecessary. Because bond vibrations tend to be both high frequency and low amplitude, one can simply fix the interatomic distance to a prescribed value with little consequence to the results of the simulation. This approach, of course, would not be valid for large molecules where torsional motion about the bonds may have to be included. Another difficulty encountered when simulating multiple chemical species is determining the appropriate Lennard-Jones parameters for interactions between unlike molecules. The results presented here use the Lorentz-Berthelot mixing rules [3]. Finite-differencing of the equations of motion was accomplished using a modification of the 'velocity Verlet' algorithm called RATTLE [4]. This algorithm constrains the bond length of the oxygen molecules to a given value within a specified tolerance through an iterative process. Both the positions and the velocities are determined at the current time step to order dt^2, and the round-off error is minimized.

Two representative cases of an oxygen droplet evaporating into a helium environment are summarized in Table 1. As a reference, the critical temperature and pressure of oxygen is 154.77 K and 5.087 MPa, respectively. The initial condition for both simulations consisted of placing a saturated droplet at 100 K into an equilibrated environment at the various conditions listed in the table. The method of the placing the droplet into the environment assured that the initial surface tension of the droplet was retained for the start of the simulation. The

simulation geometry was a cube with periodic boundaries and the time step was 2.5 femtoseconds. The potential cut-off was 2.5 σ, which refers to the intermolecular distance at which the potential between two atoms is so small as to be neglected. Energy was added to the system in order to induce evaporation by 'heating the boundaries', which amounts to scaling the velocities of the molecules in the boundary region of the cube to a value corresponding to a prescribed temperature.

A droplet in its own vapor under supercritical conditions shows significant differences in evaporation behavior, such as immediately vanishing surface tension and cloud-like density profiles [1]. The results of extending the modeling to mixtures is shown in Figures 1 and 2. These figures contain contour plots of oxygen mass fraction, density, temperature, and the average force in a cubic volume for two different helium environments at times of 250 psec and 110 psec, respectively. Because surface tension is the macroscopic manifestation of the unequal forces exerted on surface molecules in a liquid, the average force should provide an approximation of the surface tension present in the system. Hence a large surface tension would be indicated by a bright ring. The environment conditions of 300 K and 4 MPa in Figure 1 are below the critical pressure of oxygen, so subcritical behavior is expected. This is observed in the figure by a spherical droplet profile and strong surface tension. In contrast, Figure 2 contains results when the environment pressure and temperature are at 300 K and 20 MPa, which are both well above the critical point of oxygen. Although one might expect supercritical behavior, this is not observed. The droplet profile remains spherical and surface tension is retained throughout the droplet lifetime.

Case	Temperature	Pressure
1	300 K	4.0 MPa
2	300 K	20.0 MPa

Table 1: Summary of thermodynamic conditions for two different helium environments used in the LOX droplet evaporation simulations. The critical temperature and pressure of oxygen is 154.77 K and 5.087 MPa, respectively.

Equation of state and transport properties. This work involves the determination of transport coefficients and pressures of supercritical fluids by molecular dynamics (MD) simulations using the Green-Kubo formulae [5] and the virial equation of state [3], respectively. The MD program uses the effective Lennard-Jones potential, with system sizes of 256 molecules, and simulations of 500,000 timesteps for the transport coefficients computation and 50,000 timesteps for pressures. A typical timestep size of 2 fs is used for most of the simulations. The code also uses linked cell lists for efficient sorting of molecules, periodic boundary conditions and a modified velocity Verlet algorithm for particle displacement.

Simulations have been carried out on pure argon, nitrogen, and oxygen at various supercritical conditions, with self-diffusion coefficients, shear viscosity coefficients, thermal conductivity coefficients, and pressures computed for most of the conditions. Preliminary results have been compared to the National Institute of Standards and Technology (NIST) [6] values. Figure 3 shows diffusion coefficients for oxygen. It can be observed that the coefficient decreases with temperature at 3 MPa, but increases at supercritical pressures. Figures 4 and 5 show shear viscosity and thermal conductivity. The MD results compare well with the NIST values, especially at the higher temperatures. The poorer match at 160 K for the 10 and 15 MPa cases may be due to the use of an insufficient sample size as the critical temperature is approached. Figure 6 shows calculated pressures as a function of temperature for various densities. For most of the cases there is excellent agreement between the MD and NIST values. Further studies will include the computation of the properties and equation of state of liquid mixtures, and the surface of evaporating droplets. A detailed study of the error estimates of the simulations will be made.

REFERENCES

1. Little, J. K., *Simulation of Droplet Evaporation in Supercritical Environments using Parallel Molecular Dynamics*, Ph.D. thesis, The Pennsylvania State University, 1996.
2. Plimpton, S., "Fast Parallel Algorithms for Short-Range Molecular Dynamics," *J. Comp. Phys.*, **117**, pp. 1-19, 1995.
3. Allen, M. P. and Tildesly, D. J., *Computer Simulation of Liquids*, Oxford University Press, New York, NY, 1984.
4. Andersen, H. C., "RATTLE: A 'Velocity' Version of the Shake Algorithm for Molecular Dynamics Calculations," *J. Chem. Phys.*, **52**, pp. 24-34, 1983.
5. Hoheisel, C. and Vogelsang, R., "Thermal Transport Coefficients for One-Component and Two-Component Liquids from Time Correlation Functions Computed by Molecular Dynamics," *Computer Physics Report*, **18**, pp. 1-69, 1988.
6. National Institute of Standards and Technology, NIST, Thermophysical Properties of Pure Fluids Database: Version 3.0, *http://www.nist.gov/srd/nist12.htm*, Gaithersburg, MD, 1996.

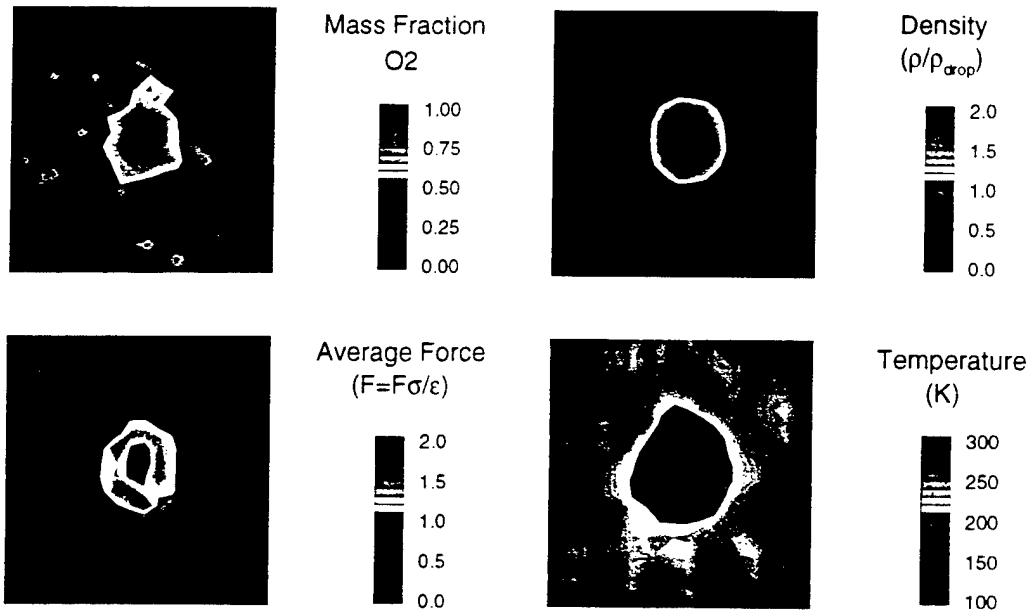

Figure 1: Contour plots of oxygen mass fraction, density, temperature, and the average force after 250 picoseconds of simulation time. The helium environment is at 300 K and 4.0 MPa, and the droplet is exhibiting subcritical evaporation behavior.

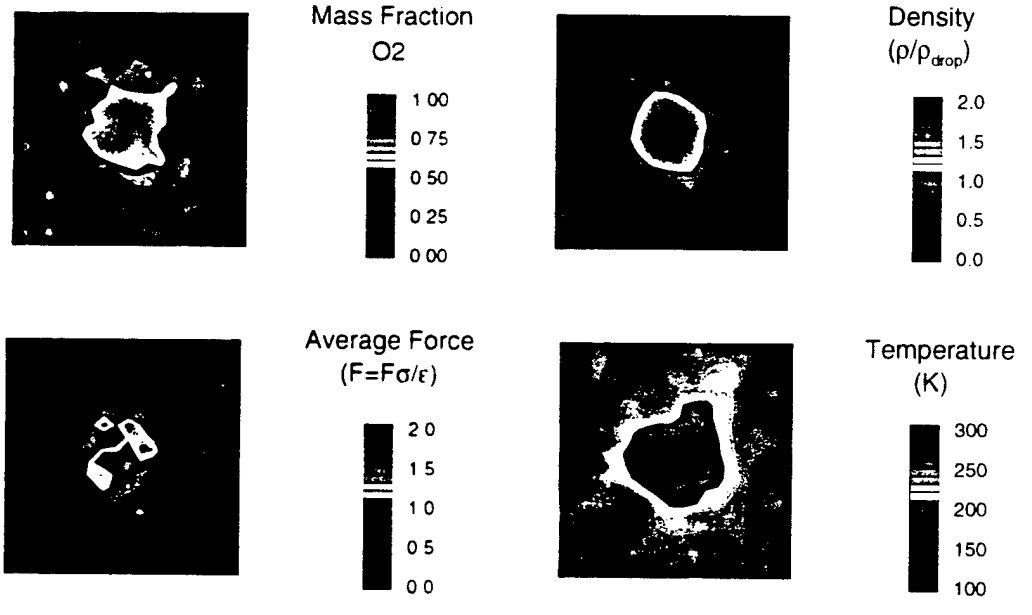

Figure 2: Contour plots of oxygen mass fraction, density, temperature, and the average force after 110 picoseconds of simulation time. The helium environment is at 300 K and 20.0 MPa, which is well above the critical point of both helium and oxygen. The droplet is still exhibiting subcritical evaporation behavior.

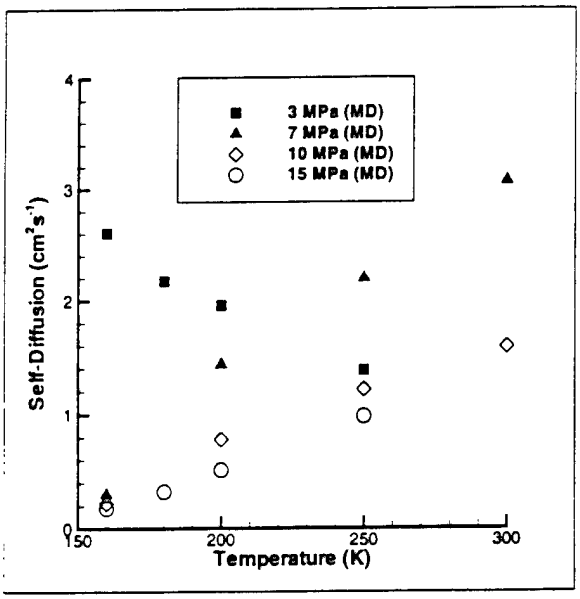

Fig. 3 Oxygen self-diffusion coefficients as a function of temperature for various pressures calculated via MD.

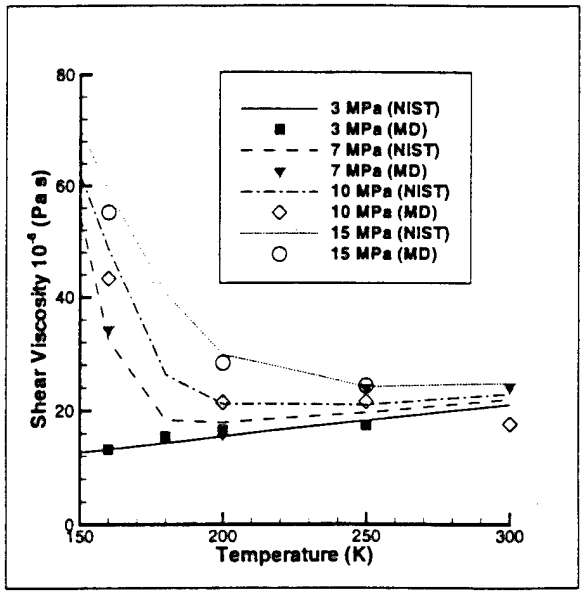

Fig. 4 Oxygen shear viscosity as a function of temperature for various pressures comparing MD and NIST calculated values.

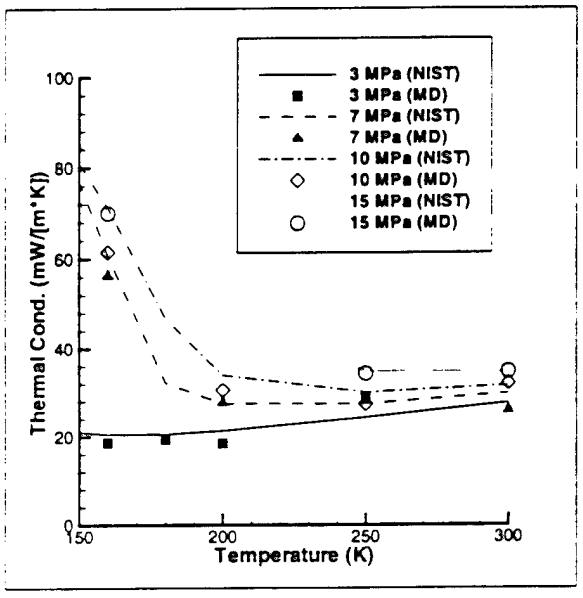

Fig. 5 Oxygen thermal conductivity as a function of temperature for various pressures comparing MD and NIST calculated values.

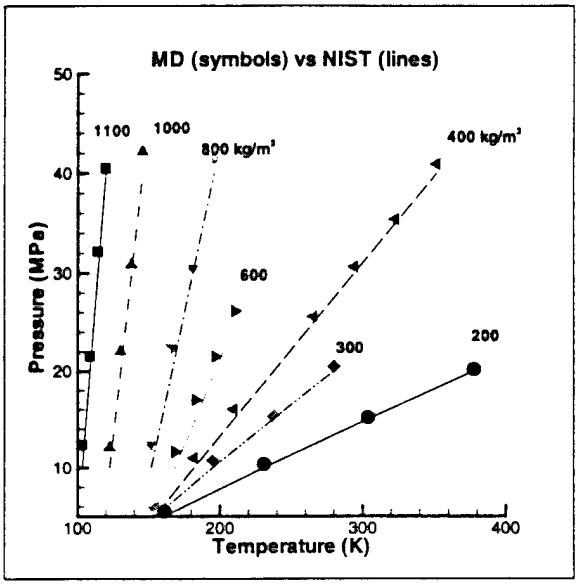

Fig. 6 Oxygen pressure as a function of temperature for various densities comparing MD and NIST calculated values.

TRANSPORT AND INTERFACIAL PHENOMENA IN MULTIPHASE COMBUSTION SYSTEMS

AFOSR Grant No. 97-1-0266
Principal Investigator: **Daniel E. Rosner**

Yale University, Department of Chemical Engineering
High Temperature Chemical Reaction Engineering Laboratory
New Haven, CT 06520-8286, USA

SUMMARY / OVERVIEW

The performance of aircraft gas turbine engines under sooting conditions and/or ramjets burning slurry fuels (leading to oxide aerosols and deposits), depends upon the formation and transport of small particles of complex morphology, often in non-isothermal combustion gas boundary layers (BLs). Aggregate formation / transport are also important in chemical reactors used to synthesize/process aerospace materials, including turbine blade coatings, optical waveguides, ceramic precursor powders,...). Accordingly, this research is directed toward providing chemical propulsion system engineers with rational new predictive techniques to deal with particle formation-transport-deposition phenomena, accounting for significant non-spherical particle morphology effects. An interactive experimental/theoretical approach is being used to gain an understanding of performance-limiting mass/energy transfer-phenomena at or near interfaces. This includes the development and exploitation of laboratory burners (Fig. 1) and new diagnostic/characterization techniques (Fig. 2). Resulting experimental data, together with the predictions of asymptotic theories (Figs. 3-6), are then used to propose and verify rational engineering correlations for future design/optimization.

TECHNICAL DISCUSSION / RECENT RESEARCH PROGRESS

Most results obtained under Grants AFOSR 94-1-0143 and 97-1-0266 during the period: 6/96-6/97 can be divided into the subsections below:

1. THERMOPHORESIS-BASED SOOT DIAGNOSTIC METHODS: THERMOPHORETIC SAMPLING PARTICLE DIAGNOSTIC (TSPD) AND THERMOCOUPLE PARTICLE DENSITOMETRY (TPD)

Last year we reported on our successful implementation (in both co-flowing laminar diffusion flames as well as counterflow diffusion flames (CDFs) (McEnally *et.al.*(1996)) of *Thermocouple Particle Densitometry* (TPD) ----a method for measuring absolute and local soot volume fractions, f_V , in flames based on the laws governing thermocouple response to *thermophoretic soot deposition*, first suggested by Eisner and Rosner (1985). Since this method is independent of (often unknown) soot optical properties (see below), is insensitive to soot morphology and size distribution, and yields spatially resolved f_V-values directly at low soot concentrations, TPD is especially applicable to spatially non-uniform and/or lightly sooting flames. However, since details of aggregated soot morphology (*eg.*, spherule diameters, fractal dimension and aggregate size distribution) are often of research and applied interest, and difficult to reliably extract from non-intrusive laser light scattering (LLS-)measurements, we have now investigated whether TEM-based thermophoretic sampling can be extended* to obtain absolute, local soot volume fractions, again making use of the laws governing *thermophoretic soot deposition* (Rosner*et.al.*(1980,1984,1988, 1991,1992) and Garcia-Ybarra and Castillo(1996)). Such a diagnostic method (Fig. 1) , which we here call: *Thermophoretic Sampling Particle Diagnostic* (TSPD), has the remarkable attribute that it is capable of giving *all* desired information about the local soot morphology/population without invoking information from other techniques, but not in "real-time". To evaluate these new and more mature methods, soot volume fractions (ppm) were recently measured in axisymmetric ethylene/air co-flowing flames. While the shape of TSPD and TPD f_V profiles (Fig.2) agreed well with published de-convoluted laser extinction measurements in a similar flame, soot volume fractions inferred from mass deposition were systematically larger than extinction results in the lowest portion of the ethylene co-flowing difffusion flame (and throughout a methane flame), evidently due to deposition of visible-light-transparent particles, known to be present in such flames. This implies that TSPD and TPD can prove to be valuable in future studies of the significance of these LLE-"invisible" soot precursors.

---

† AFOSR Contractors' Mtg : Propulsion/Airbreathing Combustion, June 17-19, 1997, Cleveland OH
‡ For research collaborators consult **REFERENCES**

**Thermophoretic sampling /TEM image analysis* (Dobbins and Megaridis, 1987, Rosner *et.al.* 1991, Koylu *et. al.* 1996) is now widely used in laboratory research on sooting flames, however , until now, not for local, absolute soot volume fraction measurements.

2. MORPHOLOGY AND TRANSPORT PROPERTIES OF FLAME-GENERATED AGGREGATES

Last year we reported (Neimark *et.al.*(1996)) that, based on our investigation of over 3000 electron microscope images of soot aggregates from a variety of laminar and turbulent *hydrocarbon*-fueled flames, combustion-generated soot aggregates should be regarded as *self-affine*, displaying statistically significant *asymmetry*. Because of their relevance to aggregate transport/radiative/stability properties, our investigations of soot aggregate morphology have continued, also using computer simulation techniques. Figure 3 shows recent results for the pdf of the angles between triplets of spherules within D_f=1.7 fractal aggregates of different size (N). This pdf will play an important role in analyzing the morphological stability of aggregates in CDFs (Xing, *et.al.*(1996), as well as their heat/mass transfer properties. Figure 4 shows our preliminary estimates of the heat loss characteristics of laser-overheated large fractal aggregates. The function shown, which is a measure of the extent of "shielding" due to spherule-spherule thermal interactions, is usually assumed to be unity in the interpretation of laser-induced incandescence (LII-) experiments to infer local soot volume fractions.

3. THEORY OF SIMULTANEOUS COAGULATION AND RESTRUCTURING

Until now, theoretical predictions of the formation, growth, coagulation, oxidation and transport in flames have been based on the (oversimplified) picture that soot particles can be treated as volume-equivalent *spheres*, locally describable by one "state" variable (*eg.*, volume or diameter). Indeed, the mathematical-computational methods which have been used to predict the evolution of soot (volume fraction) profiles for polydispersed populations (moment and sectional methods) are well-suited to the case of only one state variable. However, our recent research on both organic and inorganic combustion-generated particles (see, *eg.*, Koylu *et.al.*, (1995); Neimark *et.al.*, 1996)) demonstrates that, with the remarkable exception of *thermophoretic drift*, all important transport properties of soot particles are *morphology sensitive*, *ie.*, we must take into account the "fractal"-like morphology of actual soot *aggregates*. Typically, each is comprised of N touching spherules of mean diameter d_1, and the local population is also usually characterized by the fractal parameters: exponent D_f and the pre-factor k_g (Koylu *et.al.*,1995). Alternately, inorganic aggregates have been partially described by the *two* internal variables v and a, *viz.* volume and *surface area*---a level of description which may be adequate in the simplest of cases. In either class of situations, even apart from *chemistry* (*eg.*, chemical composition, or state of carbonization), a population of such particles at position **x** and time t would be characterized by the *multi-variate* pdf: $f(N, d_1, D_f, k_g ; \mathbf{x}, t)$ or $f(v, a ; \mathbf{x}, t)$, *not* well suited to description-prediction using moment or "sectional" (variable mesh finite-difference) methods.Anticipating that moment and sectional methods may prove to be "dead-ended" approaches to the ultimate prediction of multi-variate *pdf*s for sooting combustors, we have begun investigating the use of more versatile Monte-Carlo-based simulations of the population balance equation (PBE) (Tandon (1995), Tandon and Rosner (1997)). Indeed, we have successfully demonstrated its efficacy for the abovementioned 2-state variable (v,a) case: for the "self-preserving" (constant shape pdf): f(v,a;t) PBEdescribing an aerosol population undergoing both Brownian *coagulation*, and finite-rate *coalescence* (Tandon and Rosner(1997)). The computed unconditional dimensionless distribution function with respect to *particle suface area*, $\eta_2=a/\bar{a}$, is shown in Fig. 5, for the case of D_f=1.8 aggregates coagulating in the continuum regime for several values of the characteristic time ratio: coalescence/coagulation. Several "mixed" moments of the computed *joint pdf* (with respect to $v/\bar{v}$,$a/\bar{a}$) of future engineering interest for computing deposition rates, etc. (Rosner *et. al.*(1989)) are shown in Fig.6 for $-2 \leqslant (k,l) \leqslant +2$ and t(coalesc)/t(coag)=100, again for D_f=1.8.

CONCLUSIONS, FUTURE RESEARCH

The ability to reliably predict the transport properties and stability of *aggregated* flame-generated *particles* (carbonaceous soot, B_2O_3, Al_2O_3, ...)† is important for many technologies relevant to the U.S.A.F., especially jet engine combustor design. Indeed, realistic soot morphology is not yet even a part of chemically complex sooting *laminar* flame models, and the computational methods used to include coagulation dynamics (eg., "moment" methods) donot lend themselves to this next step. Also, some properties needed to correctly interpret the results of recently introduced laser diagnostics applied in research on soot formation/suppression (*eg.*, laser-induced incandescence (LII)) are not yet available. In our previous AFOSR program considerable experimental and theoretical progress along these lines was made /reported . This research is now being extended as described above. These experimental techniques, together with closely coupled theoretical calculations of particle birth/dynamics in counterflow diffusion flames and mixing/boundary layers, are leading to a valuable understanding of combustion-generated ultra-fine particles, including their deposition dynamics.

†Finely divided boron- and aluminum-based fuel additives for performance enhancement lead to non-carbonaceous "soots" in many air-breathing and rocket combustor situations. Moreover, trace inorganics in petroleum-based fuels, or in the air breathed for combustion (Rosner, *et.al.*,1979) likewise lead to submicron inorganic aerosols affecting system performance. In this AFOSR programe have shown that soot aggregates from a wide variety of organic and inorganic combustion systems exhibit interesting and mechanistically significant morphological similarities (Rosner (1996), Koylu *et.al.*,1995, Xing *et.al.*,1996c)

REFERENCES

Brasil, A. M., Farias, T.L., Carvalho, M.G., and Rosner, D.E., "Numerical Characterization of Morphological Features of Fractal-like Aggregates", prepared for *J. Aerosol Sci.*(1997)

Eisner, A.D. and Rosner, D.E., "Experimental Studies of Soot Particle Thermophoresis in Non-isothermal Combustion Gases Using Thermocouple Response Techniques", *Comb& Flame* **61** 153-166 (1985)

Farias, T.L., Koylu, U.O., and Carvalho, M.G., "Effects of Polydispersity of Aggregates and Primary Particles on Radiative Properties of Simulated Soot", *J. Quar Sprectroscop. Radiat. Transfer* **55** (3) 357-371 (1996)

Gomez, A., and Rosner, D.E., "Thermophoretic Effects on Particles in Counterflow Laminar Diffusion Flames", *Comb Sci. and Tech.* **89**, 335-362 (1993).

Khalil, Y.F., and Rosner, D.E., "Erosion Rate Prediction Technique for Ceramic Surfaces Exposed to High Speed Flows of Abrasive Suspensions", *J. WEAR.*, **201** , 64-79 (1996); also: *Proc. 5th World Congress ChE* (June 1996) Vol. IV, , 1013-1018.

Koylu, U., Xing, Y., and Rosner, D.E., "Fractal Morphology Analysis of Combustion-Generated Aggregates Using Angular Light Scattering and Electron Microscope Images", *Langmuir* (ACS) **11** (12) 4848-4854 (1995)

Koylu, U.O., McEnally, C., Rosner, D.E.and Pfefferle, L, "Simultaneous Measurements of Soot Volume Fraction and Particle Size/Microstructure in Flames Using a Thermophoretic Sampling Technique", *Comb & Flame* (in press, 1997)

Mackowski, D.W., Tassopoulos, M. and Rosner, D.E., "Effect of Radiative Heat Transfer on the Coagulation Dynamics of Combustion-Generated Particles", *Aerosol Sci. Technol (AAAR)* **20**, 83-99 (1994).

McEnally, C.S., Koylu, U.O., Pfefferle, L.D. and Rosner, D.E., "Soot Volume Fraction and Temperature Measurements in Laminar Non-Premixed Flames Using Thermocouples", *Comb & Flame* (in press, 1997)

Neimark, A.V., Koylu, U.O. and Rosner, D.E., "Extended Characterization of Combustion-Generated Aggregates: Self-Affinity and Lacunarities", *J. Colloid Interface Sci.* **180**,590-597 (1996)

Rosner, D.E. "Transport Phenomena and Interfacial Kinetics in Multiphase Combustion Systems", *Proc. AFOSR Contractors Mtg. on Airbreathing Combustion/Propulsion Diagnostics*, June 3-6, 1996, Virginia Beach VA,

Rosner, D.E., Mackowski, D.W and Garcia-Ybarra, P., "Size and Structure-Insensitivity of the Thermophoretic Transport of Aggregated 'Soot' Particles in Gases", *Comb. Sci & Technology* **80** (1-3), 87-101 (1991).

Rosner, D.E., Mackowski, D.W, Tassopoulos, M., Castillo, J.L., and Garcia-Ybarra, P., "Effects of Heat Transfer on the Dynamics and Transport of Small Particles in Gases", *I&EC-Research (ACS)* **31** (3), 760-769 (1992).

Rosner, D.E., **Transport Processes in Chemically Reacting Flow Systems**, Butterworth-Heinemann (Stoneham MA), 3d Printing (1990) sold out; for 4th printing contact author directly; 2d ed. in prep.

Rosner, D.E. and Park, H.., "Thermophoretically Augmented Mass, Momentum, and Energy Transfer Rates in High Particle Mass-Loaded Laminar Forced Convection Systems" *Chem Eng. Sci.* **43** (10) 2689-2704(1988)

Rosner, D.E. and Tandon, P., "Prediction and Correlation of Accessible Area of Large Multi-Particle Aggregates", *AIChE J.* **40** (7) 1167-1182 (1994)

Rosner, D.E. and Tandon, P., "Rational Prediction of Inertially Induced Particle *Deposition* Rates for a Cylindrical Target in a Dust-Laden Stream" *Chem Eng. Sci.* **50** (21) 3409-3431(1995)

Rosner, D.E., Tandon, P. and Labowsky, M.J., "Rapid Estimation of (Metal-)Cylinder *Erosion* Rates in Abrasive Dust-Laden Streams", *AIChE J.* **41** (5)1081-1098 (1995)

Rosner, D.E. and Tassopoulos, M.,"Deposition Rates from 'Polydispersed' Particle Populations of Arbitrary Spread", *AIChE J.* **35** (9) 1497-1508 (1989)

Rosner, D.E., Tassopoulos, M. and Tandon, P., "Sensitivity of Total Mass Deposition Rate and Resulting Deposit Microstructure to Morphology of Coagulation-Aged Aerosol Populations of Aggregated Primary Particles", **1st Int. Particle Technology Forum** (AIChE, IChE), Denver CO, August 17-19, 1994

Rosner, D.E., and Papadopoulos, D., "Jump, Slip, and Creep Boundary Conditions at Non-Equilibrium Gas/Solid Interfaces", *I&EC-Research (ACS)* **35** (9), 3210-3222 (1996).

Tandon, P., and Rosner, D.E., "Translational Brownian Diffusion Coefficient of Large (Multi-particle) Suspended Aggregates", *Ind Eng Chem-Res* (ACS) **34** 3265-3277(1995)

Tandon, P., and Rosner, D.E., "Monte-Carlo Simulation of of Fractal Particle Aggregation and Restructuring", J. *Colloid Int. Sci* (submitted,1997)

Tandon, P., and Rosner, D.E., "Sintering Kinetics and Transport Property Evolution of Large Multi-Particle Aggregates", *Chem. Eng. Communic.* (S.K. Friedlander issue), **151**, 147-168 (1996)

Xing, Y., Koylu, U.O., and Rosner, D.E., a) "Synthesis and Restructuring of Inorganic Nano-particles Particles in Counterflow Diffusion Flames",*Comb & Flame* **107**, 85-102(1996); also:b) Paper #88d , Vol. V, *5th World Congress ChE* (June 1996), pp. 43-48.

Xing, Y., and Rosner, D.E.,"Surface Melting of Particles: Predicting Spherule Size in Vapor-Phase Nanometer Particle Formation", Paper#V5.36, MRS Fall 1996 Meeting, Dec. 4, 1996, Boston MA; Full-length paper in preparation,1997.

Xing, Y., Rosner, D.E., Koylu, U.O. and Tandon, P., "Morphological Evolution of Oxide Nano-particles in Laminar Counterflow Diffusion Flames---Measurements and Modelling", *AIChE J.* (in press , 1997)

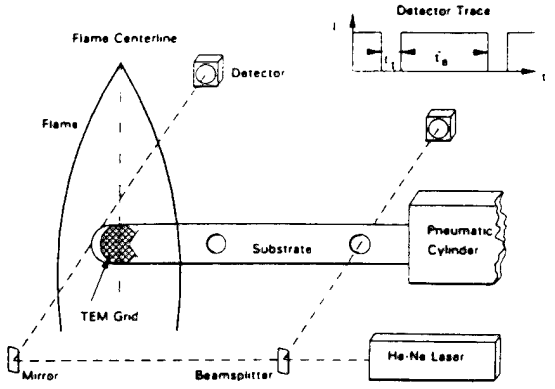

Fig. 1. Schematic of the experimental arrangement for TSPD, emphasizing methods used for precisely positioning the TEM grid relative to the ethylene diffusion flame centerline, and determining grid exposure time (after Koylu *et.al.* (1997))

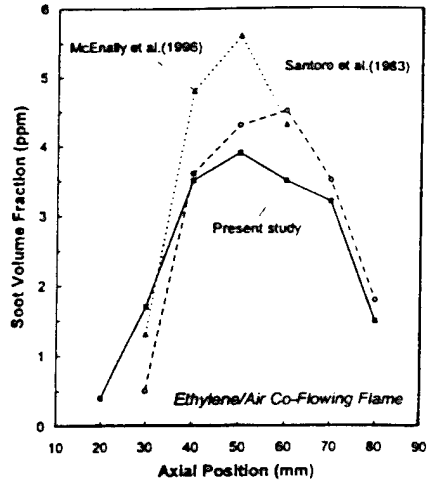

Fig. 2. Comparison of inferred local soot volume fractions (ppm) determined along the flame centerline by TSPD (this work; Koylu *et.al.*(1997)), laser light extinction (LLE) (Santoro*et al.*(1983), and thermocouple particle densitometry (TPD) (Rosner(1996),McEnally *et.al.*(1997))

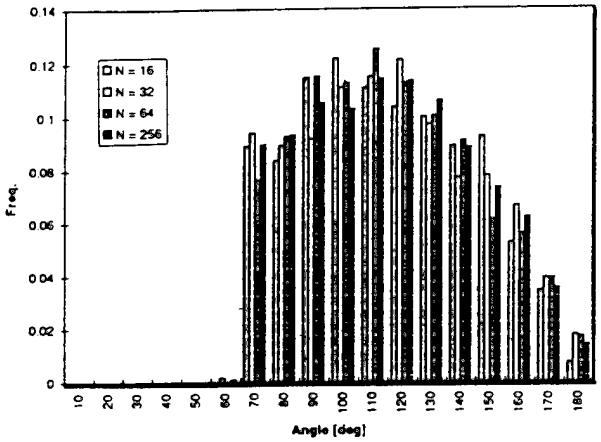

Fig. 3. Computed probability distribution functions for the angles between spherule triplets in computer-simulated cluster-cluster fractal aggregates containing N spherules (after Brasil *et.al.*(1997)

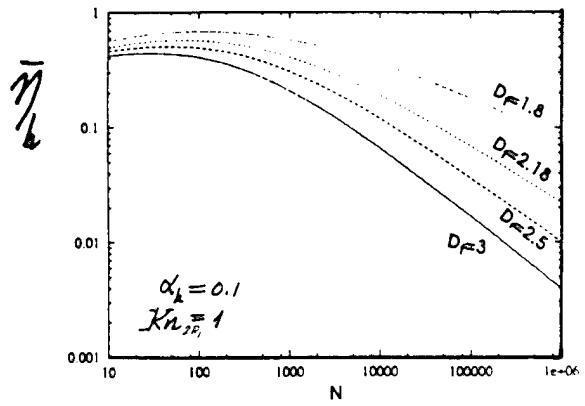

Fig. 4. Estimated correction factor to the heat loss behavior of an N-spherule la :ser pulse over-heated fractal aggregate (ratio of actual rate of heat loss by diffusion to that expected in the isolated spherule free-molecule limit); after Rosner *et.al.*(1997)

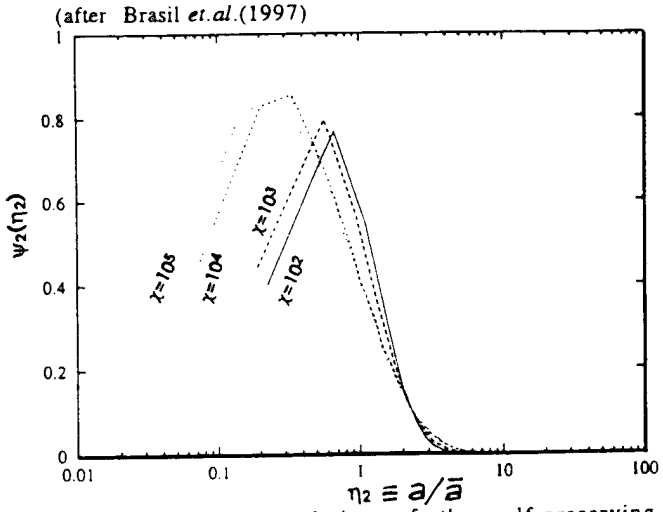

Fig. 5. Monte-Carlo simulation of the self-preserving distribution function with respect to *surface area* of a population of coagulating-restructuring D_f=1.8 particles in the continuum limit, at several values of the ratio: characteristic coalescence time/characteristic coagulation time (after Tandon and Rosner(1997))

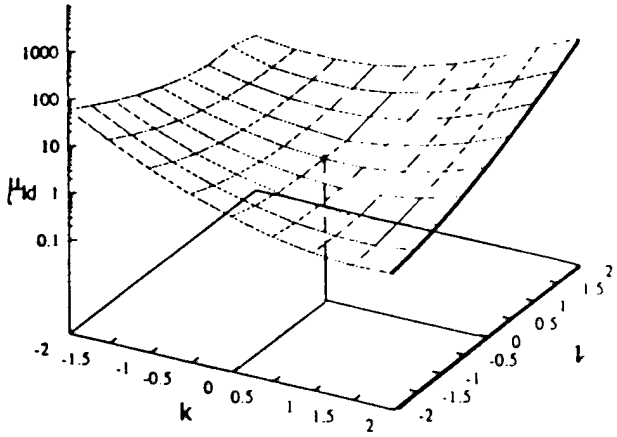

Fig. 6. Predicted 'mixed ' *moments*, μ_{kl}, of the joint probability density function with respect to particle *volume* and *area* for D_f=1.8 particles coagulating with t(coalesc)/t(coag)= 100; after Tandon and Rosner(1997))

SOOT FORMATION IN TURBULENT COMBUSTING FLOWS

AFOSR Grant/Contract No. F49620-97-1-0094

Principal Investigator: R. J. Santoro

Propulsion Engineering Research Center
and
Department of Mechanical Engineering
The Pennsylvania State University
University Park, PA 16802-2320

SUMMARY/OVERVIEW

Current interest in high performance, low emissions gas turbine engines by the Air Force underscores the need for research on soot formation processes, since soot formation is intimately involved in issues related to performance and operability. Although recent research efforts by a number of researchers have provided significant advances in terms of understanding the basic mechanisms controlling soot formation and destruction, many questions remain. In particular, an understanding of soot formation under high pressure and turbulent flame conditions is lacking. Since gas turbine combustors characteristically involve such flows, it is necessary to address these conditions if further progress is to be made. The current studies are specifically directed at providing measurements of soot formation and destruction in atmospheric and high pressure turbulent flames. Emphasis is placed on providing quantitative soot volume fraction, temperature, velocity and radical species concentration measurements for a systematic set of turbulent flame conditions. Information will also be obtained on the characteristic turbulent length scales for the various scalar quantities and their variation with flame conditions. The resulting data base is intended to provide the needed insight to develop the understanding required for implementing advanced design methodologies for future gas turbine combustors.

TECHNICAL DISCUSSION

Studies of soot formation in turbulent diffusion flames under atmospheric and elevated pressure conditions are being conducted to determine the controlling phenomena governing soot inception, growth and oxidation. Ethylene (C_2H_4) has been selected as the fuel and the soot formation process in the turbulent diffusion flames resulting from combustion of the fuel jet issuing into quiescent air is being investigated as a function of Reynolds number. Fuel jets issuing from tubes of 2.18 and 4.12 mm have been studied for Reynolds numbers ranging from 4000 to 12,000. The flame configuration selected closely follows that of Turns and Myhr [1] since a large comparative data base with respect to radiation and NO_x emissions exists for these flames.

The initial studies have focused on soot volume fraction measurements using laser-induced incandescence (LII), OH radical and polycyclic aromatic hydrocarbon (PAH) measurements using laser-induced fluorescence (LIF) and temperature measurements using Coherent Anti-Stokes

Raman Spectroscopy (CARS). The application of the LII technique for soot measurements is noteworthy since it allows quantitative soot volume fraction measurements to be obtained locally. Recent studies of the LII technique have demonstrated that it is capable of quantitative soot volume fraction measurements if an appropriate calibration source is utilized [2-4]. In the discussion that follows the soot volume fraction and OH radical concentration measurement results will be emphasized.

A schematic representation of the apparatus used to obtain soot volume fraction and OH radical concentration measurements is shown in figure 1. The frequency doubled output (532 nm) of a Nd:YAG pulse laser is divided into two separate beams using a dichroic mirror (70% reflection and 30% transmission). One of the 532 nm beams is directed into a dye laser and wavelength extender (WEX) to produce UV light at 283.55 nm which is used to excite OH radicals in the flame. The remaining 532 nm green beam is used for the LII measurements.

The output of the WEX is then recombined with the 532 nm beam and both beams are passed through a combination of spherical and cylindrical lens to produce a thin ($\approx$300 μm) planar laser sheet which passes through the center of the flame. The resulting signals are then detected at an angle of 90° with respect to the light sheet using an intensified CCD camera having a 576x384 pixel resolution. The recorded images are subsequently stored on a laboratory personal computer system.

The resulting two-dimensional images provide a wealth of information on the structure of the soot particle and OH radical fields in these turbulent diffusion flames as the Reynolds number is varied. The ability to obtain instantaneous, quantitative information on the soot volume fraction is of particular interest in the present studies. Although the research program has only recently begun, some of the initial results are worth noting. First, the instantaneous soot volume fraction measurements indicate that the maximum observed soot volume fraction is nearly an order of magnitude higher than the temporally averaged mean value for the soot volume fraction. This fact is due to the highly wrinkled structure of turbulent flames that leads to localized high concentrations of soot particles that when temporally (and consequently spatially) averaged over the flame result in significantly lower mean values. Since the impact of soot on combustion performance and emissions is dominated by local interactions, it is this information which is key to understanding how soot affects gas turbine combustor operations. Furthermore, the results indicate three distinct soot formation/destruction related regions. The first region is characterized by rapid soot growth and is typified by a shift of the soot particle laden regions towards the center of the flame as the Reynolds number is increased. However the location of the maximum mean soot volume fraction is not sensitive to the Reynolds number and occurs at the same axial distance as the Reynolds number increases from 4000 to 12,000 for a given fuel jet diameter. Laser-induced fluorescence imaging of the PAH clearly demarcate the soot growth region in these flames.

In the soot growth region, the OH radical and soot particle fields lie in distinctly different locations with the OH radicals located further from the flame centerline. Following this region of rapid growth, a mixing dominated zone observed that is strongly affected by increases in the Reynolds number. Mixing processes in this region affect the maximum soot volume fraction measured in an individual flame with the soot volume fraction decreasing with increasing Reynolds number in agreement with previous work. The final region involves the interaction of the OH radical and soot particle fields. Here the OH radical and soot regions overlap often

leading to rapid oxidation. Only the high soot concentration regions formed lower in the flame survive this process to be emitted from the flame as smoke.

Differences in the mixing characteristics between the OH radical and soot particle concentration fields have been observed in terms of the mean width (or thickness) of the structures imaged as a function of axial location in the flame (see figure 2). For the OH radicals, thin structures typically having a mean width of about 1 mm are observed low in the flame. At higher locations in the flames, the width of the OH structures increases to a mean value of about 6 mm. In contrast, the soot particle field maintains a characteristic width of between 1 and 2 mm throughout the flame with only a slight increase in width as a function of axial location. Thus, the transport and mixing of the OH and soot in these turbulent flames show distinctively different features. In the higher regions of the flame, the large OH structures are observed to overlap the soot structures and, as mentioned previously, likely contribute to the rapid oxidation of soot.

Although the above discussion highlights some of the important findings of the work to date, it is limited in the degree to which it can be used to model soot formation in turbulent flames. Current work is emphasizing complementary temperature and velocity measurements in order to more fully characterize the thermal and temporal environment in which soot forms and grows. These measurements are also being combined with laser light scattering measurements in order to investigate particle size variations observed for these turbulent diffusion flames. Additional work is also proceeding on the high pressure apparatus which will be used to study flames at pressures as high as ten atmospheres.

REFERENCES

1. Turns, S. R. and Myhr, F.H., "Oxides of Nitrogen Emissions from Turbulent Jet Flames Part I - Fuel Effects and Flame Radiation," *Combustion and Flame*, 87, pp. 319-335, 1991.
2. Quay, B., Lee, T-W., Ni, T. and Santoro, R. J., "Spatially Resolved Measurements of Soot Volume Fraction Using Laser-Induced Incandescence," *Combustion and Flame*, 97, pp. 384-392, 1994.
3. Ni, T., Pinson, J. A., Gupta, S., and Santoro, R. J., "Two-Dimensional Imaging of Soot Volume Fraction by the Use of Laser-Induced Incandescence," *Applied Optics*, 34, pp. 7083-7091, 1995.
4. Shaddix, C. R., and Smyth, K. C., "Laser-Induced Fluorescence Measurements of Production in Steady and Flickering Methane, Propane, and Ethylene Diffusion Flames," *Combustion and Flame*, 107, 418-452, 1996.

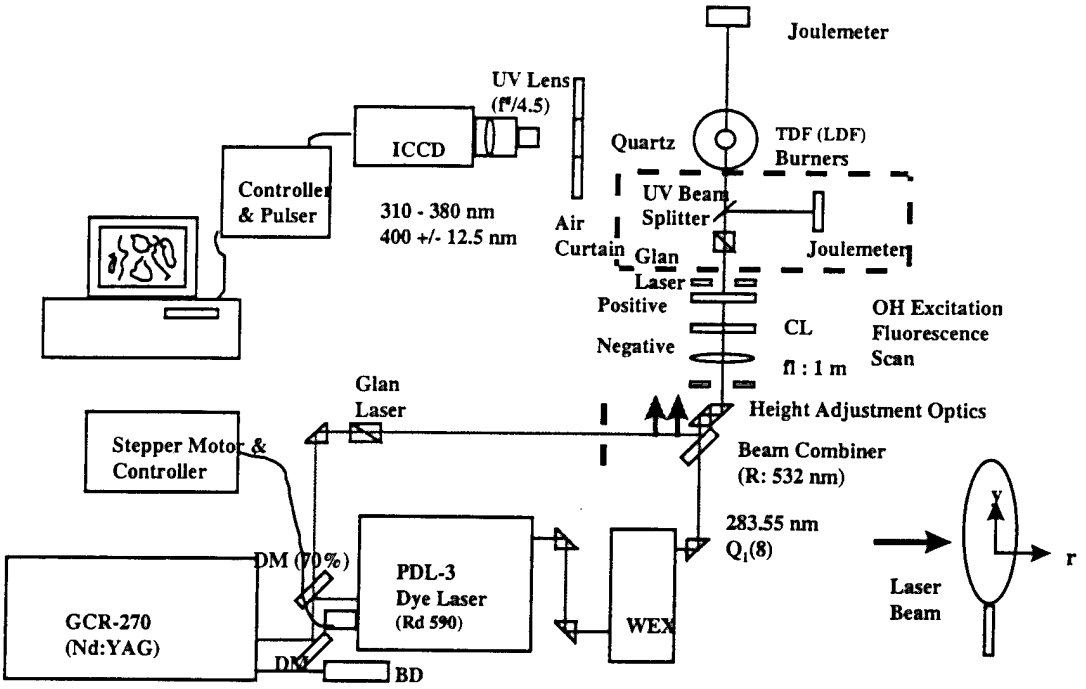

Figure 1. Optical configuration for laser-induced incandescence measurement of soot volume fraction and laser-induced fluorescence measurement of OH radicals.

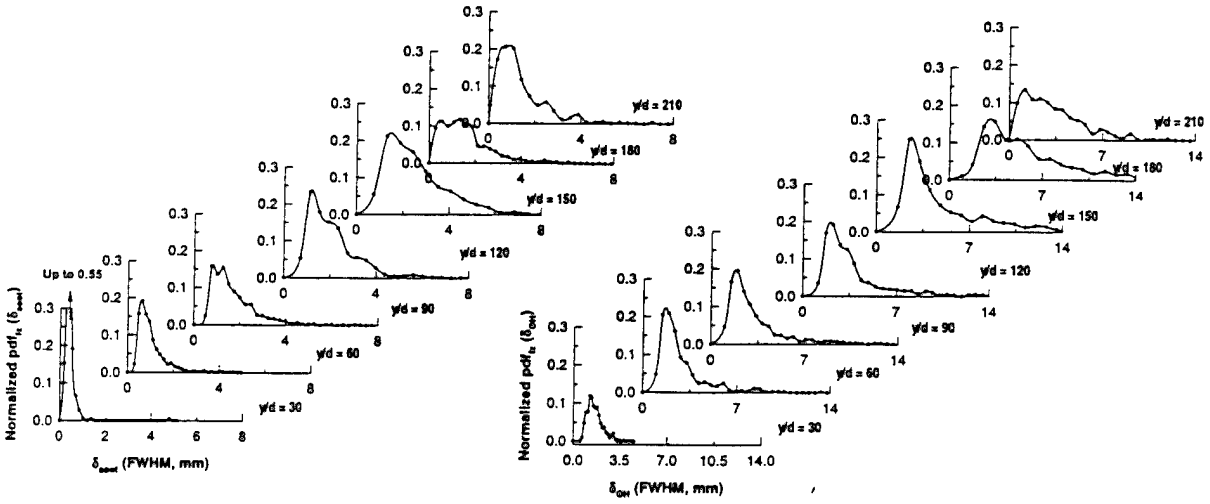

Figure 2. Probability density function of the thickness of the soot and OH zones in the Re = 12000 turbulent flame (ethylene/air).

AFOSR SPONSORED RESEARCH IN AIRBREATHING COMBUSTION

PROGRAM MANAGER: JULIAN M. TISHKOFF

AFOSR/NA
BOLLING AFB DC 20332-8050

SUMMARY/OVERVIEW: The Air Force Office of Scientific Research (AFOSR) program in airbreathing combustion currently is focused on seven areas of study: supersonic combustion, reacting flow, soot, sprays, kinetics, diagnostic methods, and thermal instability of fuels. An assessment of major research needs in each of these areas is presented.

TECHNICAL DISCUSSION

AFOSR is the single manager for Air Force basic research, including efforts based on external proposals and in-house work at Air Force laboratories. Airbreathing combustion is assigned to the AFOSR Directorate of Aerospace and Materials Sciences along with programs in rocket propulsion and fluid and solid mechanics.

Interests of the AFOSR airbreathing combustion task are given in the SUMMARY section above. Many achievements can be cited for these interests, yet imposing fundamental research challenges remain. The objective of the program is publications in the refereed scientific literature describing significant new understanding of multiphase turbulent reacting flow. Incremental improvements to existing scientific approaches, hardware development and computer codes fall outside the scope of this objective. Decisions on support for research proposals are based on scientific opportunities and technology needs.

Major emphasis has been given to research on supersonic combustion to support hypersonic airbreathing propulsion technology through the Air Force New World Vistas (NWV) study. Hypersonics is one of the NWV topics selected for financial support beginning in Fiscal Year 1997. Two areas of specific interest for scramjets are the utilization oh hydrocarbon fuels and the impact of plasma species on combustion and mixing.

An ongoing area of interest is the behavior of fuels in propulsion systems prior to combustion. Future systems will require fuels to absorb substantial thermal energy, raising fuel temperatures to supercritical thermodynamic conditions. Understanding and controlling fuel properties at these conditions will be crucial for avoiding thermal degradation and for subsequent processes within the combustor. This research activity particularly impacts the utilization of endothermic fuels in both gas turbines and scramjets.

Research on novel diagnostic methods for combustion now is a component of airbreathing combustion. This research area previously had been a separate research activity. A primary area of interest is the characterization of chemical species and thermodynamic and fluid dynamic

parameters in reacting gas-phase flow. A new research interest is the extension of quantitative optical spectroscopic methods to high pressure environments up to 10 MPa. Additional topics include measurement of primary and secondary liquid atomization and characterization of supercritical fluid behavior.

Research interests continue in understanding and controlling the formation of soot and in understanding and modeling turbulent reacting flows and fuel sprays. A new concern for turbulent reacting flows is compliance with environmental regulations both within the United States and internationally. This concern motivated the activity that has been conducted under the Department of Defense Focused Research Initiative topic, High Performance, Low Emissions Gas Turbine Combustors.

The purpose of this abstract has been to communicate AFOSR perceptions of research trends to the university and industrial research communities. However, communication from those communities back to AFOSR also is desirable and essential for creating new research opportunities. Therefore, all proposals and inquiries for fundamental research are encouraged even if the content does not fall within the areas of emphasis described herein. Comments and criticisms of current AFOSR programs also are welcome.

COMPUTATIONAL INVESTIGATION OF ATOMIZATION

(AFOSR-contract FA9620-96-1-0356)

Grétar Tryggvason
Department of Mechanical Engineering and Applied Mechanics
The University of Michigan
Ann Arbor, MI 48109-2121

SUMMARY/OVERVIEW:

Atomization of liquid fuels are studied by direct numerical simulations. The Navier-Stokes equations are solved by a finite difference/front tracking technique that allows resolution of inertial and viscous forces as well as the inclusion of surface tension at the deformable boundary between the fuel and the air. The main part of the study focuses on the secondary breakup of drops, but the primary breakup of jets is also being examined. The focus is on those aspect of the breakup that are difficult to address experimentally, such as the behavior at high pressures and temperatures.

TECHNICAL DISCUSSION

We are conduct simulations that follow the deformations and breakup of drops for both shock generated disturbances as well as gradual disturbances, fully accounting for inertial and viscous effects for both the drop and the ambient gas as well as surface tension effects. The simulations will help determine where in parameter space the various breakup modes take place, how long breakup takes, and what the resulting drop size distribution is. The effect of heat and mass transfer on the breakup process will be investigated. The goal of the investigation is to provide results that extend and compliment experimental investigations, and taken together with available experimental results, the result will provide a nearly complete picture of the process.

These computations are made possible by a recently developed numerical technique that has been used already for a number of multifluid problems. The method incorporates an explicit tracking of the drop surface with a finite difference method for the full Navier-Stokes equations for the drop and the ambient gas. Arbitrary differences in density and viscosity are possible, large surface deformations are allowed and surface tension is fully accounted for. For problems with mass and heat transfer, conservation equations for mass and energy are solved also. The technique has been used for two-dimensional, axisymmetric, and fully three-dimensional problems and validated extensively by comparisons with analytical solutions for simple cases, other numerical studies, grid refinement, and experiments.

Several simulations of the breakup of accelerated axisymmetric drops have been conducted for low density differences, we have a reasonably complete a picture of how a drop subject to a gradual disturbance breaks up. The motion is governed by three nondimensional numbers in this case, since density difference only sets the time scale. The Eotvos number is the ratio of the constant acceleration and surface tension, the Ohnsorge number is the ratio of the viscous force to the surface tension force. A second Ohnsorge number can be formed using the properties of the ambient fluid, or we can simply use the viscosity ratio as

the third nondimensional number. For small Eotvos numbers the drop remain spherical, independently of Ohnsorge number and viscosity ratio. For low Ohnsorge numbers the deformations of the drop depend only on the Eotvos number. As the Eotvos number is increased, the drops deform into a disk-like shape due to high pressure at the fore and aft stagnation points and low pressure around the equator. For relatively low Eo, the drop do not break-up, but move with a steady state deformation. Increasing the Eo further, results in a continuing deformation where most of the drop fluid ends up in a torous connected by a thin film. For these drops, the initial momentum is relatively low and once the torous is formed it falls faster than the film, which "bulges" back. Experimentally, this "bag" is seen to break eventually. Increasing the Eotvos even more, results in a different mode of breakup. The fluid initially still ends up in the rim of the drop, but the initial momentum is now sufficiently large that the ambient fluid moves the film faster than the torous, leading to a bag that extends forward of the drop. During the transition from one breakup mode to the other, we find drops that initially develop a small forward extending bag, that slows down and becomes a backward facing bag as the drop falls. The transition has been explained partially in terms of the dynamics of vorticity generated at the drop surface, and work has been started to identify the vortex dynamics of the different shear breakup modes. For nearly equal viscosities, we always find a torous connected by a thin film at high Eotwos number. The film forms a forward or backward facing bag. Only for larger viscosity ratios do we see shear breakup where most of the drop fluid remains near the center of drop and the rim is pulled of by the ambient fluid. At high Ohnsorge numbers, the boundary between the various modes move to a higher Eotvos number as the Ohnsorge number is increased. The effect of viscosity ratio must also be taken into effect.

Figure 1 shows two example from our simulations of axisymmetric break up of drops. In both cases, the drop is shown at a relatively late stage in the breakup. In addition to the shape of the drop, vorticity contours are shown on the left of the centerline and streamlines in a stationary frame of reference is shown to the right of the axis. The Ohnsorge number based on the drop properties is the same in both figures (Oh=0.0466). In the figure on the left, the Eotvos number is low (Eo=24) and the viscosities are nearly equal but in the figure on the right, Eo=144 and the viscosity ratio is equal to five.

We are currently examining the effect of larger density ratios and shock disturbances where the Eotvos number is replaced by a Weber number. Many aspects of the evolution are the same, but the dependency of the various boundaries move in parameter space. While we have done some comparisons with experimental results for the low density difference runs, experimental data is more abundant for larger ratios. Those simulations should therefore allow us to conduct more extensive comparisons.

To start looking at the shear breakup of jets, we have done several two-dimensional simulations of periodic shear layers. The Reynolds numbers have been selected to be sufficiently high so that the initial instability is well predicted by inviscid theory, but viscous effects become important at larger amplitude. The linear stability analysis predicts that surface tension stabilizes short waves and yields a wavelength with a largest linear growth rate (most unstable wave). Generally, we find that the inviscidly most unstable wavelength saturates quickly and perturbations of longer wavelength are the ones that grow to larger amplitude. Exactly which wavelength is the most dangerous one depends on the Reynolds number. We have, so far, conducted two sets of simulations, one at very small density differences and the other one at density ratios of ten. For weak stratification, surface tension prevents Kelvin-Helmholtz roll-up as seen for miscible fluids and fingers of one fluid penetrate the other fluid. The slope of these fingers depends on the nondimensional wavelength (Weber number). While viscous effects limit the growth of these fingers at low Weber numbers, high Weber number fingers can become very long. At even higher Weber numbers the interface start to exhibit a behavior more similar to the

classical nonlinear Kelvin-Helmholtz instability and rollup. The transition is complex, however, and we find intermediate states where the interface folds over once before being stretched into a long finger, for example. At larger density ratio, the evolution is no longer symmetric and we find waves of the heavy liquid that grow into the lighter one. As for the weak stratification, waves with wavelength close to the most unstable one are generally stabilized at large amplitude by viscous effects but longer wavelengths lead to a "wave breaking" where a finger of the heavy fluid is pulled into the lighter fluid by the effect of the shear. Even in the two-dimensional simulations, these fingers eventually break down into drops. The slope of the "fingers" and the size of the resulting drops depends on the nondimensional wavelength (Weber number). Figure 2 shows one example of a simulation of the evolution of the interface for the stronger stratification.

While the two-dimensional simulations give invaluable insight into the initial evolution of a wave, we believe strongly that three-dimensional effects quickly become important at large amplitude. To address the three-dimensional effects we are currently conducting three-dimensional simulations where we use initial perturbations in the cross stream direction also. Because three-dimensional computations are much more expensive and time consuming than two-dimensional ones, we are currently using lower Reynolds numbers which can be resolved on coarser grids. Two-dimensional tests have shown that the qualitative behavior is the same as at higher Reynolds numbers if the Weber number is adjusted properly. Preliminary results indicate that while the initial growth and wave steapening is essentially two-dimensional, three-dimensionality set in quickly after that and can lead to a finger that penetrates the lighter fluid parallel to the jet in a way similar to the "fiber breakup" mode seen experimentally at high Reynolds and Weber numbers in axisymmetric jets.

In addition to the shear breakup of the fluid interface, we have done a few preliminary simulations of the breakup of a fluid interface by unsteady vortical flows. The simulations are motivated by theories that predict that jet breakup is determined strongly by the turbulence level of the flow and caused by turbulent eddies colliding with the interface. Figure 3 shows results from one of those simulations where a vortex ring colliding with the interface forms a "finger" of one fluid penetrating far into the other fluid. The shape of the fluid interface is shown at four times, with time increasing to the left.

The work during the first ten months of this project has focused on axisymmetric and two-dimensional simulations of the break-up of drops and fluid interfaces. These simulations have helped establish the various modes of evolution and shown the initial deformations in both cases. We have already started fully three-dimensional simulations and expect to be putting major emphasis on those aspects during next year.

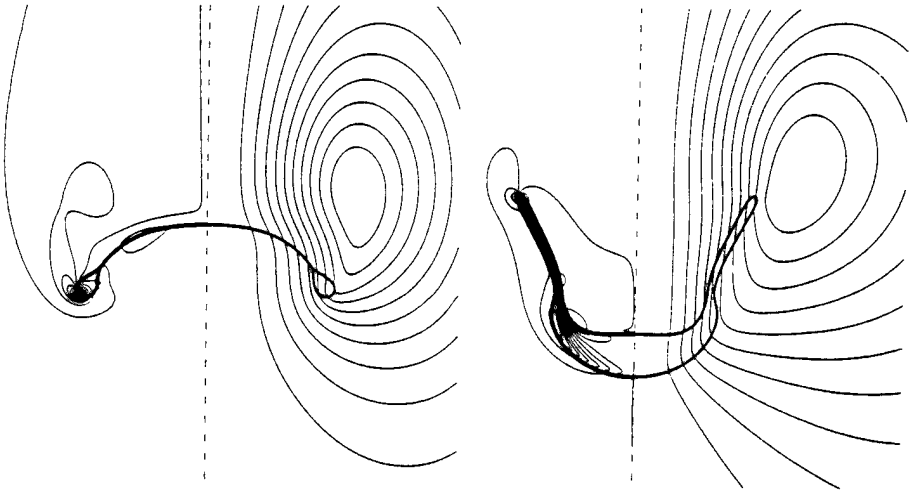

Figure 1. Two example from our simulations of axisymmetric break-up of drops. The shape of the drop and vorticity contours are shown on the left and the stream function is shown on the right. Oh=0.0466 and Eo=24 for the left frame and Eo=144 for the right frame. The viscosities are nearly equal but in the figure on the right and five for the left frame.

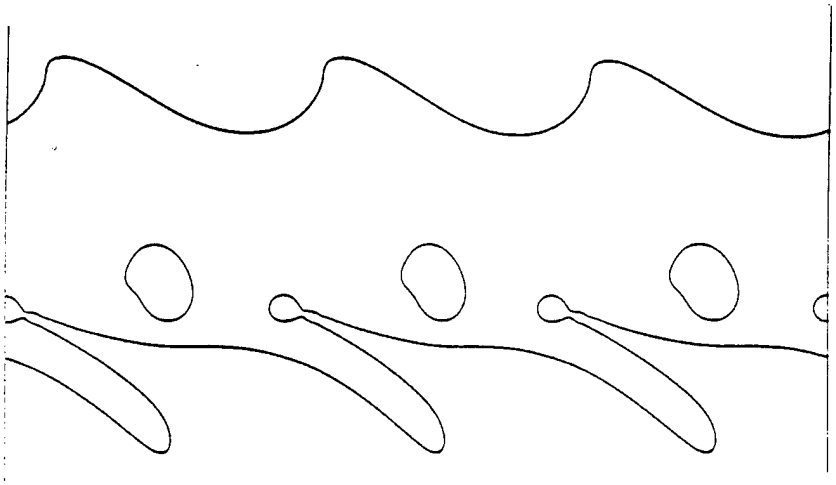

Figure 2. Simulations of the break-up of a fluid interface. The interface is shown at an early time (top) and after it has broken up. The density ratio is ten and Reynolds number is 5000, based on the perturbation wavelength. The Weber number is 5.0.

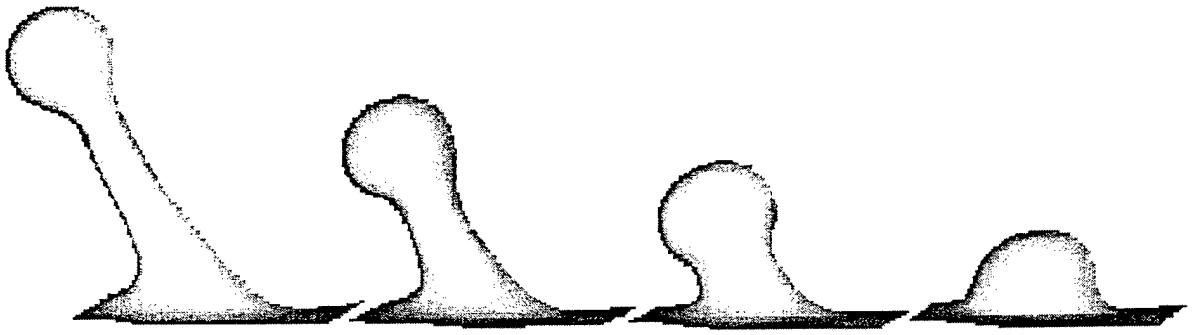

Figure 3. The results from a simulation of a vortex ring colliding with a fluid interface to form a "finger" of one fluid penetrating far into the other fluid. The shape of the fluid interface is shown at four times, with time increasing to the left.

INVITEES

Dr. M. S. Anand
Allison Engine Company
P.O. Box 420
Speed Code T-14
Indianapolis IN 46206-0420
(317)230-2828
FAX:230-3691
iemsa@agt.gmeds.com

Dr. William Anderson
AMSRL-WT-PC
US Army Research Laboratory
Aberdeen Proving Ground MD 21005-5066
(410)278-9992
DSN 298-9992
FAX: 278-7333
willie@arl.army.mil

Dr Griffin Anderson
NASA Langley Research Center
M/S 168
Hampton VA 23681
(804)864-6238
FAX:864-6243
g.y.anderson@larc.nasa.gov

Dr Kurt Annen
Aerodyne Research, Inc.
45 Manning Road
Manning Park Research Center
Billerica MA 01821-3976
(508)663-9500
FAX:663-4918
kannen@aerodyne.com

Dr William Bachalo
Aerometrics, Inc.
755 North Mary Avenue
Sunnyvale CA 94086-9175
(408)738-6688
FAX:738-6871

Mr. Lee Bain
WL/POP
Building 18
1950 Fifth Street, Suite 10
Wright-Patterson AFB OH 45433-7251
(937)255-1237
DSN 785-1237

Dr S L Baughcum
Boeing Company
P O Box 3707, MS 6H-FC
Seattle WA 98124
(425)965-0426
FAX:234-4543
baughcum@atc.boeing.com

Dr Howard Baum
National Institute of
Standards and Technology
Center for Fire Research
Gaithersburg MD 20899
(301)975-6668

Dr John Bdzil
Los Alamos National Laboratory
Los Alamos NM 87545

Dr. Bruce Beaver
Department of Chemistry
Duquesne University
Mellon Hall
Pittsburgh PA 15282-1503
(412)434-6340
FAX:434-5683

Mr. Steve Beckel
Pratt and Whitney
M/S 715-83
P.O. Box 109600
West Palm Beach FL 33410-9600

Dr Edward Beiting
Aerophysics Lab, Prop & Env Sc
The Aerospace Corporation
P O Box 92957, M5/754
Los Angeles CA 90009-2957
(310)336-7035

Dr Josette Bellan
Applied Technologies Section
Jet Propulsion Laboratory
4800 Oak Grove Drive
Pasadena CA 91109
(818)354-6959

Dr Michael Berman
AFOSR/NL
110 Duncan Avenue, Suite B115
Bolling AFB DC 20332-8050
(202)767-4963
DSN 297-4963
FAX:404-7475
michael.berman@afosr.af.mil

Dr. Robert Bill
Propulsion Dir, Army Res. Lab.
NASA Lewis Res. Ctr., MS 77-12
21000 Brookpark Road
Cleveland OH 44135-3191

Dr Mitat Birkan
AFOSR/NA
110 Duncan Avenue, Suite B115
Bolling AFB DC 20332-8050
(202)767-4938
DSN 297-4938
FAX:767-4988
mitat.birkan@afosr.af.mil

Dr Kevin Bowcutt
North American Aircraft Div.
Rockwell International Corp.
P.O. Box 3644
Seal Beach CA 90740-7644

Dr C T Bowman
Department of Mechanical
Engineering
Stanford University
Stanford CA 94305-3032
(415)723-1745
FAX:723-1748
bowman@navier.stanford.edu

Dr K N C Bray
University of Cambridge
Department of Engineering
Trumpington Street
Cambridge CB2 1PZ, England UK
0223 332744
0223 337733
FAX0223 332662

Dr Robert Breidenthal
Department of Aeronautics and
Astronautics
University of Washington, FS10
Seattle WA 98195
(206)685-1098

Dr Kenneth Brezinsky
Department of Chemical Engrg
University of Illinois-Chicago
810 S. Clinton St, Room 204
Chicago IL 60607-7000
(312)996-3424
kenbrez@tigger.cc.uic.edu

Dr Garry Brown
Department of Mechanical and
Aerospace Engineering
Princeton University
Princeton NJ 08544-5263
(609)258-6083
GLB@pucc.princeton.edu

Dr R C Brown
Aerodyne Research, Inc.
45 Manning Road
Manning Park Research Center
Billerica MA 01821-3976
(508)663-9500
FAX:663-4918

Dr. Adam Bruckner
Aerospace and Energ Rsrch Prog
University of Washington
120 Aero&Eng Rsrch Bldg FL-10
Seattle WA 98195
(206)543-6321
FAX:543-4719
bruckner@aa.washington.edu

Dr. Walter Bryzik
Propulsion Systems Division
ATTN: DRSTA-RGD
USA Tank-Automotive Command
Warren MI 48397-5000
(810)574-6461
FAX: 574-5054

Dr John D Buckmaster
Department of Aerospace
Engineering
University of Illinois
Urbana IL 61801

Dr Dennis Bushnell
NASA Langley Research Center
Mail Stop 110
Hampton VA 23681
(804)864-4546
d.m.bushnell@larc.nasa.gov

Dr Ron Butler
WL/POSF
Building 490
1790 Loop Road, N
Wright-Patterson AFB OH 45433-7103

Dr T D Butler
Group T-3
Los Alamos National Laboratory
Los Alamos NM 87545
(505)667-4156

Dr H F Calcote
Titan Corp, AeroChem Rsrch Lab
50 Washington Road
P. O. Box 2229
Princeton NJ 08543-2229
(609)716-1201
FAX:716-1204
hcalcote@titan.com

Mr. Donald Campbell
NASA Lewis Research Center
21000 Brookpark Road
Mail Stop 3-2
Cleveland OH 44135
(216)433-2929
(216)433-5266

Dr Graham V Candler
Department of Aerospace
Engineering & Mechanics
University of Minnesota
Minneapolis MN 55455

Dr Brian Cantwell
Department of
Mechanical Engineering
Stanford University
Stanford CA 94305-3032
(415)723-4825

Dr. Ismail Celik
Department of Mechanical and
Aerospace Engineering
West Virginia University
Morgantown WV 26506

Dr. Nicholas Cernansky
Mechanical Engineering Dept.
Drexel University
32nd and Chestnut Streets
Philadelphia PA 19104-2884

Dr Richard Chang
Applied Physics Department
P. O. Box 208284
Yale University
New Haven CT 06520-8284
(203)432-4272
FAX: 432-4274
RK_CHANG@RAMAN.ENG.YALE.EDU

Dr Chine I Chang
AFOSR/NA
110 Duncan Avenue, Suite B115
Bolling AFB DC 20332-8050
(202)767-0467
DSN 297-4067
FAX:767-4988
jim.chang@afosr.af.mil

Dr Tryfon Charalampopoulos
Mechanical Engineering Dept.
Louisiana State University
Baton Rouge LA 70803
(504)388-5792
(504)388-5799
FAX:388-5894

Dr. Harsha Chelliah
Department of Mechanical, Aero
and Nuclear Engineering
University of Virginia
Charlottesville VA 22903-2442
(804)924-6037
FAX:982-2037
harsha@virginia.edu

Dr. Jacqueline Chen
MS 9051
Sandia National Laboratories
P.O. Box 969
Livermore CA 94551-0969
(510)294-2586
FAX:294-1012
jhchen@sandia.gov

Dr Lea D Chen
Mechanical Engineering Dept
University of Iowa
Iowa City IA 52242
(319)335-5674
FAX:335-5669
ldchen@icaen.uiowa.edu

Dr Wai K Cheng
Department of Mechanical Engineering
MIT
Cambridge MA 02139
(617)253-4531

Dr Robert Childs
Nielsen Engineering and Research, Inc.
510 Clyde Avenue
Mountain View CA 94043-2287
(415)968-9457

Dr S Y Cho
Department of Mechanical and Aerospace Engineering
Princeton University
Princeton NJ 08544-5263

Dr M-S Chou
Building R1, Room 1044
TRW Space and Technology Group
One Space Park
Redondo Beach CA 90278
(310)812-0469
FAX:812-7589

Mr R.W. Claus
NASA Lewis Research Center
21000 Brookpark Road
Cleveland OH 44135-3127
(216)433-5869

Dr M B Colket
United Technologies Research Center
411 Silver Lane
East Hartford CT 06108
(860)610-7481
(860)658-9502
FAX:610-2151
colketmb@utrc.utc.com

Dr S M Correa
GE Research Center
K1-ES210
P. O. Box 8
Schenectady NY 12301
(518)387-5853
FAX:387-7258
correa@crd.ge.com

Dr David Crosley
Molecular Physics Department
SRI International
333 Ravenswood Avenue
Menlo Park CA 94025-3696
(415)326-6200

Dr Clayton Crowe
Department of Mechanical Engineering
Washington State University
Pullman WA 99164-2920
(509)335-3214

Dr F E C Culick
Engrg. and Appl. Sci. Dept.
California Institute of
Technology
Pasadena CA 91125
(818)395-4470

Dr E T Curran
WL/PO
Building 18
1950 Fifth Street
Wright-Patterson AFB OH 45433-7251
(513)255-2520
DSN 785-2520
FAX:476-4657

Dr Eli Dabora
Mechanical Engineering Dept
University of Connecticut
Box U-139 ME
Storrs CT 06268
(203)486-2415
(203)486-2189

Dr Werner Dahm
Department of Aerospace
Engineering
The University of Michigan
Ann Arbor MI 48109-2118
(313)764-4318
(313)761-2026
FAX:763-0578
wdahm@engin.umich.edu

Dr John Daily
Center for Combustion Research
Mechanical Engineering Dept
University of Colorado
Boulder CO 80309
(303)492-7151

Dr Ron Davis
Chemical Science and Techn Lab
Building 221, Room B312
National Inst of Stds & Tech
Gaithersburg MD 20899

Dr. PeterA. DeBarber
MetroLaser
18006 Skypark Circle #108
Irvine CA 92714-6428

Dr Pablo G Debenedetti
Department of Chemical
Engineering
Princeton University
Princeton NJ 08544-5263
(609)258-5480
PDEBENE@princeton.edu

Dr George Deiwert
NASA Ames Research Center
MS 230-2
Moffett Field CA 94035
(415)604-6198

Dr. Andrew E. DePristo
U.S. Department of Energy
ER-141, E-420
19901 Germantown Road
Germantown MD 20874-1290
(301)903-6891
FAX:903-4110
depristo@pobox.com

Dr R W Dibble
Department of Mechanical Eng
6159 Etcheverry Hall
University of California
Berkeley CA 94720
(415)642-4901
FAX:642-6163
rdibble@firebug.me.berkeley.edu

Dr Paul Dimotakis
California Institute of Tech
1201 East California Blvd.
MC 301-46
Pasadena CA 91125
(818)395-4456
(818)395-4447
dimotakis@caltech.edu

Dr Gregory Dobbs
United Technologies Research
Center - Mail Stop 90
Silver Lane
East Hartford CT 06108
(860)610-7145

Mr Lee Dodge
Southwest Research Institute
P O Drawer 28510
San Antonio TX 78284
(512)684-5111
Ext 3251

Dr Michael Drake
Physical Chemistry Department
General Motors Research Labs
Twelve Mile and Mound Roads
Warren MI 48090-9055

Dr. James F. Driscoll
Department of Aerospace Engrg
3004 FXB Building
University of Michigan
Ann Arbor MI 49109-2118
(313)939-0101
james_driscoll@engin.umich.edu

Dr. J. Philip Drummond
NASA Langley Research Center
Mail Stop 156
Hampton VA 23681-0001
(757)864-2298
FAX:864-7923
j.p.drummond@larc.nasa.gov

Dr Frederick Dryer
Department of Mechanical and
Aerospace Engineering
Princeton University
Princeton NJ 08544-5263
(609)258-5206

Dr C Dutton
Department of Mechanical and
Industrial Engineering
University of Illinois
Urbana IL 61801

Dr Harry Dwyer
Department of Mechanical
Engineering
University of California
Davis CA 95616

Dr A C Eckbreth
United Technologies Research
Center
411 Silver Lane
East Hartford CT 06108
(860)610-7269

Dr. Charles A. Eckert
Department of Chemical Engrg
Georgia Institute of
Technology
Atlanta GA 30332-0100
(404)853-9344
FAX:894-6956

Dr Raymond Edelman
WC 70
Rocketdyne
6633 Canoga Avenue
Canoga Park CA 91304
(818)586-1247

Dr J T Edwards
WL/POSF
Building 490
1790 Loop Road, N
Wright-Patterson AFB OH 45433-7103
(937)255-3524
DSN 785-3524
FAX:255-1125
edwardst@ward.appl.wpafb.af.mil

Dr. Fokion N. Egolfopoulos
Department of Mechanical Engrg
University of Southern Calif
Olin Hall 400B
Los Angeles CA 90089-1453
(213)740-0480
egolfopo@alnitak.usc.edu

Ms Charlotte Eigel
WL/POSF
Building 490
1790 Loop Road, N
Wright-Patterson AFB OH 45433-7103
(937)255-5106
DSN 785-5106

Dr Said Elghobashi
Department of Mechanical
Engineering
University of California
Irvine CA 92717
(714)856-6002

Dr Phillip Emmerman
Harry Diamond Laboratories
Attn. SLCHD-ST-RD
2800 Powder Mill Road
Adelphi MD 20783-1197
(301)394-3000

Dr K C Ernst
Pratt and Whitney Aircraft
Group
Government Products Division
West Palm Beach FL 33402

Dr G M Faeth
Department of Aerospace
Engineering
University of Michigan
Ann Arbor MI 48109-2118
(313)764-7202
FAX:763-0578
gmfaeth@engin.umich.edu

Dr. Daniel Fant
South Carolina Energy Research
and Development Center
386-2 College Avenue
Clemson SC 29634-5180
(864)656-2267
FAX:656-1429

Dr Gregory W Faris
Molecular Physics Laboratory
SRI International
333 Ravenswood Avenue
Menlo Park CA 94025-3493
(415)859-4131
FAX:859-6196
faris@mplvax.sri.com

Dr Francis Fendell
TRW Space and Technology Group
Building R1, Room 1022
One Space Park
Redondo Beach CA 90278
(213)812-0327

Dr Richard Field
U. S. Army Armament R&D Center
DRSMC-LCA-G(D)
Building 382-S
Dover NJ 07801
(201)724-5844
(201)724-5682

Dr Farley Fisher
National Science Foundation
Chemical and Thermal Syst Div
4201 Wilson Boulevard
Arlington VA 22230
ffisher@nsf.gov

Dr Arthur Fontijn
Department of Chemical and
Environmental Engineering
Rensselaer Polytechnic Inst.
Troy NY 12180-3590
(518)276-6508
FAX:276-4030
fontijn@rpitsmts.edu

Dr. David E. Foster
Engine Research Center
University of Wisconsin
Madison WI 53706
(608)263-1617

Dr Michael Frenklach
Department of Mechanical
Engineering
University of California
Berkeley CA 94720-1740
(510)643-1676
FAX:642-6163
myf@euler.berkeley.edu

Mr Jack Fultz
WL/POPR
Wright-Patterson AFB OH 45433-6563
(937)255-2175
DSN 785-2175

Dr Bish Ganguly
WL/POOD
2645 Fifth Street, Suite 13
Wright-Patterson AFB OH 45433-7919
(937)255-2923
DSN 785-2923
FAX:476-4095

Dr Alon Gany
Faculty of Aerospace Engrg
Technion-Israel Institute of
Technology
32000 Haifa, ISRAEL
972-4-8292554
FAX:972-4-8230956
gany@aerodyne.technion.ac.il

Dr Alan Garscadden
WL/CA
Building 45
2130 Eighth Street, Suite 1
Wright-Patterson AFB OH 45433-7542
(937)255-9400
DSN 785-9400
FAX:785-6641

Dr Ahmed Ghoniem
Department of Mechanical
Engineering
MIT
Cambridge MA 02139
(617)253-2295
FAX:253-5981
ghoniem@mit.edu

Mr R Giffen
General Electric Company
Aircraft Engine Group
Neumann Way
Cincinnati OH 45215

Dr P Givi
Department of Mechanical and
Aerospace Engineering
State University of New York
Buffalo NY 14260

Dr Irvin Glassman
Department of Mechanical and
Aerospace Engineering
Princeton University
Princeton NJ 08544-5263
(609)258-5199
(813)442-1118
FAX:258-5963
glassman@princeton.edu

Dr Mark Glauser
AFOSR/NA
110 Duncan Avenue, Suite B115
Bolling AFB DC 20332-8050
(202)767-4936
DSN 297-4936
FAX:767-4988

Dr. Jay P. Gore
School of Mechanical Engrg
Purdue University
1003 Chaffee Hall
West Lafayette IN 47907-1003
(317)494-1500
FAX:494-0530

Dr A D Gosman
Department of Mechanical Engrg
Imperial College of Science
and Technology
London WS7 2BX UK

Dr Larry Goss
Research Applications Division
Systems Research Labs, Inc.
2800 Indian Ripple Road
Dayton OH 45440-3696
(513)252-2706

Dr Frederick Gouldin
Department of Mechanical and
Aerospace Engineering
Cornell University
Ithaca NY 14853-5692
(607)255-5280

Dr F Grinstein
Laboratory for Computational
Physics & Fluid Dynamics
Naval Research Laboratory
Washington DC 20375-5344

Dr Ephraim Gutmark
Mechanical Engineering Dept
2508 CEBA
Louisiana State University
Baton Rouge LA 70803
(504)388-5899
(504)388-5792
FAX:388-5924
gutmark@me.lsu.edu

Dr. Mark A. Hagenmaier
WL/POPS
Building 18
1950 Fifth Street, Suite 10
Wright-Patterson AFB OH 45433-7251
(937)255-5210
DSN 785-5210
FAX:476-4659
hagenma@possum.appl.wpafb.af.mil

Dr. Robert B. Hall
SAF AQR
1919 South Eads Street
Suite 100
Arlington VA 22202-3053
(703)746-8914
DSN 286-8914
(703)746-8918
hall@aqpo.hq.af.mil

Dr Robert D. Hancock
WL/POSC
Building 490
1790 Loop Road, N
Wright-Patterson AFB OH 45433-7103
(937)255-7487
DSN 785-7487
FAX:255-1125
hancockr@ward.appl.wpafb.af.mil

Dr Ronald Hanson
Department of Mechanical
Engineering
Stanford University
Stanford CA 94305-3032
(415)723-4023
FAX:723-1748
rhanson@cdr.stanford.edu

Dr Stephen Harris
Physical Chemistry Department
General Motors Research Labs
30500 Mound Road
Warren MI 48090-9055
(313)986-1305

Dr D L Hartley
Sandia National Laboratories
MS0735
Albuquerque NM 87185-5800

Dr Simon Henbest
Airframes & Engines Division
Aero & Maritime Research Lab
P O 4331
Melbourne, Victoria AUSTRALIA 3001
(03)647 7585
FAX:646 6771
henbests@aedmel.arl.dsto.gov.au

Dr Cecil F. Hess
MetroLaser
18006 Skypark Circle
Suite 108
Irvine CA 92714-6428
(714)553-0688
FAX:553-0495

Dr L Hesselink
Department of Aeronautics and
Astronautics
Stanford University
Stanford CA 94305-3032
(415)723-3466

Dr E D Hirleman
Department of Mechanical and
Aerospace Engineering
Arizona State University
Tempe AZ 85287
(602)965-3895
FAX:965-1384

Mr Norman Hirsch
WL/POPR
Wright-Patterson AFB OH 45433-6563
(937)255-2175
DSN 785-2175

Dr David Hofeldt
125 Mechanical Engineering
111 Church Street, S E
University of Minnesota
Minneapolis MN 55455
(612)625-2045

Mr Robert Holland
United Technologies Chemical
Systems Division
P O Box 49028
San Jose CA 95161-9028
(408)224-7656

Dr Hans G Hornung
Graduate Aeronautical Labs
California Institute of
Technology
Pasadena CA 91125
(818)395-4551
hans@galcit.caltech.edu

Dr David Huestis
Molecular Physics
SRI International
333 Ravenswood Avenue
Menlo Park CA 94025-3493
(415)859-3464
(415)325-4568
FAX:859-6196
huestis@mp1vax.sri.com

Dr Lawrence Hunter
Applied Physics Laboratory
Johns Hopkins University
Johns Hopkins Road
Laurel MD 20707-6099
(301)953-5000
Ext. 7406

Dr A K M F Hussain
Mechanical Engineering Dept
4800 Calhoun Road
University of Houston
Houston TX 77204-4792
(713)743-4545
FAX:743-4503
mece1w@jetson.uh.edu

Dr Essam A Ibrahim
Department of Mechanical
Engineering
Tuskegee University
Tuskegee AL 36088
(205)727-8974
FAX:727-8090
emeei@acd.tusk.edu

Dr Thomas Ishii
Department of Electrical
Engineering
Marquette University
Milwaukee WI 53233
(414)288-6998
FAX:288-7082

Dr. Joseph Janni
AFOSR/CC
110 Duncan Avenue, Suite B115
Bolling AFB DC 20332-8050
(202)767-5017
DSN 297-5017
FAX:767-6213
janni@afosr.af.mil

Dr Jay Jeffries
SRI International
333 Ravenswood Avenue
Menlo Park CA 94025-3493
(415)859-6341
(415)473-1553
FAX:859-6196
jeffries@mp1vax.sri.com

Mr. Jeff Jensen
Kaiser-Marquardt
16555 Staycoy Street
Van Nuys CA 91406

Mr Gordon Jensen
United Technologies Chemical
Systems Division
P O Box 49028
San Jose CA 95161-9028
(408)365-5552

Dr Sheridan Johnston
Combustion Sciences
Sandia National Laboratories
Livermore CA 94551-0969
(510)294-2138

Mr. Craig Johnston
Lockheed Advanced Dev. Company
Lockheed-Martin Corporation
1011 Lockheed Way
Palmdale CA 93599-7212

Dr K Kailasanath
Code 6410, LCP&FD
US Naval Research Laboratory
4555 Overlook Avenue, SW
Washington DC 20375-5344
(202)767-2402
FAX:767-4798
KAILASANATH@lcp.nrl.navy.mil

Dr Ann Karagozian
Department of Mechanical and
Aerospace Engineering
University of California, LA
Los Angeles CA 90095-1597
(310)825-5653
FAX:206-4830
ark@seas.ucla.edu

Dr Laurence R Keefe
Nielsen Engineering and
Research, Inc.
510 Clyde Avenue
Mountain View CA 94043-2287
(415)968-9457
FAX:968-1410

Dr Dennis Keefer
University of Tennessee
Space Institute
Gas Diagnostics Research Div.
Tullahoma TN 37388-8897
(615)455-0631

Dr Arnold Kelly
Department of Mechanical and
Aerospace Engineering
Princeton University
Princeton NJ 08544-5263
(609)258-5221

Dr John Kelly
Altex Technologies Corporation
650 Nuttman Road
Suite 114
Santa Clara CA 95054
(408)980-8610

Dr Lawrence A Kennedy
Department of Mechanical
Engineering
The Ohio State University
Columbus OH 43210-1107
(614)292-5782

Dr Ian Kennedy
Mechanical & Aero Engrg
University of California,
Davis
Davis CA 95616-5294
(916)752-2796
FAX:752-4158
IMKENNEDY@ucdavis.edu

Dr James Kezerle
Gas Research Institute
8600 West Bryn Mawr Avenue
Chicago IL 60631
(312)399-8331

Dr G B King
Department of Mechanical
Engineering
Purdue University
West Lafayette IN 47907
(317)494-6518
kinggb@ecn.purdue.edu

Dr Merrill K King
NASA Headquarters
Code SNB
300 E Street, SW
Washington DC 20546
(202)358-0818

Dr William H Kirchhoff
Division of Chemical Sciences
Office of Basic Energy Science
Department of Energy
Washington DC 20585
(301)903-5820
william.kirchhoff%er@mailgw.er.doe.gov

Dr. David E. Klett
Mechanical Engineering Dept
North Carolina Agricultural
and Technical State Univ
Greensboro NC 27401-3209

Dr Charles Kolb
Aerodyne Research, Inc.
45 Manning Road
Manning Park Research Center
Billerica MA 01821-3976
(508)663-9500
FAX:663-4918

Dr Wolfgang Kollmann
Mechanical & Aerospace Engrg
University of California,
Davis
Davis CA 95616-5295
(916)752-4152
FAX:752-4158
wkollmann@ucdavis.edu

Dr George Kosaly
Mechanical Engineering Dept
University of Washington
Box 352600
Seattle WA 98195-2600
(206)543-6933
FAX:685-8047
kosaly@u.washington.edu

Mr David Kruczynski
Attn SLCBR-IBA
Interior Ballistics Division
Army Research Laboratory
Aberdeen Proving Gnd MD 21005-5066
(410)278-6202
DSN 298-6202

Dr Kenneth Kuo
Department of Mechanical
Engineering
Pennsylvania State University
University Park PA 16802
(814)865-6741
FAX:863-3203

Dr. Ming-Chia Lai
Department of Mechanical Engrg
Wayne State University
Detroit MI 48202

Dr Samuel C Lambert
WL/CA-M
101 West Eglin Boulevard
Suite 101
Eglin AFB FL 32542-6810
(904)882-3002
DSN 872-3002
FAX:882-3006

Dr Marshall Lapp
High Temperature Interfaces
Division
Sandia National Laboratories
Livermore CA 94551-0969
(510)294-2435

Dr John Larue
Department of Mechanical
Engineering
University of California
Irvine CA 92717

Dr A Laufer
Office of Energy Research
U. S. Department of Energy
1000 Independence Avenue, N.W.
Washington DC 20585
(202)903-5820
allan.laufer%er@mailgw.er.doe.gov

Dr Normand Laurendeau
Department of Mechanical
Engineering
Purdue University
West Lafayette IN 47907
(317)494-2713
Laurende@ecn.purdue.edu

Dr Moshe Lavid
ML Energia, Inc.
P. O. Box 1468
Princeton NJ 08540
(609)799-7970

Dr C K Law
Department of Mechanical and
Aerospace Engineering
Princeton University
Princeton NJ 08544-5263
(609)258-5271
FAX:258-6233
cklaw@princeton.edu

Dr C C Lee
Environmental Protection
Agency
Cincinnati OH 45268
(513)569-7520

Dr Spiro Lekoudis
Office of Naval Research
Mechanics Division, Code 432
800 North Quincy Street
Arlington VA 22217-5000
(703)696-4406

Dr Anthony Leonard
Graduate Aeronautical Labs
California Institute of
Technology
Pasadena CA 91125
(818)395-4465

Dr Jay Levine
OLAC PL/RKFA
10 East Saturn Boulevard
Edwards AFB CA 93524-7600
(805)275-6179
DSN 525-5454
FAX:275-6233
levine@plablink.ple.af.mil

Dr Chiping Li
Naval Research Laboratory
Code 6910, CCP&FD
Washington DC 20375-5344
(202)767-3254
FAX:767-4078
LI@lcp.nrl.navy.mil

Dr Paul Libby
Department of AMES 0310
9500 Gilman Drive
University of California
La Jolla CA 92093-0310
(619)534-3168
FAX:534-4543
libby@ames.ucsd.edu

Dr Wilbert Lick
Department of Mechanical and
Environmental Engineering
University of California
Santa Barbara CA 93106

Dr Hans Liepmann
Graduate Aeronautical Labs
California Institute of
Technology
Pasadena CA 91125
(818)395-4535

Dr. Charles L. Liotta
Department of Chemical Engrg
Georgia Institute of
Technology
Atlanta GA 30332-0100
(404)853-9344
FAX:894-6956

Dr Marshall Long
Department of Mechanical
Engineering
Yale University
New Haven CT 06520
(203)432-4229

Dr Lyle N Long
Department of Aerospace Engrg
233 Hammond Building
Pennsylvania State University
University Park PA 16802
(814)865-1172
lnl@long.aero.psu.edu

Dr F E Lytle
Department of Chemistry
Purdue University
West Lafayette IN 47907
(317)494-5261

Dr Bruce MacDonald
Research Applications Division
Systems Research Labs, Inc.
2800 Indian Ripple Road
Dayton OH 45440-3696
(513)252-2706

Dr Edward Mahefkey
WL/POOC-5
Wright-Patterson AFB OH 45433-6563
(937)255-6241
DSN 785-6241

Mr Nick Makris
SA-ALC/SFT
Kelly AFB TX 78241-5000
AV945-8212
FAX:945-9964

Dr David Mann
U. S. Army Research Office
P. O. Box 12211
4300 South Miami Boulevard
Research Triangle Pk NC 27709-2211
(919)549-4249
DSN 832-4249
FAX:549-4310
dmann@aro-emh1.army.mil

Dr Nagi Mansour
Computational Fluid Mechanics
Branch, RFT 202A-1
NASA Ames Research Center
Moffett Field CA 94035
(415)604-6420

Dr Frank Marble
Engrg. and Appl. Sci. Dept.
California Institute of
Technology
Pasadena CA 91125
(818)395-4784

Dr John Marek
NASA Lewis Research Center
21000 Brookpark Road
Cleveland OH 44135-3127

Dr Bruce Masson
PL/LIDD
3550 Aberdeen Avenue, SE
Building 401
Kirtland AFB NM 87117-5776
(505)844-0208
DSN 244-0208

Dr James McDonald
Code 6110
Naval Research Laboratory
Chemistry Division
Washington DC 20375-5342
(202)767-3340
DSN 297-3340

Dr D K McLaughlin
233 Hammond Building
Pennsylvania State University
University Park PA 16802
(814)865-2569

Dr James McMichael
AFOSR/NA
110 Duncan Avenue, Suite B115
Bolling AFB DC 20332-8050
(202)767-4936
DSN 297-4936
FAX:767-4988
james.mcmichael@afosr.af.mil

Dr Constantine M Megaridis
University of Illinois-Chicago
Mechanical Engineering Dept
842 West Taylor Street
Chicago IL 60607-7022
(312)996-3436
(312)996-5317
FAX: 413-0447
cmm@dino.me.uic.edu

Dr A M Mellor
Mech & Matls Engrg Dept
512 Kirkland Hall
Vanderbilt University
Nashville TN 37240
(615)343-6214
FAX:343-6687

Dr Lynn Melton
Programs in Chemistry
University of Texas, Dallas
P. O. Box 830688
Richardson TX 75083-0688
(972)883-2913
(972)680-2163
FAX:883-2925
melton@utdallas.edu

Dr R Metcalfe
Department of Mechanical
Engineering
University of Houston
Houston TX 77004
(713)749-2439

Dr Michael M Micci
Department of Aerospace Engrg
233 Hammond Building
Pennsylvania State University
University Park PA 16802
(814)863-0043
(814)692-8751
FAX:865-7092
micci@henry2.aero.psu.edu

Dr Richard Miller
Office of Naval Research
Mechanics Division, Code 432
800 North Quincy Street
Arlington VA 22217-5000
(202)696-4406
FAX:696-0934
miller@ocnr-hq.navy.mil

Dr Andrzej Miziolek
Ignition and Combustion Branch
Interior Ballistics Division
Army Research Laboratory
Aberdeen Proving Gnd MD 21005-5066
(410)278-6157
FAX:278-6094

Dr Parviz Moin
Center for Turbulence Research
Stanford University
Stanford CA 94305-3032
(415)725-2081

Dr. H. C. Mongia
Manager, Combustion Technology
GE Aircraft Engines
One Neumann Way, M/D A404
Cincinnati OH 45215-6301
(513)243-2552
FAX:243-2538

Dr P J Morris
233-L Hammond Building
Pennsylvania State University
University Park PA 16802
(814)863-0157

Dr Edward Mularz
Attn: AMSRL-VP-C
NASA Lewis Res. Ctr., MS 77-12
21000 Brookpark Road
Cleveland OH 44135-3191
(216)433-5850
FAX:433-3720
Edward.Mularz@lerc.nasa.gov

Dr M G Mungal
Department of Mechanical
Engineering
Stanford University
Stanford CA 94305-3032
(415)725-2019
(408)257-6702
FAX:723-1748
mungal@leland.stanford.edu

Dr Phillip E Muntz
Department of Aerospace Engrg
Univ of Southern California
854 West 36th Place, RRB 101
Los Angeles CA 90089-1191
(213)740-5366

Dr Arje Nachman
AFOSR/NM
110 Duncan Avenue, Suite B115
Bolling AFB DC 20332-8050
(202)767-5028
DSN 297-5028
FAX:404-7496
arje.nachman@afosr.af.mil

Dr Abdollah Nejad
WL/POPT
Building 18
1950 Fifth Street, Suite 10
Wright-Patterson AFB OH 45433-7251
(937)255-9991
DSN 785-9991
FAX:255-1759
nejadas@possum.appl.wpafb.af.mil

Dr Herbert Nelson
Code 6110, Chemistry Division
Naval Research Laboratory
4555 Overlook Avenue, SW
Washington DC 20375-5342
(202)767-3686

Dr David Nixon
NWING, Inc.
883 North Shoreline Boulevard
Suite B200
Mountain View CA 94043
(415)254-0202
FAX961-9286

Dr G B Northam
NASA Langley Research Center
MS 188B
Hampton VA 23681
(804)864-6248
g.b.northam@larc.nasa.gov

Dr. Michael Nusca
AMSRL-WT-PC
US Army Research Laboratory
Aberdeen Proving Ground MD 21005-5066
(410)278-6108
DSN 298-6108
FAX: 278-7333
nusca@arl.army.mil

Dr A K Oppenheim
Department of Mechanical
Engineering
University of California
Berkeley CA 94720
(415)642-0211

Dr Elaine Oran
LCP&FD, Code 6404
US Naval Research Laboratory
4555 Overlook Avenue, SW
Washington DC 20375-5344
(202)767-2960
FAX:767-4798
ORAN@lcp.nrl.navy.mil

Dr Simon Ostrach
Case Western Reserve Univ
Department of Mechanical and
Aerospace Engineering
Cleveland OH 44106

Dr T E Parker
Engineering Division
Colorado School of Mines
Golden CO 80401-1887
(303)273-3657
FAX:273-3602
tparker@mines.colorado.edu

Dr Timothy Parr
Naval Air Warfare Center
Weapons Division
C02392
China Lake CA 93555-6001
(619)939-3367
FAX:939-6569
t.parr@genie.geis.com

Dr. Phillip H. Paul
MS 9051
Sandia National Laboratories
P. O. Box 969
Livermore CA 94551-9051
(510)294-1465
FAX: 294-1012
phpaul@sandia.gov

Dr Alex Pechenik
AFOSR/NA
110 Duncan Avenue, Suite B115
Bolling AFB DC 20332-8050
(202)767-4962
DSN 297-4962
FAX:767-4988
alex.pechenik@afosr.af.mil

Dr S S Penner
Center for Energy and
Combustion Research, 0411
University of California
La Jolla CA 92093-0411
(619)534-4284

Dr Richard Peterson
Department of Mechanical
Engineering
Oregon State University
Corvallis OR 97331-6001
(503)754-2567

Dr Lisa Pfefferle
Department of Chemical
Engineering
Yale University
New Haven CT 06520-8286
(203)432-2222
FAX:432-7232
pfefferle@htcre.eng.yale.edu

Dr Emil Pfender
Department of Mechanical Engrg
125 Mechanical Engineering
The University of Minnesota
Minneapolis MN 55455

Dr W M Pitts
National Institute of
Standards and Technology
Center for Fire Research
Gaithersburg MD 20899
(301)975-6486

Dr Robert Pitz
Department of Mechanical and
Materials Engineering
Vanderbilt University
Nashville TN 37235
(615)322-0209
FAX:343-8730
pitzrw@ctrvan.vanderbilt.edu

Dr S B Pope
Department of Mechanical and
Aerospace Engineering
Cornell University
Ithaca NY 14853-1301
(607)255-4314
FAX:255-1222
pope@mae.cornell.edu

Dr C L Proctor II
Department of Mechanical
Engineering
University of Florida
Gainesville FL 32611
(904)392-7555

Dr Herschel Rabitz
Department of Chemistry
Princeton University
Princeton NJ 08544-1009
(609)258-3917
FAX:258-6746

Dr. Larry Rahn
MS 9056
Sandia National Laboratories
Box 969
Livermore CA 94551-0969
(510)294-2091
FAX: 294-1012
rahn@sandia.gov

Dr S R Ray
National Institute of
Standards and Technology
Center for Chemical Engrg
Gaithersburg MD 20899

Dr. Mohan K. Razdan
Allison Engine Company
P.O. Box 420
Speed Code T-14
Indianapolis IN 46206-0420
(317)230-6404
FAX:230-3691
iemkr@agt.gmeds.com

Mr. Robert Reed
Sverdrup Technology, Inc.
AEDC
1099 Avenue C
Arnold AFB TN 37389-9013
(615)454-4648
DSN 340-4648
(615)454-6317

Dr R G Rehm
National Institute of
Standards and Technology
Center for Fire Research
Gaithersburg MD 20899
(301)975-2704

Dr Rolf D Reitz
Mechanical Engineering Dept
University of Wisconsin
1500 Johnson Drive
Madison WI 53706
(608)262-0145
FAX:262-6717

Dr M Renksizbulut
Department of Mechanical
Engineering
University of Waterloo
Waterloo, Ontario CN N2L 3G1
(519)885-1211
Ext 3977

Dr Eli Reshotko
Case Western Reserve Univ
Department of Mechanical and
Aerospace Engineering
Cleveland OH 44106
(216)368-6447
FAX:368-6445
exr3@po.cwru.edu

Dr David Reuss
Fluid Mechanics Department
General Motors Research Labs
30500 Mound Road
Warren MI 48090-9055
(313)986-0029

Dr William Reynolds
Department of Mechanical
Engineering
Stanford University
Stanford CA 94305-3032
(415)723-3840

Dr. Kyung T. Rhee
Department of Mechanical and
Aerospace Engineering
Rutgers, The State Univ of NJ
Piscataway NJ 08854

Dr James Riley
Mechanical Engineering Dept
University of Washington
Seattle WA 98195
(206)543-5347
73671.737@Compuserve.com

Dr Michael Roco
National Science Foundation
Chemical and Thermal Syst Div
4201 Wilson Boulevard
Arlington VA 22230
mroco@nsf.gov

Mr Wayne Roe
OLAC PL/XRX
5 Pollux Drive
Edwards AFB CA 93523-5000
(805)275-5206
DSN 525-5206
FAX:275-5852

Mr. Gerald A. Roffe
GASL
77 Raynor Avenue
Ronkonkoma NY 11779

Dr Won B Roh
Department of Engrg Physics
Air Force Institute of
Teechnology
Wright-Patterson AFB OH 45433-6583

Dr U S Rohatgi
Department of Nuclear Energy
Brookhaven National Laboratory
Upton NY 11973
(516)282-2475

Dr Glenn Rolader
Science Applications
International Corporation
1247-B N Eglin Parkway
Shalimar FL 32579
DSN 872-0391
(904)882-0391

Dr W M Roquemore
WL/POSC
Building 490
1790 Loop Road, N
Wright-Patterson AFB OH 45433-7103
(937)255-6813
DSN 785-6813
FAX:255-1125
melr@snake.appl.wpafb.af.mil

Dr Anatol Roshko
Graduate Aeronautical Labs
California Institute of
Technology
Pasadena CA 91125
(818)395-4484

Dr Daniel Rosner
Department of Chemical
Engineering
Yale University
New Haven CT 06520-8286
(203)432-4391
FAX:432-7232
Daniel.Rosner@QuickMail.Yale.edu

Dr John Ross
Department of Chemistry
Stanford University
Stanford CA 94305-3032
(415)723-9203

Dr Gabriel Roy
Office of Naval Research
Mechanics Division, Code 1132
800 North Quincy Street
Arlington VA 22217-5000
(703)696-4406
FAX:696-0934
roy@ocnr-hq.navy.mil

Mr Kurt Sacksteder
NASA Lewis Research Center
MS 500-217
21000 Brookpark Road
Cleveland OH 44135
(216)433-2857

Dr Leonidas Sakell
AFOSR/NA
110 Duncan Avenue, Suite B115
Bolling AFB DC 20332-8050
(202)767-4935
DSN 297-4935
FAX:767-4988
len.sakell@afosr.af.mil

Dr Michael Salkind
President
Ohio Aerospace Institute
22800 Cedar Point Road
Cleveland OH 44142
(216)962-3002
FAX:962-3120
MichaelSalkind@oai.org

Dr Mohammad Samimy
Ohio State University
Mechanical Engineering Dept
206 West 18th Street
Columbus OH 43210-1107
(614)422-6988
(614)848-9439
FAX:292-3163
msamimy@magnus.acs.ohio-state.edu

Dr G S Samuelsen
Department of Mechanical
Engineering
University of California
Irvine CA 92717
(714)856-5468

Dr Billy Sanders
University of California
Davis CA 95616

Dr Joseph Sangiovanni
United Technologies Research
Center
Silver Lane
East Hartford CT 06108
(860)610-7328

Dr Lakshmi Sankar
School of Aerospace Engrg
Georgia Institute of
Technology
Atlanta GA 30332
(404)894-3014

Dr Domenic Santavicca
Department of Mechanical
Engineering
Pennsylvania State University
University Park PA 16802
(814)863-1863

Dr R J Santoro
Department of Mechanical
Engineering
Pennsylvania State University
University Park PA 16802-2320
(814)863-1285
FAX:865-3389
rjs2@email.psu.edu

Dr Sutanu Sarkar
Department of Applied Mech
and Engr Science, MC 0411
University of California
La Jolla CA 92093-0411
(619)534-8243
FAX: 534-7599
sarkar@ames.ucsd.edu

Mr William Scallion
NASA Langley Research Center
Mail Stop 408
Hampton VA 23665
(804)864-5235

Dr Klaus Schadow
Naval Air Warfare Center
Code 3892
China Lake CA 93555-6001
(619)939-6532
DSN 437-6532
FAX:939-6569

Dr John Schaefer
Energy and Environmental Div.
Acurex Corporation
555 Clyde Ave., P. O. Box 7555
Mountain View CA 94039

Dr W H Schofield
Aeronautical Research Labs
506 Lorimer St, Fishermen's Bn
Box 4331, P O
Melbourne, Victoria AUSTRALIA 3001

Maj Scott Schreck
AFOSR/NM
110 Duncan Avenue, Suite B115
Bolling AFB DC 20332-8050
(202)767-5028
DSN 297-5028
FAX:404-7496
scott.schreck@afosr.af.mil

Dr. Ernest Schwarz
Propulsion Systems Division
ATTN: DRSTA-RGD
USA Tank-Automotive Command
Warren MI 48397-5000

Mr. Lee Scuderi
McDonnell Douglas Aerospace
P.O. Box 516
St. Louis MO 63166-0516

Dr D J Seery
United Technologies Research
Center
Silver Lane
East Hartford CT 06108

Dr. Corin Segal
AeMES Department
University of Florida
P.O. Box 116250
Gainesville FL 32611-6250
(352)392-6132
FAX:392-7303
corin@AeMES.aero.ufl.edu

Dr Hratch Semerjian
National Institute of
Standards and Technology
Chem Sci & Tech Laboratory
Gaithersburg MD 20899
(301)975-3145
FAX:975-3845
HRATCH@micf.nist.gov

Dr Robert V. Serauskas
Gas Research Institute
8600 West Bryn Mawr Avenue
Chicago IL 60631
(312)399-8208
FAX:864-2774
rserausk@gri.org

Dr K Seshadri
Center for Energy and
Combustion Research, 0407
University of California
La Jolla CA 92093-0407
(619)534-4876

Dr G S Settles
309 Mechanical Engrg Building
Pennsylvania State University
University Park PA 16802
(814)863-1504

Dr Robert Shaw
Division of Chemical and
Biological Sciences
U S Army Research Office
Research Triangle Park NC 27709-2211
(919)549-0641

Dr. Adam Siebenhaar
Aerojet Propulsion Division
P.O. Box 13222
Sacramento CA 95813-6000

Mr David Siegel
Chief of Naval Research,
804 BCT1
800 North Quincy Street
Arlington VA 22217-5660
(703)696-4771
FAX:696-4274

Dr William Sirignano
Department of Mechanical and
Aerospace Engineering
University of California
Irvine CA 92717-3975
(714)824-3700
FAX:824-3773
sirignan@uci.edu

Dr Gregory Smith
Department of Chem Kinetics
SRI International
333 Ravenswood Avenue
Menlo Park CA 94025-3493
(415)859-3496

Mr. Davey Smith
Northrop Grumman Corporation
B-2 Division Dayton Office
2850 Presidential Dr., Ste 100
Fairborn OH 45324

Dr Alan Stanton
Southwest Sciences, Inc.
1570 Pacheco Street
Suite E-11
Santa Fe NM 87501
(505)984-1322

Dr F Dee Stevenson
Office of Basic Energy Science
U. S. Department of Energy
1000 Independence Avenue, N W
Washington DC 20585

Dr David Stewart
Department of Theoretical and
Applied Mechanics
University of Illinois
Urbana IL 61801

Dr Anthony Strawa
NASA Ames Research Center
MS 230-2
Moffett Field CA 94035
(415)604-3437

Dr Robert M. Stubbs
Mail Stop 5-11
NASA Lewis Research Center
21000 Brookpark Road
Cleveland OH 44135-3127
(216)433-6303
FAX:433-5802
rstubbs@lerc.nasa.gov

Dr Geoffrey J Sturgess
ISSI
3845 Woodhurst Court
Dayton OH 45430
(513)252-2706

Dr B Sturtevant
Engrg and Appl Sci Dept
California Institute of
Technology
Pasadena CA 91125

Dr G Sullins
Applied Physics Laboratory
Johns Hopkins University
Johns Hopkins Road
Laurel MD 20707-6099
(301)953-5000

Dr Larry Talbot
Department of Mechanical
Engineering
University of California
Berkeley CA 94720
(415)642-6780

Dr. Douglas Talley
OLAC PL/RKFA
9 Antares Road
Edwards AFB CA 93524-7660
(805)275-6174
DSN 525-6174

Dr. Richard Tankin
Mechanical Engineering Dept
Northwestern University
Evanston IL 60208-3111
(847)491-3532
FAX:491-3915

Dr Julian Tishkoff
AFOSR/NA
110 Duncan Avenue, Suite B115
Bolling AFB DC 20332-8050
(202)767-0465
DSN 297-0465
FAX:767-4988
julian.tishkoff@afosr.af.mil

Dr T Y Toong
Department of Mechanical
Engineering
MIT
Cambridge MA 02139
(617)253-3358

Dr Michael Trenary
Department of Chemistry
The University of Illinois
Chicago IL 60680

Dr James Trolinger
MetroLaser
18006 Skypark Circle
Suite 108
Irvine CA 92714-6428
(714)553-0688
FAX:553-0495
jtrolinger@vmsa.oac.uci.edu

Dr P J Waltrup
Applied Physics Laboratory
Johns Hopkins University
Johns Hopkins Road
Laurel MD 20707-6099
(301)953-5000
Ext. 5626

Dr Joe Wanders
AL/EQS
139 Barnes Drive
Tyndall AFB FL 32403-5319
(904)283-6026
DSN 523-6026

Dr David Weaver
OLAC PL/RKFA
10 East Saturn Boulevard
Edwards AFB CA 93524-7660
(805)275-6177
DSN 525-6177
FAX:275-5471
weaver@scihpl.ple.af.mil

Dr Charles Westbrook
Lawrence Livermore National
Laboratories
P. O. Box 808
Livermore CA 94550

Dr. Phillip R. Westmoreland
Department of Chemical
Engineering
University of Massachusetts
Amherst MA 01003
(413)545-1750
(413)545-2507
(413)545-1647
westm@ecs.umass.edu

Dr James Whitelaw
Department of Mechanical Engrg
Imperial College of Science
and Technology
London SW7 2BX UK

Dr Forman Williams
Center for Energy and
Combustion Research, 0310
University of California
La Jolla CA 92093-0310
(619)534-5492
(619)534-4285
FAX: 534-5354
faw@ames.ucsd.edu

Dr Michael Winter
United Technologies Research
Center
411 Silver Lane, MS/90
East Hartford CT 06108
(860)610-7805
(860)397-1420
FAX:610-7911
mw@utrc.utc.com

Mr Steve Wirick
WL/AAWW-3
Wright-Patterson AFB OH 45433-6543
(937)255-4174
DSN 785-4174
FAX:476-4642

Dr Bernard T Wolfson
Wolfson Associates
International
4797 Lake Valencia Blvd West
Palm Harbor FL 33563
(813)786-3007

Dr Timothy Troutt
Department of Mechanical
Engineering
Washington State University
Pullman WA 99164-2920

Dr. Gretar Tryggvason
Dept of Mech Engrg & Appl Mech
2350 Hayward, Room 2250
The University of Michigan
Ann Arbor MI 48109-2125
(313)763-1049
FAX:764-4256
gretar@umich.edu

Dr Allen Twarowski
Rockwell International Sci Ctr
1049 Camino dos Rios
P O Box 1085
Thousand Oaks CA 91360
(805)373-4576
FAX:373-4775
ajtwarow@scimail.remnet.rockwell.com

Dr C J Ultee
United Technologies Research
Center
Silver Lane
East Hartford CT 06108

Dr A D Vakili
University of Tennessee
Space Institute
Tullahoma TN 37388

Dr John Vanderhoff
Ballistic Research Laboratory
DRSMC-BLI(A)
Aberdeen Proving Ground MD 21005
(410)278-6642

Dr S P Vanka
Department of Mechanical
and Industrial Engrg
University of Illinois
Urbana IL 61801

Dr James Verdieck
Rockwell International
Rocketdyne Div, M/S FA26
6633 Canoga Avenue
Canoga Park CA 91303
(818)700-4709

Dr Juan A. Vitali
WL/FIVCO (Stop 37)
139 Barnes Drive, Suite 2
Tyndall AFB FL 32403-5323
(904)283-9708
DSN 523-9708
FAX:283-9707
75023.56@compuserve.com

Dr Robert Vondra
PO Box 596
Wrightwood CA 92397
(619)249-3451

Dr Joda Wormhoudt
Aerodyne Research, Inc.
45 Manning Road
Manning Park Research Center
Billerica MA 01821-3976
(508)663-9500
FAX:663-4918

Dr J M Wu
University of Tennessee
Space Institute
Tullahoma TN 37388

Dr. Vigor Yang
Propulsion Engrg Rsrch Ctr
The Pennsylvania State Univ
111 Research Building East
University Park PA 16802-2320
(814)863-1502
FAX: 865-4784
vigor@arthur.psu.edu

Dr Richard Yetter
Department of Mechanical and
Aerospace Engineering
Princeton University
Princeton NJ 08544-5263
(609)258-2947
FAX:258-1939
rich@dante.princeton.edu

Dr Pui-kuen Yeung
School of Aerospace Engrg
Georgia Institute of
Technology
Atlanta GA 30332-0150
(404)894-9341
FAX:894-2760
yeung@peach.gatech.edu

Dr Shaye Yungster
Institute for Computational
Mechanics in Propulsion
NASA Lewis Research Ctr
Cleveland OH 44135
(216)433-6680

Dr Michael Zachariah
National Institute of
Standards and Technology
Center for Chemical Engrg
Gaithersburg MD 20899
(301)975-2063

Mr Fred Zarlingo
Code 3246
Naval Air Warfare Center
China Lake CA 93555-6001
(619)939-7395
DSN 437-7395

Dr. Ben T. Zinn
School of Aerospace Engrg
Georgia Institute of
Technology
Atlanta GA 30332-0150
(404)894-3033
(404)894-3032
FAX:894-2760
ben.zinn@aerospace.gatech.edu

Dr E E Zukoski
Engrg. and Appl. Sci. Dept.
California Institute of
Technology
Pasadena CA 91125
(818)395-4785